



**L-Università ta' Malta**  
**Faculty of Engineering**

MASTER OF SCIENCE IN ENGINEERING DISSERTATION

---

# Control Analysis and Validation of a High Dynamic Motor Starter

---

DANIEL LENDI

*Supervised by:*

DR. ING. REIKO RAUTE

*Co-supervised by:*

PROF. ING. SIMON G. FABRI

*A dissertation submitted in partial fulfilment of the requirements for the degree of  
Master of Science in Engineering*

*by the*

Faculty of Engineering

February 2021



L-Università  
ta' Malta

## **University of Malta Library – Electronic Thesis & Dissertations (ETD) Repository**

The copyright of this thesis/dissertation belongs to the author. The author's rights in respect of this work are as defined by the Copyright Act (Chapter 415) of the Laws of Malta or as modified by any successive legislation.

Users may access this full-text thesis/dissertation and can make use of the information contained in accordance with the Copyright Act provided that the author must be properly acknowledged. Further distribution or reproduction in any format is prohibited without the prior permission of the copyright holder.

# Control Analysis and Validation of a High Dynamic Motor Starter

## *Abstract*

Connecting a motor directly to the supply can lead to an inrush current equal to 5-8 times the rated current of motor during starting. This can negatively affect the power source the motor is connected to and other equipment connected to the same power source. Hence, dedicated motor starters are employed for motors exceeding a certain size. One such motor starter is the soft starter, which reduces the voltage applied to the motor during starting. The novel High Dynamic Motor Starter (HDMS) is a soft starter for single-phase induction motors based on the Buck converter principle. It reduces the inrush supply current during starting, while still supplying a sufficiently high motor current in order to start the motor. The HDMS contains an input LC filter in order to reduce the ripple on the supply current, which may cause stability issues due to its natural resonance frequency.

This dissertation carries out a stability analysis of the novel HDMS prototype. For this analysis, the HDMS is modelled in state space form and a component-level simulation model is established. A state feedback regulator is proposed as an alternative current control system and the performance of both current control systems is compared. The performance is based on locked rotor tests and motor soft-starts. During the locked rotor tests, the supply and motor winding currents and the resulting starting torque are recorded. Flicker tests are carried out for both locked rotor and motor soft-starting tests in order to investigate the current controllers' effect on the power source. Based on these performance tests, a current controller is chosen and finally tested for robustness towards variations in the motor winding and grid impedance parameters.

# Contents

<b>Abstract</b>	<b>i</b>
<b>Contents</b>	<b>ii</b>
<b>List of Figures</b>	<b>vi</b>
<b>List of Tables</b>	<b>x</b>
<b>List of Acronyms</b>	<b>xi</b>
<b>List of Symbols</b>	<b>xii</b>
<b>1 Introduction</b>	<b>1</b>
1.1 Objectives . . . . .	1
1.2 Dissertation Layout . . . . .	2
<b>2 Technical Background</b>	<b>3</b>
2.1 Introduction . . . . .	3
2.2 Introduction to State Space Theory . . . . .	3
2.3 Non-linear Systems . . . . .	5
2.4 Non-linear Control Methods . . . . .	6
2.5 Limit Cycles . . . . .	6
2.6 Linearisation around an Equilibrium Point . . . . .	9
2.6.1 Jacobian Linearisation of State Space Systems . . . . .	10
2.7 Single Phase Induction Motors . . . . .	12
2.8 Soft Starters . . . . .	13
2.9 High Dynamic Motor Starter . . . . .	14
2.9.1 Introduction . . . . .	14
2.9.2 Circuit Description . . . . .	15
2.9.3 Regions of Operation . . . . .	16
2.9.4 Control Algorithm . . . . .	18
2.9.5 Software Implementation . . . . .	19
<b>3 Simulation Model</b>	<b>23</b>
3.1 Introduction . . . . .	23
3.2 Low-Voltage Test . . . . .	23

---

3.3	Determination of Filter Characteristics . . . . .	26
3.4	Simulation Model . . . . .	29
3.5	Conclusion . . . . .	30
<b>4</b>	<b>System Stability Analysis</b>	<b>32</b>
4.1	Introduction . . . . .	32
4.2	Stability Analysis of the Plant . . . . .	32
4.2.1	State Space Representation of the Plant . . . . .	32
4.2.2	Linearisation of Plant Equations . . . . .	34
4.2.3	Stability Analysis of Plant Equations . . . . .	35
4.3	Stability Analysis of Closed-Loop System . . . . .	38
4.3.1	State Space Representation of Closed-Loop System . . . . .	38
4.3.2	Linearisation of Closed-Loop System Equations . . . . .	39
4.3.3	Stability Analysis of Closed-Loop System Equations . . . . .	41
4.3.3.1	Linear Closed-Loop Model Analysis . . . . .	46
4.3.3.2	Phase Plane Analysis of Limit Cycle at 325V . . . . .	50
4.3.3.3	Lower Threshold of Limit Cycle . . . . .	55
4.3.4	Stability Analysis of Power Electronics Simulation . . . . .	61
4.4	Conclusion . . . . .	68
<b>5</b>	<b>Hardware Setup</b>	<b>70</b>
5.1	Introduction . . . . .	70
5.2	Test Setup . . . . .	70
5.3	Load Cell Calibration . . . . .	75
5.4	Conclusion . . . . .	78
<b>6</b>	<b>State Feedback Regulator</b>	<b>79</b>
6.1	Introduction . . . . .	79
6.2	State Feedback Regulator Methodology . . . . .	79
6.3	Design of State Feedback Regulator . . . . .	81
6.3.1	Regulator Equilibrium Point . . . . .	81
6.3.2	Pole Placement of State Feedback Regulator . . . . .	83
6.3.2.1	Controllability Matrix . . . . .	83
6.3.2.2	Pole Placement through direct substitution . . . . .	83
6.3.3	Controller Testing . . . . .	85
6.3.3.1	Mathematical Simulation Model . . . . .	85
6.3.3.2	Step Response . . . . .	86
6.3.3.3	Voltage Sweep Test . . . . .	87
6.3.3.4	Controller Tuning . . . . .	89
6.3.3.5	Power Electronics Simulation Test . . . . .	92
6.3.3.6	Hardware Test . . . . .	94
6.4	Conclusion . . . . .	96
<b>7</b>	<b>Performance Tests</b>	<b>97</b>
7.1	Introduction . . . . .	97

---

7.2	Direct On Line Start . . . . .	100
7.3	30% Duty Cycle Controller Design . . . . .	102
7.3.1	State Feedback Regulator . . . . .	102
7.3.1.1	Locked Rotor Simulation Results . . . . .	102
7.3.1.2	Locked Rotor Hardware Results . . . . .	104
7.3.1.3	Motor Soft-Start Hardware Results . . . . .	106
7.3.2	HDMS Prototype Controller . . . . .	106
7.3.2.1	Locked Rotor Simulation Results . . . . .	106
7.3.2.2	Locked Rotor Hardware Results . . . . .	108
7.3.2.3	Motor Soft-Start Hardware Results . . . . .	109
7.3.3	Conclusion . . . . .	110
7.4	40% Duty Cycle Controller Design . . . . .	111
7.4.1	Introduction . . . . .	111
7.4.2	State Feedback Regulator . . . . .	111
7.4.2.1	Locked Rotor Simulation Results . . . . .	111
7.4.2.2	Locked Rotor Hardware Results . . . . .	113
7.4.2.3	Motor Soft-Start Hardware Results . . . . .	114
7.4.3	HDMS Prototype Controller . . . . .	115
7.4.3.1	Locked Rotor Simulation Results . . . . .	115
7.4.3.2	Locked Rotor Hardware Results . . . . .	116
7.4.3.3	Motor Soft-Start Hardware Results . . . . .	117
7.4.4	Conclusion . . . . .	118
7.5	50% Duty Cycle Controller Design . . . . .	119
7.5.1	State Feedback Regulator . . . . .	119
7.5.1.1	Locked Rotor Simulation Results . . . . .	119
7.5.1.2	Locked Rotor Hardware Results . . . . .	121
7.5.1.3	Motor Soft-Start Hardware Results . . . . .	122
7.5.2	HDMS Prototype Controller . . . . .	123
7.5.2.1	Locked Rotor Simulation Results . . . . .	123
7.5.2.2	Locked Rotor Hardware Results . . . . .	124
7.5.2.3	Motor Soft-Start Hardware Results . . . . .	125
7.5.3	Conclusion . . . . .	126
7.6	Robustness Testing . . . . .	127
7.6.1	Introduction . . . . .	127
7.6.2	50% increase in motor winding parameters . . . . .	127
7.6.3	50% reduction in motor winding parameters . . . . .	128
7.6.4	Addition of grid impedance . . . . .	130
7.7	Conclusion . . . . .	132
<b>8</b>	<b>Conclusion</b>	<b>134</b>
<b>9</b>	<b>Future Work</b>	<b>137</b>

**A Flicker Test Reports**

**141**

# List of Figures

2.1	Block diagram representing the general state space system of equations	4
2.2	Pole-zero map and step response for example system . . . . .	7
2.3	Examples of (a) stable, (b) unstable and (c) semi-stable limit cycles	8
2.4	Plot of a function $y = f(x)$ with a linearised model around $x^*, y^*$ . .	9
2.5	Diagram of single phase motor with start capacitor . . . . .	12
2.6	Diagram of single phase motor soft starter . . . . .	13
2.7	Plot of typical soft-start firing angle sequence . . . . .	14
2.8	Circuit diagram of HDMS . . . . .	15
2.9	Plot of operating regions . . . . .	16
2.10	Plot of duty cycle . . . . .	17
2.11	Plot of supply current, motor winding current and voltage . . . . .	18
2.12	Diagram of HDMS compensator . . . . .	18
2.13	Flowchart of HDMS interrupt routine . . . . .	21
2.14	Plot of soft-start with currents and device states . . . . .	22
3.1	Equivalent circuit of single phase motor with low AC voltage . . . . .	23
3.2	Diagram of motor winding at standstill . . . . .	24
3.3	Plot of main winding voltage and current for parameter acquisition	24
3.4	Plot of main winding voltage and current for parameter acquisition with new setup . . . . .	26
3.5	Diagram of step response test for ADC filter characteristics . . . . .	26
3.6	Plot of supply current and synchronisation signal . . . . .	27
3.7	Plot of actual and approximated supply current . . . . .	28
3.8	S-function and PWM generation implemented in simulation model .	29
3.9	Simscape simulation model circuitry . . . . .	31
4.1	Circuit diagram of plant including input LC-filter and damping resistor	33
4.2	Simulation of non-linear plant differential equations . . . . .	36
4.3	Duty cycle ramp applied to plant . . . . .	36
4.4	Plant state variables with duty cycle ramp applied . . . . .	37
4.5	Block diagram of complete closed-loop system . . . . .	38
4.6	Simulation of non-linear closed-loop system differential equations . .	41
4.7	Supply voltage applied to closed-loop system . . . . .	42
4.8	Closed-loop system state variables due to first supply voltage step .	44
4.9	Closed-loop system state variables due to supply voltage steps . . .	45
4.10	System poles for supply voltages $50V \rightarrow 350V$ . . . . .	47

4.11	Pole-zero map for linear model at $v_S = 325V$ . . . . .	49
4.12	Step response for linear model at $v_S = 325V$ . . . . .	49
4.13	Phase trajectory for $i_S$ and $v_C$ . . . . .	51
4.14	Plot of $i_S$ and $v_C$ against time . . . . .	51
4.15	Phase trajectories of $i_S$ and $v_C$ for different initial conditions . . . . .	53
4.16	Plot of $i_S$ and $v_C$ against time for different initial conditions . . . . .	54
4.17	Pole-zero map for linear model at $v_S = 55.1V$ . . . . .	55
4.18	Step response for linear model at $v_S = 55.1V$ . . . . .	56
4.19	Pole-zero map for linear model at $v_S = 55.2V$ . . . . .	57
4.20	Step response for linear model at $v_S = 55.2V$ . . . . .	57
4.21	System state variables for supply voltage $v_S = 55.1V$ . . . . .	59
4.22	System state variables for supply voltage $v_S = 55.2V$ . . . . .	60
4.23	Closed-loop system state variables of power electronics model due to first supply voltage step . . . . .	62
4.24	Plot of capacitor voltage for first supply voltage step . . . . .	63
4.25	Closed-loop system state variables of power electronics model due to supply voltage steps . . . . .	64
4.26	Closed-loop system state variables of power electronics model due to supply voltage steps without low-pass filter in the supply current measurement . . . . .	65
4.27	Block diagram of complete closed-loop system with low-pass filter . . . . .	66
4.28	System poles with low-pass filter for supply voltages $50V \rightarrow 350V$ . . . . .	68
5.1	Block diagram representing the configuration of the hardware setup . . . . .	71
5.2	Photo of hardware setup . . . . .	72
5.3	Photo of HDMS prototype, terminal block, protection and debugger . . . . .	73
5.4	Photo of single-phase motor test setup . . . . .	74
5.5	Photo of single-phase motor nameplate . . . . .	75
5.6	Plot of weight vs. force sensor output voltage . . . . .	77
5.7	Plot of RMS current vs. force for DOL locked rotor tests . . . . .	78
6.1	Diagram of proposed state feedback regulator . . . . .	80
6.2	Closed-loop poles of designed state feedback regulator . . . . .	85
6.3	Mathematical simulation model of state feedback regulator . . . . .	86
6.4	Mathematical simulation model step response of supply current . . . . .	87
6.5	Plot of supply voltage for voltage sweep test . . . . .	87
6.6	Responses of duty cycle and supply current to supply voltage sweep for designed controller . . . . .	88
6.7	Tuned closed-loop poles . . . . .	89
6.8	Responses of duty cycle and supply current to supply voltage sweep with tuned controller . . . . .	91
6.9	Responses of duty cycle and supply current of tuned controller in power electronics model . . . . .	93
6.10	Plot of supply voltage sweep on hardware prototype . . . . .	94

---

6.11	Responses of duty cycle and supply current of tuned controller on hardware prototype . . . . .	95
7.1	Flicker test diagram . . . . .	98
7.2	Illustration of the half period RMS measurement . . . . .	99
7.3	Direct on line locked rotor test . . . . .	100
7.4	Direct on line start . . . . .	101
7.5	30% state feedback regulator simulation model duty cycle response	103
7.6	30% state feedback regulator simulation model supply and motor winding current response . . . . .	103
7.7	30% state feedback regulator hardware duty cycle response . . . . .	104
7.8	30% state feedback regulator hardware supply and motor winding current response . . . . .	104
7.9	30% state feedback regulator hardware supply and motor winding current response with auxiliary winding connected . . . . .	105
7.10	Motor soft-start with 30% state feedback regulator . . . . .	106
7.11	30% HDMS prototype current controller simulation model duty cycle response . . . . .	107
7.12	30% HDMS prototype current controller simulation model supply and motor winding current response . . . . .	107
7.13	30% HDMS prototype current controller hardware duty cycle response	108
7.14	30% HDMS prototype current controller hardware supply and motor winding current response . . . . .	109
7.15	Motor soft-start with 30% HDMS prototype current controller . . .	110
7.16	40% state feedback regulator simulation model duty cycle response	112
7.17	40% state feedback regulator simulation model supply and motor winding current response . . . . .	112
7.18	40% state feedback regulator hardware duty cycle response . . . . .	113
7.19	40% state feedback regulator hardware supply and motor winding current response . . . . .	113
7.20	Motor soft-start with 40% state feedback regulator . . . . .	114
7.21	40% HDMS prototype current controller simulation model duty cycle response . . . . .	115
7.22	40% HDMS prototype current controller simulation model supply and motor winding current response . . . . .	115
7.23	40% HDMS prototype current controller hardware duty cycle response	116
7.24	40% HDMS prototype current controller hardware supply and motor winding current response . . . . .	117
7.25	Motor soft-start with 40% HDMS prototype current controller . . .	118
7.26	50% state feedback regulator simulation model duty cycle response	120
7.27	50% state feedback regulator simulation model supply and motor winding current response . . . . .	120
7.28	50% state feedback regulator hardware duty cycle response . . . . .	121
7.29	50% state feedback regulator hardware supply and motor winding current response . . . . .	121

7.30	Motor soft-start with 50% state feedback regulator . . . . .	122
7.31	50% HDMS prototype current controller simulation model duty cycle response . . . . .	123
7.32	50% HDMS prototype current controller simulation model supply and motor winding current response . . . . .	123
7.33	50% HDMS prototype current controller hardware duty cycle response	124
7.34	50% HDMS prototype current controller hardware supply and motor winding current response . . . . .	125
7.35	Motor soft-start with 50% HDMS prototype current controller . . .	126
7.36	Duty cycle response for 50% increase in motor winding parameters .	128
7.37	Supply and motor winding currents response for 50% increase in motor winding parameters . . . . .	128
7.38	Duty cycle response for 50% reduction in motor winding parameters	129
7.39	Supply and motor winding currents response for 50% reduction in motor winding parameters . . . . .	129
7.40	Supply and motor winding currents response for $2 \times Z_{test}$ . . . . .	130
7.41	Duty cycle response for $2 \times Z_{test}$ with new $K_1$ and $K_I$ . . . . .	131
7.42	Supply and motor winding currents response for $2 \times Z_{test}$ with new $K_1$ and $K_I$ . . . . .	131
A.1	DOL flicker test result for locked rotor test . . . . .	141
A.2	DOL flicker test result for soft-start . . . . .	142
A.3	30% state feedback regulator flicker test result for locked rotor test	143
A.4	30% state feedback regulator flicker test result for soft-start . . . .	144
A.5	30% HDMS prototype current controller flicker test result for locked rotor test . . . . .	145
A.6	30% HDMS prototype current controller flicker test result for soft-start	146
A.7	40% state feedback regulator flicker test result for locked rotor test	147
A.8	40% state feedback regulator flicker test result for soft-start . . . .	148
A.9	40% HDMS prototype current controller flicker test result for locked rotor test . . . . .	149
A.10	40% HDMS prototype current controller flicker test result for soft-start	150
A.11	50% state feedback regulator flicker test result for locked rotor test	151
A.12	50% state feedback regulator flicker test result for soft-start . . . .	152
A.13	50% HDMS prototype current controller flicker test result for locked rotor test . . . . .	153
A.14	50% HDMS prototype current controller flicker test result for soft-start	154

# List of Tables

3.1	Simscape simulation component parameters . . . . .	30
4.1	Plant simulation parameters . . . . .	36
4.2	Closed-loop system simulation parameters . . . . .	42
5.1	Force sensor output voltages with increase in weight . . . . .	76
5.2	DOL locked rotor test data . . . . .	77
6.1	System parameters for equilibrium point . . . . .	82
6.2	Designed and tuned controller parameters . . . . .	90
7.1	30% controller parameters . . . . .	102
7.2	30% controller results . . . . .	110
7.3	40% controller parameters . . . . .	111
7.4	40% controller results . . . . .	118
7.5	50% controller parameters . . . . .	119
7.6	50% controller results . . . . .	126

# List of Acronyms

HDMS - High Dynamic Motor Starter

MCST - Malta Council for Science and Technology

DC - Direct Current

AC - Alternating Current

RMS - Root Mean Square

DOL - Direct On-Line

MCB - Miniature Circuit Breaker

OL - Thermal Overload Relay

PWM - Pulse Width Modulation

IGBT - Insulated-Gate Bipolar Transistor

ADC - Analogue to Digital Converter

LTI - Linear Time-Invariant

# List of Symbols

$n$  - System order

$t$  - Time

$\zeta$  - Damping coefficient

$\omega$  - Angular frequency

$\omega_n$  - Natural frequency of oscillation

$\omega_d$  - Damped frequency of oscillation

$G(s)$  - S-domain transfer function

$G_c(s)$  - S-domain compensator transfer function

$G_f(s)$  - S-domain filter transfer function

$v_S$  - Supply voltage

$v_C$  - Capacitor voltage

$i_T$  - Total supply current

$i_S$  - Supply current

$i_{aux}$  - Auxiliary winding current

$i_L$  - Motor winding current

$d$  - Duty cycle

$i_{ref}$  - Reference current

$e$  - Error term

$K_I$  - Compensator forward gain

$K_1$  - Compensator feedback gain

$T_S$  - Sampling time interval

$F_S$  - Sampling frequency

$R_S$  - Stator resistance

$L_{\sigma S}$  - Stator leakage inductance

$R_{R'}$  - Rotor resistance referred to stator

$L_{\sigma R'}$  - Rotor leakage inductance referred to stator

$R_1$  - LC filter resistance

$L_1$  - LC filter inductance

$C$  - LC filter capacitance

$R_2$  - Motor winding resistance

$L_2$  - Motor winding inductance

# Chapter 1

## Introduction

The HDMS introduces a novel single-phase motor soft-starting technique, which is based on the Direct Current (DC) Buck converter principle. The Buck converter principle allows for the reduction in the supply current during the starting of the motor, while supplying an amplified motor winding current. This results in a reduced supply current, while still producing a sufficient starting torque due to the amplified motor winding current. The Buck converter operating principle is applied to an Alternating Current (AC) voltage source through three operating regions. It is active during regions 1 and 3, representing the positive and negative half cycles of the motor winding current respectively. During region 2, where the current magnitude is rather low, the motor winding is connected directly to the supply. In this region, the motor winding current changes polarity during its zero-crossover. Without region 2, the polarity of the motor winding current near its zero-crossover may be detected incorrectly due to inaccuracies in the current measurement. In order to reduce the Buck converter current ripple experienced by the supply, an input LC filter is used. This LC filter introduces a resonance frequency, which may affect the system stability.

### 1.1 Objectives

This dissertation aims to analyse the stability of the novel HDMS prototype's current control system. The HDMS prototype is not a result of the work carried out in this dissertation, as it was provided by the industrial partner; Carlo Gavazzi Malta Ltd. This analysis is to be achieved through modelling in state space form and through the establishment of a component-level simulation model. For this dissertation an alternative current control system is proposed and the performance

of both current control systems is compared. The performance of the current controllers is evaluated on their resulting supply and motor winding current peak and Root Mean Square (RMS) values, their resulting starting torques, motor soft-starting time and their flicker test performance. The better performing current control system is to be chosen for robustness testing.

## 1.2 Dissertation Layout

Chapter 2 provides a familiarisation on the topologies adapted for this dissertation. The operating principle of the HDMS and its current control system are explained in more detail.

In Chapter 3 the component-level simulation model established in this dissertation for the HDMS prototype is explained in detail. This consists of the motor winding parameter estimation, the determination of the voltage and current measurement filter characteristics and how the HDMS microcontroller was emulated.

In Chapter 4, the stability analysis of the HDMS prototype current control system is carried out. The analysis was carried out on both the Buck converter circuit and on the closed-loop system, consisting of the Buck converter and the current controller.

Chapter 5 provides an overview of the hardware component setup used for this dissertation. The motor test setup established to record the starting torque produced by the single-phase induction motor for different controller settings is shown. Furthermore, the calibration procedure of the load cell used for this test setup is explained.

The alternative current controller proposed for this dissertation is covered in Chapter 6. The design procedure of this controller is explained in detail and it is tested both in simulation and on the hardware prototype.

Chapter 7 provides a performance comparison of the proposed and the HDMS prototype current controllers. The performance of the controllers is compared based on locked rotor and motor soft-starting tests. The flicker test performance of both controllers is considered in order to investigate the effect of the controllers on the power supply. In addition, robustness testing is carried out for variation in the motor winding and grid impedance parameters.

Lastly, Chapter 8 concludes the dissertation, summarising the work carried out, while Chapter 9 provides suggestions for further work.

# Chapter 2

## Technical Background

### 2.1 Introduction

This chapter introduces the topologies used throughout this dissertation in order to provide a sufficient level of familiarisation.

### 2.2 Introduction to State Space Theory

The representation of systems in state space forms an essential part of modern control theory. In contrast to conventional control theory, this approach may be applied to systems with multiple inputs and multiple outputs, to linear and non-linear systems and to time variant and time invariant systems alike [1].

In state space, a system represented by an  $n^{\text{th}}$ -order differential equation is re-expressed as  $n$  first-order differential equations. Hence, any system may be expressed by the state and output equations defined by (2.1) and (2.2) [1]. These indicate that both the system's state and output depend on the system's state variable  $x$ , the input  $u$  and time  $t$ .  $\dot{x}$  denotes that this is a first-order derivative of the state variable  $x$  and is called a system state.

$$\dot{x}(t) = f(x, u, t) \tag{2.1}$$

$$y(t) = g(x, u, t) \tag{2.2}$$

If these equations are linear or linearised around an equilibrium point, then they may be expressed by the linear equations (2.3) and (2.4) [1], to which the principle of superposition applies.

$$\dot{x} = Ax + Bu \quad (2.3)$$

$$y = Cx + Du \quad (2.4)$$

As most systems are of order  $n > 1$ , these equations take the form of matrices, since a set of  $n$  first-order differential equations are to be represented. Hence  $A$  represents the state matrix,  $B$  the input matrix,  $C$  the output matrix and  $D$  the direct transmission matrix [1]. A block diagram representing the linear, continuous-time set of equations stated in (2.3) and (2.4) may be seen in Figure 2.1.

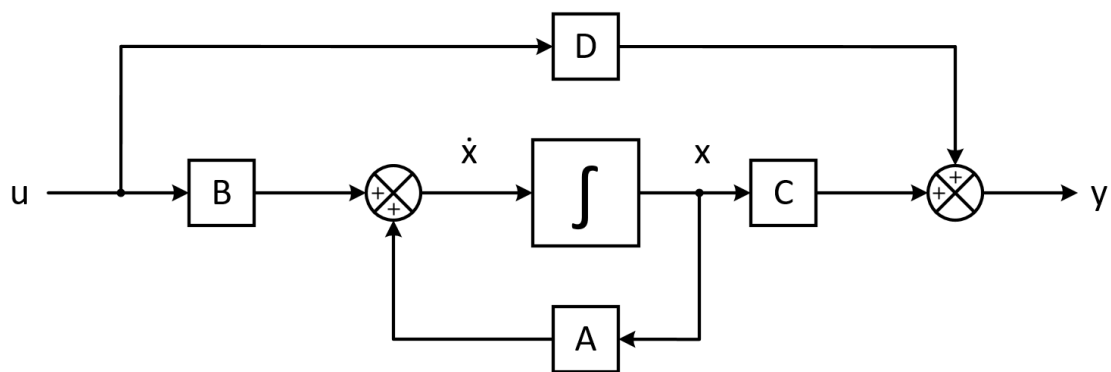


FIGURE 2.1: Block diagram representing the general state space system of equations

## 2.3 Non-linear Systems

Linear systems obey the superposition principle [1]. This means that if a system produces output  $y_1$  due to the input  $u_1$  and  $y_2$  due to  $u_2$ , then if an input  $u = u_1 + u_2$  is applied to the system, an output  $y = y_1 + y_2$  may be expected. In a non-linear system, on the other hand, this may not be applied. Therefore, non-linear system dynamics, in contrast to linear system dynamics, may come across as more complex and unpredictable.

Since non-linear systems are more complex than their linear counterparts, powerful analysis tools used for linear control systems, such as transfer functions and frequency domain analysis may not be applied. These may only be applied if the non-linear system is linearised around an equilibrium point. The linearised system will accurately approximate the non-linear system's dynamics for small deviations from the equilibrium point. The farther the linearised system deviates from this equilibrium, the less accurate the approximation becomes.

Non-linear systems exhibit certain phenomena exclusive to them. Some of these are [2]:

- Finite escape time
- Multiple equilibrium points
- Limit cycles

Finite escape time exists in non-linear systems, implying that an unstable system's state/s may go to infinity in finite time. Linear unstable systems on the other hand, can have their state/s go to infinity but only as  $t \rightarrow \infty$ . Non-linear systems may also have multiple isolated equilibrium points, whereas linear systems only have a single equilibrium point. Hence, a non-linear system might converge to a different equilibrium point depending on its initial conditions. Furthermore, non-linear systems may exhibit limit cycles, which are stable sustained oscillations. These limit cycles occur with a fixed frequency and amplitude, which are independent of the system's initial conditions. A linear system may also exhibit sustained oscillations, however their amplitude depends on the system's initial conditions and may easily decay if the system is perturbed.

## 2.4 Non-linear Control Methods

In contrast to linear system controller design techniques, there is no general approach in designing a non-linear controller. However, there exist a collection of alternatives and complementary techniques, which are all suitable for particular classes of non-linear systems [2]. Some examples of these control techniques are feedback linearisation, robust control and gain-scheduling, where robust control is not exclusive to non-linear control.

In feedback linearisation, a system transformation is carried out to transform the system into a linear system in order to then apply linear design techniques. This can be achieved by applying a control input designed to cancel out the system's non-linearities.

Robust control, on the other hand, is a technique in which a controller is designed for the nominal model of the system and taking also into consideration certain system parameter variations.

In gain-scheduling a number of operating points, covering the entire operation range, are chosen. The system is then linearised around these operating points and a linear controller is designed. The parameters of this linear controller are then adjusted in between these operating points.

## 2.5 Limit Cycles

Limit cycles, which are a phenomenon exclusive to non-linear systems, may be analysed either in the time domain or through phase plane analysis. Phase plane analysis is a graphical method used to study the behaviour of a system's motion trajectories for different initial conditions. Rather than plotting a state variable, say  $x_1$ , against time, two state variables, say  $x_1$  and  $x_2$ , are plotted in the phase plane. The phase plane is a two dimensional plane. This method is usually reserved for first and second-order systems as it is computationally and geometrically complex [2].

A limit cycle is a phenomenon for non-linear systems similar to a linear system with a set of purely imaginary poles/eigenvalues  $\pm j\omega_d$ . An example of such a marginally stable system is given by (2.5).

$$G(s) = \frac{100}{s^2 + 100} \quad (2.5)$$

Such a set of imaginary poles leads to an undamped oscillatory response with a non-decaying amplitude, as displayed in Figure 2.2.

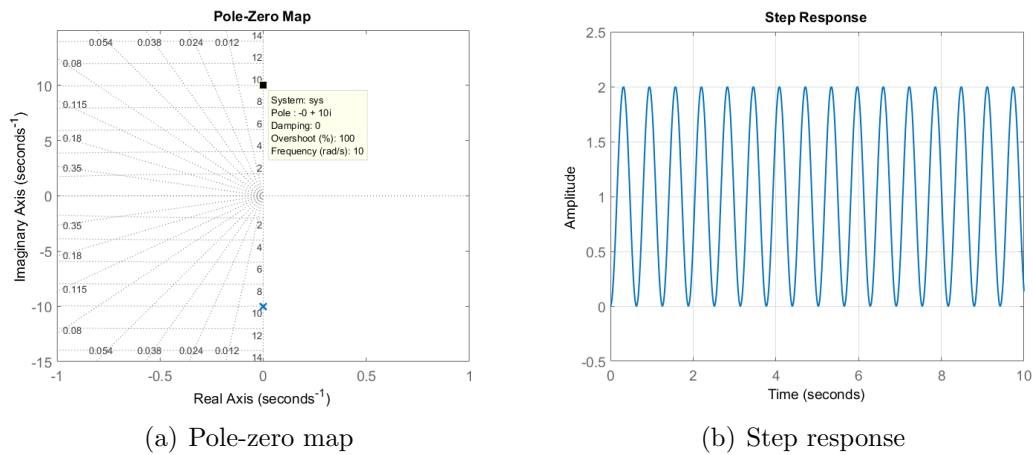


FIGURE 2.2: Pole-zero map and step response for example system

The oscillation that is present in both linear marginally stable systems and non-linear systems with a limit cycle implies that the system has a non-trivial periodic solution [3]. Non-trivial solutions in this case excludes solutions such as equilibrium points.

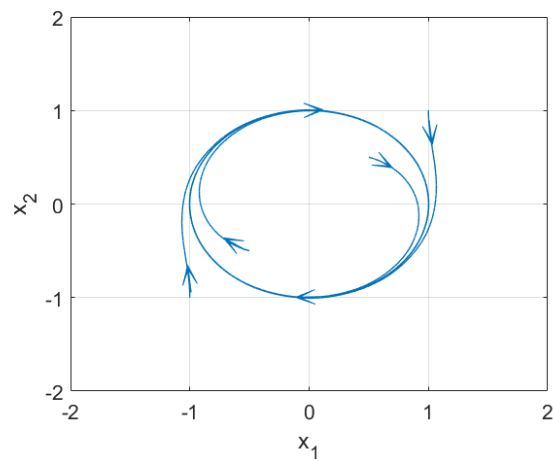
The existence of limit cycles may be predicted through a theorem such as the Poincare-Bendixson Theorem. However, this theorem is limited to second order systems and there exist no equivalent theorems for higher order systems [2].

Limit Cycles are mainly classified into three categories; stable, unstable and semi-stable limit cycles [2].

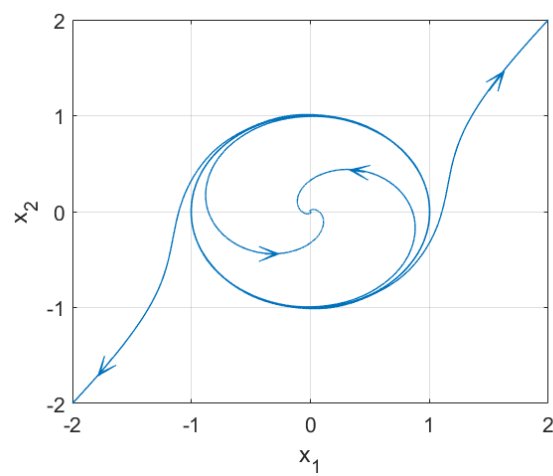
Figure 2.3(a) shows a stable limit cycle. With such a limit cycle, all trajectories in its vicinity will converge to the limit cycle, no matter what the system's initial conditions are, as  $t \rightarrow \infty$ .

An unstable limit cycle, on the other hand, is defined by the property that all trajectories in the vicinity of the limit cycle will diverge from it as  $t \rightarrow \infty$ . This may be seen below in Figure 2.3(b).

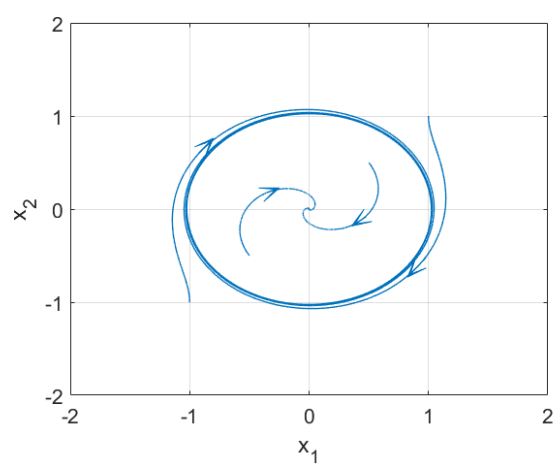
Lastly, a semi-stable limit cycle leads to some of the trajectories in its vicinity to diverge from it, and some to converge to it as  $t \rightarrow \infty$ . This is illustrated in Figure 2.3(c).



(a) Stable limit cycle



(b) Unstable limit cycle



(c) Semi-stable limit cycle

FIGURE 2.3: Examples of (a) stable, (b) unstable and (c) semi-stable limit cycles

## 2.6 Linearisation around an Equilibrium Point

A non-linear system may be linearised under the conditions that the point around which the system is linearised is an equilibrium point [1]. If the deviations from this chosen equilibrium point are small enough, then the linearised model of the non-linear system approximates its dynamic behaviour sufficiently. This means that the linearised model is based on a localised model of the non-linear system and it responds similarly to small changes. These small changes represent the dynamic response of the system at this equilibrium point, as long as they remain small enough. Applying this to a mathematical function results in a tangent, which yields the same result as the function itself for a small change  $\delta x$ , as can be seen in Figure 2.4. The equilibrium point of the function  $y = f(x)$  is defined by the point  $(x^*, y^*)$ .

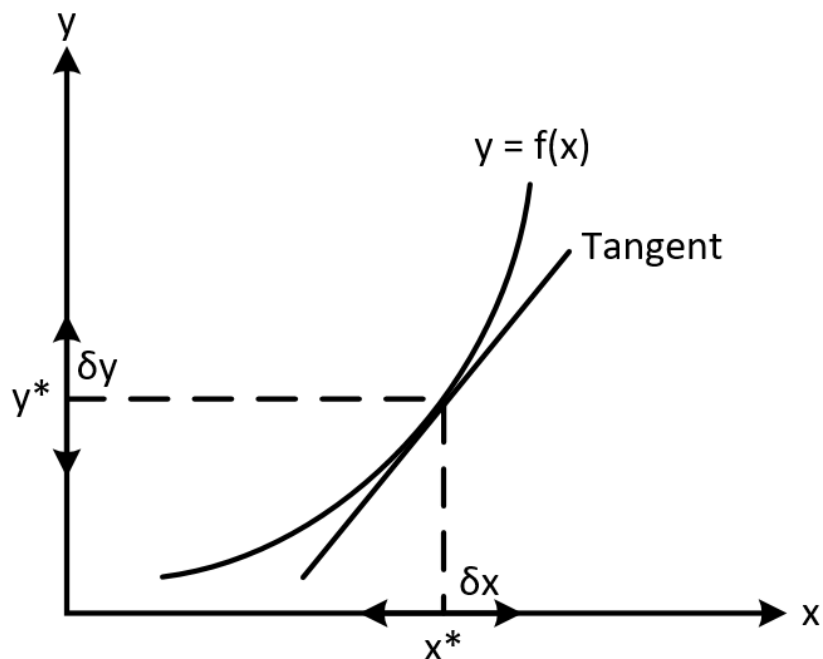


FIGURE 2.4: Plot of a function  $y = f(x)$  with a linearised model around  $x^*, y^*$

Such a linear approximation can be achieved through the Taylor Series expansion [1]. For the function  $y = f(x)$ , the Taylor Series expansion results in (2.6).

$$y = f(x^*) + \frac{df}{dx}(x - x^*) + \frac{1}{2!} \frac{d^2f}{dx^2}(x - x^*)^2 + \dots \quad (2.6)$$

Given that only small variations in  $x$  take place for the linear approximation of  $y = f(x)$ , then the higher order terms may be neglected. Furthermore, evaluating  $y = f(x)$  at  $x^*$  is equal to the equilibrium point  $y^*$ . This leads to (2.7), where  $K = \left. \frac{df}{dx} \right|_{x=x^*}$  and which is of a linear nature as long as the deviation from the equilibrium point is kept small.

$$y - y^* = K(x - x^*) \quad (2.7)$$

### 2.6.1 Jacobian Linearisation of State Space Systems

A linear system with multiple inputs and outputs may be represented as a set of functions, depending on the state variables and the inputs, describing the system's states as represented by the linear equations (2.8) and (2.9) [1].

$$\dot{\mathbf{x}} = \mathbf{A}\mathbf{x} + \mathbf{B}\mathbf{u} \quad (2.8)$$

$$\mathbf{y} = \mathbf{C}\mathbf{x} + \mathbf{D}\mathbf{u} \quad (2.9)$$

A non-linear system, on the other hand, must be linearised first before it may be represented in this format. A general way of expressing a non-linear forced system in state space is given by equations (2.10) and (2.11) [1].

$$\dot{\mathbf{x}} = \mathbf{f}(\mathbf{x}, \mathbf{u}) \quad (2.10)$$

$$\mathbf{y} = \mathbf{g}(\mathbf{x}, \mathbf{u}) \quad (2.11)$$

Such a non-linear system may be linearised around an equilibrium point, where  $\dot{\mathbf{x}} = \mathbf{0}$ . Evaluating this for a given input, defined by  $\mathbf{u} = \mathbf{u}^*$ , results in the state variables at equilibrium, defined by  $\mathbf{x} = \mathbf{x}^*$ . For this equilibrium point, the Taylor Series expansion may be applied, as expressed in (2.12) [1].

$$\mathbf{f}(\mathbf{x}, \mathbf{u}) = \mathbf{f}(\mathbf{x}^*, \mathbf{u}^*) + \left( \frac{\partial \mathbf{f}}{\partial \mathbf{x}} \right)_{\mathbf{x}=\mathbf{x}^*} (\mathbf{x} - \mathbf{x}^*) + \left( \frac{\partial \mathbf{f}}{\partial \mathbf{u}} \right)_{\mathbf{u}=\mathbf{u}^*} (\mathbf{u} - \mathbf{u}^*) + \dots \quad (2.12)$$

At the equilibrium point,  $\mathbf{f}(\mathbf{x}^*, \mathbf{u}^*) = \mathbf{0}$ , as the equations are first-order differential equations. The matrices  $\left(\frac{\partial \mathbf{f}}{\partial \mathbf{x}}\right)_{\mathbf{x}=\mathbf{x}^*}$  and  $\left(\frac{\partial \mathbf{f}}{\partial \mathbf{u}}\right)_{\mathbf{u}=\mathbf{u}^*}$  may be represented by the terms  $\mathbf{A}$  and  $\mathbf{B}$  respectively.

Neglecting the higher order terms, by assuming that the deviations from the established equilibrium point remain small, the linearised system may be expressed by (2.13). Since  $\delta \dot{\mathbf{x}} = (\dot{\mathbf{x}} - \dot{\mathbf{x}}^*)$ , where  $\mathbf{x}^*$  represents a vector of constants, being the equilibrium values for the state variables, then  $\delta \dot{\mathbf{x}} = \dot{\mathbf{x}}$ . Hence:

$$\dot{\mathbf{x}} = \mathbf{A}\delta\mathbf{x} + \mathbf{B}\delta\mathbf{u} \quad (2.13)$$

Where  $\delta\mathbf{x}$  and  $\delta\mathbf{u}$  represent the deviations from the equilibrium point values for the state variables and the input variables respectively. These are of the form  $\delta\mathbf{x} = \mathbf{x} - \mathbf{x}^*$  and  $\delta\mathbf{u} = \mathbf{u} - \mathbf{u}^*$ . Furthermore,  $\mathbf{A}$  and  $\mathbf{B}$  are the Jacobian matrices evaluated at the equilibrium point. If the system is of order  $n = 3$ , with two input variables, then the Jacobian matrices may be expressed as shown in (2.14), where the equilibrium point values  $\mathbf{x}^*$  and  $\mathbf{u}^*$  are to be substituted.

$$\mathbf{A} = \begin{pmatrix} \frac{\partial \dot{x}_1}{\partial x_1} & \frac{\partial \dot{x}_1}{\partial x_2} & \frac{\partial \dot{x}_1}{\partial x_3} \\ \frac{\partial \dot{x}_2}{\partial x_1} & \frac{\partial \dot{x}_2}{\partial x_2} & \frac{\partial \dot{x}_2}{\partial x_3} \\ \frac{\partial \dot{x}_3}{\partial x_1} & \frac{\partial \dot{x}_3}{\partial x_2} & \frac{\partial \dot{x}_3}{\partial x_3} \end{pmatrix}_{\substack{\mathbf{x}=\mathbf{x}^* \\ \mathbf{u}=\mathbf{u}^*}} \quad \mathbf{B} = \begin{pmatrix} \frac{\partial \dot{x}_1}{\partial u_1} & \frac{\partial \dot{x}_1}{\partial u_2} \\ \frac{\partial \dot{x}_2}{\partial u_1} & \frac{\partial \dot{x}_2}{\partial u_2} \\ \frac{\partial \dot{x}_3}{\partial u_1} & \frac{\partial \dot{x}_3}{\partial u_2} \end{pmatrix}_{\substack{\mathbf{x}=\mathbf{x}^* \\ \mathbf{u}=\mathbf{u}^*}} \quad (2.14)$$

## 2.7 Single Phase Induction Motors

Due to its low cost and high reliability, the single phase induction motor is widely used in domestic applications, such as fans, refrigerators, compressors and pumps [4] [5]. A single phase induction motor consists of a rotor and a stationary winding, referred to as the stator winding. The rotor can be a wound or squirrel cage type rotor.

Single phase induction motors are not self-starting, as the net starting torque produced by the single phase AC supply applied at the stator is equal to zero [6]. In order to make such a motor self-starting, an auxiliary winding is added to the stator. This auxiliary winding ensures that the motor produces a positive net torque at standstill, making the motor self-starting.

To further increase this starting torque, a start capacitor may be added to the auxiliary winding. Such a start capacitor is larger than the auxiliary capacitor and is disconnected, typically by means of a centrifugal switch, once the motor has reached a certain speed. Such a configuration is illustrated in Figure 2.5 below. While such a start capacitor improves the starting torque of the motor, it introduces an additional expense and source of failure.

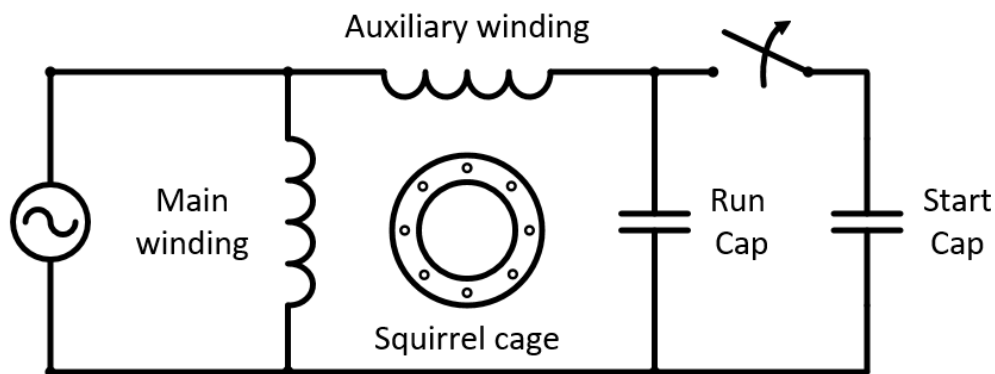


FIGURE 2.5: Diagram of single phase motor with start capacitor

## 2.8 Soft Starters

Single phase induction motors can be started without a dedicated starter using just a main contactor and a thermal overload relay to protect the motor windings from overheating. Such a configuration is referred to as a Direct On-Line (DOL) start. However, such a start leads to the motor drawing between 6-8 times its rated current during the starting period. While such a large inrush current produces a high starting torque, it can cause considerable voltage drops in the supply voltage. This affects equipment and other customers connected to the same supply, especially in domestic applications and gets more significant with an increase in motor size. Furthermore, such a high starting torque may be larger than necessary in certain applications causing unnecessary mechanical stress [7].

One type of motor starter that is used to reduce the motor inrush current and thus the effect on the supply voltage is the soft starter. A circuit diagram of the traditional single phase motor soft starter consisting of back-to-back thyristors, Miniature Circuit Breaker (MCB), main contactor (K) and a Thermal Overload Relay (OL), is shown in Figure 2.6.

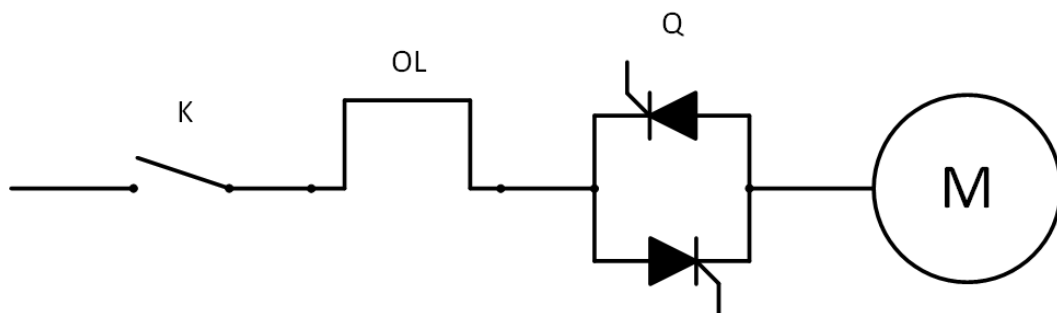


FIGURE 2.6: Diagram of single phase motor soft starter

A soft starter reduces the inrush current by ramping up the voltage applied to the motor windings. This is done by increasing the firing angle of the thyristors. A typical firing angle sequence of a soft-start is illustrated in Figure 2.7 [8]. The figure shows the firing angle of the thyristor decreasing with time, which leads to the thyristors conducting for a larger portion of the supply voltage. This increases the average voltage applied to the motor windings and subsequently increases the motor winding current and motor speed. While a reduction in the inrush current is beneficial due to the aforementioned reasons, the disadvantage of such a soft-start is the resulting reduction in the motor torque. This will lead to an increased starting time and in some applications may lead to the motor not being able to start due to an insufficient starting torque in some high torque applications.

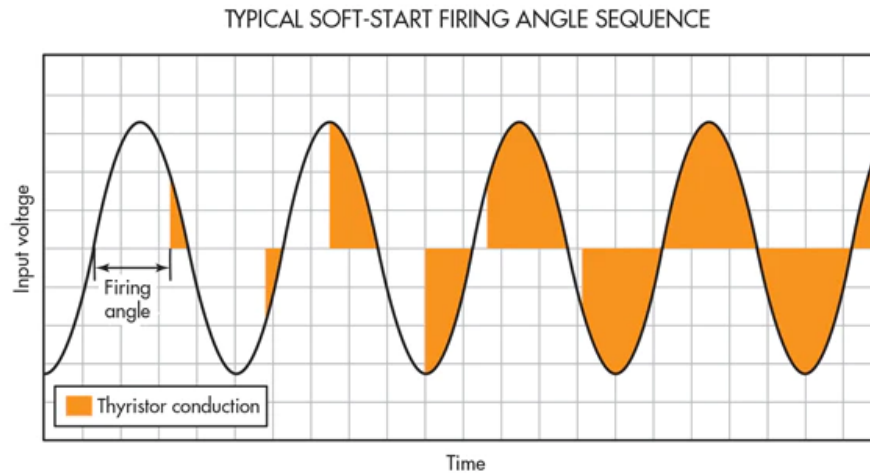


FIGURE 2.7: Plot of typical soft-start firing angle sequence

While they are still not widely used in the industry, recent advances in technology have allowed the introduction of micro-controllers and Insulated-Gate Bipolar Transistor (IGBT)s in the soft starter topology [9]. In contrast to the thyristor-based soft starter, where the motor winding voltage is controlled through the firing angle, it is instead controlled through the variation of the duty cycle applied to the IGBTs' Pulse Width Modulation (PWM) signal [10]. This concept allows for a simpler control approach [10] and is implemented for DC machines in [9] [11]. In [10], the authors prove that this IGBT soft starter approach allows for energy conservation in a three-phase soft starter, due to the fact that the high PWM frequency does not introduce lower-order harmonics, compared to the traditional approach, which results in a more sinusoidal motor winding current [10].

## 2.9 High Dynamic Motor Starter

### 2.9.1 Introduction

The HDMS is a novel approach to the single phase motor starter. Similarly to conventional soft starters, the HDMS also reduces the average voltage applied to the motor winding in order to reduce the inrush current drawn from the supply. The HDMS circuitry is based on the Buck Converter, which is used to decrease DC voltages by applying a duty cycle to a switching device. In this manner, based on the average model approach [12],  $V_{OUT} = d \times V_{IN}$  and consequently  $I_{IN} = d \times I_{OUT}$ . As the power in such a converter remains constant, except for some losses, the voltage at the converter output is reduced and the current will be increased such that  $P_{IN} = P_{OUT}$ . The duty cycle is applied to its switching devices through a

PWM signal. Through this concept, the HDMS is able to reduce the current drawn from the supply without reducing the motor winding current as much. This results in increased starting torque produced by the motor.

## 2.9.2 Circuit Description

The HDMS circuit diagram is shown in Figure 2.8. The switching device used is the IGBT. The circuit consists of four IGBTs, which are placed in pairs of two and connected in a common emitter configuration.

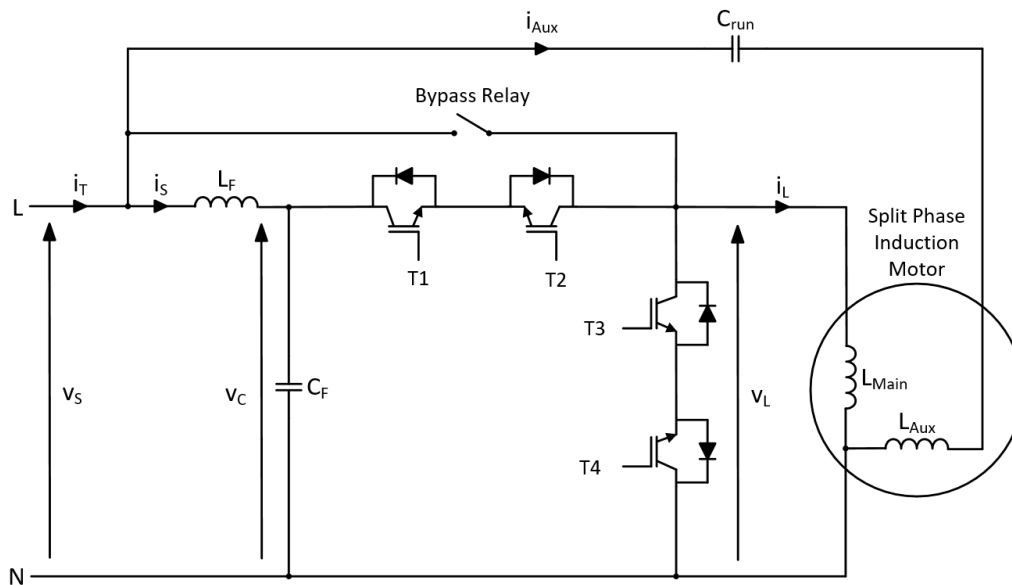


FIGURE 2.8: Circuit diagram of HDMS

An LC-filter is placed at the input of the converter in order to reduce the current ripple experienced by the supply. This consists of the components  $L_F = 190\mu H$  and  $C_F = 4.7\mu F$ . The filter resonance frequency is defined by (2.15).

$$f_{LC} = \frac{1}{2\pi\sqrt{L_F C_F}} = 5.325kHz \quad (2.15)$$

The transistors T1 and T2 are used to connect the motor main winding to the supply. The common emitter configuration allows to do this for either polarity of the supply voltage. Consider the positive AC half cycle of the motor winding current  $i_L$ . When T1 conducts, T2 is switched off and the current is allowed to pass through T2's diode. During the negative half cycle of the motor winding current  $i_L$ , when T2 conducts, T1 is switched off and the current is allowed to pass through T1's diode. Transistors T3 and T4 along with their diodes provide a free-wheeling path for the motor winding current when the winding is disconnected from the supply. The transistors are again connected in the common emitter configuration to

allow operation for either polarity of the supply voltage. The transistors conduct in pairs depending on the polarity of the supply voltage. During the positive half cycle, T1 connects the main winding to the supply and T4 provides the free-wheeling path. For the negative half cycle, T2 operates together with T3.

The auxiliary winding is connected directly to the supply to ensure it is energised when the motor is started. Once the motor is started, the bypass relay is engaged to connect the motor winding directly to the supply. This is done to reduce the utilisation of the IGBTs in order to lengthen their life-time.

The current  $i_S$  is controlled in the control algorithm, as the total supply current  $i_T$  also contains the auxiliary current  $i_{aux}$ .

### 2.9.3 Regions of Operation

As already mentioned, the HDMS operates for both polarities of the supply voltage. This requires attention during the zero crossing of the main winding current  $i_L$ . The measurement of the motor winding current  $i_L$  is naturally affected by noise. However, the switching of the wrong Buck converter IGBT set may cause large voltage spikes across the switching devices and consequently the motor winding. For protection, varistors are placed across the switching devices. However, the main solution to this problem is the introduction of three operating regions. An example of these operating regions with the supply and motor winding currents  $i_S$  and  $i_L$  is presented in Figure 2.9. The corresponding duty cycle for this example is shown in Figure 2.10.

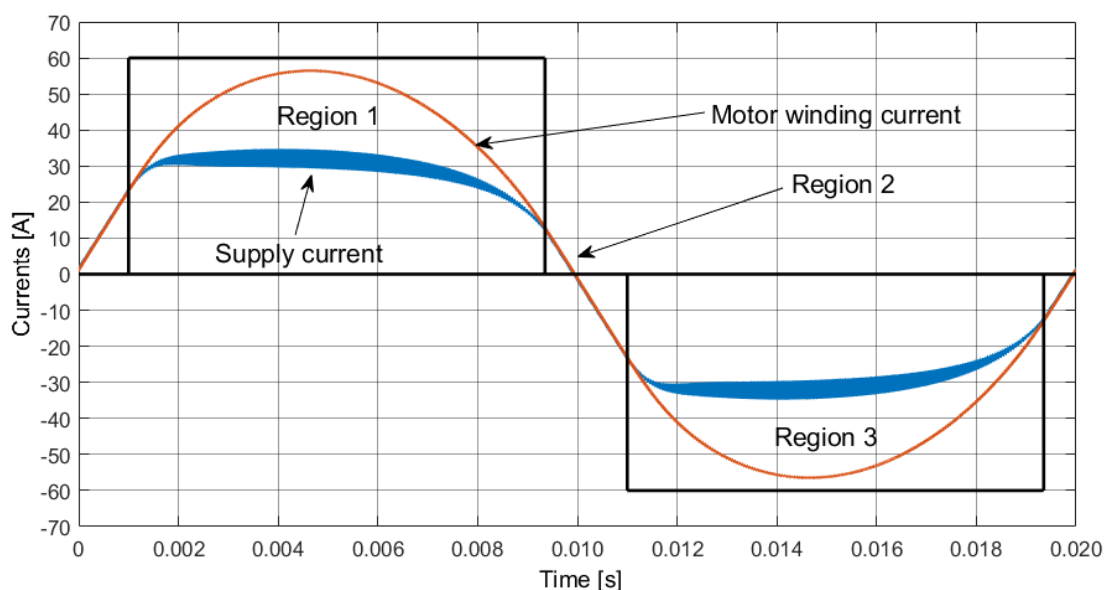


FIGURE 2.9: Plot of operating regions

Region 1 is defined as the region of operation during the positive half cycle of the motor winding current  $i_L$ . It occurs when  $i_L$  is greater than a fixed value. As can be seen in the figure, in this example, region 1 is entered at a value of  $i_L > 25A$  and it is exited at  $i_L < 15A$ . In region 1 only T1 and T4 are operated, while T2 and T3 are permanently off. Region 2 represents the region of operation as  $i_L$  crosses from the positive to the negative half cycle. During this period it must be ensured that the IGBTs T1 and T2 remain switched on, connecting the motor winding directly to the supply. T3 and T4 are permanently off in this region. As  $i_L$  reaches a value of  $i_L < -25A$ , region 3 is entered. This region is identical to region 1, however it is defined by the negative half cycle of  $i_L$ . In this region, only T2 and T3 are used for switching, while T1 and T4 are permanently off.

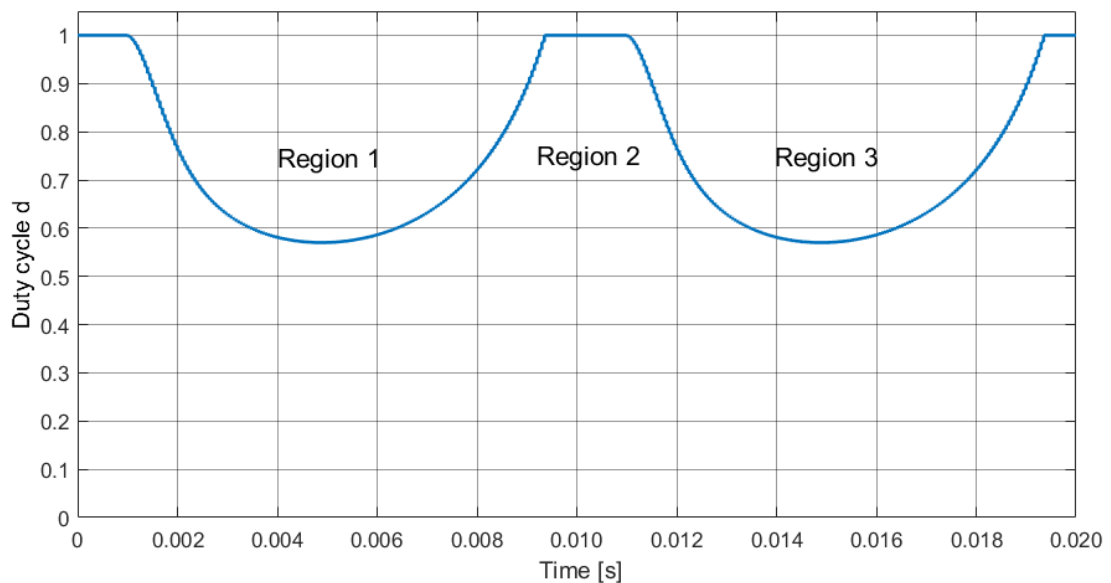


FIGURE 2.10: Plot of duty cycle

From Figure 2.10, the duty cycle can be seen to decrease and increase again during regions 1 and 3. Most importantly however, the duty cycle is equal to  $d = 1.0 = 100\%$  during region 2, which ensures that the motor winding is connected directly to the supply during the motor winding current zero-crossing.

Figure 2.11 shows the motor winding voltage together with the supply and motor winding currents. During regions 1 and 3, the IGBTs are switching on and off according to the duty cycle. However, during region 2, as the motor winding current crosses from positive to negative, no switching takes place as the motor winding is connected directly to the supply.

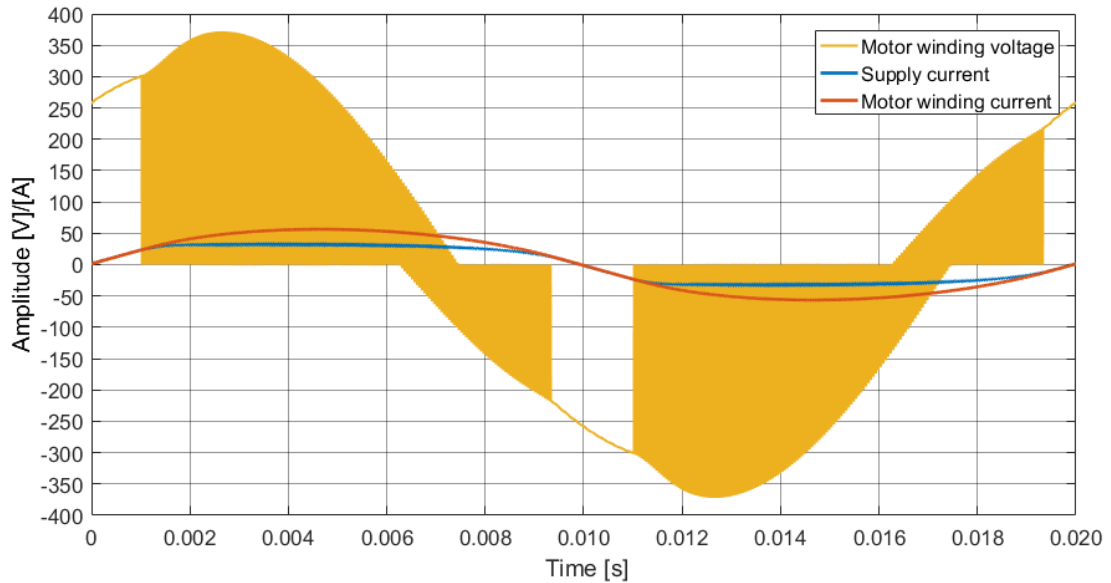


FIGURE 2.11: Plot of supply current, motor winding current and voltage

### 2.9.4 Control Algorithm

In this section, the implementation of the previously explained regions of operation is explained. The implemented compensator is shown in Figure 2.12.

This consists of an integral compensator, which produces the duty cycle  $d$  for the PWM signal applied to the IGBTs from the error signal. In its feedback path, a gain  $K_1$  is introduced. Hence, the compensator consists of the forward gain  $K_I$  and the feedback gain  $K_1$ . The gain in the feedback path is introduced to lower the compensator bandwidth. This is done to avoid excitation of the LC-filter resonance frequency.

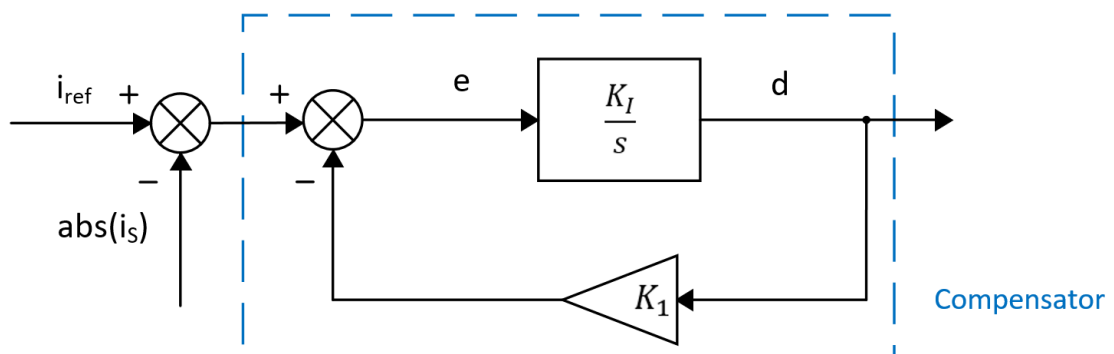


FIGURE 2.12: Diagram of HDMS compensator

The compensator transfer function  $G_c(s)$  is shown in (2.16). The compensator bandwidth in the HDMS prototype is kept low as  $K_I = 50A^{-1}$  and  $K_1 = 35A$ , which results in a cut-off frequency of  $f_c = 278.52\text{Hz}$ .

$$G_c(s) = \frac{K_I}{s + K_1 K_I} \quad (2.16)$$

The compensator requires the measurement of the absolute value of the supply current  $i_S$ , to ensure operation for both polarities. This current does not contain the auxiliary winding current, as this is not to be changed. The supply current is regulated, rather than the motor winding current  $i_L$ , in order to achieve the smoothest possible supply current regulation. The resulting duty cycle is then applied to the IGBTs via a PWM signal.

It is possible to control  $i_S$ , rather than  $i_L$ , without violating the zero-crossing condition of the motor winding current, as during region 2 the motor winding is connected directly to the supply. Hence, during this region  $i_L = i_S$ . This is done by ensuring that the duty cycle generated by the compensator is equal to  $d = 1.0 = 100\%$  during region 2, as was shown in the previous example waveforms.

### 2.9.5 Software Implementation

The HDMS prototype's contains the STM32F407, a 32-bit 168MHz microcontroller [13]. It emulates the current controller previously explained by a digital algorithm, which is implemented in a 20kHz interrupt routine. The procedure of implementing the algorithm in the digital domain is laid out in the following steps.

The duty cycle  $d$  generated by the compensator may be expressed by (2.17). The error term  $e$  may be expressed as  $e = i_{err} - dK_1$ , where  $i_{err} = i_{ref} - i_S$ .

$$d = e \left( \frac{K_I}{s} \right) \quad (2.17)$$

The control transfer function (2.16) is defined in continuous-time, denoted by the Laplace  $s$ -term. Therefore, a transformation must be applied to the system in order to implement it digitally. For this, the Bilinear Transform [14] is used, which demands the substitution of (2.18), where  $T_S$  is the sampling time interval and  $z$  denotes the  $Z$ -Transform variable.

$$s = \frac{2(1 - z^{-1})}{T_S(1 + z^{-1})} \quad (2.18)$$

Substituting this into (2.17), the control algorithm may be expressed as shown in (2.19), which may be implemented in the digital domain.  $F_S$  represents the 20kHz sampling frequency of the microcontroller.

$$d_{(k)} = \frac{K_I}{2F_S + K_1 K_I} \left[ i_{err(k)} + i_{err(k-1)} + d_{(k-1)} \left( \frac{2F_S}{K_I} - K_1 \right) \right] \quad (2.19)$$

The subscript  $k$  denotes the current microcontroller sample, whereas  $(k-1)$  denotes the sample of the previous iteration. Thus, the microcontroller must store the values of the previous iteration's  $i_{err}$  and  $d$  in order to calculate the current iteration's duty cycle  $d$ .

Figure 2.13 provides a simplified flowchart outlining the major steps found in the 20kHz interrupt routine, which carries out a complete motor soft-start. The first step in the interrupt routine is to sample all the relevant data, such as the supply and motor winding currents  $i_S$  and  $i_L$ , for example. The motor soft-start is divided into different stages, denoted by the 'device state', DS. Initially, this is equal to INITIALISATION. When this device state is entered, variable offsets in the ADC measurements are removed and the device is initialised. Upon completion, the device state is set to READY, for the next interrupt routine iteration. At the end of each iteration, logged data is saved, if this has been enabled. This logged data is sent to a computer via USB, where it may be plotted in Matlab.

In the READY state, the data logging is enabled among other steps. Once this is done, DS is set to PREPARE RAMPING. In the PREPARE RAMPING state, the main relays are switched on, connecting the supply voltage to the soft starter. The PWM outputs are also enabled in preparation for the following device state. Once the RAMPING state is entered, the control algorithm starts to be executed. A duty cycle  $d$  is generated from the previously stated control law in (2.19) and applied to the IGBTs. Once it is sensed that the motor has started, the device state is set to BYPASS. In the BYPASS state, the IGBTs are switched off and the motor is directly connected to the supply through a bypass relay. The HDMS prototype remains in this state until a control signal indicates to stop the motor.

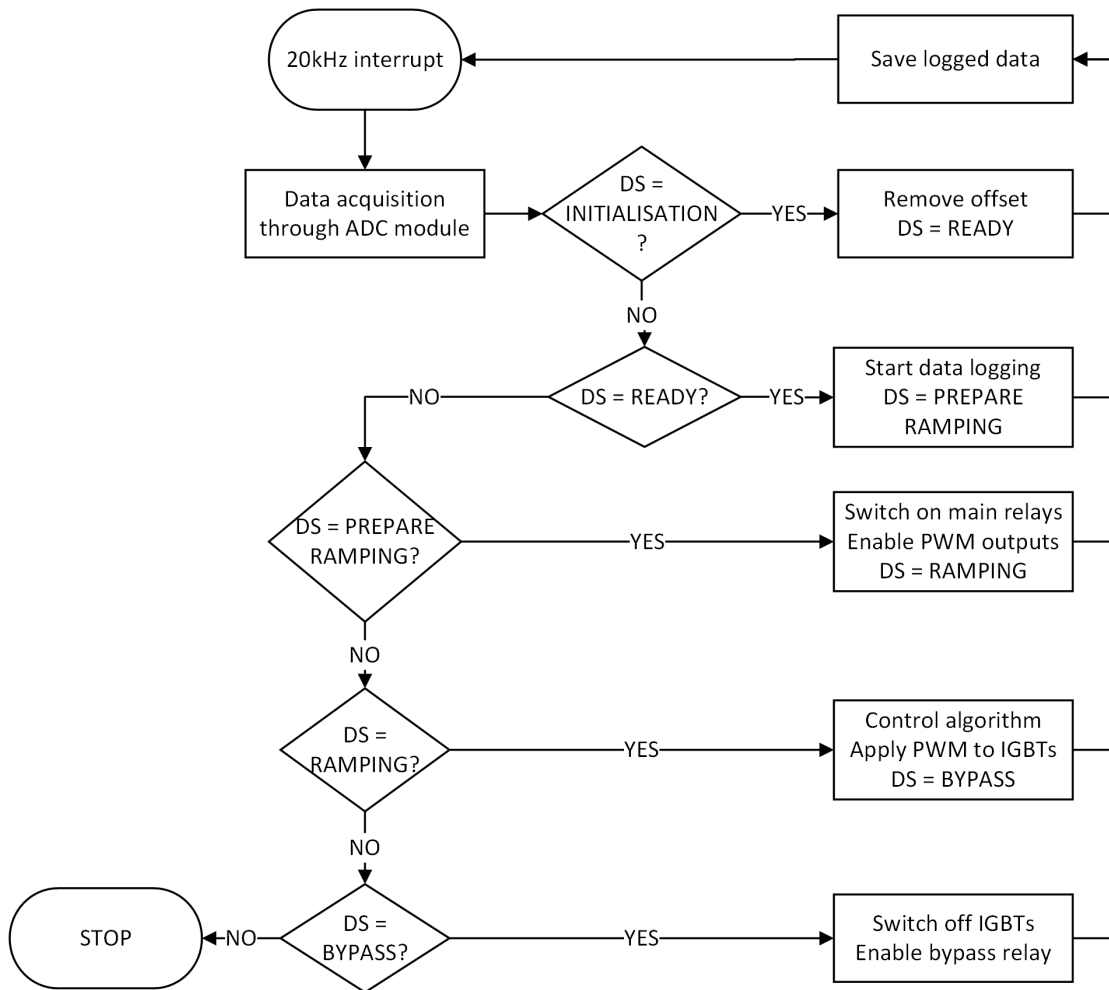


FIGURE 2.13: Flowchart of HDMS interrupt routine

Figure 2.14 provides an example for a full motor soft-start with the device states, total and motor winding currents. Initially, the device state is READY. As the motor start is initiated at approximately  $t = 0.1\text{s}$ , this changes to PREPARE RAMPING, where the main relays are switched on and the PWM outputs are enabled. Switching on the main relays allows for the auxiliary current to energise the auxiliary winding. Hence, during this device state the total current is equal to the auxiliary current. At approximately  $t = 0.2\text{s}$ , the RAMPING device state is entered and the control algorithm is enabled. The PWM signals are applied to the IGBTs according to the duty cycle produced by the control algorithm. Both supply and motor winding currents can be seen to remain within a fixed amplitude during this device state until the motor approaches its rated speed. Shortly after  $t = 1.6\text{s}$ , the device state increases another two times, which represents the BYPASS device state. During this device state, the currents reduce as the motor has reached its rated speed. The motor winding is connected directly to the supply through the

bypass relay. The total and motor winding currents are not equal in the bypass mode due to a phase shift between the auxiliary and supply currents.

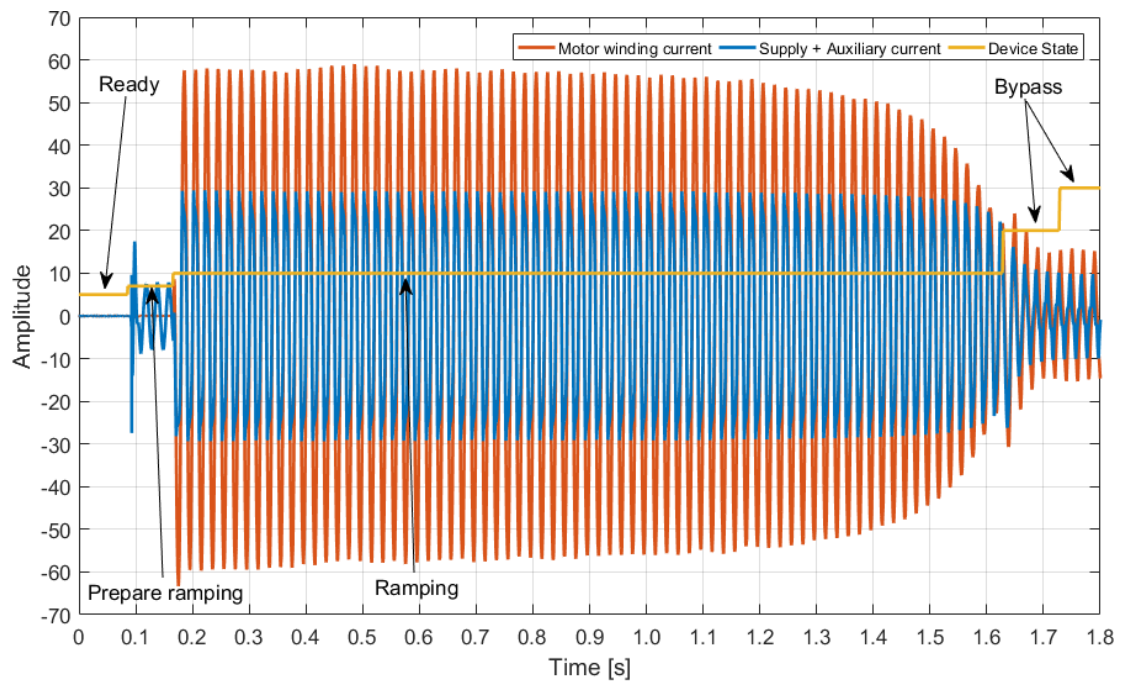


FIGURE 2.14: Plot of soft-start with currents and device states

# Chapter 3

## Simulation Model

### 3.1 Introduction

This chapter covers the estimation of the single-phase induction motor parameters along with the simulation model of the HDMS circuit and control algorithm. The simulation model was implemented in Matlab Simulink using the Simscape library and is used throughout this dissertation.

### 3.2 Low-Voltage Test

In order to measure the motor winding resistance and leakage inductance of the single phase motor used, a low amplitude AC voltage was applied to it. The rotor is locked for this experiment to prevent it from rotating. A static rotor is what the HDMS current controller initially experiences when carrying out a motor start. With a low AC voltage applied to the single phase motor, the magnetising branch may be neglected and its equivalent diagram [15] [16] may be represented as shown in Figure 3.1. The dash denotes the equivalent rotor quantity referred to the stator winding.

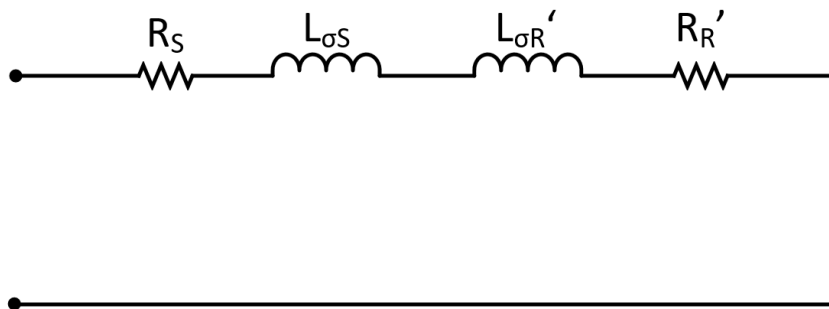


FIGURE 3.1: Equivalent circuit of single phase motor with low AC voltage

The equivalent motor winding diagram at standstill consisting of the rotor and stator parameters is shown in Figure 3.2 below. This represents an RL-load.

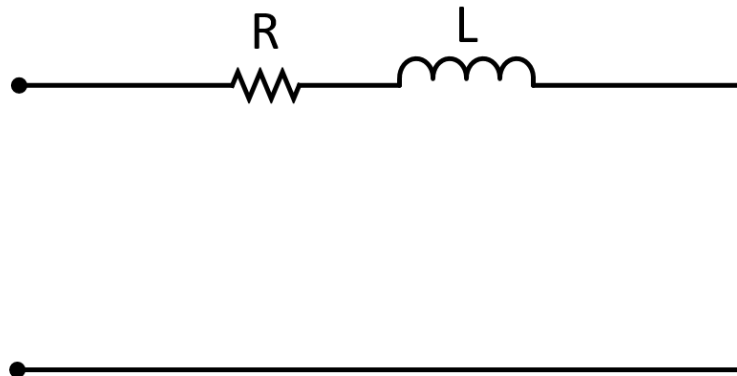


FIGURE 3.2: Diagram of motor winding at standstill

The impedance that this equivalent circuit represents can be expressed as a complex number, consisting of a magnitude and a phase. This is expressed in (3.1).

$$Z = |Z|\angle\phi \quad (3.1)$$

The practically measured main winding voltage and current of the single phase motor can be seen in Figure 3.3.

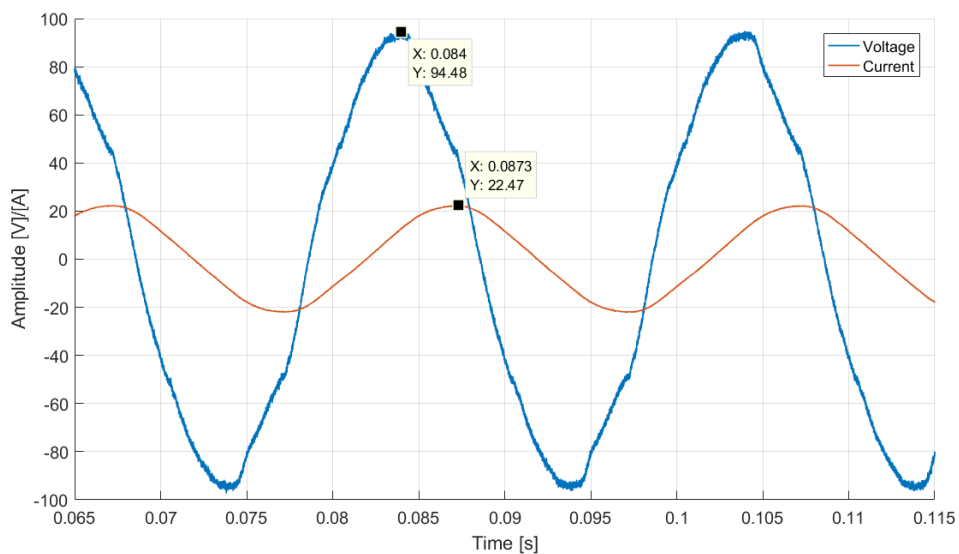


FIGURE 3.3: Plot of main winding voltage and current for parameter acquisition

The magnitude of the complex impedance may be calculated by dividing the peaks of the voltage and the current waveforms, which are indicated in Figure 3.3. The phase of the impedance may be found from the time difference between the peaks, or the zero crossings, and the frequency of the waveforms. The frequency is 50Hz. The magnitude and phase values are calculated as follows:

$$|Z| = \sqrt{R^2 + (\omega L)^2} = \frac{94.48V}{22.47A} = 4.20\Omega \quad (3.2a)$$

$$\phi = \tan^{-1} \left( \frac{\omega L}{R} \right) = \frac{2\pi(0.0873s - 0.084s)}{0.02s} = 1.04rad = 59.4^\circ \quad (3.2b)$$

From these results, the total resistance and inductance of the motor winding may be calculated. The values of the resistance and inductance were found to be:

$$R = 2.16\Omega \quad (3.3a)$$

$$L = 11.65mH \quad (3.3b)$$

This test was carried out using a variable auto-transformer, or variac, which allowed the application of a low voltage. However, this introduced some distortion in the voltage waveform, which may be seen in Figure 3.3. Once better equipment, which will be shown in Chapter 5, was available, the same test was repeated. The resulting waveforms are shown in Figure 3.4.

The parameters resulting from this test are shown in (3.4). As this represents only a minor discrepancy of well below 10%, the previously obtained parameters are confirmed to be accurate.

$$R = 2.29\Omega \quad (3.4a)$$

$$L = 11.78mH \quad (3.4b)$$

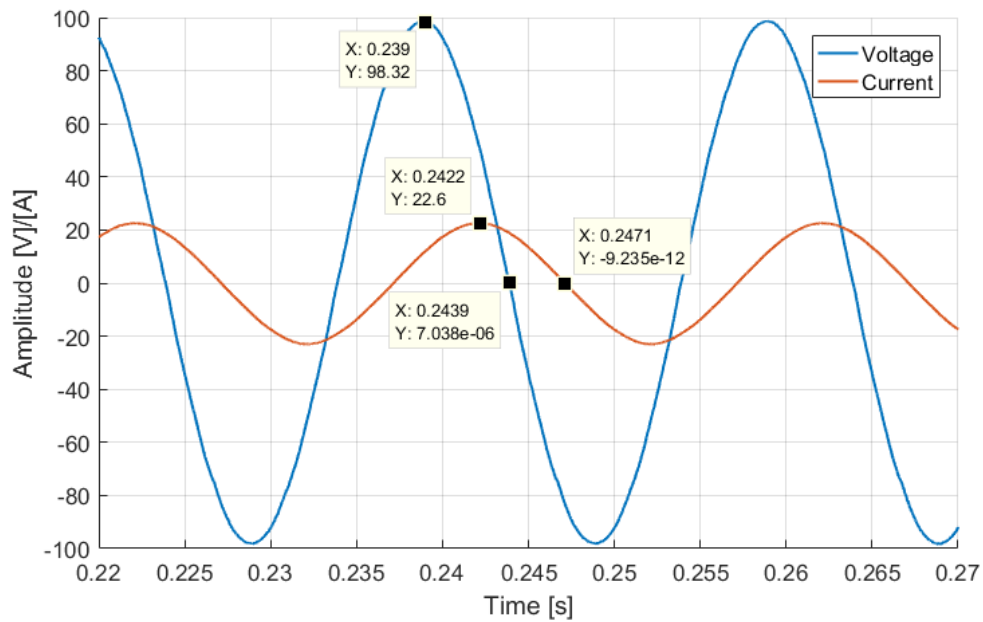


FIGURE 3.4: Plot of main winding voltage and current for parameter acquisition with new setup

### 3.3 Determination of Filter Characteristics

This simulation model aims to accurately simulate the behaviour of the HDMS prototype. In the hardware prototype of the HDMS, the supply and motor winding currents are measured through the use of current transducers and then filtered, before they reach the Analogue to Digital Converter (ADC)-pins of the microcontroller. These filters are implemented in the form of RC first-order low-pass filters and aim to filter out the 20kHz switching frequency introduced by the discretisation of the control algorithm. The component values of these RC filters were not available and hence in order to obtain the resulting filter characteristic, an analysis of the filter step response was carried out. This test is illustrated in Figure 3.5, where  $G_f(s)$  represents the filter transfer function.

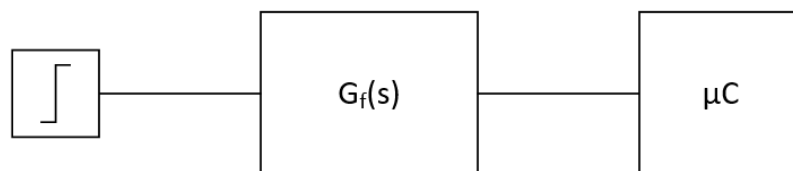


FIGURE 3.5: Diagram of step response test for ADC filter characteristics

A step in the supply current  $i_S$  was applied at the current transducers. The resulting supply current was captured both on an oscilloscope and on the microcontroller. The microcontroller was programmed to set an output pin high once it detects this step. The voltage of this microcontroller pin is referred to as  $V_{sync}$ . This was captured again by both the oscilloscope and the microcontroller data logging routine and serves as a means to synchronise the captured supply current waveforms. The synchronised supply current waveforms are displayed in Figure 3.6 together with the synchronisation signals  $V_{sync}$ . Clearly, the filter reduces the amplitude of the measured current and appears to have a rather low cut-off frequency, as it filters out most of the noise captured by the oscilloscope.

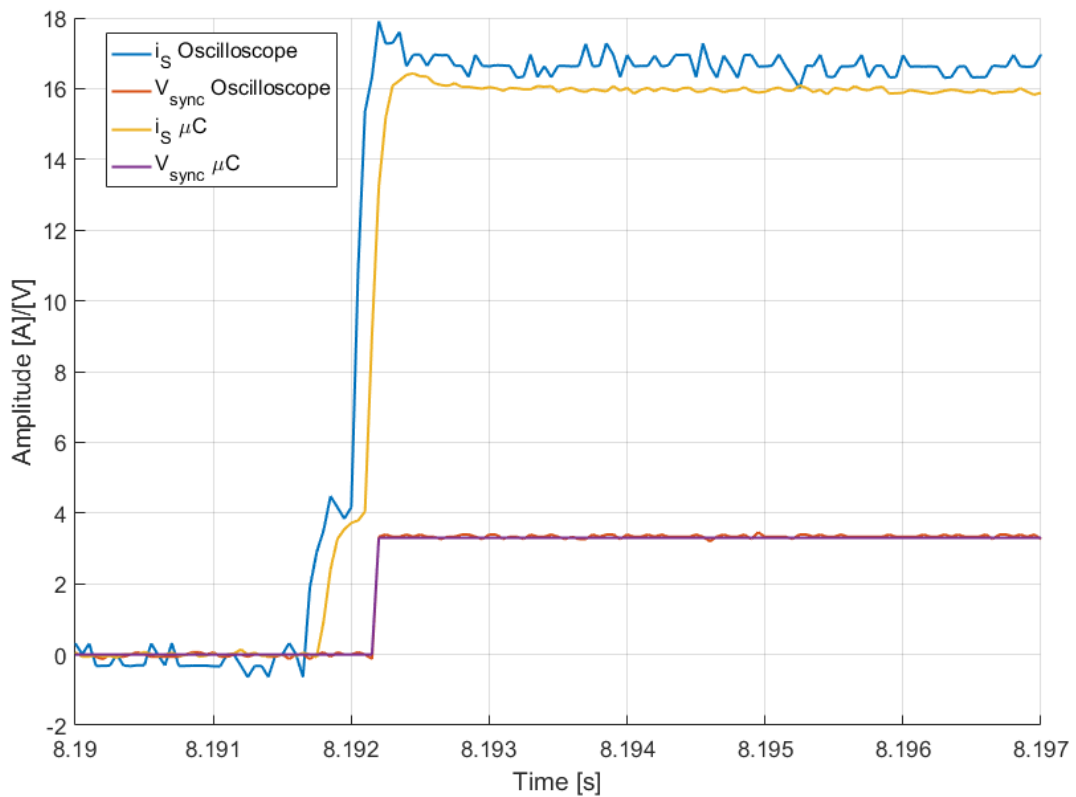


FIGURE 3.6: Plot of supply current and synchronisation signal

The captured supply current waveforms were used to obtain a first-order transfer function with no zeroes through the System Identification toolbox and some further tuning in Matlab. The supply current waveform captured by the oscilloscope was used as the input to the transfer function and the one captured by the microcontroller was used as the output. The low-pass filter transfer function obtained is shown in (3.5) below. This low-pass filter thus has a cut-off frequency of  $14451 \text{rads}^{-1} / 2\pi = 2300 \text{Hz}$ .

$$G_f(s) = \frac{13978}{s + 14451} \quad (3.5)$$

Figure 3.7 shows in gray the supply current captured by the oscilloscope, in yellow the current captured by the microcontroller and in orange the current approximated by the obtained transfer function. The approximated current was obtained by applying the current captured by the oscilloscope to the obtained transfer function using the *lsim* function in Matlab. From this plot, one can conclude that the obtained transfer function in (3.5) approximates the current captured by the microcontroller sufficiently.

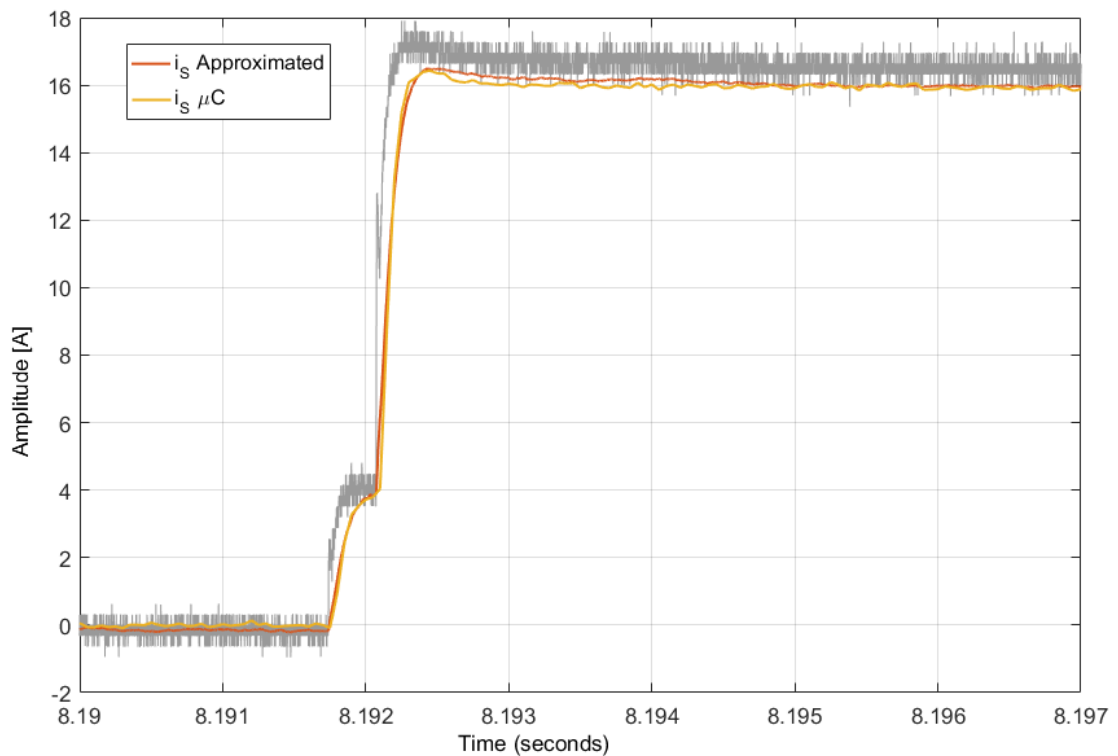


FIGURE 3.7: Plot of actual and approximated supply current

### 3.4 Simulation Model

In order to emulate as closely as possible the behaviour of the HDMS microcontroller's real time algorithm, an s-function was used in the simulation model. The s-function was programmed in C++ and set to update at a rate of 20kHz in order to match the real application's main interrupt function frequency. Figure 3.8 shows the s-function and PWM generation implemented in the simulation model.

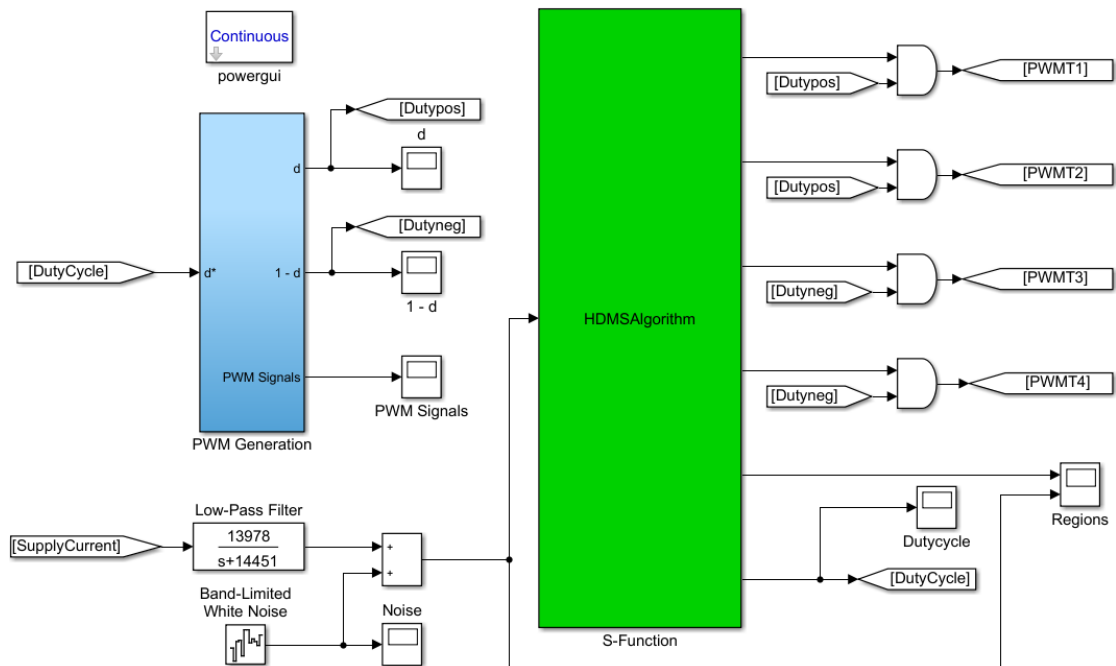


FIGURE 3.8: S-function and PWM generation implemented in simulation model

The previously obtained low-pass filter transfer function filters the measured supply current. This was combined with band-limited white noise to imitate the measurement errors of the ADC in the real application.

The supply current is the only input to the s-function. The control algorithm was implemented in the s-function using the Bilinear Transformation. The duty cycle that the control algorithm produces is passed onto the PWM generation subsystem. This subsystem consists of a 20kHz triangular wave, which is compared to the value of the duty cycle in order to generate the PWM signals. Two PWM signals are generated, which correspond to  $d$  and  $1 - d$  in order to implement the three operating regions with the switching devices.

Depending on the value of the supply current, the s-function was set to enable or disable the PWM signals applied to the IGBTs. This was implemented through the use of AND-gates to control which region of operation is executed.

The simulation model circuitry is shown in Figure 3.9. This simulation model consists of the main components of the HDMS prototype, being the damped LC low-pass input filter, the switching devices, being IGBTs and the RL-load, representing the motor winding at standstill. The parameters used for the aforementioned components are tabulated in Table 3.1.

TABLE 3.1: Simscape simulation component parameters

Parameter	Symbol	Value
LC-filter damping resistor	$R_1$	$0.2\Omega$
LC-filter inductance	$L_1$	$190\mu H$
LC-filter capacitance	$C$	$4.7\mu F$
Motor winding resistance	$R_2$	$2.16\Omega$
Motor winding inductance	$L_2$	$11.65mH$

### 3.5 Conclusion

This chapter has shown how the motor winding parameters of the single-phase induction motor were obtained through the application of a low AC voltage. The motor winding was represented as an equivalent RL-load. Furthermore, the simulation model used to simulate the HDMS prototype was explained. This includes an s-function for the implementation of the microcontroller code, a low-pass filter which is present on the prototype in order to filter out the 20kHz switching frequency and a PWM module.

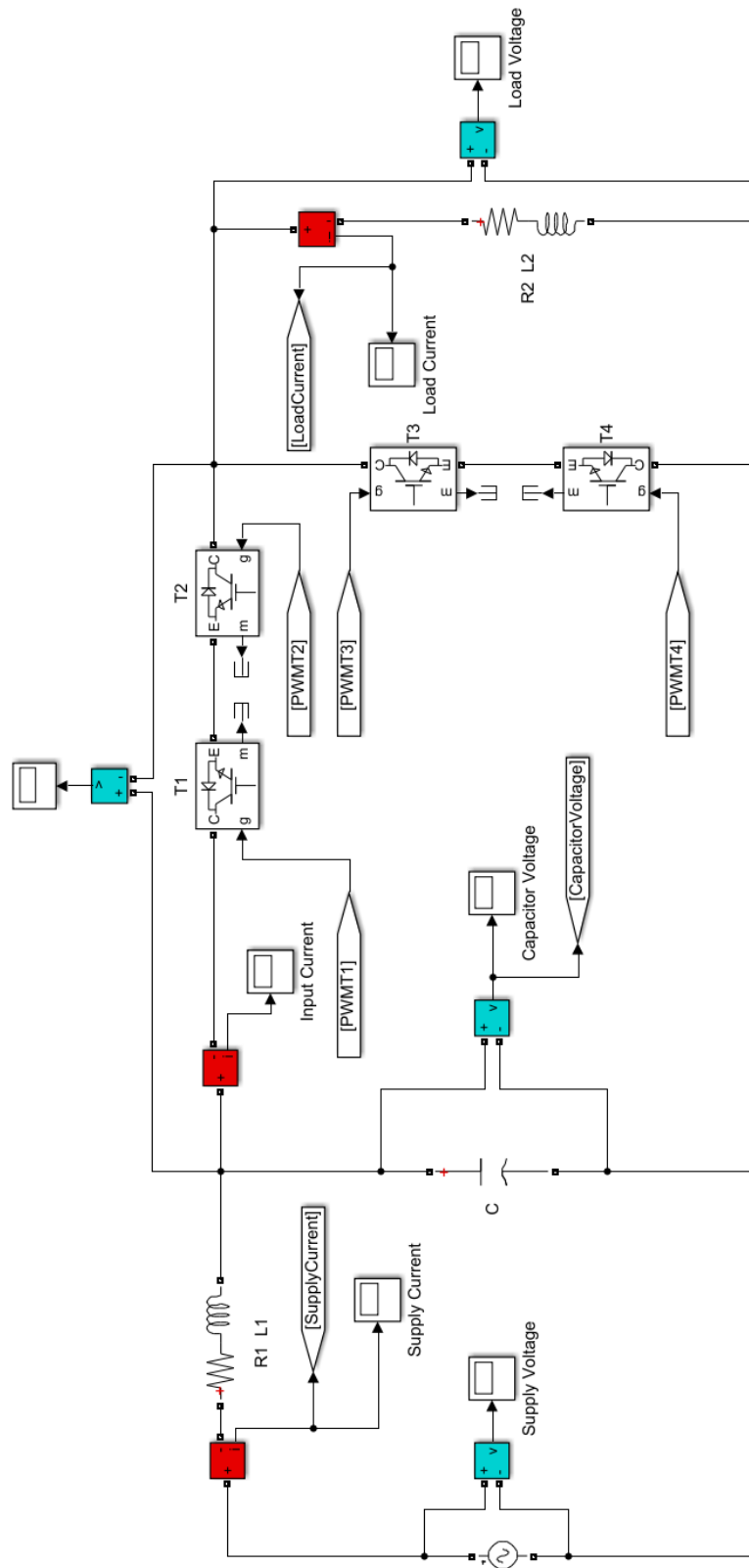


FIGURE 3.9: Simscape simulation model circuitry

# Chapter 4

## System Stability Analysis

### 4.1 Introduction

This chapter covers the stability analysis of the HDMS current control system. For this, the system is first modelled in state space. The system is then analysed for stability in both open-loop and closed-loop.

### 4.2 Stability Analysis of the Plant

#### 4.2.1 State Space Representation of the Plant

The circuit used for this project is simplified and can be seen in Figure 4.1. It consists of four IGBTs, the motor RL winding obtained in the previous chapter and the input LC-filter. This Buck converter circuit is driven from a single-phase AC supply of  $v_S = 325V_{rms}$  at a frequency of  $f_S = 50\text{Hz}$ .

In electrical circuits, capacitor voltages or inductor currents are usually selected as state variables, due to their ability to store energy. Hence, in this circuit the state variables comprise the supply current  $i_S$  passing through inductance  $L_1$  of the damped LC-filter, the capacitor voltage  $v_C$  and the load current  $i_L$  passing through the inductance  $L_2$  of the motor winding. Inputs to the plant are the supply voltage  $v_S$  and the duty cycle  $d$  applied to the IGBTs.

The system modelling of this Buck converter is based on the average model [12], where it is assumed that the load voltage  $v_L$  is equal to the duty cycle  $d$  times the supply voltage  $v_S$ . Since this converter contains a damped input LC-filter, which introduces a voltage drop, the load voltage becomes equal to the duty cycle  $d$  times the capacitor voltage  $v_C$ .

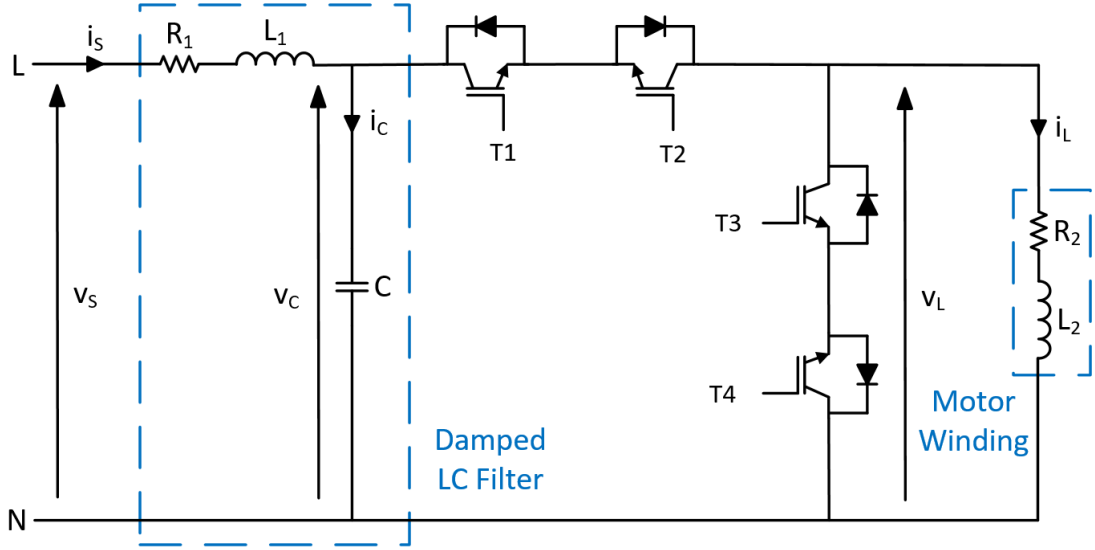


FIGURE 4.1: Circuit diagram of plant including input LC-filter and damping resistor

The supply voltage  $v_S$  is equal to the voltage drop across the inductance  $L_1$ , the resistance  $R_1$  and the capacitor voltage  $v_C$ . This may be rearranged as follows:

$$v_S = L_1 \frac{di_S}{dt} + R_1 i_S + v_C \quad \therefore \frac{di_S}{dt} = \frac{1}{L_1} v_S - \frac{R_1}{L_1} i_S - \frac{1}{L_1} v_C \quad (4.1)$$

The load voltage may be expressed in terms of the capacitor voltage, as they are in parallel. However, it is equal to the average capacitor voltage depending on the duty cycle of the IGBTs. This is expressed in (4.2).

$$dv_C = i_L R_2 + L_2 \frac{di_L}{dt} \quad \therefore \frac{di_L}{dt} = \frac{d}{L_2} v_C - \frac{R_2}{L_2} i_L \quad (4.2)$$

For the last state variable, the supply current  $i_S$  is considered. This current is equal to the summation of both the capacitor current and, depending on the duty cycle  $d$ , the load current  $i_L$ . This is formulated in (4.3).

$$i_S = C \frac{dv_C}{dt} + di_L \quad \therefore \frac{dv_C}{dt} = \frac{1}{C} i_S - \frac{d}{C} i_L \quad (4.3)$$

From (4.1) through (4.3), it follows that the system may be expressed as a set of functions  $\mathbf{f}(\mathbf{x}, \mathbf{u})$ , as expressed in (4.4).

$$\mathbf{f}(\mathbf{x}, \mathbf{u}) = \begin{pmatrix} \dot{i}_S \\ \dot{i}_L \\ \dot{v}_C \end{pmatrix} = \begin{pmatrix} \frac{1}{L_1}v_S - \frac{R_1}{L_1}i_S - \frac{1}{L_1}v_C \\ \frac{d}{L_2}v_C - \frac{R_2}{L_2}i_L \\ \frac{1}{C}i_S - \frac{d}{C}i_L \end{pmatrix} \quad (4.4)$$

### 4.2.2 Linearisation of Plant Equations

An important assumption made in this dissertation is that the supply voltage  $v_S$  is considered to be a disturbance rather than an input to the system, as it may not be controlled and is slow-changing at 50Hz. Considering the expressions of the states representing the load current  $\dot{i}_L$  and the capacitor voltage  $\dot{v}_c$ , one can notice the multiplication of state variables with the plant input  $d$  in  $\frac{dv_c}{L_2}$  and  $\frac{di_L}{C}$ . This implies that the system is non-linear and hence certain analysis tools, reserved for Linear Time Invariant (LTI) systems, may not be applied. However, the non-linear system may be linearised around an equilibrium point and its equivalent linear approximation may be analysed using tools such as the frequency response. In this manner, the results obtained for the non-linear system may be verified through the linear approximation for small deviations from the chosen equilibrium point.

In order to linearise this system around an equilibrium point, the input variable  $u^*$  for that equilibrium point, must be chosen first. Using this value, the state variables  $\mathbf{x}^*$  are then calculated at the equilibrium point by equating the functions in (4.4) to zero:  $\mathbf{f}(\mathbf{x}, u^*) = \mathbf{0}$  and solving for  $\mathbf{x}^*$ . Furthermore, the Jacobian matrices  $\mathbf{A}$  and  $\mathbf{B}$  must be evaluated at the equilibrium point. These are given in (4.5) and (4.6).

$$\mathbf{A} = \begin{pmatrix} \frac{\partial \dot{i}_S}{\partial i_S} & \frac{\partial \dot{i}_S}{\partial i_L} & \frac{\partial \dot{i}_S}{\partial v_C} \\ \frac{\partial \dot{i}_L}{\partial i_S} & \frac{\partial \dot{i}_L}{\partial i_L} & \frac{\partial \dot{i}_L}{\partial v_C} \\ \frac{\partial \dot{v}_C}{\partial i_S} & \frac{\partial \dot{v}_C}{\partial i_L} & \frac{\partial \dot{v}_C}{\partial v_C} \end{pmatrix}_{\substack{\mathbf{x}=\mathbf{x}^* \\ u=u^*}} = \begin{pmatrix} -\frac{R_1}{L_1} & 0 & -\frac{1}{L_1} \\ 0 & -\frac{R_2}{L_2} & \frac{d^*}{L_2} \\ \frac{1}{C} & -\frac{d^*}{C} & 0 \end{pmatrix} \quad (4.5)$$

$$\mathbf{B} = \begin{pmatrix} \frac{\partial \dot{i}_S}{\partial d} \\ \frac{\partial \dot{i}_L}{\partial d} \\ \frac{\partial \dot{v}_C}{\partial d} \end{pmatrix}_{\substack{\mathbf{x}=\mathbf{x}^* \\ u=u^*}} = \begin{pmatrix} 0 \\ \frac{v_C^*}{L_2} \\ -\frac{i_L^*}{C} \end{pmatrix} \quad (4.6)$$

The complete linearised model of this system in state space form, that is valid in the vicinity of an equilibrium point  $(\mathbf{x}^*, u^*)$  may then be represented by (4.7). The variables  $\bar{\mathbf{x}}$  and  $\bar{u}$  represent the small deviations from the equilibrium point  $\mathbf{x} - \mathbf{x}^*$  and  $u - u^*$  respectively.

$$\begin{pmatrix} \dot{i}_S \\ \dot{i}_L \\ \dot{v}_C \end{pmatrix} = \begin{pmatrix} -\frac{R_1}{L_1} & 0 & -\frac{1}{L_1} \\ 0 & -\frac{R_2}{L_2} & \frac{d^*}{L_2} \\ \frac{1}{C} & -\frac{d^*}{C} & 0 \end{pmatrix} \begin{pmatrix} \bar{i}_S \\ \bar{i}_L \\ \bar{v}_C \end{pmatrix} + \begin{pmatrix} 0 \\ \frac{v_C^*}{L_2} \\ -\frac{i_L^*}{C} \end{pmatrix} \bar{d} \quad (4.7)$$

### 4.2.3 Stability Analysis of Plant Equations

A simulation model based on the non-linear set of differential equations in (4.4) was implemented to be able to analyse their behaviour across a range of values for the duty cycle  $d$ . This simulation model is shown in Figure 4.2. Each summation point represents a differential equation for one of the state equations. Integrator blocks then integrate these differential equations to obtain the corresponding state variable. For the analysis, the supply voltage was set to its peak value  $v_S = 325V$ , as this represents the worst case scenario. The duty cycle, which is the input to the open-loop system, was applied in the form of a ramp with a gradient of 1, such that it will reach its maximum value within one second. The initial capacitor voltage  $v_C$  was assumed to be fully charged and thus equal to the supply voltage  $v_S$  at  $t = 0s$ .



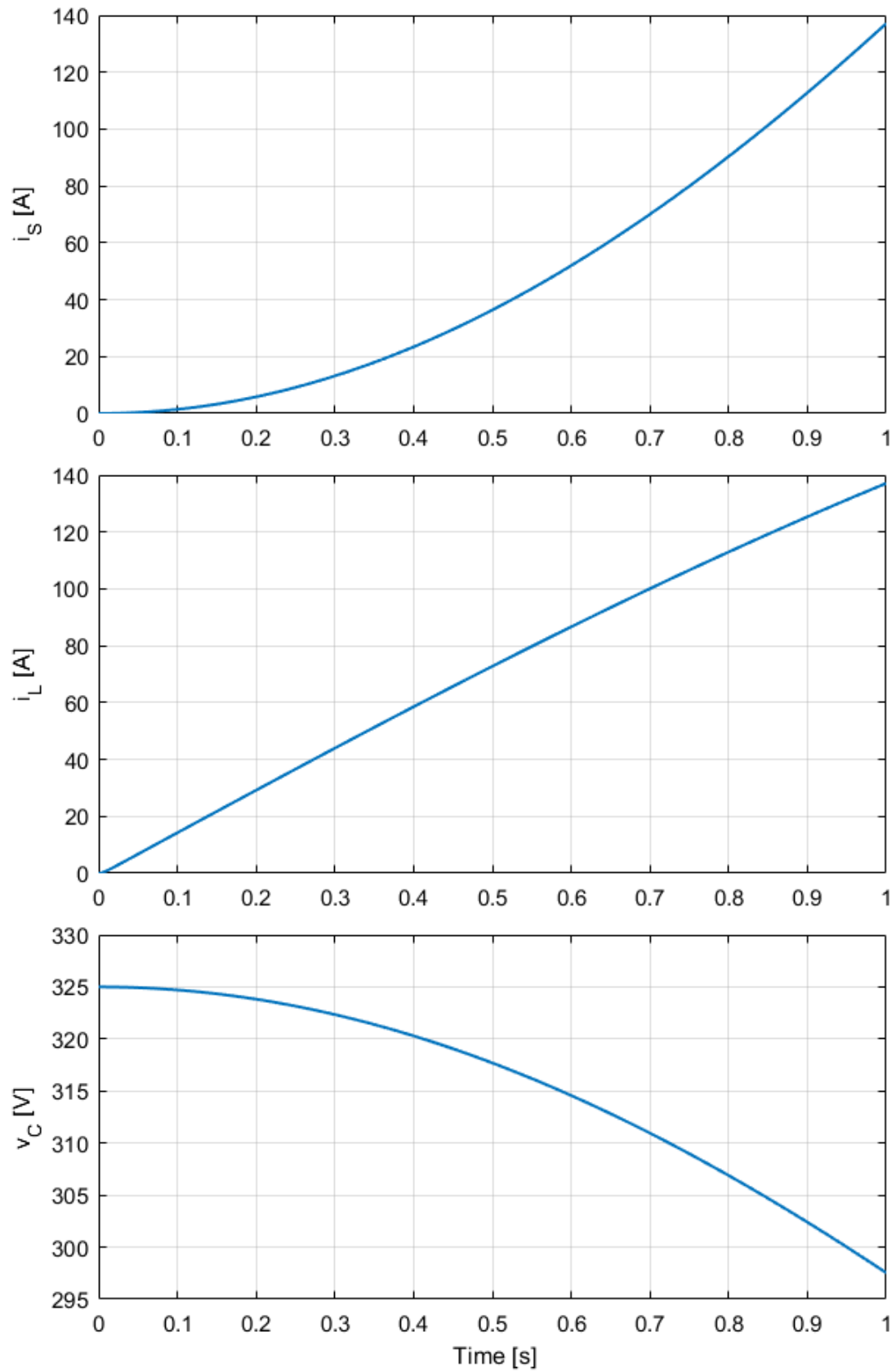


FIGURE 4.4: Plant state variables with duty cycle ramp applied

### 4.3 Stability Analysis of Closed-Loop System

#### 4.3.1 State Space Representation of Closed-Loop System

The complete closed-loop system comprising the compensator and the plant is shown in Figure 4.5. The duty cycle generated by the compensator is applied to the IGBTs of the plant to produce the desired supply current  $i_s$ . The duty cycle is multiplied by a factor  $K_1$  and subtracted from the reference current  $i_{ref}$  along with the supply current  $i_s$ .

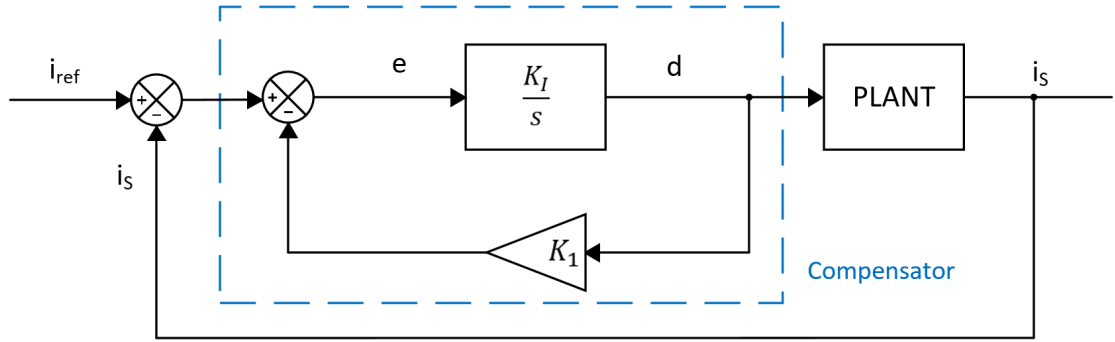


FIGURE 4.5: Block diagram of complete closed-loop system

The implemented compensator consists of an integrator with a feedback gain. The compensator's transfer function, which was previously derived in (2.16), is stated again in (4.8).

$$G_c(s) = \frac{K_I}{s + K_1 K_I} \quad (4.8)$$

This integrator introduces another state variable, effectively making the closed-loop system of order  $n = 4$ . The fourth state variable was chosen to be the duty cycle  $d$  and it may be expressed as:

$$d = e \left( \frac{K_I}{s} \right) \quad \therefore \dot{d} = K_I(i_{ref} - dK_1 - i_s) \quad (4.9)$$

Hence, by combining (4.1) - (4.3) and (4.9), the complete closed-loop system may be expressed by (4.10), where  $\mathbf{x} = (i_s, i_L, v_C, d)^T$  and  $u = i_{ref}$  represent the state vector and input respectively. The duty cycle for the closed-loop system is now a state rather than an input, as it was for the plant. It is replaced as an input by the reference current  $i_{ref}$ .

$$\mathbf{f}(\mathbf{x}, \mathbf{u}) = \begin{pmatrix} \dot{i}_S \\ \dot{i}_L \\ \dot{v}_C \\ \dot{d} \end{pmatrix} = \begin{pmatrix} \frac{1}{L_1}v_S - \frac{R_1}{L_1}i_S - \frac{1}{L_1}v_C \\ \frac{d}{L_2}v_C - \frac{R_2}{L_2}i_L \\ \frac{1}{C}i_S - \frac{d}{C}i_L \\ K_I(i_{ref} - dK_1 - i_S) \end{pmatrix} \quad (4.10)$$

### 4.3.2 Linearisation of Closed-Loop System Equations

For this system, the Jacobian matrices  $\mathbf{A}$  and  $\mathbf{B}$  are defined by (4.11) and (4.12) respectively.

$$\mathbf{A} = \begin{pmatrix} \frac{\partial \dot{i}_S}{\partial i_S} & \frac{\partial \dot{i}_S}{\partial i_L} & \frac{\partial \dot{i}_S}{\partial v_C} & \frac{\partial \dot{i}_S}{\partial d} \\ \frac{\partial \dot{i}_L}{\partial i_S} & \frac{\partial \dot{i}_L}{\partial i_L} & \frac{\partial \dot{i}_L}{\partial v_C} & \frac{\partial \dot{i}_L}{\partial d} \\ \frac{\partial \dot{v}_C}{\partial i_S} & \frac{\partial \dot{v}_C}{\partial i_L} & \frac{\partial \dot{v}_C}{\partial v_C} & \frac{\partial \dot{v}_C}{\partial d} \\ \frac{\partial \dot{d}}{\partial i_S} & \frac{\partial \dot{d}}{\partial i_L} & \frac{\partial \dot{d}}{\partial v_C} & \frac{\partial \dot{d}}{\partial d} \end{pmatrix}_{\substack{\mathbf{x}=\mathbf{x}^* \\ \mathbf{u}=\mathbf{u}^*}} = \begin{pmatrix} -\frac{R_1}{L_1} & 0 & -\frac{1}{L_1} & 0 \\ 0 & -\frac{R_2}{L_2} & \frac{d^*}{L_2} & \frac{v_C^*}{L_2} \\ \frac{1}{C} & -\frac{d^*}{C} & 0 & -\frac{i_L^*}{C} \\ -K_I & 0 & 0 & -K_I K_1 \end{pmatrix} \quad (4.11)$$

$$\mathbf{B} = \begin{pmatrix} \frac{\partial \dot{i}_S}{\partial i_{ref}} \\ \frac{\partial \dot{i}_L}{\partial i_{ref}} \\ \frac{\partial \dot{v}_C}{\partial i_{ref}} \\ \frac{\partial \dot{d}}{\partial i_{ref}} \end{pmatrix}_{\substack{\mathbf{x}=\mathbf{x}^* \\ \mathbf{u}=\mathbf{u}^*}} = \begin{pmatrix} 0 \\ 0 \\ 0 \\ K_I \end{pmatrix} \quad (4.12)$$

The complete linearised model of this system in state space form around an equilibrium point  $(\mathbf{x}^*, \mathbf{u}^*)$  may then be represented by (4.13).

$$\begin{pmatrix} \dot{i}_S \\ \dot{i}_L \\ \dot{v}_C \\ \dot{d} \end{pmatrix} = \begin{pmatrix} -\frac{R_1}{L_1} & 0 & -\frac{1}{L_1} & 0 \\ 0 & -\frac{R_2}{L_2} & \frac{d^*}{L_2} & \frac{v_C^*}{L_2} \\ \frac{1}{C} & -\frac{d^*}{C} & 0 & -\frac{i_L^*}{C} \\ -K_I & 0 & 0 & -K_I K_1 \end{pmatrix} \begin{pmatrix} \bar{i}_s \\ \bar{i}_L \\ \bar{v}_C \\ \bar{d} \end{pmatrix} + \begin{pmatrix} 0 \\ 0 \\ 0 \\ K_I \end{pmatrix} \begin{pmatrix} \bar{i}_{ref} \end{pmatrix} \quad (4.13)$$

### 4.3.3 Stability Analysis of Closed-Loop System Equations

A simulation model based on the non-linear differential equations obtained in (4.10) was implemented to observe the system dynamics for a range of input conditions. While performing a motor soft-start, the input  $i_{ref}$  is not changed in the HDMS. It remains constant and only the supply voltage  $v_S$  changes with time. For this reason, the system is analysed for changes in the supply voltage. The supply voltage in this analysis ranges from  $v_S = 50V \rightarrow 350V$  in increments of  $50V$ . The supply voltage is applied as a summation of step functions, allowing the system to settle in between each step. In this manner, the behaviour of all the system state variables may be observed for each voltage level. The complete system can be seen in Figure 4.6. The duty cycle  $d$  is limited, such that it remains between 0 and 1, which represents a duty cycle of 0 and 100% respectively.

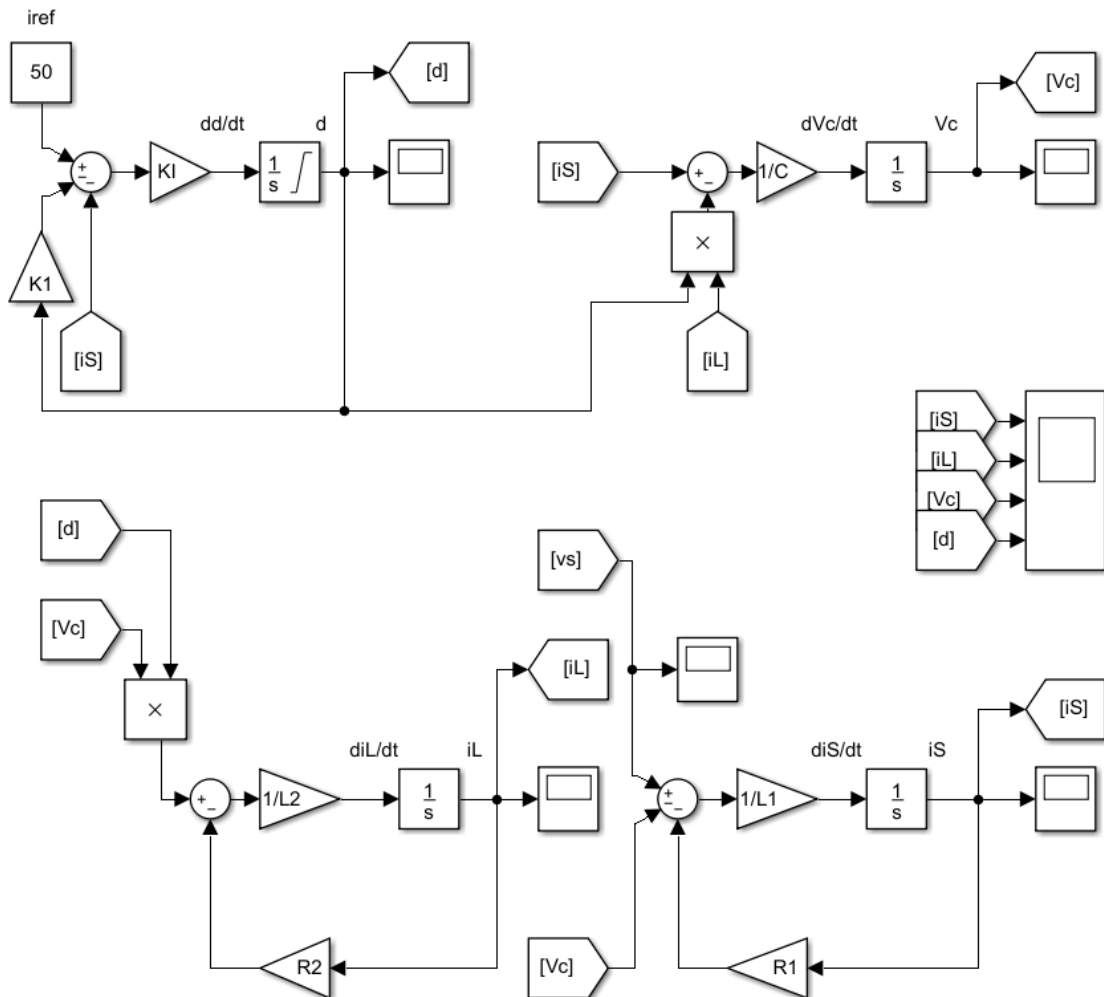


FIGURE 4.6: Simulation of non-linear closed-loop system differential equations

All the parameters of this closed-loop system are listed in Table 4.2 below. These replicate the parameters present in the HDMS hardware prototype.

TABLE 4.2: Closed-loop system simulation parameters

Parameter	Symbol	Value
LC-filter damping resistor	$R_1$	$0.2\Omega$
LC-filter inductance	$L_1$	$190\mu H$
LC-filter capacitance	$C$	$4.7\mu F$
Motor winding resistance	$R_2$	$2.16\Omega$
Motor winding inductance	$L_2$	$11.65mH$
Compensator forward gain	$K_I$	$50A^{-1}$
Compensator feedback gain	$K_1$	$35A$
Fixed reference current	$i_{ref}$	$45A$

The supply voltage  $v_S$  applied to this non-linear closed-loop system as a summation of step functions is shown in Figure 4.7. The supply voltage can be seen to start at a value of 50 and increase in steps of 50V every 0.1s, reaching its final value of 350V at  $t = 0.6s$ . The steps in voltage are spaced by 100ms in order to ensure that the system state variables settle.

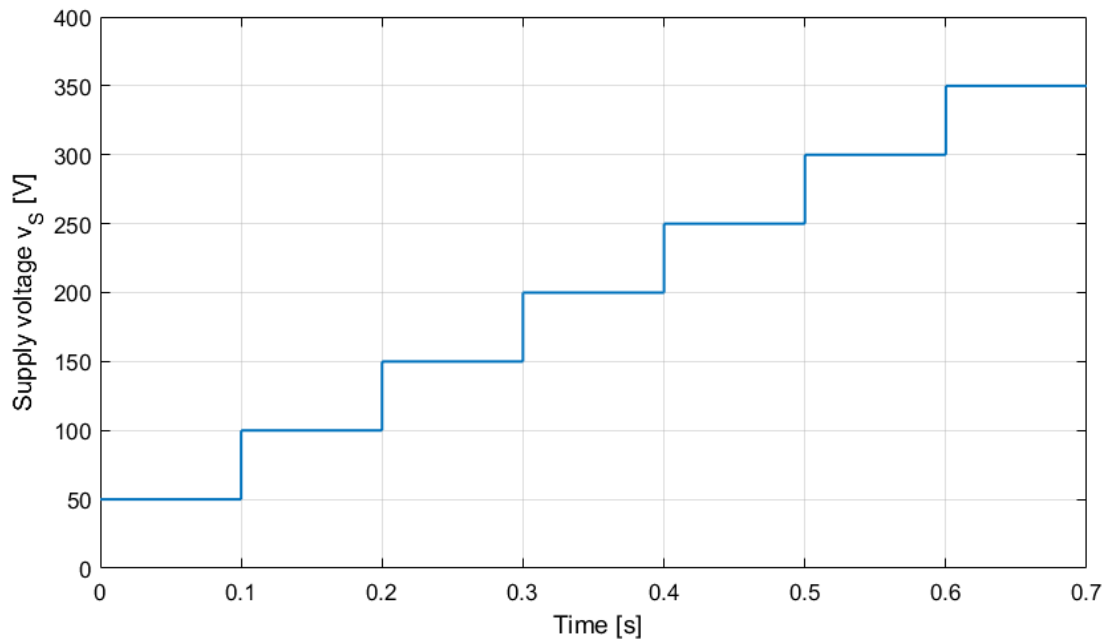


FIGURE 4.7: Supply voltage applied to closed-loop system

The effect that the first step of this supply voltage has on the individual state variables of the closed-loop system may be seen in Figure 4.8. As the system starts off with zero initial conditions, the supply voltage of  $v_S = 50V$  causes the duty cycle to rise to 100%. After remaining saturated for some time, it settles to its steady state value. The state variables  $i_S$  and  $v_C$  exhibit a very low damping oscillatory transient, which indicates that the system may already be very close to the stability margin. These oscillations occur at the LC-filter resonance frequency, which is  $f_{LC} = 5.325\text{kHz}$ . However, they eventually die out and all state variables, including  $i_L$ , settle to a constant steady state value.

Figure 4.9 shows the state variables' response due to all supply voltage steps. At  $t = 0.1\text{s}$ , the supply voltage steps from  $50V \rightarrow 100V$ . It can be seen that the system state variables begin to oscillate and that these oscillations remain present in all state variables. The duty cycle  $d$  however, can be seen to reach its saturation limit during these oscillations. This affects the amplitude of the oscillations.

The state variables again oscillate at a frequency of  $5.325\text{kHz}$ , which is the LC-filter resonance frequency. They also oscillate at a fixed amplitude, which depends on the amplitude of the supply voltage. This can be seen in the figure, as the amplitude of the oscillations increases with each step in the supply voltage. However, the frequency of oscillation remains the same. This behaviour indicates the presence of a limit cycle and shall be further investigated in the following sections.

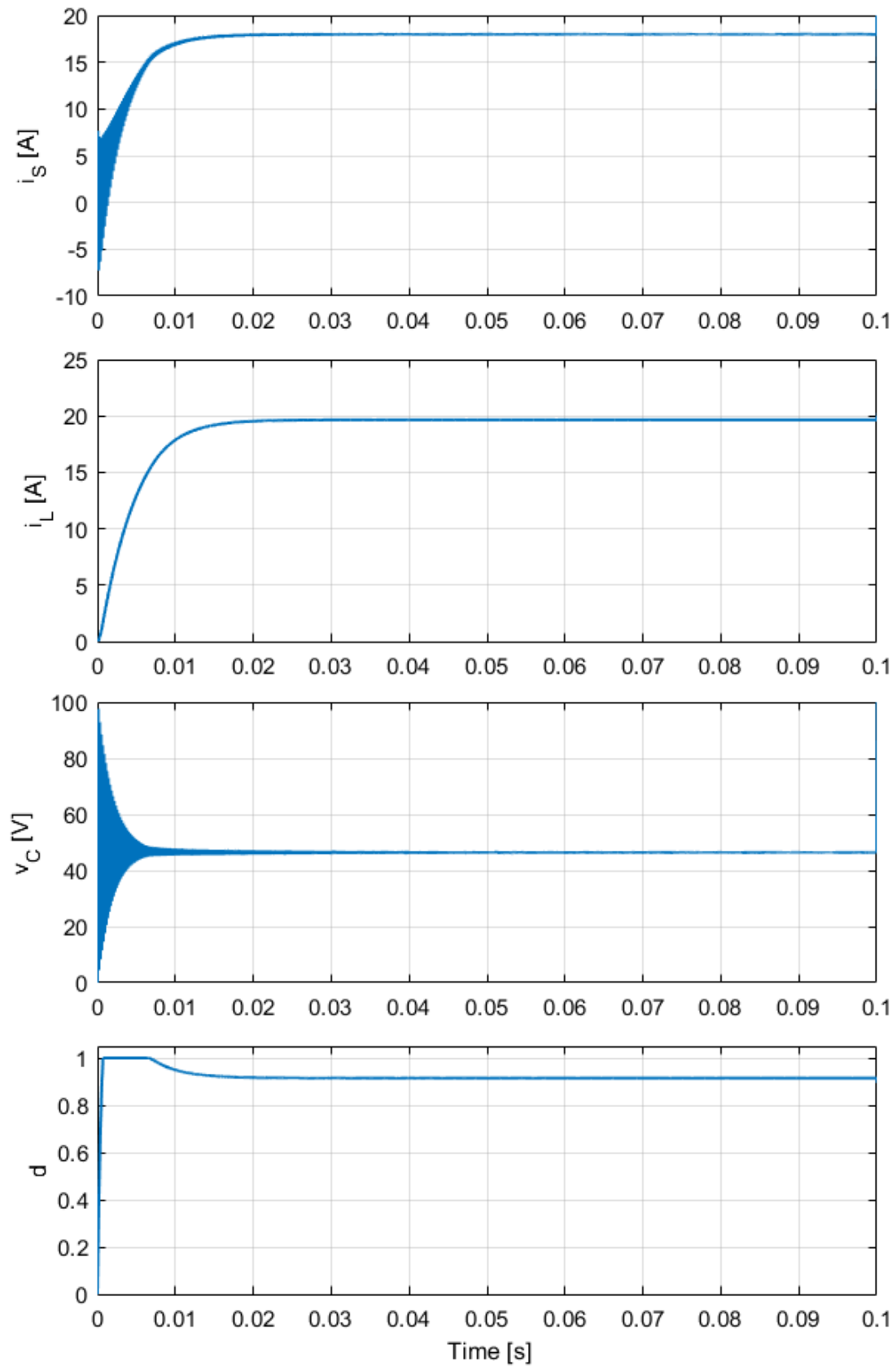


FIGURE 4.8: Closed-loop system state variables due to first supply voltage step

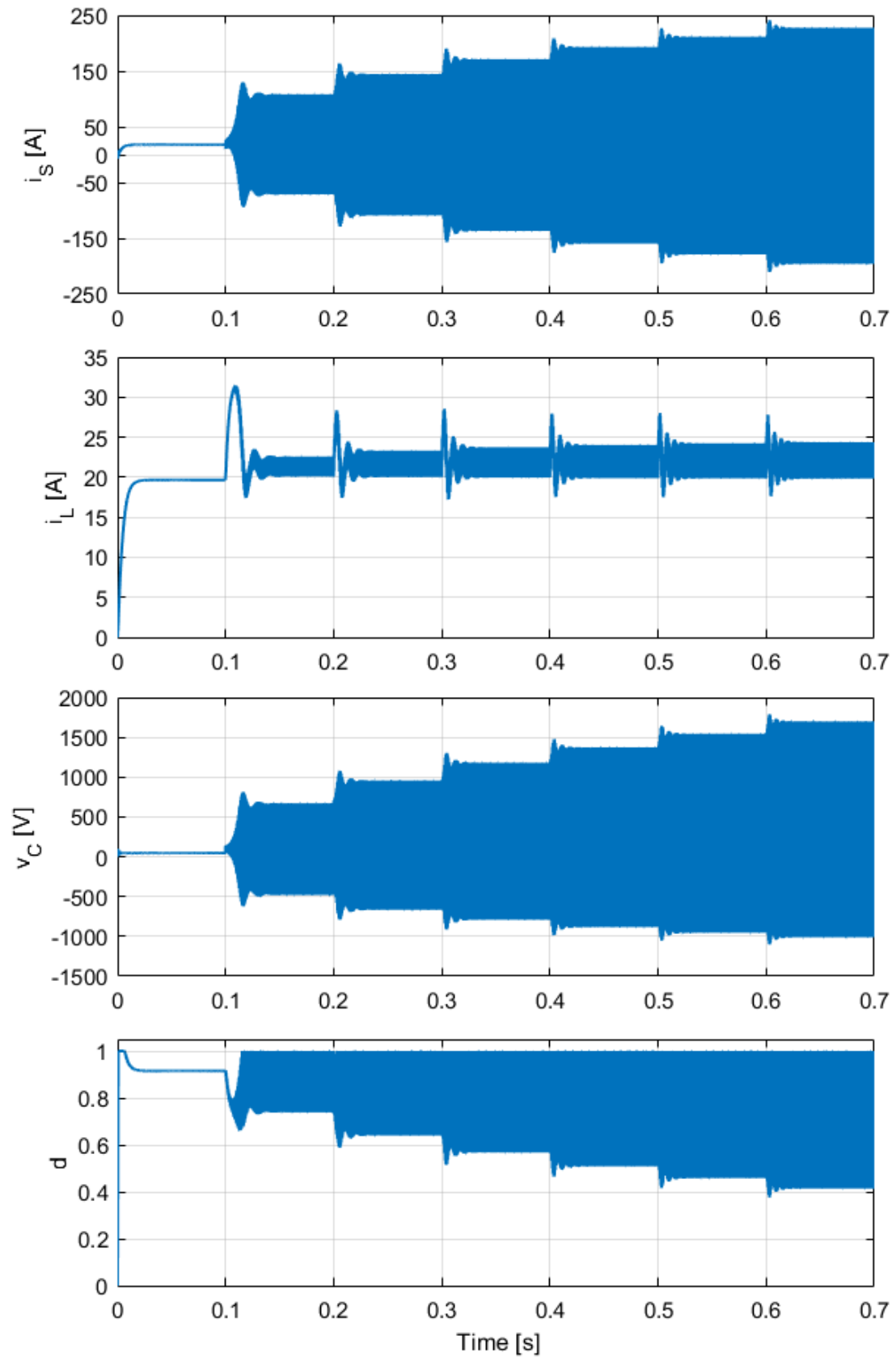


FIGURE 4.9: Closed-loop system state variables due to supply voltage steps

### 4.3.3.1 Linear Closed-Loop Model Analysis

For this analysis, the closed-loop model is linearised for the supply voltages applied in the previous section. These operating points cover the entire operating range of the HDMS. The stability properties of the system around these operating points may then be studied through the use of traditional linear system analysis tools. This is carried out in this section by solving the system equations for different instances of the supply voltage  $v_S$ . Using these solutions, which represent equilibrium points, a linear model may be obtained describing the system dynamics around these equilibrium points. By converting this newly obtained linear state space system to a transfer function, the system may be analysed for stability using the frequency domain. Since the supply current  $i_S$  represents the system's output, this transfer function will represent the system dynamics for  $G(s) = \frac{i_S}{v_S}$ . As derived in Section 4.3.1, the system is described by the differential equations shown in (4.14).

$$\begin{pmatrix} \dot{i}_S \\ \dot{i}_L \\ \dot{v}_C \\ \dot{d} \end{pmatrix} = \begin{pmatrix} \frac{1}{L_1}v_S - \frac{R_1}{L_1}i_S - \frac{1}{L_1}v_C \\ \frac{d}{L_2}v_C - \frac{R_2}{L_2}i_L \\ \frac{1}{C}i_S - \frac{d}{C}i_L \\ K_I(i_{ref} - dK_1 - i_S) \end{pmatrix} \quad (4.14)$$

By letting  $\mathbf{f}(\mathbf{x}) = \mathbf{0}$ , the system state variables may be solved for the equilibrium point defined by the fixed reference current  $i_{ref}$  and a value of supply voltage  $v_S$ . For this, the following steady state equations are obtained.

$$f_1 = 0 \quad \rightarrow \quad i_S = \frac{1}{R_1}(v_S - v_C) \quad (4.15a)$$

$$f_2 = 0 \quad \rightarrow \quad v_C = \frac{R_2}{d}i_L \quad (4.15b)$$

$$f_3 = 0 \quad \rightarrow \quad i_L = \frac{i_S}{d} \quad (4.15c)$$

$$f_4 = 0 \quad \rightarrow \quad d = \frac{1}{K_1}(i_{ref} - i_S) \quad (4.15d)$$

By substituting the steady state equations in (4.15), eventually one can express the supply current  $i_S$  as the cubic polynomial shown in (4.16).

$$R_1 i_S^3 - i_S^2 (v_S + 2R_1 i_{ref}) + i_S (2v_S i_{ref} + R_1 i_{ref}^2 + K_1^2 R_2) - v_S i_{ref}^2 = 0 \quad (4.16)$$

Solving this cubic polynomial will yield three solutions for the supply current  $i_S$ , of which only the real solution of magnitude less than  $i_{ref}$  is to be considered. From this solution, the equilibrium values of the remaining state variables may be computed. The linearised state space system for the chosen equilibrium point may then be obtained by substituting these values along with the system parameters into the  $\mathbf{A}$  and  $\mathbf{B}$  matrices of (4.13).

The Jacobian matrix  $\mathbf{A}$  provides information about the stability of the system through its eigenvalues. Finding these eigenvalues provides the location of the system poles. Linearising the system for the supply voltage steps applied in the previous section, namely for  $v_S = 50V \rightarrow 350V$  will thus provide information about the system stability as the supply voltage changes. In other words, the non-linear system stability is analysed through the system poles of a series of linearised models covering the supply voltage range. The system behaviour in terms of the poles of the linearised models over the complete operating range of  $v_S$  can be seen in Figure 4.10.

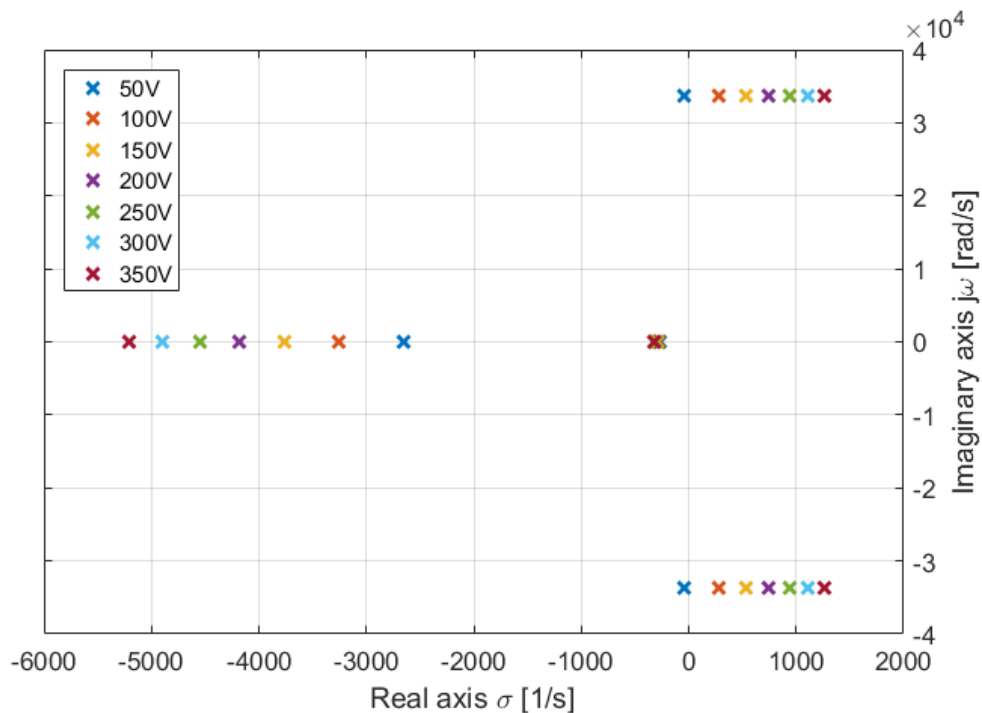


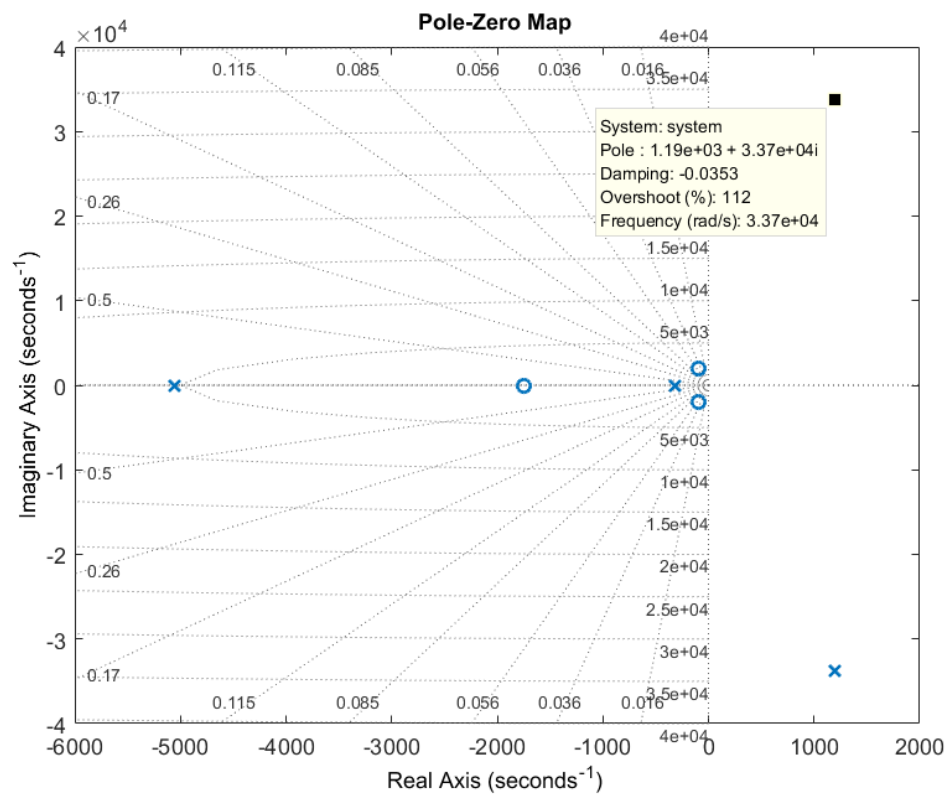
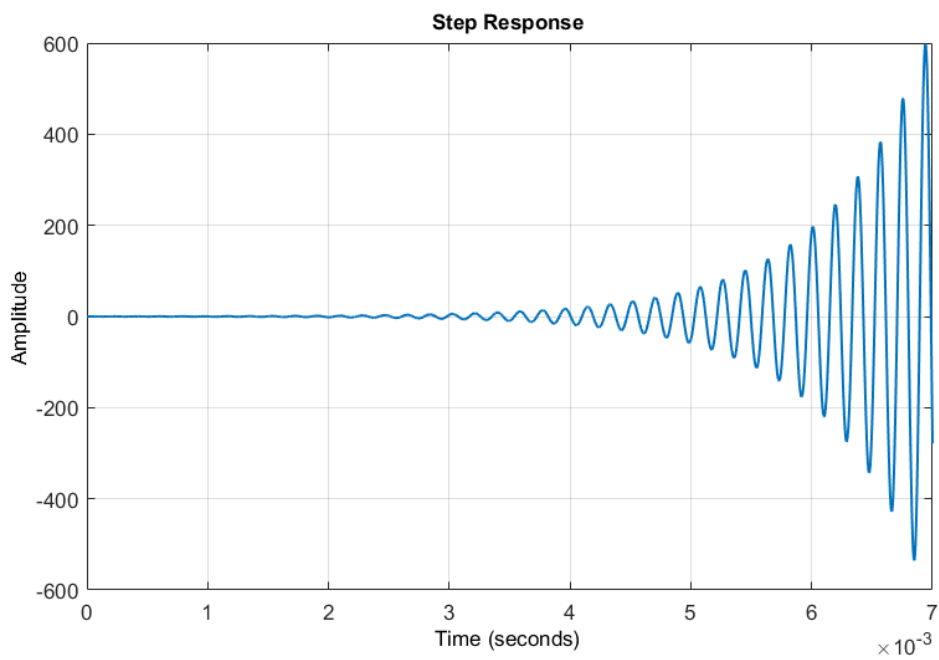
FIGURE 4.10: System poles for supply voltages  $50V \rightarrow 350V$

From this plot one can conclude that, from a linear analysis point of view, the system appears to be unstable for values of supply voltage  $v_S$  greater than  $50V$ . Clearly, somewhere between  $v_S = 50V$  and  $v_S = 100V$ , the system poles cross from the left-hand side to the right-hand side of the real axis, denoted by  $\sigma$ . In a linear system, this results in oscillations with exponentially increasing amplitude.

The complementary complex pole pairs, responsible for the oscillatory response, have a large imaginary part compared to their real part. This indicates very lowly damped oscillations, since the value of the damping coefficient  $\zeta$  equals the cosine of the angle that the complex pole makes with the origin. This angle, due to the large imaginary portion of the complex pole, is close to  $90^\circ$  and hence low damping coefficients  $\zeta < 0.1$  are obtained.

The peak of the supply voltage equals  $v_S = 325V$  and thus represents the worst case scenario input condition. The linearised model with this input condition is considered and further analysed to complement these results. Figure 4.11 shows the pole-zero map for the closed-loop system with a supply voltage of  $v_S = 325V$ . This shows the complex pole pair on the right-hand side of the real axis, as expected.

The frequency of the resulting oscillations is  $3.37 \times 10^4 rad/s$  which translates to  $5.364kHz$ . This matches the frequency of the  $5.325kHz$  sustained oscillations, which was previously measured in Section 4.3.3. The minor discrepancy is due to rounding. The fact that the complex pole pair of this linearised system is on the right-hand side of the real axis further indicates the possibility of a limit cycle. Figure 4.12 shows the step response of this linearised system. As one would expect from a linear system with unstable poles, the step response exhibits exponentially increasing oscillations at a frequency of  $5.325kHz$ .

FIGURE 4.11: Pole-zero map for linear model at  $v_S = 325V$ FIGURE 4.12: Step response for linear model at  $v_S = 325V$

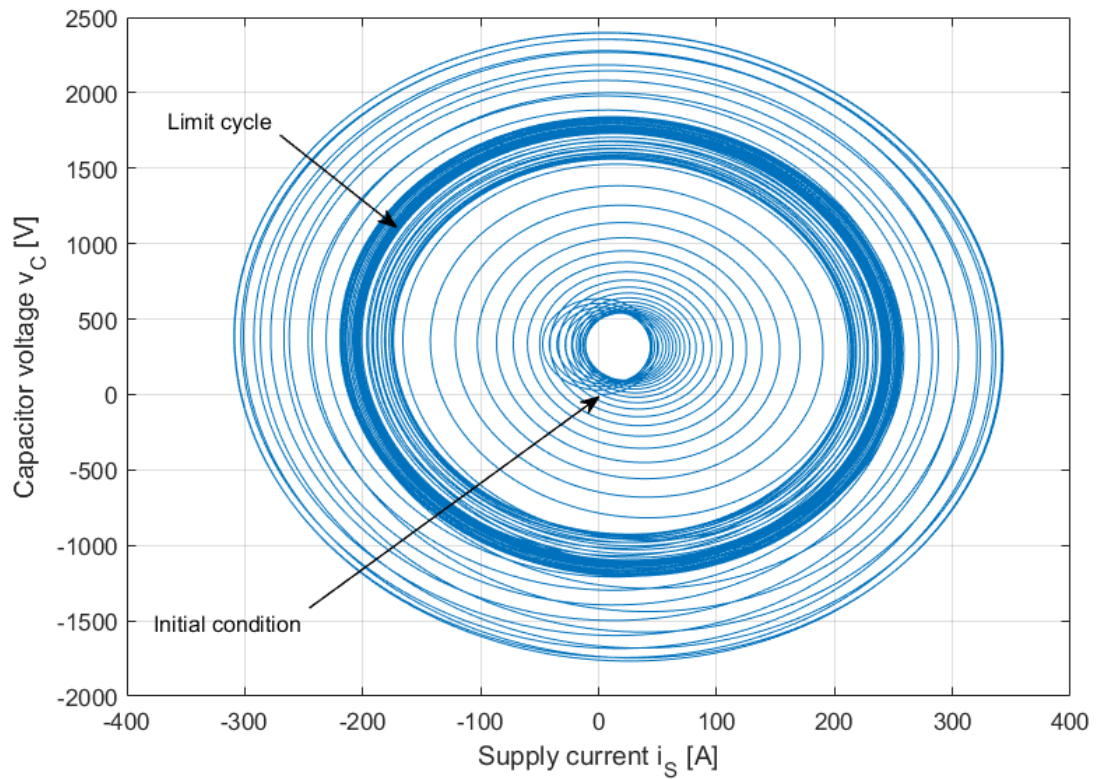
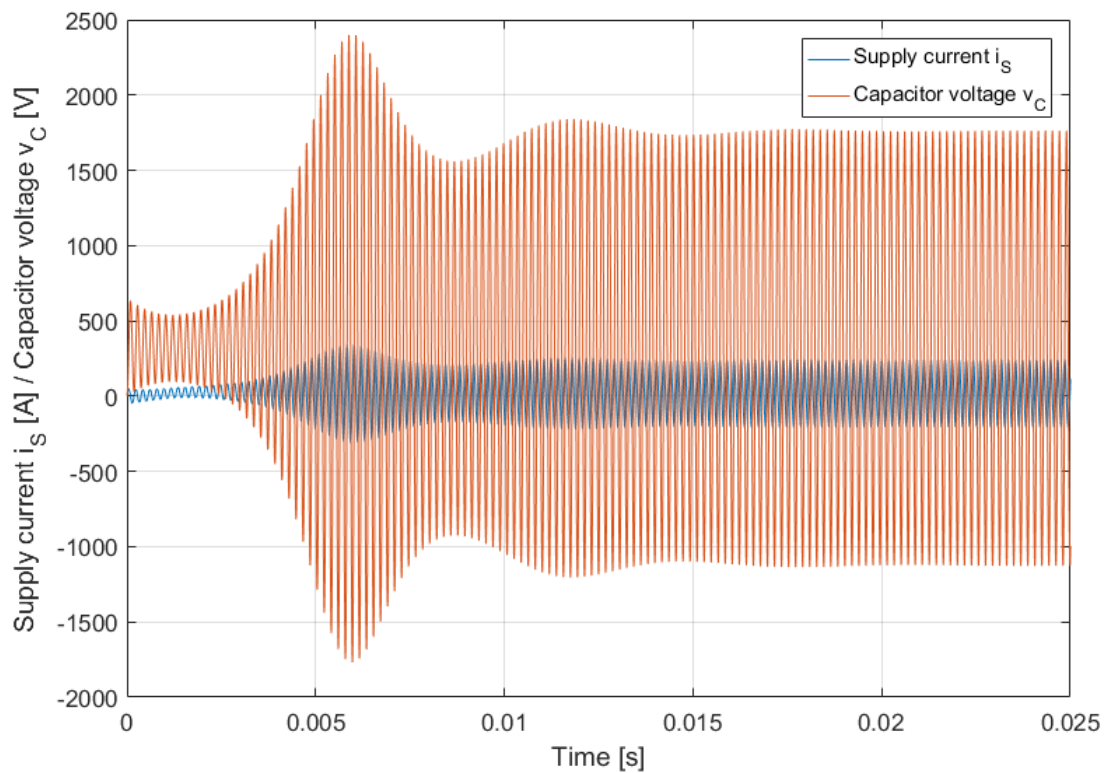
### 4.3.3.2 Phase Plane Analysis of Limit Cycle at 325V

In order to further study the behaviour of this limit cycle, the phase plane of the non-linear system is analysed. For this, two state variables are plotted against each other rather than one state variable against time. In the phase plane time is not an axis but rather is interpreted as the trajectory, hence as time passes one moves further along the phase trajectory.

The system of non-linear equations was set up in a Matlab function and *ode45* was used to solve the differential equations for 1.0s at sufficient time increments. Starting with zero initial conditions, the state variables  $x_1 = i_S$  and  $x_3 = v_C$  were plotted against each other, as shown in Figure 4.13.

The state variables can be seen to both start from 0, as zero initial conditions were used for this plot. They then converge towards the inner circle in an oscillatory fashion. From this inner circle, the state variables start to grow further in amplitude. However, due to the low damping factor observed previously, the state variables increase in a lowly damped oscillatory fashion. The phase trajectory first considerably overshoots the limit cycle and then undershoots it. Eventually the trajectory settles on the limit cycle, where the limit cycle is represented indicated in the figure.

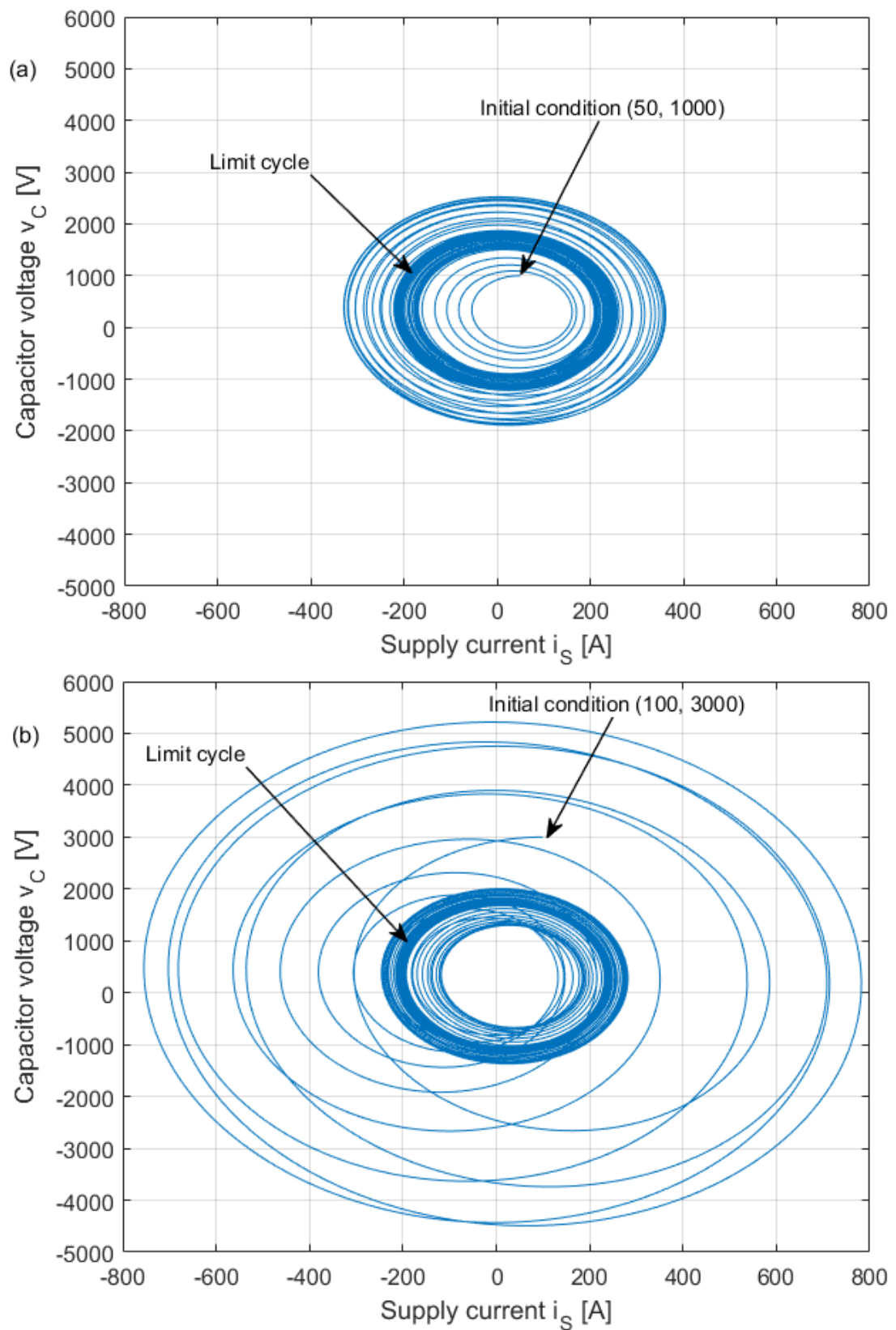
This behaviour is confirmed in Figure 4.14, which shows the state variables  $i_S$  and  $v_C$  changing with time. The initial transient represents the section of the phase trajectory converging towards the inner circle. This inner circle is the section of Figure 4.14 where the oscillations in  $v_C$  are the narrowest. From this point onwards the state variables increase in a lowly damped oscillatory fashion. A large overshoot occurs, followed by an undershoot before they eventually settle to their fixed amplitude and fixed frequency oscillations, as also observed in the phase plane.

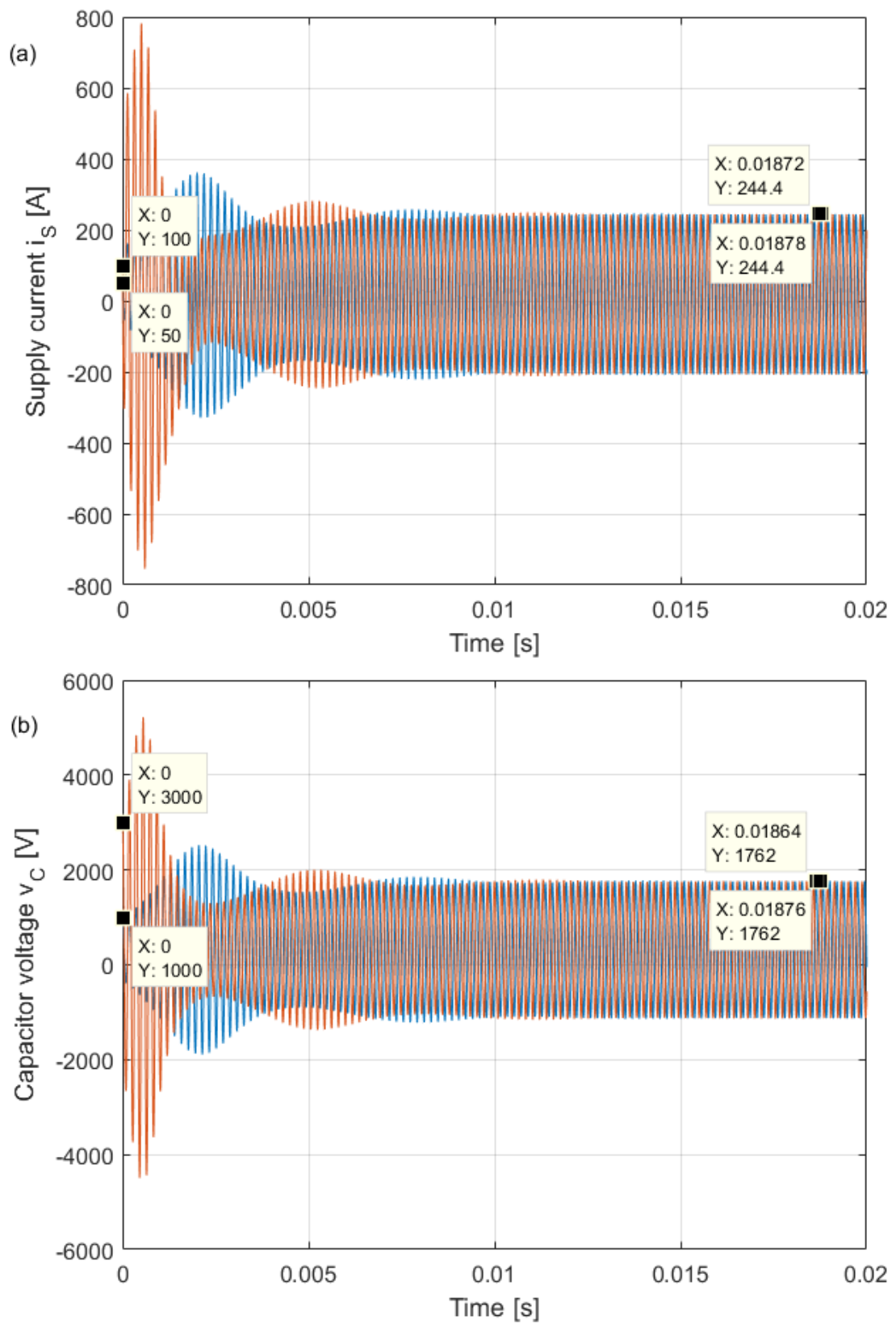
FIGURE 4.13: Phase trajectory for  $i_S$  and  $v_C$ FIGURE 4.14: Plot of  $i_S$  and  $v_C$  against time

In order to investigate the stability properties of the limit cycle, a phase portrait is considered. A phase portrait is a collection of phase trajectories in the phase plane, containing different initial conditions. However, in order to keep the plots observable, two separate phase trajectories were plotted in separate plots. These phase trajectories were started with different initial conditions, one inside the limit cycle and the other one outside the limit cycle. This can be seen in Figure 4.15, where the initial conditions are highlighted along with the limit cycle. Plot (a) shows the phase trajectory with the initial conditions inside the limit cycle and plot (b) shows the phase trajectory with initial conditions outside the limit cycle.

The trajectory starting inside the limit cycle first overshoots it. This is followed by an undershoot and it eventually settles on the limit cycle, similarly to the case where zero initial conditions were considered. The trajectory starting outside the limit cycle also overshoots it at first, then undershoots it before settling on the limit cycle. This behaviour suggests a stable limit cycle, as all trajectories in its vicinity converge to it. Several further initial conditions were used to confirm this, however they were not included as the plots become impractical to analyse.

In order to once more confirm this behaviour, the state variables  $i_S$  and  $v_C$  were plotted against time for these different initial conditions. This can be seen in Figure 4.16, where plot (a) represents  $i_S$  and plot (b) represents  $v_C$ . The initial conditions were all highlighted using data cursors. The red plots represent the initial condition (100A, 3000V) and the blue plots represent the initial condition (50A, 1000V). For both state variables and initial conditions, identical behaviour may be observed, as previously seen in the phase trajectories. It is to be noted that in both cases, starting inside and outside the limit cycle, the state variables converge to the fixed amplitude of the limit cycle's oscillation. This fixed amplitude is indicated by data cursors in the plots. The only difference being a slight phase shift in the state variables due to the different initial conditions.

FIGURE 4.15: Phase trajectories of  $i_S$  and  $v_C$  for different initial conditions

FIGURE 4.16: Plot of  $i_S$  and  $v_C$  against time for different initial conditions

### 4.3.3.3 Lower Threshold of Limit Cycle

The purpose of this section is to identify at which value of the supply voltage  $v_S$  the limit cycle first occurs. This is to be identified by considering the linearised model of the system and observing its closed-loop poles. The value of the supply voltage  $v_S$ , for which the poles cross over to the right hand side of the real axis is to be considered the lower threshold of the limit cycle. A sweep of supply voltages was applied and it was observed that the imaginary axis is crossed somewhere between  $v_S = 55.1V$  and  $v_S = 55.2V$ . In other words, linearising the system around a supply voltage greater than  $v_S = 55.1V$  results in an unstable linear system.

Figure 4.17 shows the pole-zero map for the system linearised around a supply voltage  $v_S = 55.1V$ . From this it can be seen that the real part of the complex pole amounts to  $-0.558$ , which is very close to 0. The damping coefficient  $\zeta$  is equal to only  $1.66 \times 10^{-5}$ . It is of such a small value as the complex pole makes an angle of  $\tan^{-1} \left( \frac{3.37 \times 10^4}{0.558} \right) = 89.9991^\circ$  with the origin. This indicates that the system will exhibit negligible damping, leading to behaviour similar to an undamped or marginally stable system.

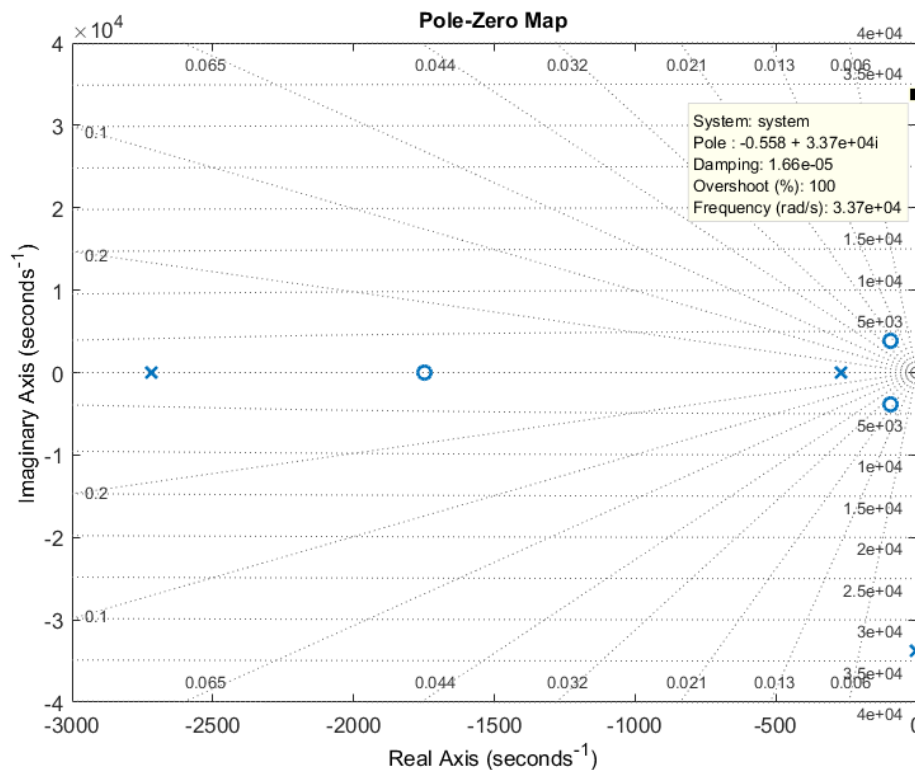


FIGURE 4.17: Pole-zero map for linear model at  $v_S = 55.1V$

A step response is applied to this linearised system to further investigate its properties. This step response can be seen in Figure 4.18. After some initial transient, the system can be seen to exhibit almost undamped oscillations. These oscillations decrease at a very slow rate due to the small damping coefficient previously observed. This may be seen from the data cursors in Figure 4.18, where after approximately 30ms the amplitude of the oscillations decreased only by 0.002.

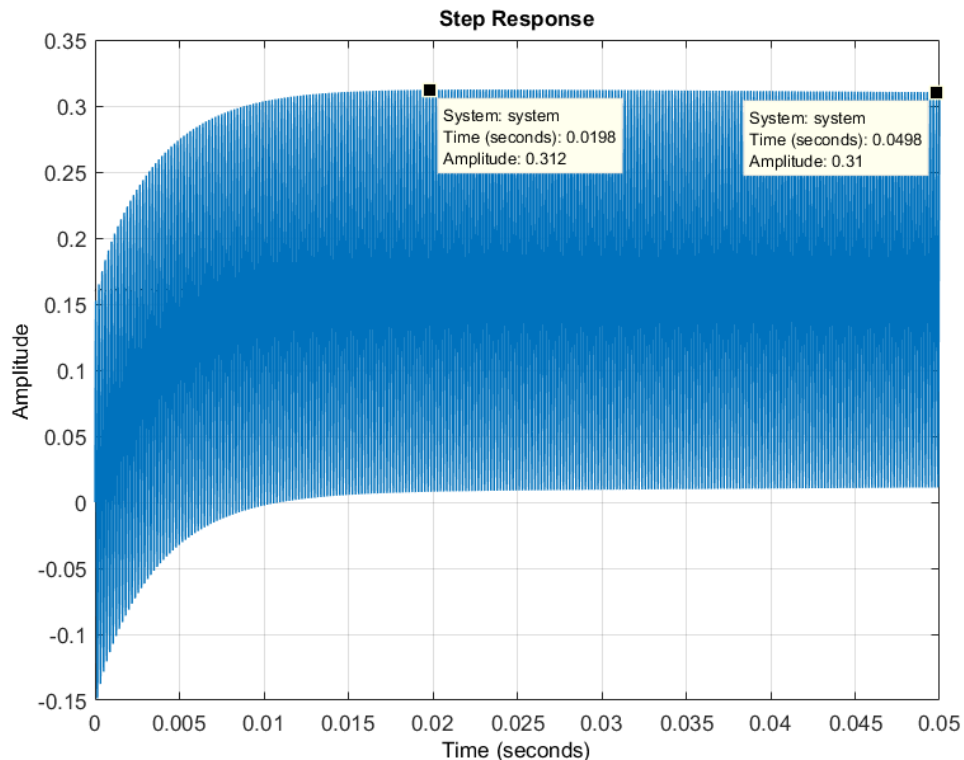
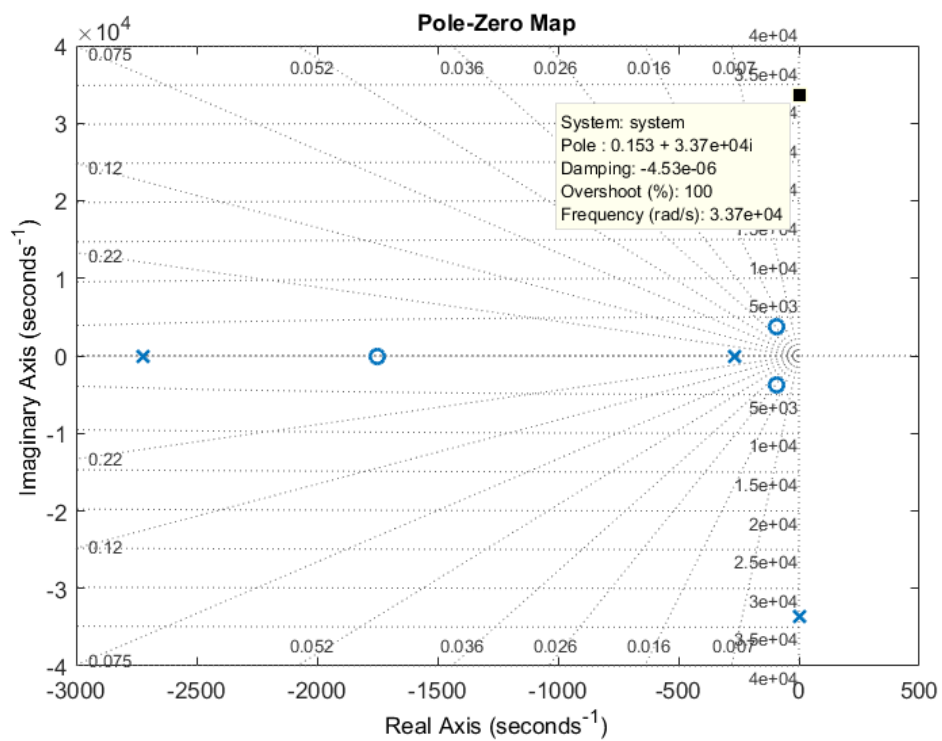
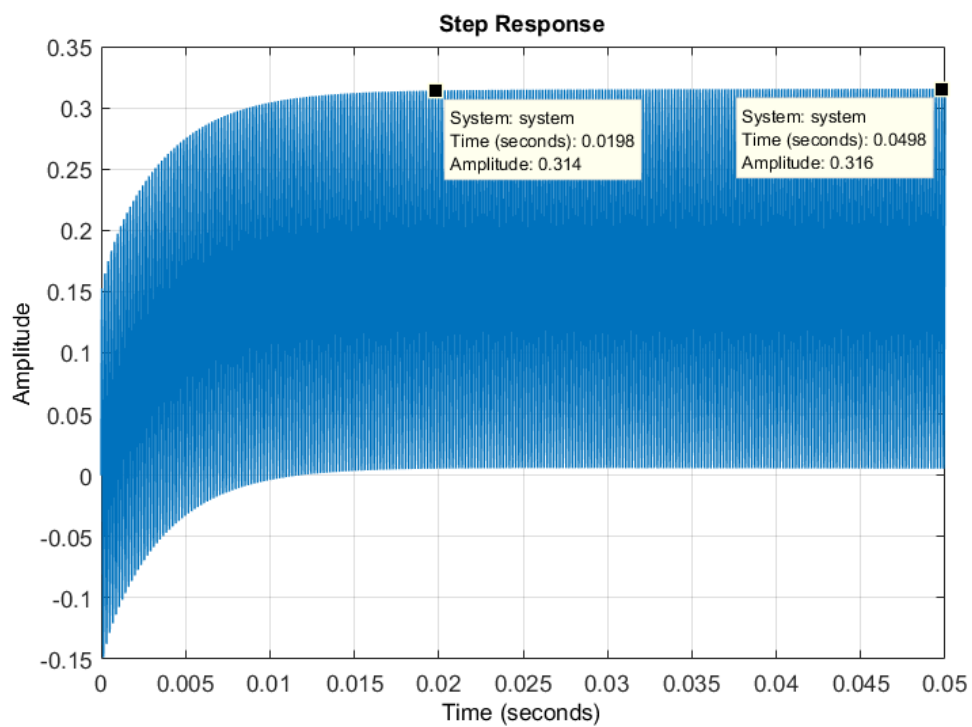


FIGURE 4.18: Step response for linear model at  $v_S = 55.1V$

Figure 4.19 shows the pole-zero map for the system linearised around a supply voltage  $v_S = 55.2V$ . For this system it can be seen that the complex pole contains a positive real part, indicating an unstable system. The damping coefficient  $\zeta$  is again equal to  $-3.77 \times 10^{-6}$ . In this case it indicates very slowly growing oscillations, rather than decreasing ones.

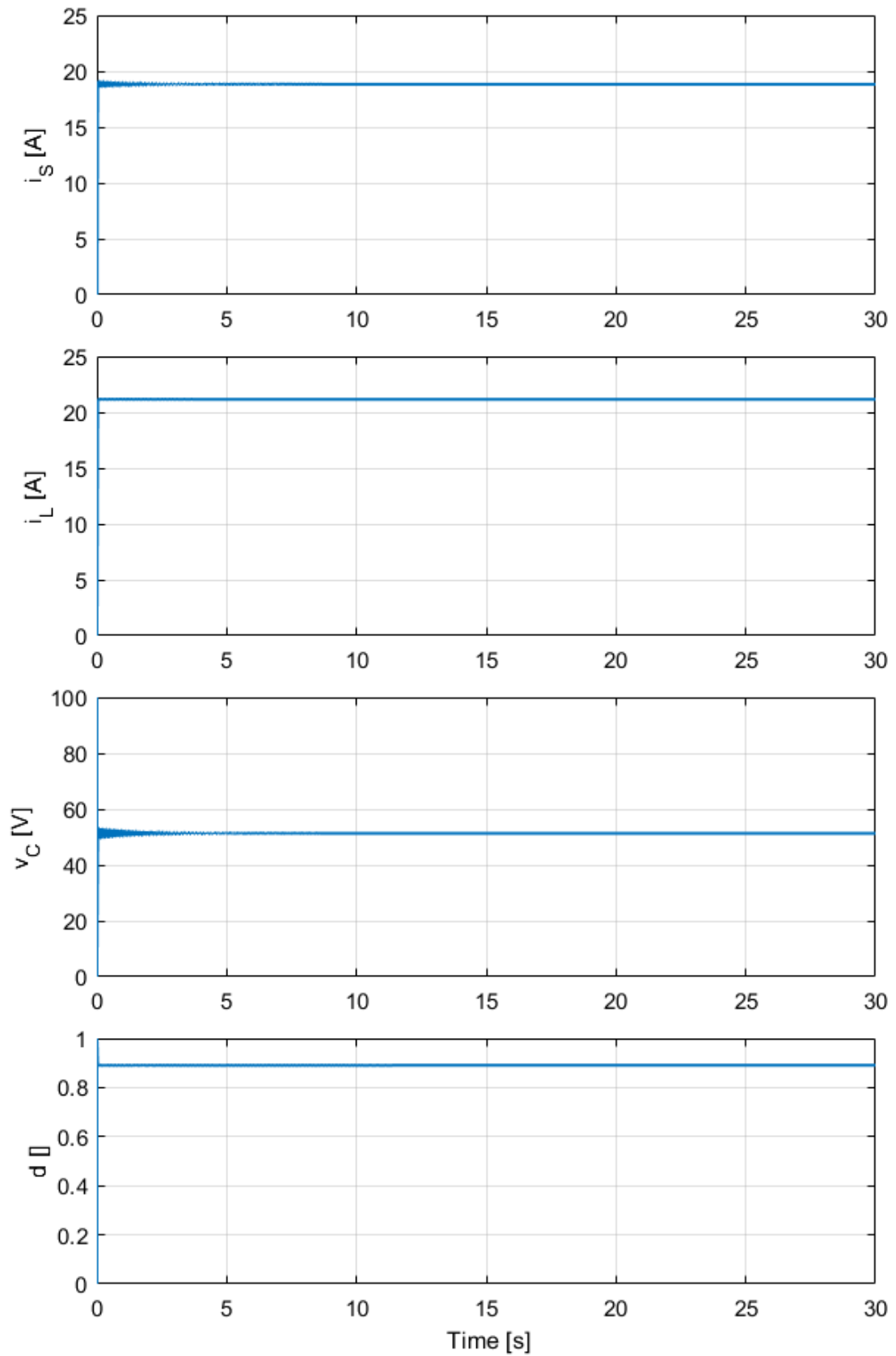
Lastly, Figure 4.20 shows the step response for the system linearised around a supply voltage  $v_S = 55.2V$ . The oscillations were again observed for 30ms. During this period an increase in the amplitude of the oscillations of 0.002 can be seen. This confirms that the linear system is now unstable.

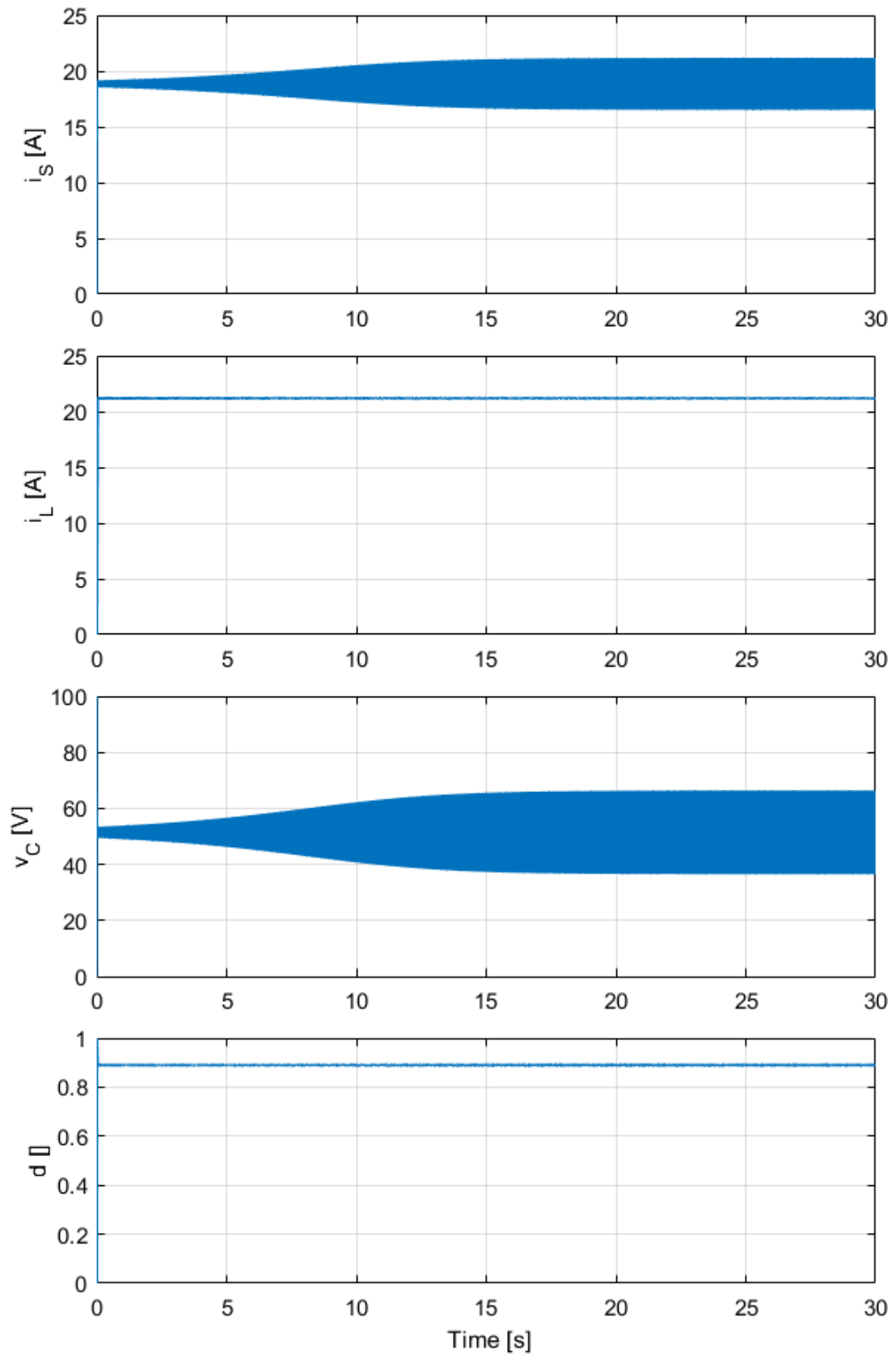
FIGURE 4.19: Pole-zero map for linear model at  $v_S = 55.2V$ FIGURE 4.20: Step response for linear model at  $v_S = 55.2V$

In order to confirm the behaviour observed in these linearised systems, the values of supply voltage  $v_S = 55.1V$  and  $v_S = 55.2V$  were applied to the simulation model covered in Section 4.3.3. The simulation was run for 30s to ensure that enough time is provided for the system to reach steady state due to the low damping factors and magnitudes of the real part of the poles observed. Such low values indicate the presence of long lasting transients.

Figure 4.21 shows all the system state variables of the non-linear closed-loop model when a supply voltage  $v_S = 55.1V$  is applied to the system. As expected from the linear model analysis, a low damping factor causes the system to take a few seconds to recover from initial oscillations. This is most visible in the capacitor voltage  $v_C$ . However, the state variables settle to their steady state values and remain stable.

Figure 4.22, on the other hand, shows all the system state variables when a supply voltage  $v_S = 55.2V$  is applied to the system. From the state variables  $i_S$  and  $v_C$  it can be clearly seen that the oscillations increase until they reach their fixed amplitude and frequency. Their amplitude depends on the magnitude of  $v_S$ . At this value of supply voltage  $v_S$  the linearised system is unstable, hence these fixed frequency and amplitude oscillations confirm what was expected from the linearised system.

FIGURE 4.21: System state variables for supply voltage  $v_S = 55.1V$

FIGURE 4.22: System state variables for supply voltage  $v_S = 55.2V$

#### 4.3.4 Stability Analysis of Power Electronics Simulation

The occurrence of this limit cycle is further investigated in the power electronics simulation, which more closely matches the real application. This simulation model considers the discrete implementation of the control algorithm in the real application, as opposed to the previous simulation model, which is based on the average model of the Buck converter.

A supply voltage in the form of a summation of step voltages is again applied to the system, as was done previously in Figure 4.7. The system response to the first supply voltage step of  $v_S = 50V$  may be seen in Figure 4.23. Similarly to what was observed for the system response in Section 4.3.3 for the system equations, the state variables can be seen to exhibit a low damping oscillatory transient. This is visible in the supply current  $i_S$  and the capacitor voltage  $v_C$ . This oscillatory transient occurs at the resonance frequency of  $f_{LC} = 5.325\text{kHz}$  and eventually dissipates.

As the duty cycle enters out of saturation, all state variables stabilise. The capacitor voltage appears to oscillate, however a clearer view of this is shown in Figure 4.24. The voltage  $v_C$  is not oscillating, but rather experiences a ripple due to the charging and discharging of the capacitor. The ripple occurs at a rate of 20kHz, indicated by the data points in the figure. This is the frequency at which the micro-controller's control algorithm is implemented. Such a ripple is now visible, in contrast to the previous simulation model, as the circuit is implemented with switching devices and a discrete control algorithm, as it is done in the real application.

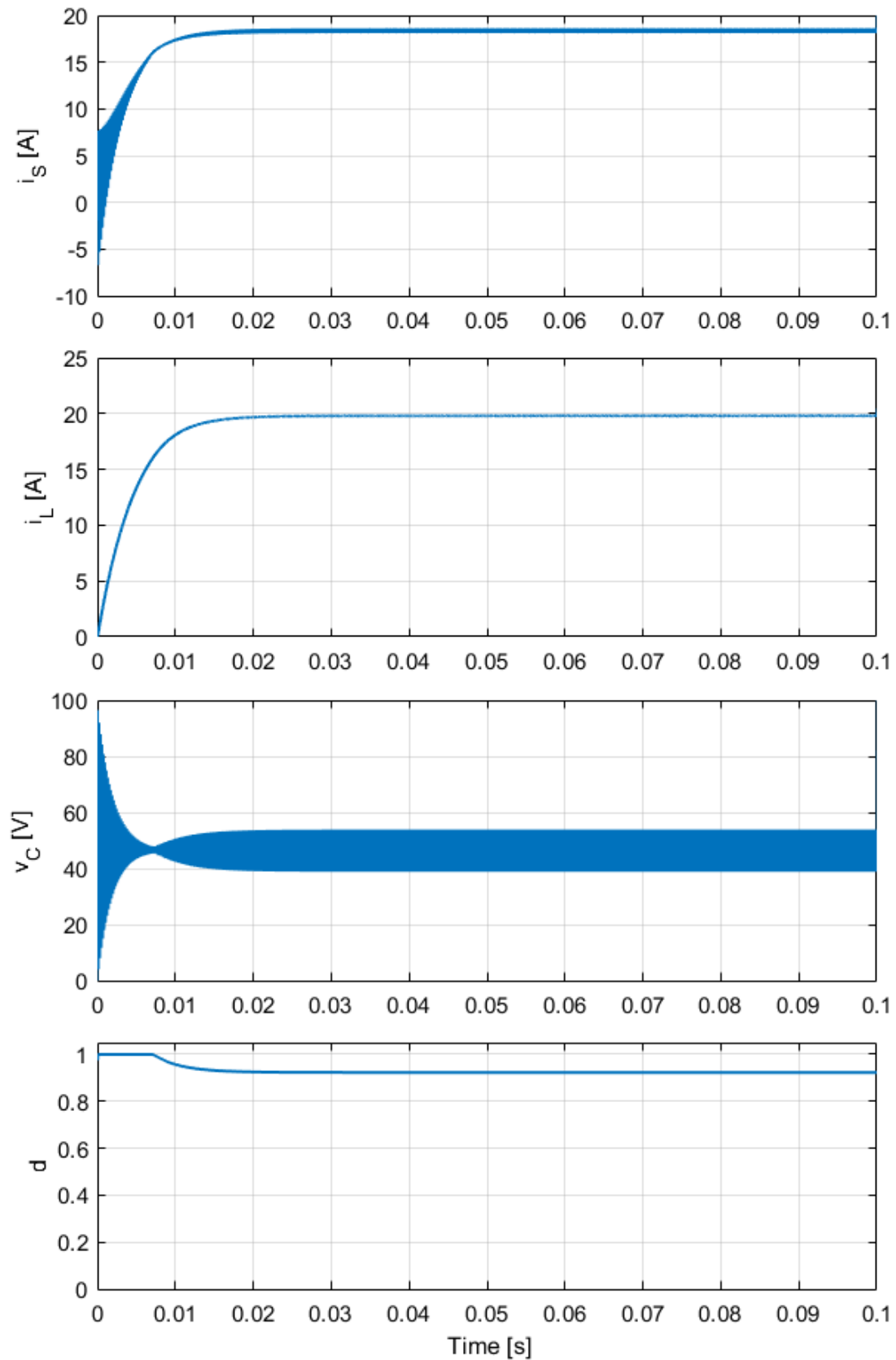


FIGURE 4.23: Closed-loop system state variables of power electronics model due to first supply voltage step

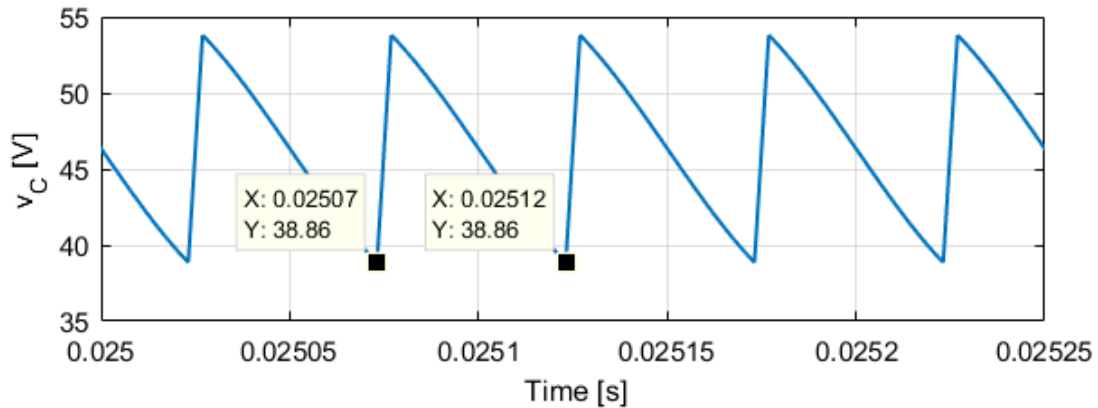


FIGURE 4.24: Plot of capacitor voltage for first supply voltage step

Figure 4.25 shows the system response to all supply voltage steps. From this figure, it can be seen that the system remains stable for the entire range of supply voltage considered. For each step in the supply voltage, a transient may be observed, again most visible in the supply current  $i_S$  and capacitor voltage  $v_C$ . The ripple in the capacitor voltage increases in amplitude with each step in the supply voltage. This is to be expected as the supply current grows larger with each step, causing a larger ripple in the capacitor voltage.

From the analysis carried out in Section 4.3.3, it was predicted that the system enters a limit cycle at a certain supply voltage level. However, the system remains stable during this test, not exhibiting any sustained oscillations. This stability stems from the low-pass filters implemented in the data acquisition of the control algorithm. The cut-off frequency of the low-pass filter implemented for the supply current lies at 2300Hz. Considering that the resonance frequency lies at 5.325kHz, this is filtered out enough for the system to remain stable for all supply voltage levels, well above the tested operating range. Hence, the HDMS hardware prototype is expected to remain stable for its intended application, with a supply voltage range from  $0V \rightarrow 325V$ .

In order to confirm this conclusion, the low-pass filter for  $i_S$  was removed in the simulation model. The system response to the supply voltage steps is shown in Figure 4.26. This figure shows that the system enters a limit cycle between  $v_S = 100V$  and  $v_S = 150V$ . All state variables can be seen to oscillate with constant amplitude. The oscillations occur at a frequency of approximately 5.325kHz. The amplitude of the oscillations increase with each step of the supply voltage, as their amplitude depends on the supply voltage level. The frequency remains constant throughout, which is indicative of a limit cycle.

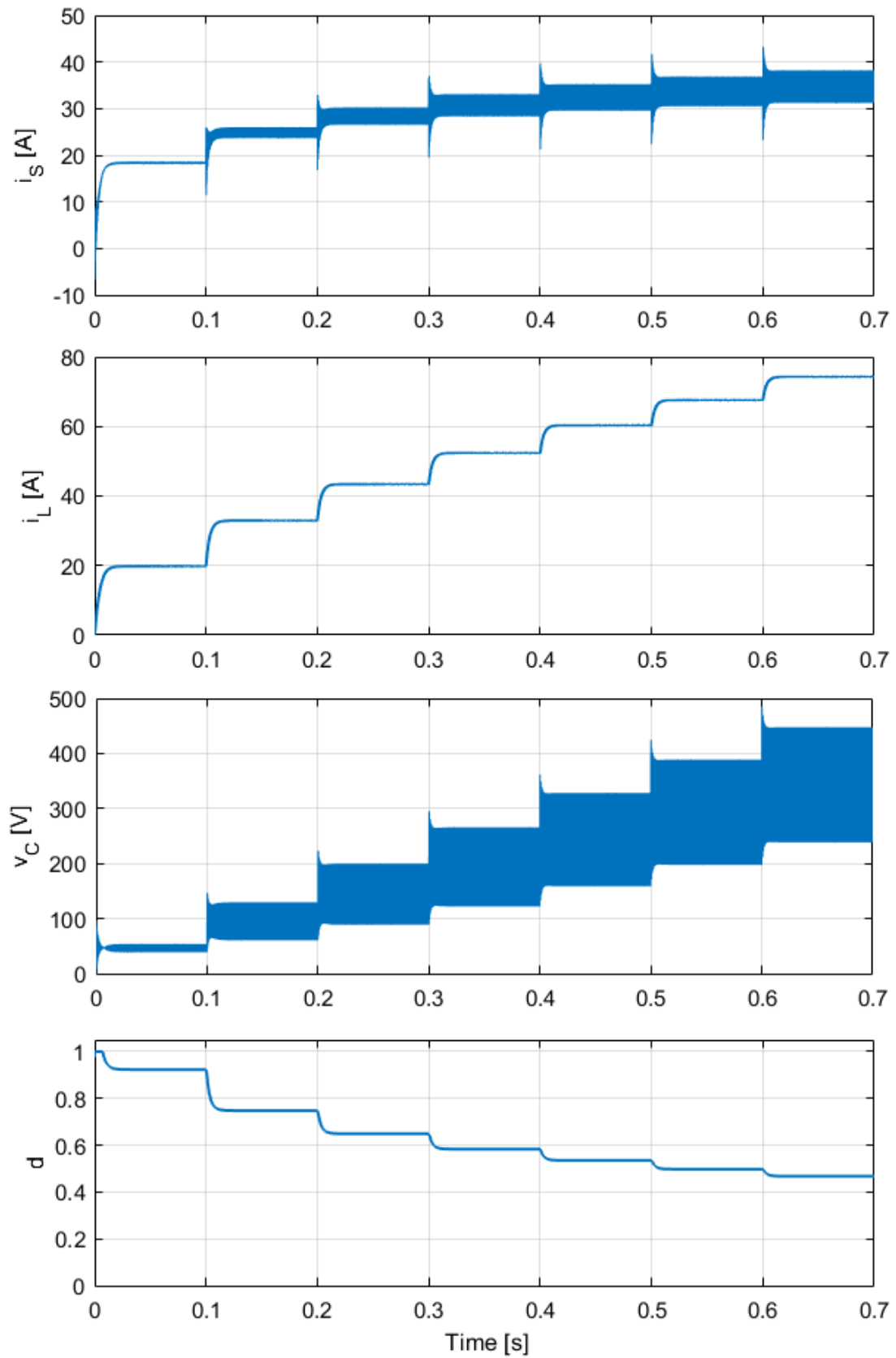


FIGURE 4.25: Closed-loop system state variables of power electronics model due to supply voltage steps

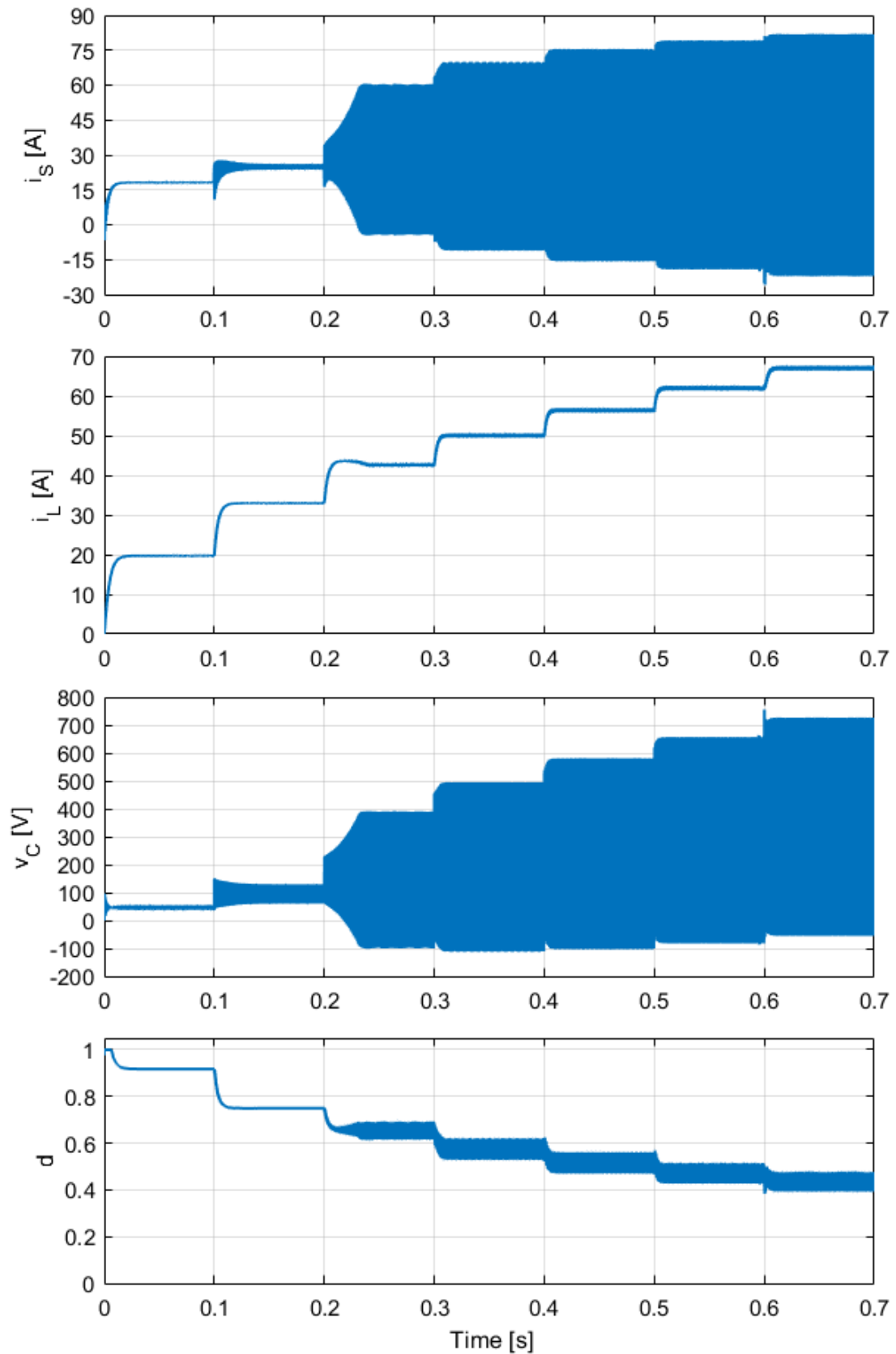


FIGURE 4.26: Closed-loop system state variables of power electronics model due to supply voltage steps without low-pass filter in the supply current measurement

The lower threshold of the limit cycle was found to be at approximately  $v_S = 124V$  in this simulation model, compared to the  $v_S = 55.1V$  previously found in Section 4.3.3.3. This discrepancy occurs due to several factors. These mainly include the discrete time implementation of the control algorithm and the implementation of non-ideal switching devices as opposed to average model approach.

In order to prove that the system stability stems from this low-pass filter, the system is analysed with the low-pass filtered supply current  $i'_S$ . The resulting closed-loop system diagram is illustrated in Figure 4.27.

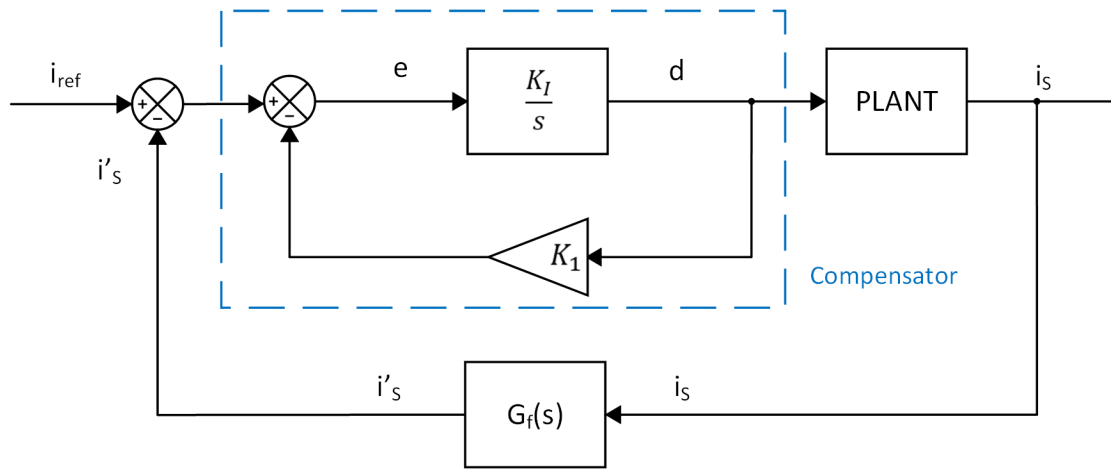


FIGURE 4.27: Block diagram of complete closed-loop system with low-pass filter

The low-pass filter, denoted by  $G_f(s)$  in the diagram, is expressed in (4.17), which was previously obtained in Chapter 3.

$$G_f(s) = \frac{13978}{s + 14451} = \frac{0.97}{\frac{s}{14451} + 1} \quad (4.17)$$

This low-pass filter does not affect the system equations for the supply current  $i_S$ , motor winding current  $i_L$  and capacitor voltage  $v_C$ . However, the duty cycle now depends on the low-pass filtered supply current  $i'_S$ , rather than the unfiltered supply current  $i_S$ . Hence, a new system state is to be considered for this current, namely  $i'_S$ , which is derived in (4.18). This increases the system order to five and the state space representation of this fifth order system is expressed in (4.19).

$$\frac{i'_S}{i_S} = \frac{13978}{s + 14451} \quad \therefore \frac{di'_S}{dt} = 13978i_S - 14451i'_S \quad (4.18)$$

$$\mathbf{f}(\mathbf{x}, \mathbf{u}) = \begin{pmatrix} \dot{i}_S \\ \dot{i}_L \\ \dot{v}_C \\ \dot{d} \\ \dot{i}'_S \end{pmatrix} = \begin{pmatrix} \frac{1}{L_1}v_S - \frac{R_1}{L_1}i_S - \frac{1}{L_1}v_C \\ \frac{d}{L_2}v_C - \frac{R_2}{L_2}i_L \\ \frac{1}{C}i_S - \frac{d}{C}i_L \\ K_I(i_{ref} - dK_1 - i'_S) \\ 13978i_S - 14451i'_S \end{pmatrix} \quad (4.19)$$

For these system equations, the Jacobian matrix  $\mathbf{A}$  was obtained in order to investigate the stability properties of the closed-loop system poles. The resulting  $\mathbf{A}$  matrix is shown in (4.20).

$$\mathbf{A} = \begin{pmatrix} -\frac{R_1}{L_1} & 0 & -\frac{1}{L_1} & 0 & 0 \\ 0 & -\frac{R_2}{L_2} & \frac{d^*}{L_2} & \frac{v_C^*}{L_2} & 0 \\ \frac{1}{C} & -\frac{d^*}{C} & 0 & -\frac{i_L^*}{C} & 0 \\ 0 & 0 & 0 & -K_I K_1 & -K_I \\ 13978 & 0 & 0 & 0 & -14451 \end{pmatrix} \quad (4.20)$$

The Jacobian matrix was again evaluated for the supply voltage steps  $v_S = 50V \rightarrow 350V$ , as was previously done in Figure 4.10. The resulting closed-loop system poles are shown in Figure 4.28. From this figure, it can be concluded that the closed-loop system poles no longer cross into the right-hand side of the real axis, as they did without the low-pass filter. A supply voltage of approximately  $v_S = 300V$  and higher results in an additional complex pole pair, apart from the dominant complex pole pair near the stability margin. However, the oscillatory response from this pole pair is of a relatively high frequency and relatively highly damped, compared to the dominant poles. This provides an analytical confirmation that the system stability stems from the low-pass filter in the supply current measurement.

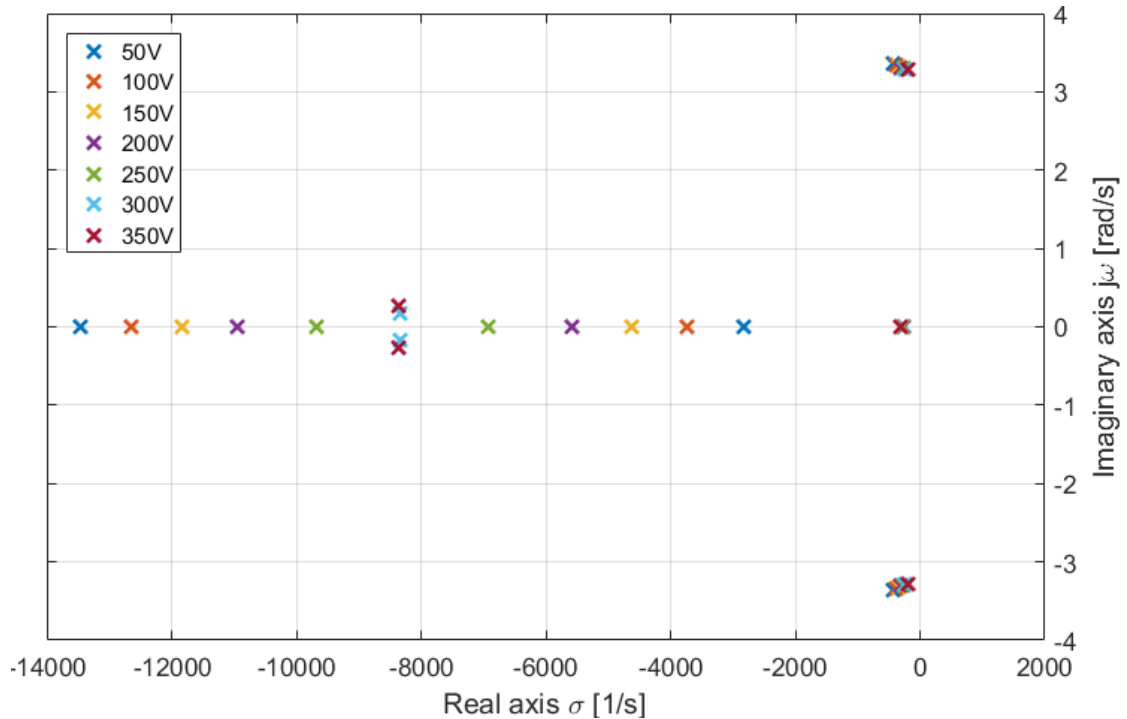


FIGURE 4.28: System poles with low-pass filter for supply voltages  $50V \rightarrow 350V$

## 4.4 Conclusion

This chapter has covered the stability analysis of the HDMS prototype. The plant was first modelled and analysed in open-loop for its stability. The analysis was based on the dynamic equations of the system and on the average Buck converter model. This was found to be non-linear, but stable.

The closed-loop system was modelled and analysed next by applying supply voltage steps in increments of  $50V$ , covering the entire operating range of the HDMS. The system was found to enter sustained oscillations of fixed amplitude and frequency, which is indicative of limit cycles and was thus further investigated. A linear model analysis, linearising the system around the supply voltage steps applied, has helped to confirm the presence of this limit cycle and to identify at what magnitude of  $v_S$  the system enters the limit cycle. Furthermore, the properties of the limit cycle at the peak voltage were analysed, leading to the conclusion that the system exhibits a stable limit cycle. This is due to the system converging to the limit cycle for different initial conditions.

---

Lastly, the system stability was analysed using the component-level power electronics simulation model. By contrast with the previous dynamic model simulations, based on the average model, this was found to remain stable and not exhibit limit cycles. This was attributed to the low-pass filter present in the data acquisition of the control algorithm, which was proven analytically. In the actual hardware prototype, this is present in the form of RC first order low-pass filters just before the microcontroller's ADC pins. Testing the stability of the component-level simulation model without including such a filter has confirmed what was found in the analysis based on the average model. However, a discrepancy in the supply voltage at which the system enters the limit cycle was noted. This discrepancy occurs due to reasons such as the discrete time implementation of the control algorithm and the fact that the initial simulation model is based on the average model of the Buck converter, which omits the switching devices. Hence, in conclusion, the hardware prototype is expected to remain stable during its intended application.

# Chapter 5

## Hardware Setup

### 5.1 Introduction

This chapter covers the hardware setup used to acquire the practical results for this dissertation. The main components of the setup and how they are connected will be explained and illustrated. Finally, the calibration of the sensor used to measure the motor starting torque will be shown.

### 5.2 Test Setup

A block diagram illustrating the overall setup used to conduct the hardware tests for this dissertation is provided in Figure 5.1. The hardware setup comprises the following main components:

- Power supply
- Flicker impedance
- Circuit protection
- HDMS prototype
- Microcontroller debugger
- Single-phase motor

The power supply is programmable in its amplitude and frequency and provides the single-phase  $230V_{rms}$  50Hz voltage, which the HDMS uses in its intended application. A flicker impedance is connected in series to the power supply. This

flicker impedance is used to investigate the severity of the flicker introduced during each motor start. This will provide further information regarding the performance of the HDMS current control algorithm, apart from the starting torque. The flicker tests are carried out in accordance to IEC 61000-3-11 [17].

Protection circuitry is included in the setup. This consists of a MCB and a thermal overload protection relay OL. The supply is then connected to the HDMS terminal block. This connects the HDMS to the supply voltage and also to the single-phase motor. Lastly, the HDMS' microcontroller is connected to a laptop through a debugger. This allows to program the HDMS and to manually initiate the soft-starting sequence. The data logged by the microcontroller during the tests carried out is also sent to the laptop via USB, such that it may be plotted on MATLAB.

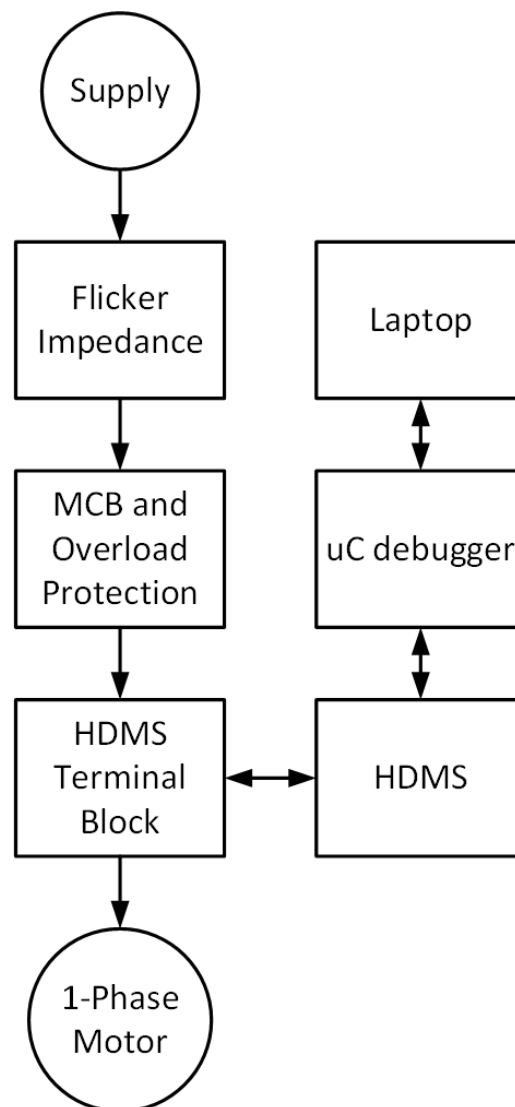


FIGURE 5.1: Block diagram representing the configuration of the hardware setup

Figure 5.2 provides a picture of the overall setup just described. The oscilloscope is used to measure relevant signals such as the supply and main winding currents and voltages and the voltage output of the load cell, which measures the starting torque. The DC power supply provides 12V for the HDMS electronic circuitry and 5V for the load cell. The motor is enclosed by a metal wire mesh cage for safety purposes. The encircled section will be detailed in the following figure.

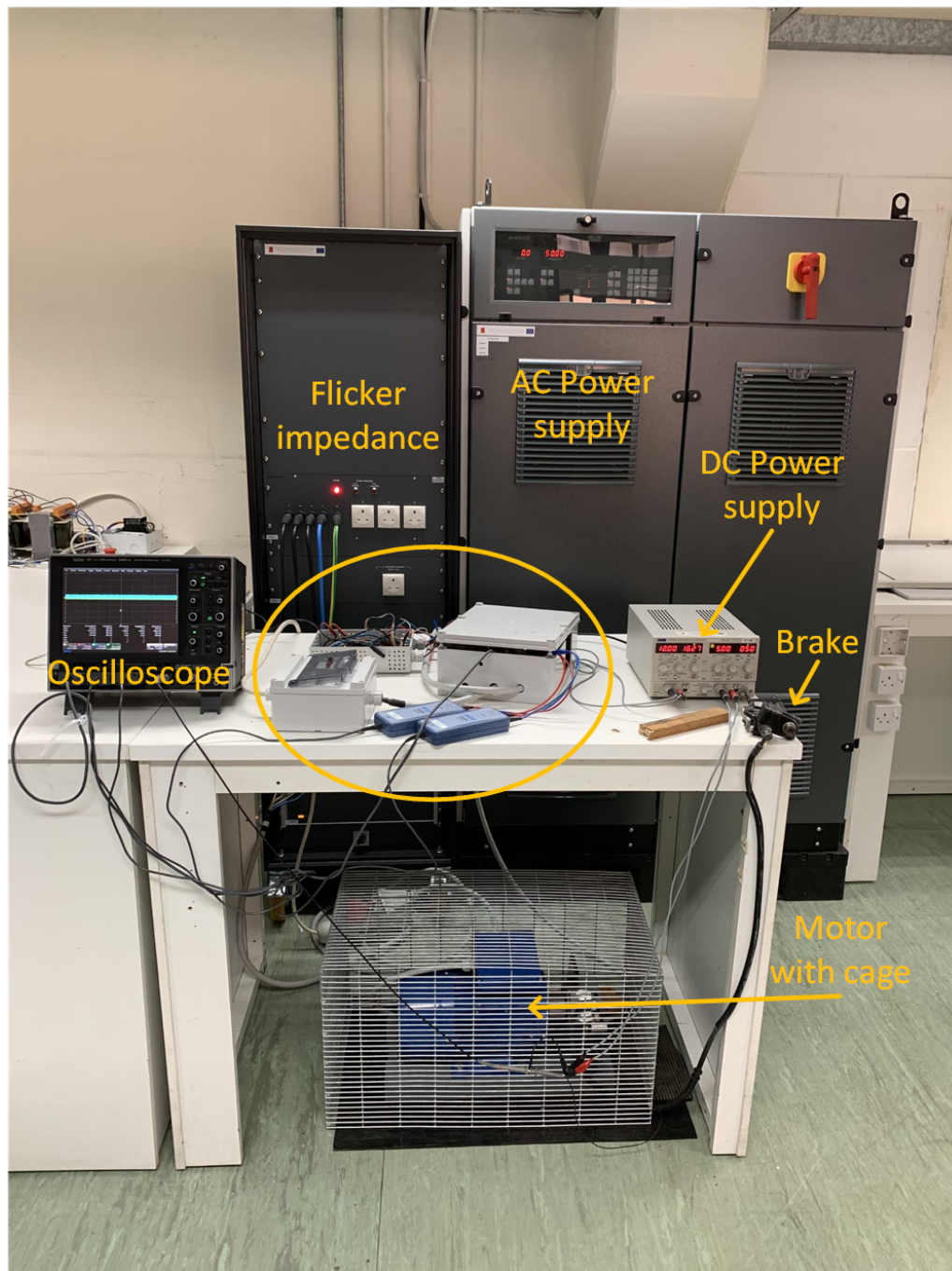


FIGURE 5.2: Photo of hardware setup

Figure 5.3 shows a picture of the protection components, the HDMS prototype, terminal block and the microcontroller debugger. Since all connections to and from the HDMS and motor are made at the terminal block, the current clamps and voltage probes are connected at this point.

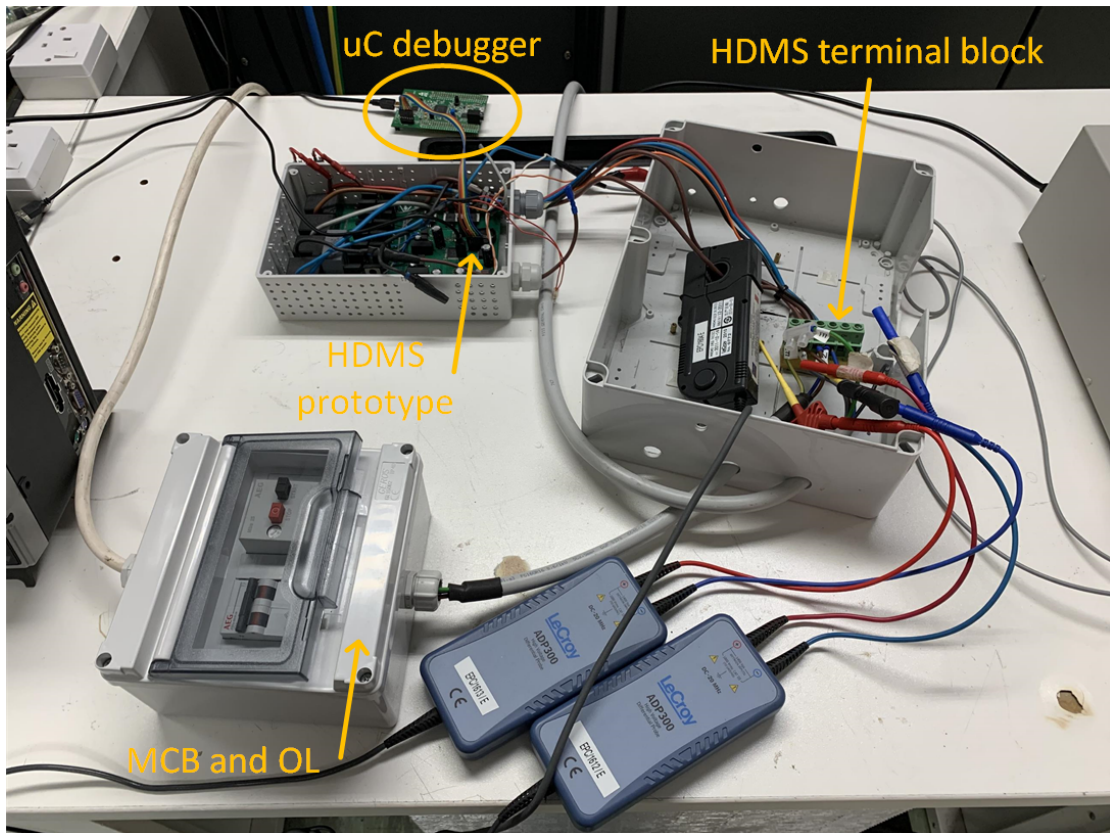


FIGURE 5.3: Photo of HDMS prototype, terminal block, protection and debugger

Figure 5.4 shows the test setup used to measure the starting torque produced by the single-phase motor. This consists of a steel base to which the motor is fixed through bolts, a disc brake and the load cell. The setup is placed on a rubber mat, which aims to reduce mechanical vibrations. When the disc brake is engaged and the motor is powered, the disc mounted on the motor shaft attempts to rotate in the indicated direction of rotation. This applies a force on the load cell, which is placed 10cm horizontally from the center of rotation. Knowing these parameters, the torque can be calculated from the force reading produced by the load cell.

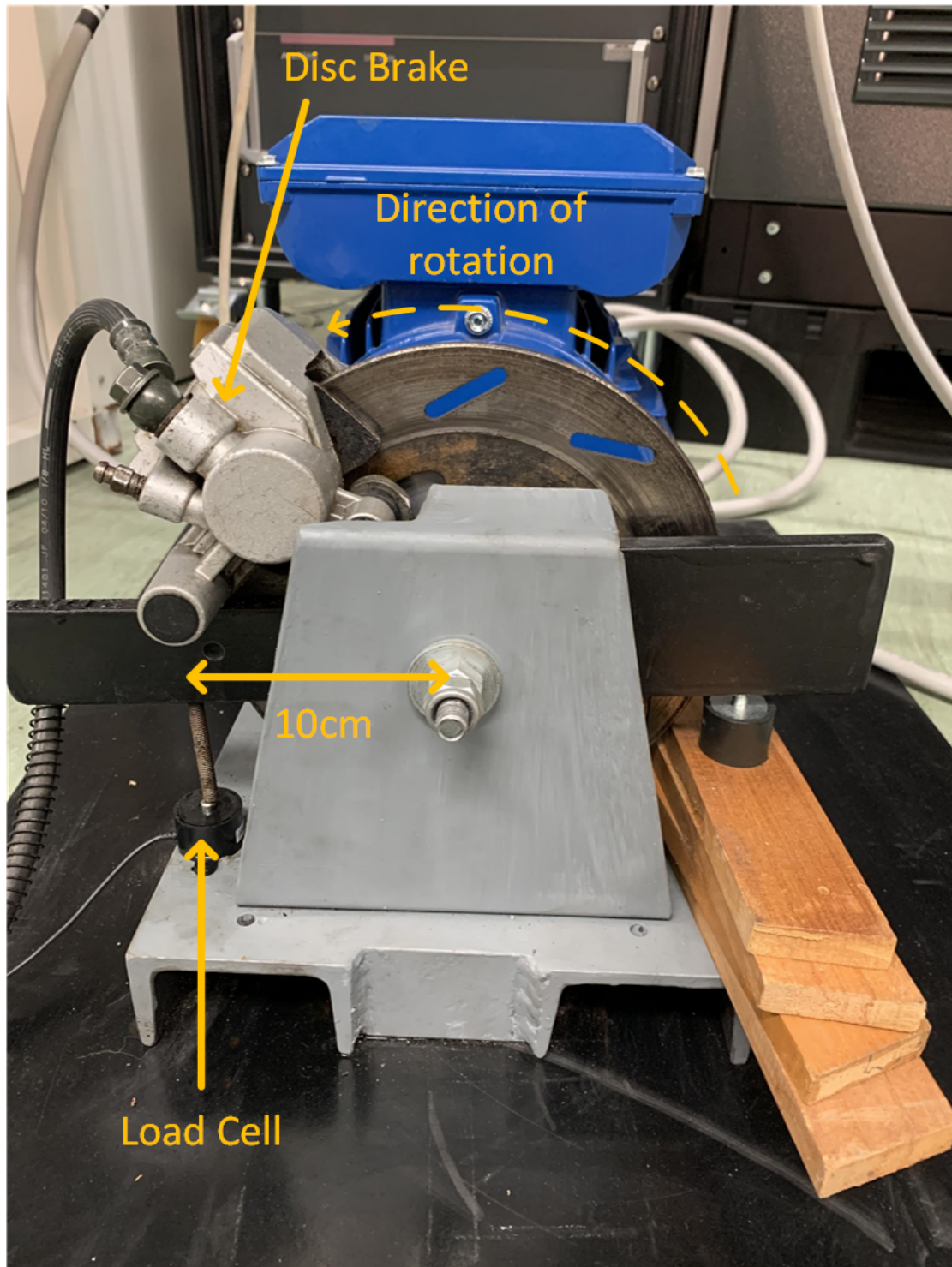


FIGURE 5.4: Photo of single-phase motor test setup

Figure 5.5 shows the nameplate of the motor used in this test setup, which contains the motor ratings.

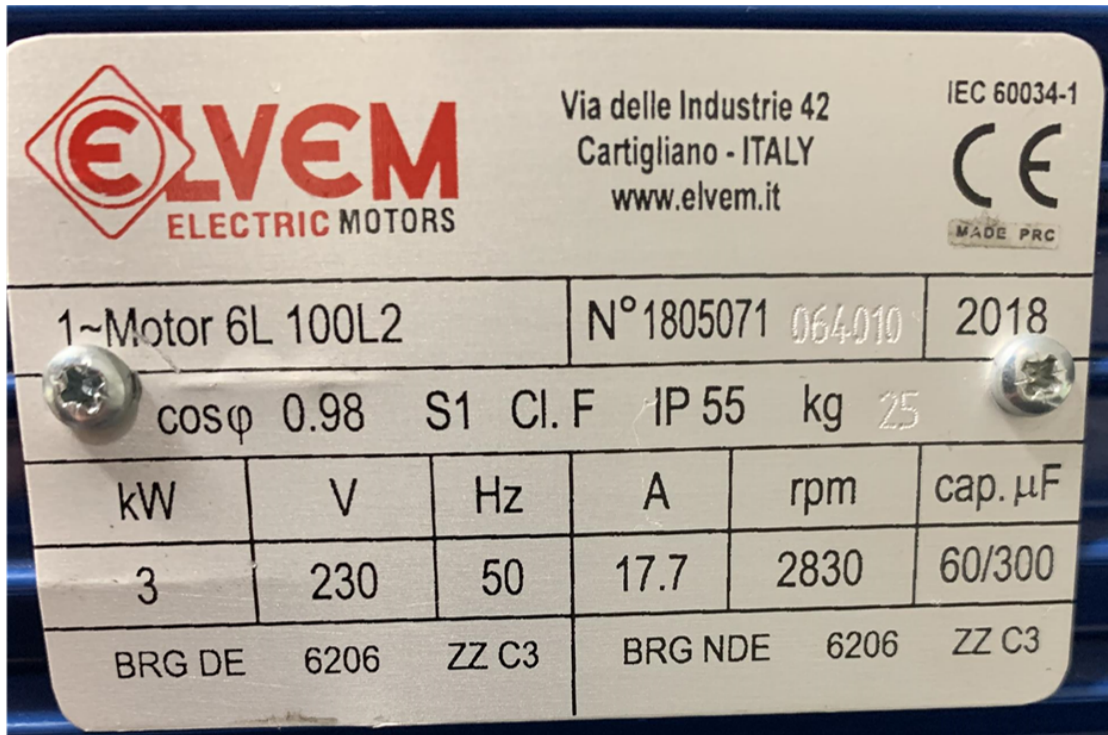


FIGURE 5.5: Photo of single-phase motor nameplate

### 5.3 Load Cell Calibration

The force sensor used to measure the starting torque produced by the motor is the compression load cell FC2231-0000-0050-L. This load cell can measure up to  $50\text{ lbf} = 22.68\text{ kg}$ . It is supplied with  $5V_{DC}$  and its output voltage span is typically  $4V$  with a typical zero force output of  $0.5V$  [18].

From these parameters it is expected to see an increase in the output voltage of  $4V/22.68\text{ kg} = 180\text{ mV kg}^{-1}$ . The force sensor was calibrated with dumbbell weights in increments of  $0.5\text{ kg}$  up to  $10\text{ kg}$ . The resulting output voltage of the force sensor is tabulated in Table 5.1.

TABLE 5.1: Force sensor output voltages with increase in weight

Weight [kg]	$V_{out}$ [V]
0	0.56
0.5	0.66
1.0	0.76
1.5	0.84
2.0	0.94
2.5	1.04
3.0	1.14
3.5	1.24
4.0	1.34
4.5	1.44
5.0	1.52
5.5	1.62
6.0	1.70
6.5	1.78
7.0	1.86
7.5	1.96
8.0	2.02
8.5	2.12
9.0	2.22
9.5	2.30
10.0	2.40

The tabulated data is plotted in Figure 5.6 together with a linear approximation of the data, obtained through the linear data fitting tool in Matlab. The resulting linear approximation of the data is provided in (5.1), where  $m$  [kg] represents mass. This confirms the expected  $180mVkg^{-1}$  increase in the output voltage of the force sensor.

$$V_{out} = 0.59 + 0.18 \times m \quad (5.1)$$

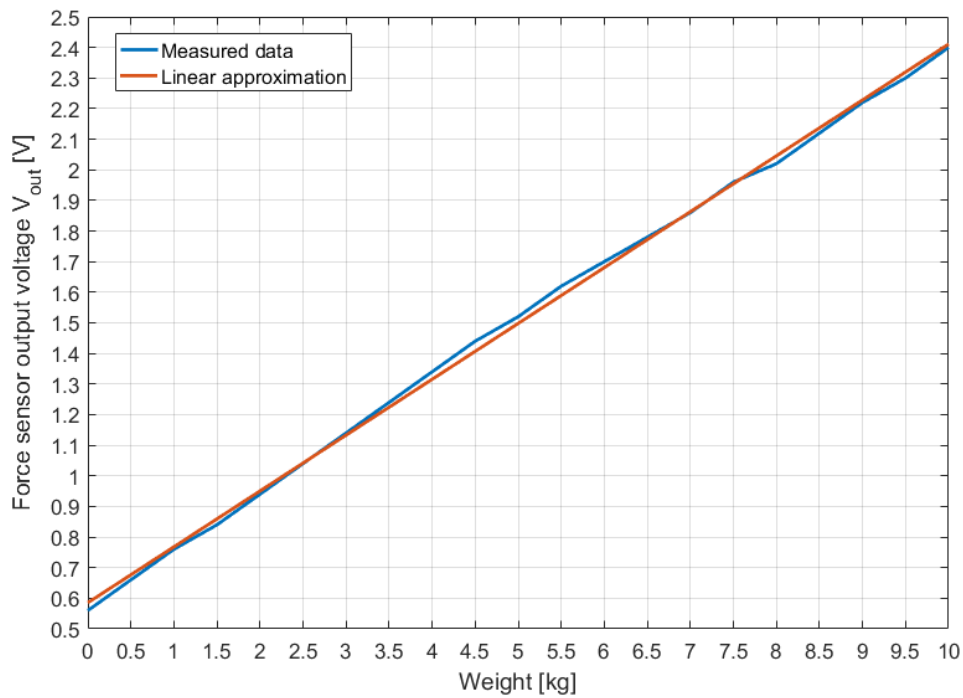


FIGURE 5.6: Plot of weight vs. force sensor output voltage

The force sensor has also been tested under DOL starting conditions, which means that the motor was connected directly to the supply without the HDMS soft starter prototype. The disc brake was engaged to lock the rotor in order to be able to measure the produced starting torque. This was repeated for a range of supply voltages  $50V_{rms} \rightarrow 220V_{rms}$  in increments of approximately  $25V_{rms}$ . The resulting current and starting torque was measured for each value of supply voltage. The resulting data is tabulated in Table 5.2.

TABLE 5.2: DOL locked rotor test data

Supply voltage $V_S$ [ $V_{rms}$ ]	Supply current $I_S$ [ $A_{rms}$ ]	Force [N]
50	11.13	0.47
75	16.46	1.66
100	22.57	1.74
125	31.26	3.45
160	42.77	7.03
190	56.14	15.04
220	68.66	22.72

The tabulated data is plotted in Figure 5.7. The measured data is again approximated, but by a quadratic approximation this time. This confirms what is expected from theory, namely that the torque produced by the motor is proportional to the provided current squared  $T \propto I^2$ .

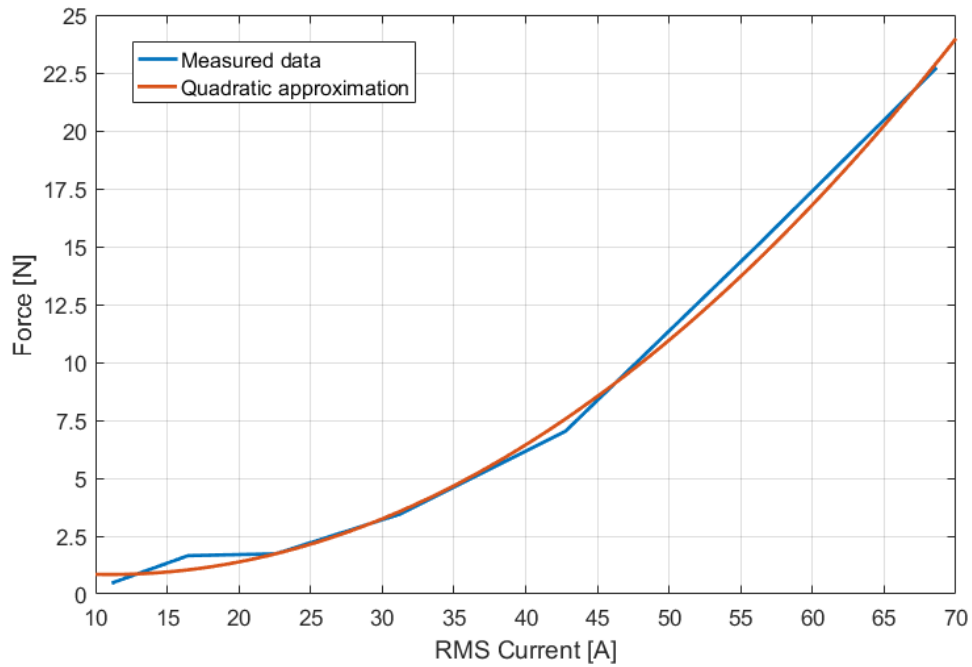


FIGURE 5.7: Plot of RMS current vs. force for DOL locked rotor tests

## 5.4 Conclusion

This chapter has presented the hardware setup used to carry out the hardware tests for this dissertation. The working principle of the test setup used to acquire the motor starting torque was explained and the procedure carried out to verify proper operation of the force sensor was presented.

# Chapter 6

## State Feedback Regulator

### 6.1 Introduction

This chapter covers the proposed alternative controller for the HDMS prototype. The non-linear system was controlled using a state feedback approach. In this chapter, the design, implementation and testing of the proposed alternative controller for the HDMS prototype is shown.

### 6.2 State Feedback Regulator Methodology

The state feedback regulator operates on a linear system model. As has been established previously in the system stability analysis in Chapter 4, the system in use is of non-linear nature. The state feedback regulator is hence designed for a linearised model of the non-linear system. The non-linear plant defined by  $\dot{\mathbf{x}} = \mathbf{f}(\mathbf{x}, u)$ , is linearised to  $\dot{\bar{\mathbf{x}}} = \mathbf{A}\bar{\mathbf{x}} + \mathbf{B}\bar{u}$ , where  $\bar{\mathbf{x}} = \mathbf{x} - \mathbf{x}^*$  and  $\bar{u} = u - u^*$ . The linearised equivalent of the system equations is shown again in (6.1), where  $*$  denotes the equilibrium point value. A state feedback regulator designed for such a linearised system will work accurately for small deviations from the designed equilibrium point. If the operating point deviates from the equilibrium point, then the controller cannot guarantee that the desired specifications are met.

$$\begin{pmatrix} \dot{i}_S \\ \dot{i}_L \\ \dot{v}_C \end{pmatrix} = \begin{pmatrix} -\frac{R_1}{L_1} & 0 & -\frac{1}{L_1} \\ 0 & -\frac{R_2}{L_2} & \frac{d^*}{L_2} \\ \frac{1}{C} & -\frac{d^*}{C} & 0 \end{pmatrix} \begin{pmatrix} \bar{i}_s \\ \bar{i}_L \\ \bar{v}_C \end{pmatrix} + \begin{pmatrix} 0 \\ \frac{v_C^*}{L_2} \\ -\frac{i_L^*}{C} \end{pmatrix} \begin{pmatrix} \bar{d} \end{pmatrix} \quad (6.1)$$

The proposed controller [19] [20], which regulates the system to a reference input with full state feedback, is presented in Figure 6.1. This regulator is designed to drive the system towards an equilibrium point and does not increase the system order ( $n = 3$ ), as opposed to the prototype's currently implemented regulator. The control law of the proposed regulator is defined by  $u = -\mathbf{K}\mathbf{x} + gr$ , with  $r$  being the reference ( $i_{ref} - i_S^*$ ) and  $\mathbf{K} = [K_1 \ K_2 \ K_3]$  the state feedback gain matrix.

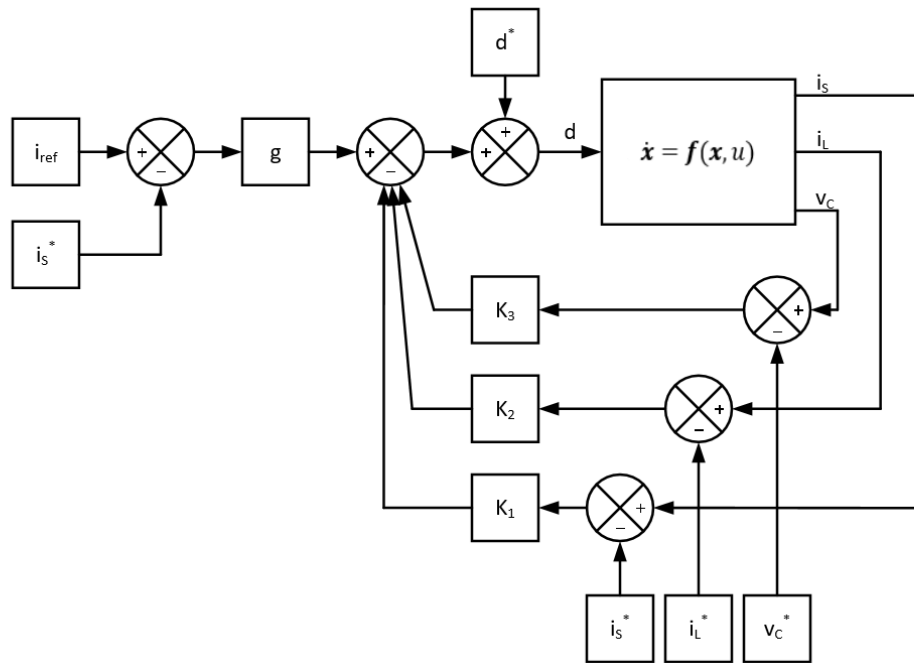


FIGURE 6.1: Diagram of proposed state feedback regulator

The proposed regulator drives the system  $\dot{\mathbf{x}} = \mathbf{f}(\mathbf{x}, u)$  towards a reference value for the supply current denoted by  $i_{ref} - i_S^*$ . All state variables are measured and from them the calculated equilibrium point values ( $i_S^*, i_L^*, v_C^*$ ) are subtracted. This is done to obtain the error from the desired equilibrium point. The state variables are then multiplied by their respective state feedback gain. The generated duty cycle is added to  $d^*$ . This provides the actual duty cycle for the non-linear system. The gain  $g$  is required to ensure that there is a dc unity gain between the reference input and the output. This gain is computed during the regulator design stage using the equilibrium point state variables. It is defined by (6.2), where  $\mathbf{K} = [K_1 \ K_2 \ K_3]$  and  $C = [1 \ 0 \ 0]$ .

$$g = \frac{-1}{\mathbf{C}(\mathbf{A} - \mathbf{BK})^{-1}\mathbf{B}} \quad (6.2)$$

## 6.3 Design of State Feedback Regulator

### 6.3.1 Regulator Equilibrium Point

As previously explained, the proposed state feedback regulator operates on a linearised model of the HDMS prototype. The regulator is designed for an equilibrium point defined by the input variable, which is the duty cycle  $d$ . The non-linear system is stated again in (6.3) for convenience, as this was already obtained in Chapter 4.

The equilibrium point is obtained by letting the system equations equal to zero  $\dot{\mathbf{x}} = \mathbf{f}(\mathbf{x}, u) = \mathbf{0}$  for a value of duty cycle  $d$  and supply voltage  $v_S$ . As this regulator is to operate for a changing and non-controllable supply voltage  $v_S$ , the peak amplitude  $v_S = 325V$  was considered for the linearisation process.

This value of supply voltage was chosen such that the controller is active around the peak supply voltage. Hence, the controller should be able to regulate the system to its equilibrium point values in the vicinity of the peak supply voltage. As the supply voltage deviates from its peak value, the controller will naturally produce a larger duty cycle due to a lower supply voltage  $v_S$ . This occurs as the controller will attempt to keep the state variables equal to their equilibrium point values. Hence, the controller will naturally drive the duty cycle towards  $d = 1.0 = 100\%$  with a large enough deviation in  $v_S$  from its peak value. This ensures that the HDMS may enter region 2, where the motor winding is connected directly to the supply, before the motor winding current's zero-crossing. Such a controller characteristic is critical to the operation of the HDMS and will lead to a duty cycle shaped similarly to the one observed for the HDMS prototype's current control algorithm in Chapter 2.

$$\mathbf{f}(\mathbf{x}, u) = \begin{pmatrix} \dot{i}_S \\ \dot{i}_L \\ \dot{v}_C \end{pmatrix} = \begin{pmatrix} \frac{1}{L_1}v_S - \frac{R_1}{L_1}i_S - \frac{1}{L_1}v_C \\ \frac{d}{L_2}v_C - \frac{R_2}{L_2}i_L \\ \frac{1}{C}i_S - \frac{d}{C}i_L \end{pmatrix} \quad (6.3)$$

Letting the system equations equal to zero yields the state variable equations at the equilibrium point, denoted by the star \*. These are shown in (6.4).

$$f_1 = 0 \quad \rightarrow \quad i_S^* = \frac{d^2 v_S}{R_2 + R_1 d^2} \quad (6.4a)$$

$$f_2 = 0 \quad \rightarrow \quad i_L^* = \frac{d v_S}{R_2 + R_1 d^2} \quad (6.4b)$$

$$f_3 = 0 \quad \rightarrow \quad v_C^* = \frac{v_S}{R_2 + R_1 d^2} \quad (6.4c)$$

By using the system parameters listed in Table 6.1 below, these state variables may be evaluated. The equilibrium point state variables are obtained with a duty cycle of  $d = 0.4 = 40\%$  at the peak of the supply voltage  $v_S = 325V$ . This value of duty cycle was chosen as it results in the HDMS producing values of supply and main winding currents  $i_S$  and  $i_L$  similar to the already implemented HDMS prototype's algorithm.

TABLE 6.1: System parameters for equilibrium point

Parameter	Symbol	Value
Supply voltage	$v_S$	325V
Duty cycle	$d$	0.4
LC-filter damping resistor	$R_1$	0.2Ω
LC-filter inductance	$L_1$	190μH
LC-filter capacitance	$C$	4.7μF
Motor winding resistance	$R_2$	2.16Ω
Motor winding leakage inductance	$L_2$	11.65mH

The substitution of these parameters yields the state variables as shown in (6.5).

$$i_S^* = 23.72A \quad (6.5a)$$

$$i_L^* = 59.31A \quad (6.5b)$$

$$v_C^* = 320.26V \quad (6.5c)$$

### 6.3.2 Pole Placement of State Feedback Regulator

#### 6.3.2.1 Controllability Matrix

With all the linearised system parameters known, the state feedback regulator may be designed using the pole placement approach. This assumes that all state variables are available for feedback. In order to be able to place the closed-loop system poles at any desired location, the system is first checked for state controllability. For complete state controllability, the controllability matrix  $[B \ AB \ \dots \ A^{(n-1)}B] = [B \ AB \ A^2B]$ , where the system order  $n = 3$ , requires to be of full rank. This controllability matrix has been found to be of full rank. Hence, the poles may be placed at any desired location. The controllability matrix is shown in (6.6).

$$[B \ AB \ A^2B] = \begin{pmatrix} 0 & \frac{i_L^*}{L_1 C} & \frac{d^* v_C^*}{L_1 L_2 C} - \frac{R_1 i_L^*}{L_1^2 C} \\ \frac{v_C^*}{L_2} & -\frac{1}{L_1} \left( \frac{R_2 v_C^*}{L_2} + \frac{d^* i_L^*}{C} \right) & \frac{v_C^*}{L_2^2} \left( \frac{R_2^2}{L_2} - \frac{d^{*2}}{C} \right) + \frac{R_2 i_L^* d^*}{L_2^2 C} \\ -\frac{i_L^*}{C} & -\frac{d^* v_C^*}{L_2 C} & \frac{R_2 v_C^* d^*}{L_2^2} + \frac{i_L^*}{C^2} \left( \frac{1}{L_1} + \frac{d^{*2}}{L_2} \right) \end{pmatrix} \quad (6.6)$$

#### 6.3.2.2 Pole Placement through direct substitution

The closed-loop poles of the system are determined through the eigenvalues of the matrix  $\mathbf{A} - \mathbf{BK}$ , where  $\mathbf{K}$  is the state feedback gain matrix  $\mathbf{K} = [K_1 \ K_2 \ K_3]$ , for this third-order system. This state feedback gain matrix may be evaluated using the direct substitution method. This is shown in (6.7), where  $\mathbf{I}$  represents the identity matrix and  $\lambda_1, \lambda_2, \lambda_3$  represent the desired poles.

$$|s\mathbf{I} - \mathbf{A} + \mathbf{BK}| = (s + \lambda_1)(s + \lambda_2)(s + \lambda_3) \quad (6.7)$$

Expanding the right-hand side of this equation yields (6.8):

$$(s + \lambda_1)(s + \lambda_2)(s + \lambda_3) = s^3 + s^2(\lambda_1 + \lambda_2 + \lambda_3) + s(\lambda_1\lambda_2 + \lambda_1\lambda_3 + \lambda_2\lambda_3) + \lambda_1\lambda_2\lambda_3 \quad (6.8)$$

Hence, the values of the feedback gain matrix  $\mathbf{K}$  may be chosen such that the desired closed-loop poles are obtained. This is achieved by comparing the coefficients of similar powers of  $s$ . Evaluating the left-hand side of (6.7), for the respective coefficients of  $s$  yields:

$$s^3 \rightarrow 1 \quad (6.9a)$$

$$s^2 \rightarrow \frac{1}{L_1 L_2 C} (R_2 L_1 C + L_1 C K_2 v_C^* + R_1 L_2 C - L_1 L_2 K_3 i_L^*) \quad (6.9b)$$

$$s^1 \rightarrow \frac{1}{L_1 L_2 C} (L_1 d^{*2} - R_2 L_1 K_3 i_L^* - L_1 K_3 d^* v_C^* - L_1 K_2 d^* i_L^* - R_1 L_2 K_3 i_L^* + R_1 R_2 C + R_1 C K_2 v_C^* + L_2 + L_2 K_1 i_L^*) \quad (6.9c)$$

$$s^0 \rightarrow \frac{1}{L_1 L_2 C} (R_1 d^{*2} - R_1 R_2 K_3 i_L^* - R_1 K_3 d^* v_C^* - R_1 K_2 d^* i_L^* + K_1 v_C^* d^* + R_2 + K_2 v_C^* + R_2 K_1 i_L^*) \quad (6.9d)$$

The closed-loop poles are placed in a way that the system acts as a second-order dominant system. In other words, the third pole is placed such that its transient effect may be neglected. For this system, the design parameters comprise the damping coefficient  $\zeta = 0.9$  and the natural frequency of oscillation  $\omega_n = 2\pi \times 1200\text{Hz} = 7540\text{rad/s}$ . This results in the poles stated in (6.10), where  $\omega_d = \omega_n \sqrt{1 - \zeta^2}$ , with the third pole placed at  $-60000s^{-1}$ .

$$\begin{aligned} (s + \zeta\omega_n + j\omega_d)(s + \zeta\omega_n - j\omega_d)(s + 60000) \\ = (s + 6786 + j3287)(s + 6786 - j3287)(s + 60000) \quad (6.10) \\ = s^3 + 73572s^2 + 820005165s + 341109900000 \end{aligned}$$

These poles are visualised in the  $s$ -plane through Figure 6.2. Comparing the coefficients of these poles with the coefficients found in (6.9), the feedback gain matrix  $\mathbf{K}$  may be found, as it is the only unknown. This leads to (6.11).

$$K_1 = -0.0046 \quad (6.11a)$$

$$K_2 = 0.1084 \quad (6.11b)$$

$$K_3 = -0.0055 \quad (6.11c)$$

Knowing the value of the feedback gain matrix  $\mathbf{K}$ , the gain  $g$  may also be calculated:

$$g = \frac{-1}{\mathbf{C}(\mathbf{A} - \mathbf{BK})^{-1}\mathbf{B}} = 0.1385 \quad (6.12)$$

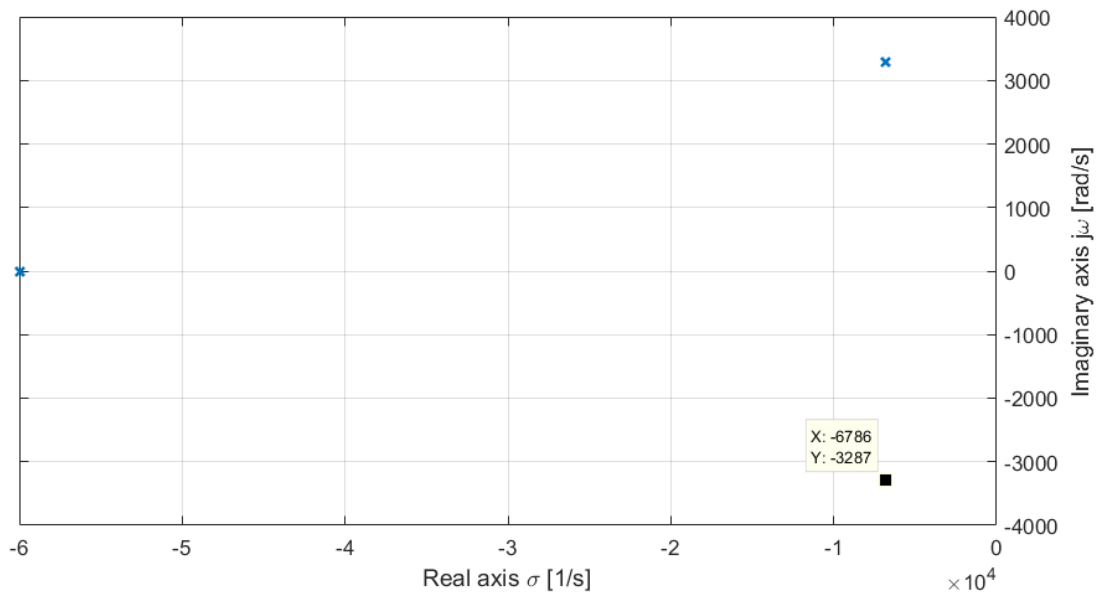


FIGURE 6.2: Closed-loop poles of designed state feedback regulator

### 6.3.3 Controller Testing

#### 6.3.3.1 Mathematical Simulation Model

A simulation model of the state feedback regulator regulating the non-linear plant was implemented in Simulink in order to verify that the designed controller operates as designed for. This simulation model may be seen in Figure 6.3, where the plant block contains the system equations previously stated in (6.3).

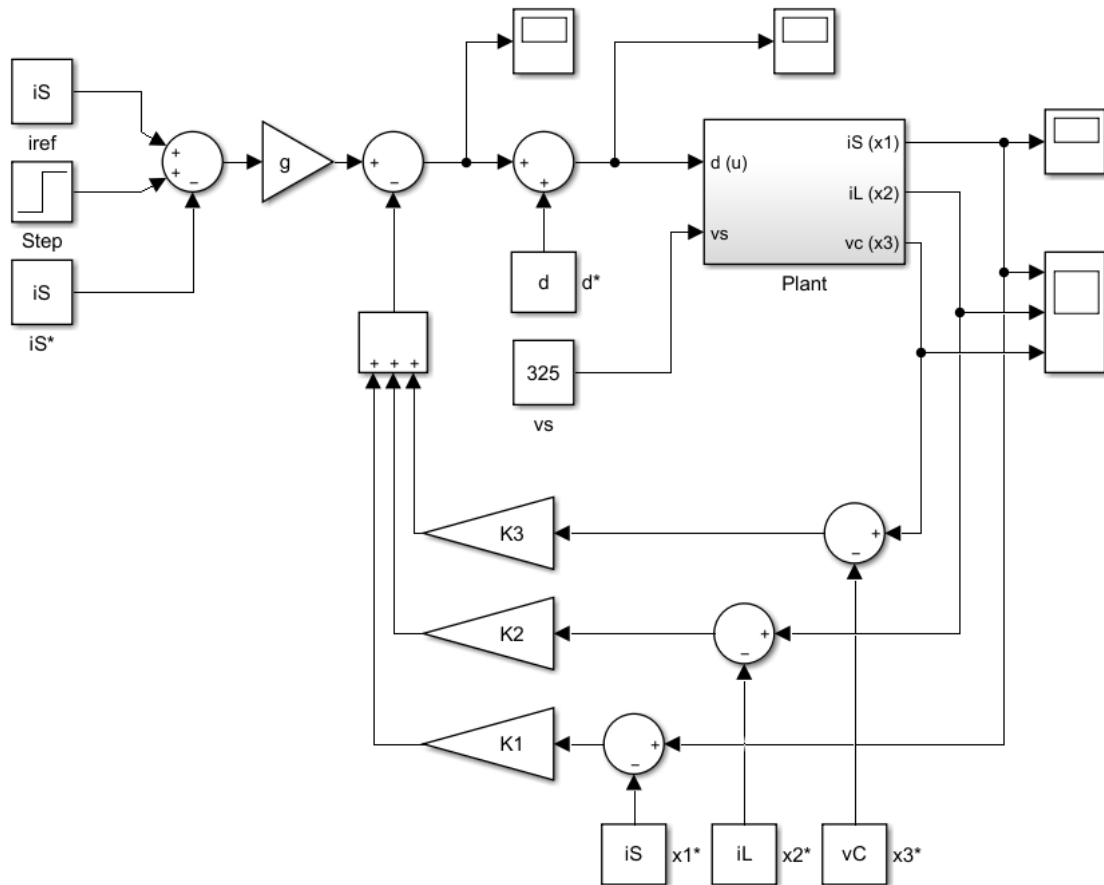


FIGURE 6.3: Mathematical simulation model of state feedback regulator

### 6.3.3.2 Step Response

The system is allowed to settle to the equilibrium point with a supply voltage  $v_S = 325V$  and a step in the reference current, which is the supply current  $i_{ref}$ , is issued at  $t = 0.02s$ . This step increases the value of the reference supply current from its equilibrium point value of  $23.72A$  to  $24.72A$ . The response of the supply current to this step in the reference current may be seen in Figure 6.4. The supply current settles at  $24.74A$ , instead of  $24.72A$  in an underdamped manner with minimal oscillations due to the high damping coefficient  $\zeta = 0.9$ . A minor discrepancy is expected, as the controller will lose accuracy due to the deviation from the operating point it is linearised about. As this deviation is further increased, the discrepancies will become more significant. This test verifies that the designed state feedback regulator responds adequately to steps in the reference current.

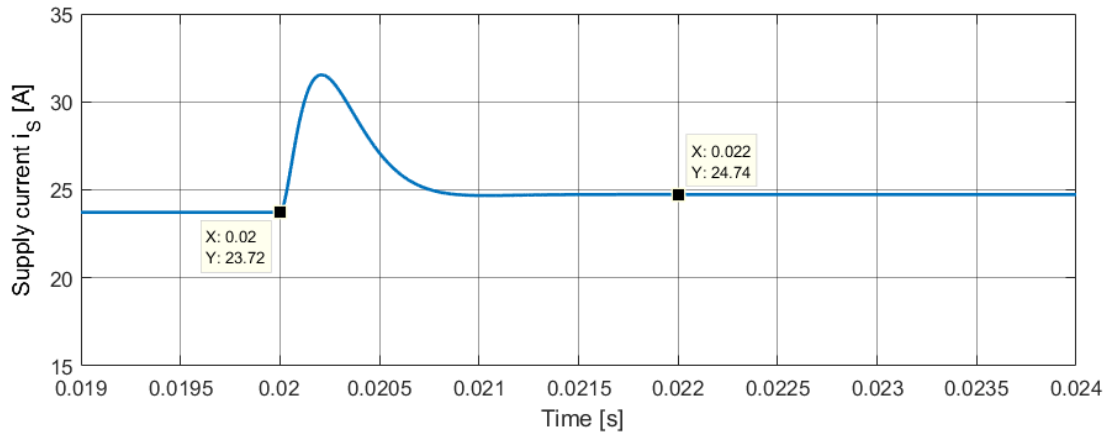


FIGURE 6.4: Mathematical simulation model step response of supply current

### 6.3.3.3 Voltage Sweep Test

To more closely match the operating conditions of the real application, a voltage sweep of the sinusoidal supply voltage is applied to the system, consisting of two full cycles. This voltage sweep, which is shown in Figure 6.5 below, peaks at  $v_S = \pm 325V$  and has a frequency of 50Hz. Furthermore, the reference current is kept fixed at its equilibrium point value  $i_{ref} = 23.72A$  and the duty cycle is limited to  $d = 1.0 = 100\%$ , as it is done in the actual application. Two cycles are applied as the system starts with zero initial conditions, which will have an effect on the system response. The controller implemented in this simulation model does not operate for both half cycles of the supply voltage. It is sufficient to observe only the positive half cycle at this stage, as both half cycles are identical. It is however essential to ensure that the duty cycle reaches a value of  $d = 1.0 = 100\%$  before the current's zero-crossing, ensuring that the HDMS prototype enters region 2.

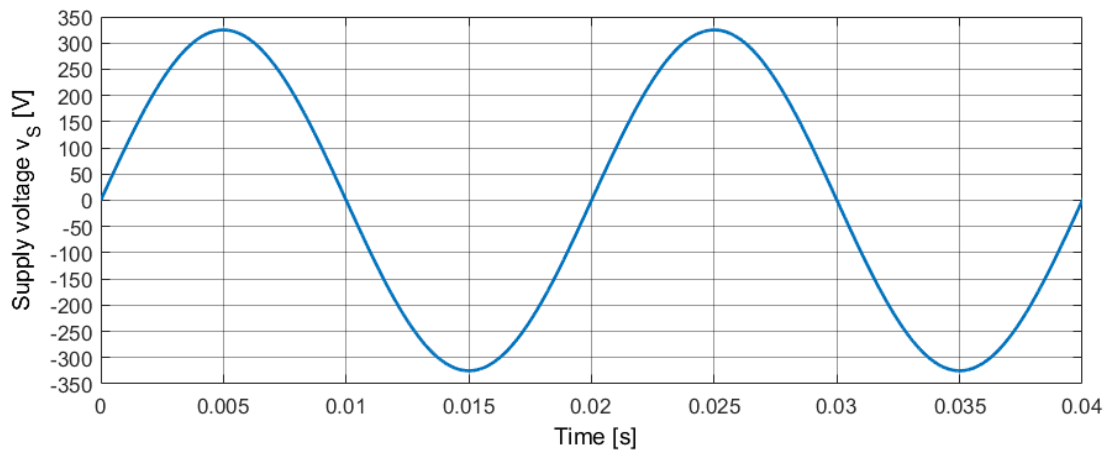
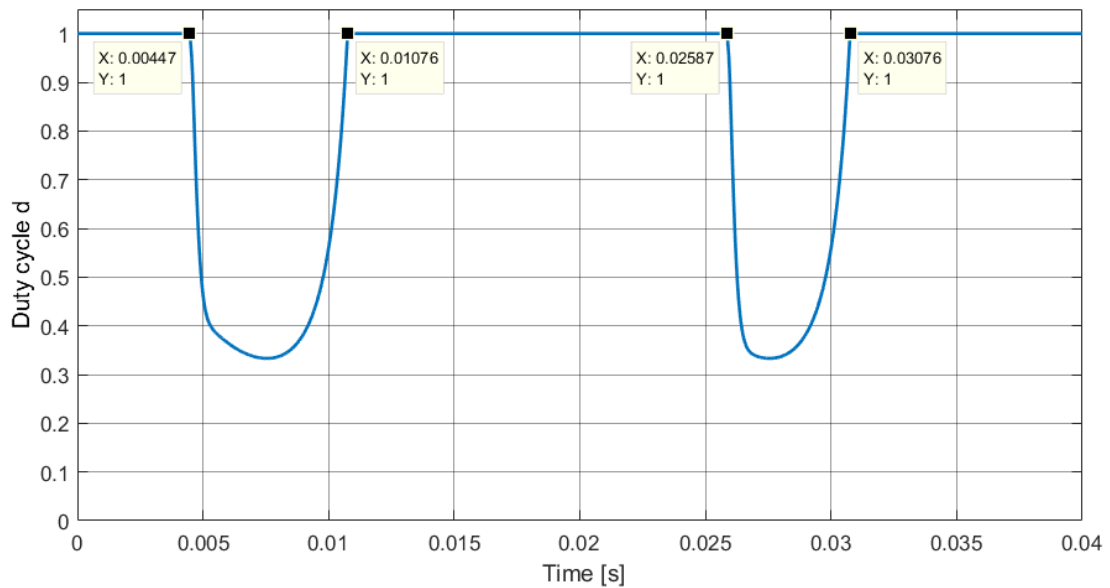
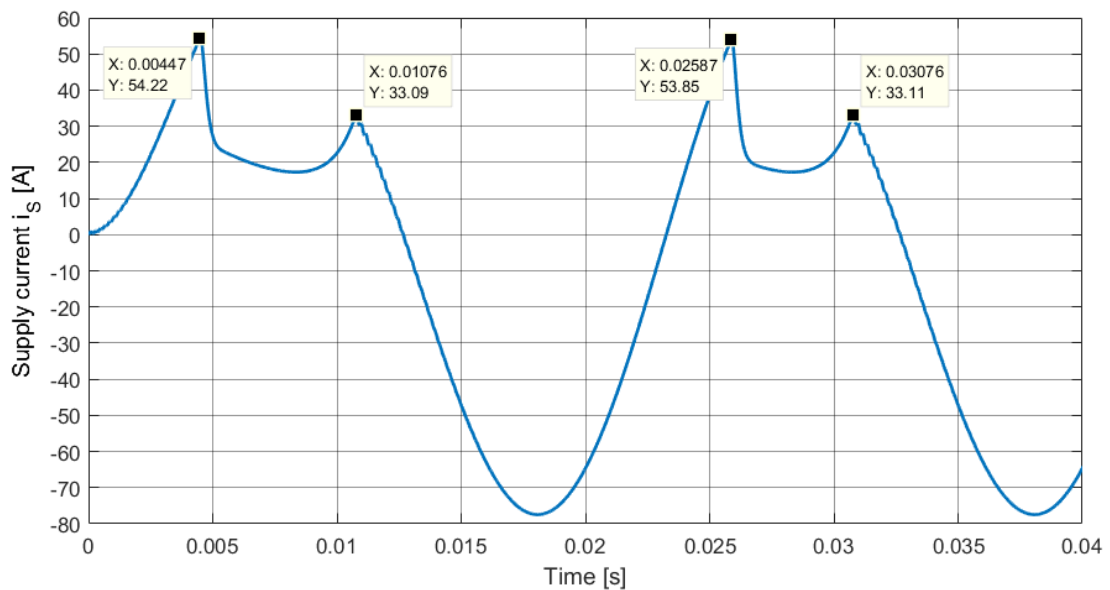


FIGURE 6.5: Plot of supply voltage for voltage sweep test

The responses of the the duty cycle  $d$  and supply current  $i_S$  are shown in Figures 6.6(a) and 6.6(b) respectively.



(a) Response of duty cycle to supply voltage sweep



(b) Response of supply current to supply voltage sweep

FIGURE 6.6: Responses of duty cycle and supply current to supply voltage sweep for designed controller

The duty cycle remains equal to  $d = 1.0$  until  $t = 0.00447s$ , which results in the supply current overshooting its equilibrium point value to  $i_S = 54.22A$ . The duty cycle then decreases to approximately  $d = 0.35$  before it rises to  $d = 1.0$  again. This results in the supply current reducing and slightly undershooting the equilibrium point value  $i_S^* = 23.72A$ . As the duty cycle rises to  $d = 1.0$  again, the

supply current also increases resulting in a second peak of  $i_S = 33.09A$ . A similar response is obtained during the second supply voltage cycle. The duty cycle is of the desired shape, meaning that it is active around the peak of the supply voltage and otherwise rises to  $d = 1.0$ , allowing the HDMS to enter region 2. This is critical to its operation and must occur before the current's zero-crossing. However, the shape of the supply current is not desirable and hence the controller's response is tuned through its poles to obtain a more ideal system response, where the supply current rises to its equilibrium point value and remains in its vicinity until the controller enters region 2.

### 6.3.3.4 Controller Tuning

The state feedback regulator operated as desired when subjected to a change in the reference current, verifying its design process. When it was subjected to a changing supply voltage, which is the scenario in the intended application, it did not produce a desirable response. The state feedback regulator expects a change in its reference, rather than a change in the supply voltage. Hence, it must be tuned to produce a desirable response under the intended operating conditions. This was achieved by heuristically changing the location of the closed-loop poles through  $\zeta$  and  $\omega_n$  to achieve a complex complementary pole pair and the third pole, which is purely real. The resulting closed-loop poles, which produced a satisfactory system response, are shown in Figure 6.7.

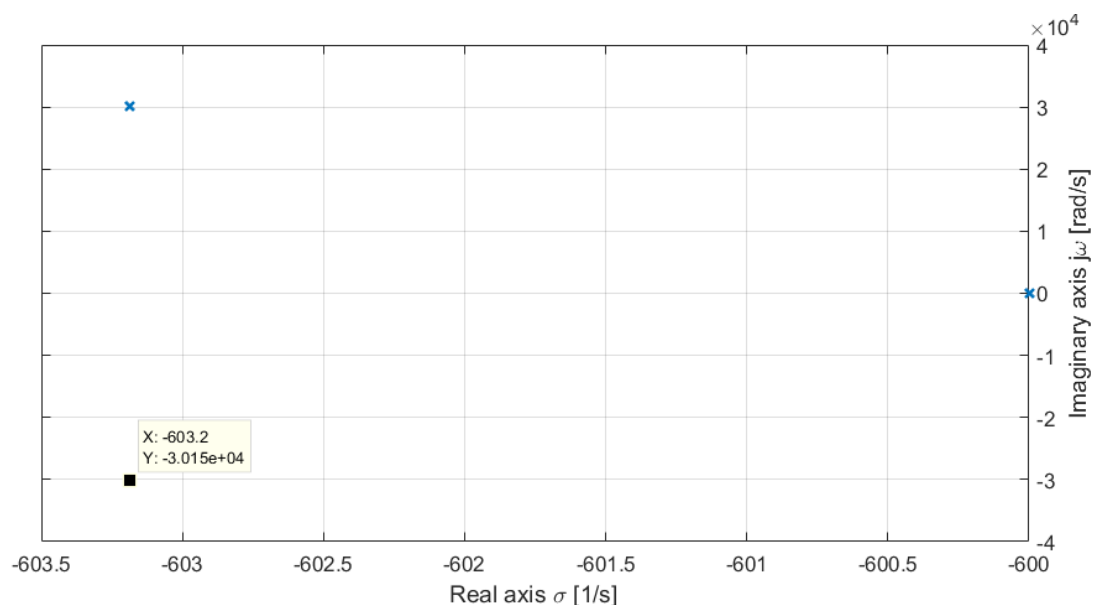


FIGURE 6.7: Tuned closed-loop poles

This configuration causes pole interaction, as there is not sufficient distance between them. Hence, the system no longer behaves like a second-order dominant system, as previously designed for. However, this configuration results in a desirable system response to the changing supply voltage. The parameters of the designed and tuned controllers are tabulated in Table 6.2.

TABLE 6.2: Designed and tuned controller parameters

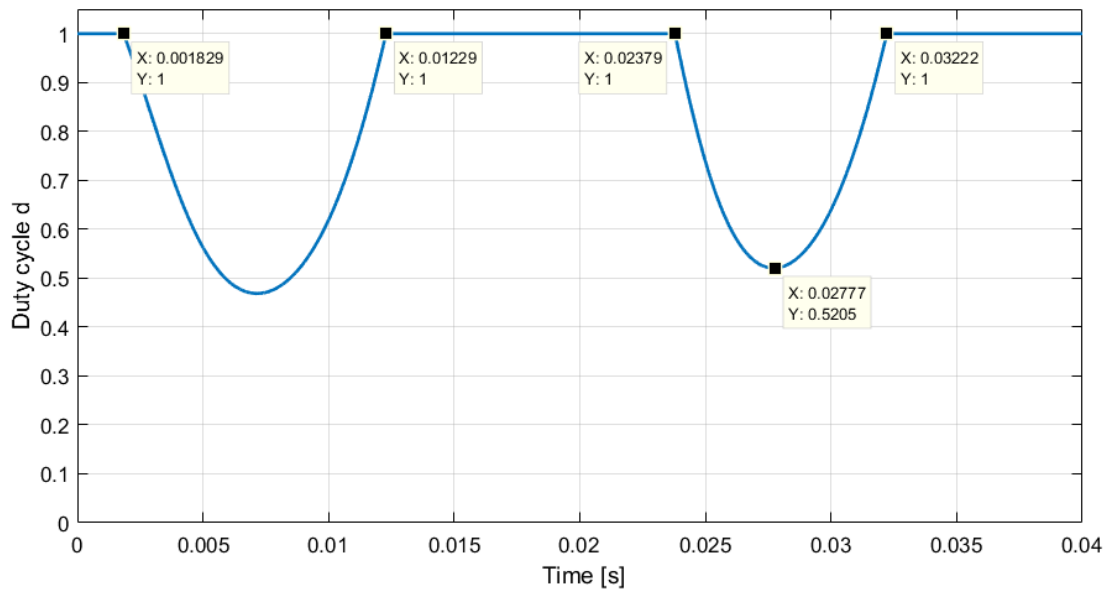
Parameter	Designed Controller	Tuned Controller
$\zeta$ [ ]	0.9	0.02
$\omega_n$ [rad/s]	$2\pi \times 1200$	$2\pi \times 4800$
Real Pole [1/s]	-60,000	-600
$K_1$ [ ]	-0.0046	-0.0031
$K_2$ [ ]	0.1084	0.0136
$K_3$ [ ]	-0.0055	$-1.545 \times 10^{-5}$
$g$ [ ]	0.1385	0.0222

The response of the duty cycle and supply current for the tuned controller are shown in Figure 6.8(a) and 6.8(b) respectively. The duty cycle can be seen to now initially be saturated at  $d = 1.0$  until  $t = 0.0018s$ . It then drops slightly below  $d = 0.5$  and returns to  $d = 1.0$  for the zero-crossing of the supply current. This allows the supply current to rise close to the equilibrium point value of  $i_S^* = 23.72A$ . The duty cycle returns to a value of  $d = 1.0$  for the zero-crossing of the supply current at  $t = 0.0123s$ , at which the supply current is equal to  $i_S = 11.24A$ .

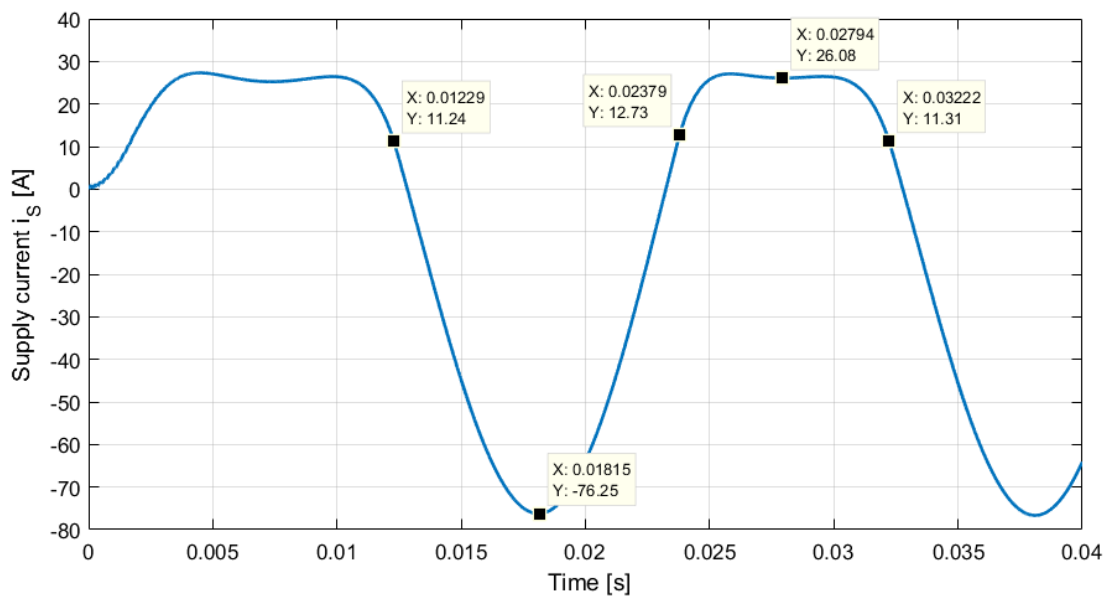
With a duty cycle  $d = 1.0$ , the motor winding is connected directly to the supply voltage. Thus, it is ensured that no damage is caused to the switching devices, as no switching is carried out during the zero-crossing of the motor winding current  $i_L$ . The supply current is kept at around  $26.08A$  for most of the positive supply voltage half-cycle. This results in good current reduction when compared to the negative half cycle, where the controller is currently not active and a supply current  $i_S = -76.25A$  is produced.

The duty cycle reaches  $d = 0.52$  in the second positive half-cycle. The system was designed for a duty cycle of  $d = 0.4$ , however this is not guaranteed to occur as the system is subjected to a changing supply voltage, rather than a change in the reference supply current and may thus not have enough time to settle to the designed value.

This response is satisfactory, as it results in good current reduction and the duty cycle is driven to  $d = 1.0$  at approximately  $i_S = 11.24A$ , which ensures that region 2 is entered early enough. The controller exits region 2 when  $i_S = 12.73A$  after the negative half cycle.



(a) Response of duty cycle to supply voltage sweep with tuned controller



(b) Response of supply current to supply voltage sweep with tuned controller

FIGURE 6.8: Responses of duty cycle and supply current to supply voltage sweep with tuned controller

### 6.3.3.5 Power Electronics Simulation Test

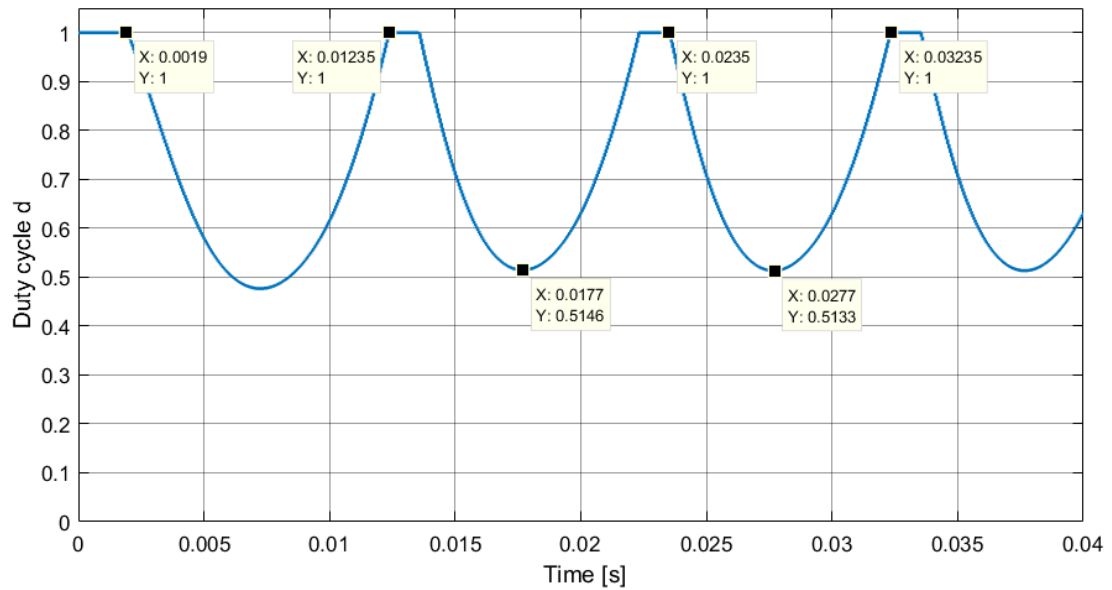
The tuned state feedback regulator was implemented in the *s-function* of the Simscape power electronics simulation model shown in Chapter 3. The implemented control law is presented in (6.13).

$$u = d^* + g \times I_{ref} - [K_1(i_S - i_S^*) + K_2(i_L - i_L^*) + K_3(v_C - v_C^*)] \quad (6.13)$$

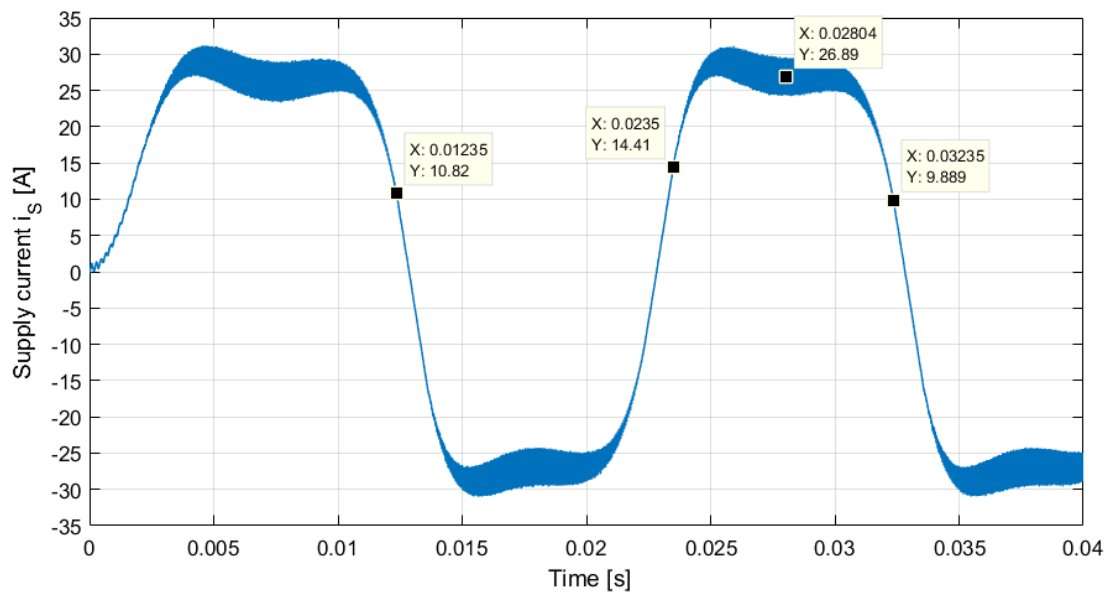
The response of the duty cycle and supply current to two full cycles of the supply voltage is shown in Figures 6.9(a) and 6.9(b) respectively. The control algorithm is implemented for both positive and negative polarities. As this control algorithm is digitised and the simulation model is no longer based on the average model of the Buck converter, some discrepancies are expected. Additionally, the 20kHz switching frequency will be observable in the supply current. For measurements, the average value of the supply current is considered.

The duty cycle initially remains saturated at  $d = 1.0$  until  $t = 0.0019s$ , as the system is initialised with zero initial conditions. This is equivalent when compared to the simulation of the mathematical model, which remained saturated until  $t = 0.0018s$ . The duty cycle also reaches  $d = 1.0$  at a slightly lower value of the supply current, namely at  $i_S = 10.82A$  rather than  $i_S = 11.24A$ . In the second positive half-cycle, region 2 is entered when  $i_S = 9.90A$ , compared to the previous simulation model, which entered region 2 when  $i_S = 11.31A$ . Region 2 is exited after the negative half-cycle when  $i_S = 14.41A$ , compared to the previously observed  $i_S = 12.73A$ . These discrepancies occur due to the delay introduced by the low-pass filters introduced in the s-function voltage and current measurement, in order to match the actual application. However, region 2 is still entered at a sufficiently high value of  $i_S$  in order to avoid switching of the IGBTs during the main winding current zero-crossing.

During both positive and negative half-cycles, the duty cycle reaches a value of  $d = 0.51$ , compared to the previous value of  $d = 0.52$ . The supply current can be seen to overshoot initially to slightly less than  $i_S = 30.0A$ . It settles at an average of  $26.89A$  after the first cycle, which is very close to the  $i_S = 26.08A$  seen from the mathematical model.



(a) Duty cycle response of tuned controller in power electronics model



(b) Supply current response of tuned controller in power electronics model

FIGURE 6.9: Responses of duty cycle and supply current of tuned controller in power electronics model

### 6.3.3.6 Hardware Test

The state feedback regulator algorithm was implemented on the HDMS hardware prototype's software using the control law previously stated in (6.13). The 50Hz  $230V_{rms}$  supply voltage during this test is shown in Figure 6.10. For this test, two full cycles are again considered.

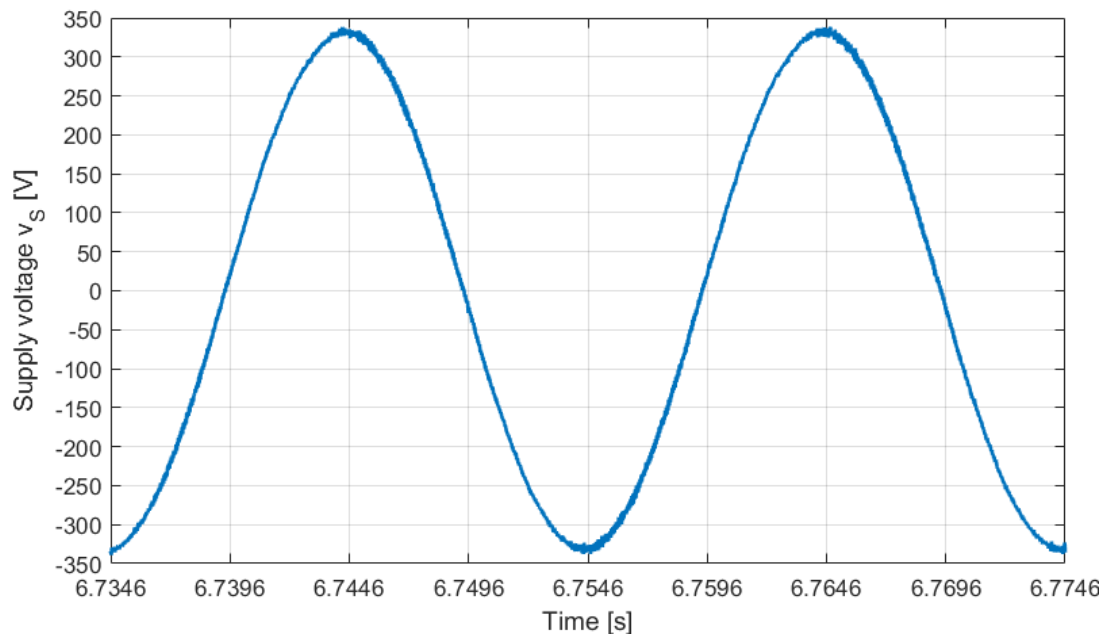
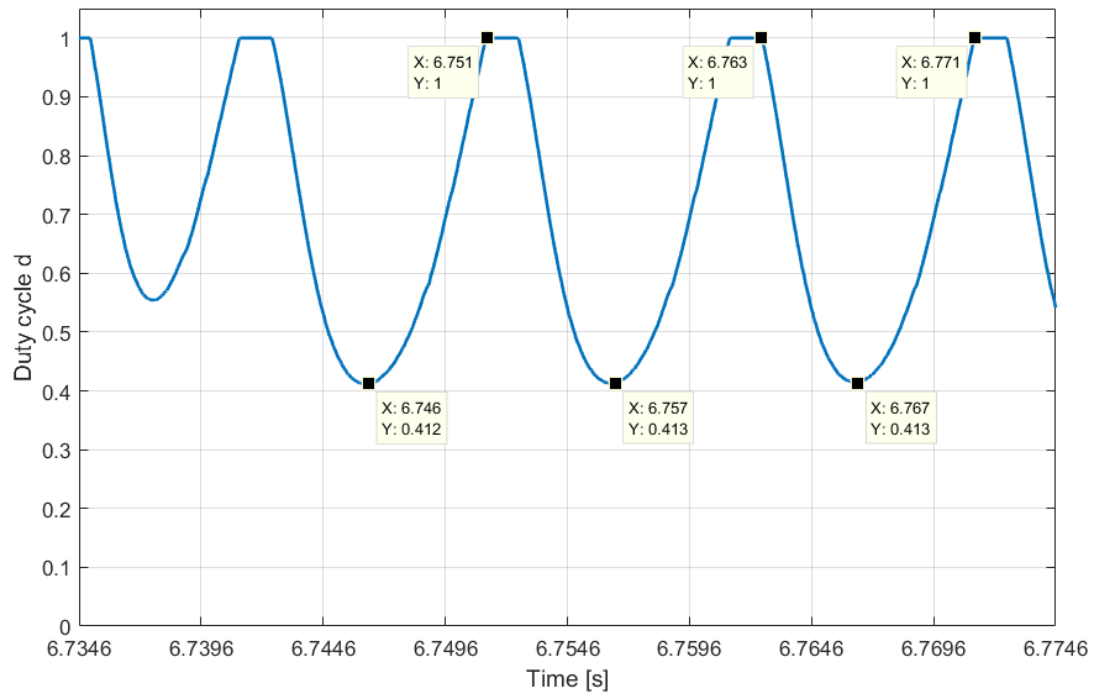


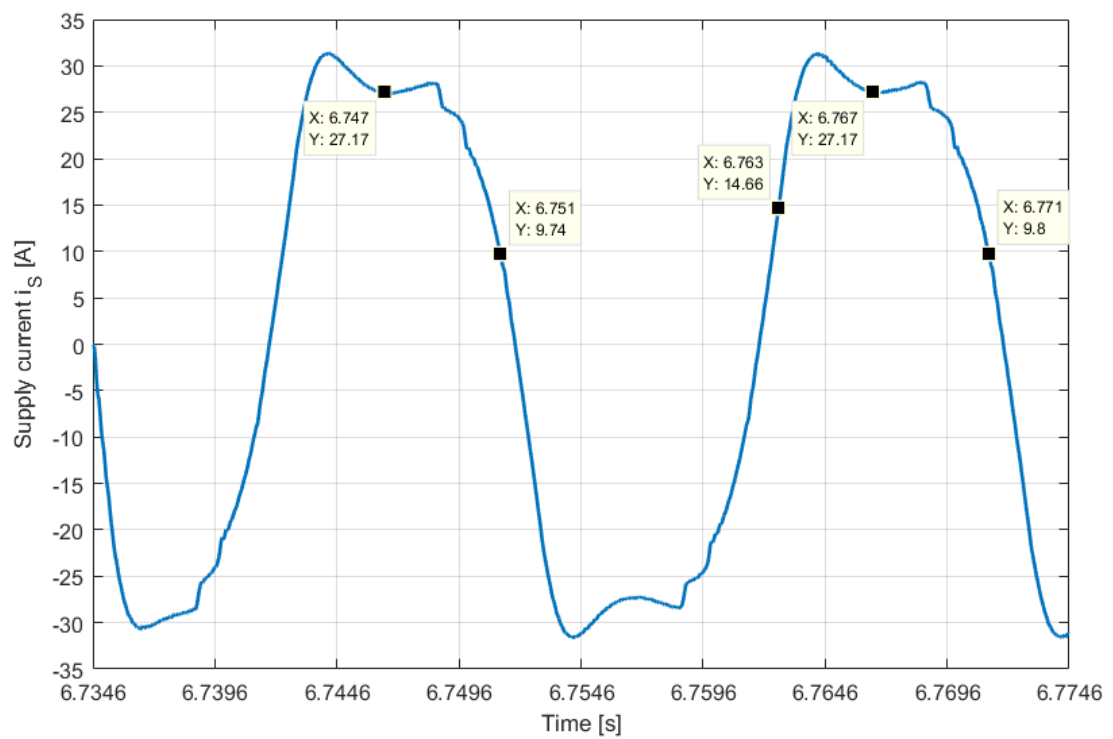
FIGURE 6.10: Plot of supply voltage sweep on hardware prototype

The response of the duty cycle and the supply current to two cycles of the supply voltage captured by the microcontroller can be seen in Figures 6.11(a) and 6.11(b) respectively. The duty cycle and supply current can be seen to initially not reach the same value as for the following half cycles. This occurs as the supply voltage is already at its negative peak at the beginning of the test. It is to be noted that the supply current is averaged by the microcontroller and hence the 20kHz switching effect is not visible. This is done for the control algorithm.

For the following cycles however, the duty cycle can be seen to reach a value of  $d = 0.413 = 0.41$ , compared to the  $d = 0.51$  from the previous simulation model. The supply current on the other hand reaches a value of  $i_S = 27.17A$ , whereas the simulation model reached  $i_S = 26.89A$ . Additionally, the algorithm can be seen to enter region 2 when  $i_S = 9.80A$  and exits region 2 when  $i_S = 14.66A$ , compared to the previous  $i_S = 9.90A$  and  $i_S = 14.41A$  respectively. While a discrepancy of approximately 20% occurs in the value of the duty cycle, the supply current still behaves comparable to the power electronics simulation model.



(a) Duty cycle response of tuned controller on hardware prototype



(b) Supply current response of tuned controller on hardware prototype

FIGURE 6.11: Responses of duty cycle and supply current of tuned controller on hardware prototype

## 6.4 Conclusion

This chapter has presented the state feedback regulator, which serves as an alternative controller for the HDMS prototype. For the controller design, the equilibrium point of the desired operating point was first obtained. The controllability matrix was found to be of full rank, which allows the system poles to be placed at any desired location. This was achieved by placing the system poles through direct substitution.

While the state feedback regulator performed as desired for a change in the reference current, it did not perform as desired for a change in the supply voltage, which is its intended application. Hence, the controller was tuned by heuristically changing the system poles to a configuration which resulted in a desirable system response when subjected to a changing supply voltage. The obtained system poles resulted in good supply current reduction while obeying the required regions of operation. The tuned state feedback regulator design was verified in the power electronics simulation model and in the actual hardware prototype. The supply current response was comparable in both simulation model and hardware prototype, while the duty cycle response contained some discrepancy.

# Chapter 7

## Performance Tests

### 7.1 Introduction

This chapter covers the controller hardware tests carried out on the HDMS prototype. A DOL motor start is initially carried out in order to provide a performance contrast to the proposed HDMS soft starter current controllers. Three current controller design operating points are proposed and their performances are compared. This is done for both the state feedback regulator and the HDMS prototype's current controller. The aim is to produce comparable winding currents for both controllers, which should result in comparable starting torques. As the controllers operate based on different control algorithms, they produce differently shaped supply currents.

The state feedback regulator is designed such that its supply current peak is flattened as much as possible. The aim of this is to reduce the negative effect of the supply current peak on the flicker test result. The HDMS current controller is designed to produce a more rounded supply current peak. This makes it more sinusoidal compared to the state feedback regulator, while still reducing its peak amplitude. The effect of the supply current shape is investigated through a flicker test. Hence, the performance of both controller designs is compared through the produced starting torque and the flicker test result.

Each designed operating point is tested in the component-level simulation model introduced in Chapter 3 and on the HDMS hardware prototype. The design is carried out on the locked rotor motor winding parameters without the auxiliary winding connected, as the controllers have no effect on the auxiliary winding current. The controller performance during the first half-cycle is not considered throughout

this chapter, as it represents a transient. The auxiliary winding is then connected in order to carry out a starting torque test and a full motor soft-start. A flicker test is carried out for both the starting torque test and the full motor soft-start.

As mentioned in Chapter 5, the flicker tests are carried out in compliance with IEC 61000-3-11 and with custom parameters provided by the project's industrial partner. Figure 7.1 provides a diagram of the flicker test, where EUT stands for the equipment under test. The line and neutral resistance and reactance values in compliance with IEC 61000-3-11 standard are provided in (7.1) [21].

$$R_A = 0.15\Omega \quad (7.1a)$$

$$X_A = j0.15\Omega \quad (7.1b)$$

$$R_N = 0.10\Omega \quad (7.1c)$$

$$X_N = j0.10\Omega \quad (7.1d)$$

This reference impedance serves to emulate typical cable impedances present between a substation and the consumer. The flicker meter then measures the voltage drop across this impedance and determines whether this is within the acceptable range.

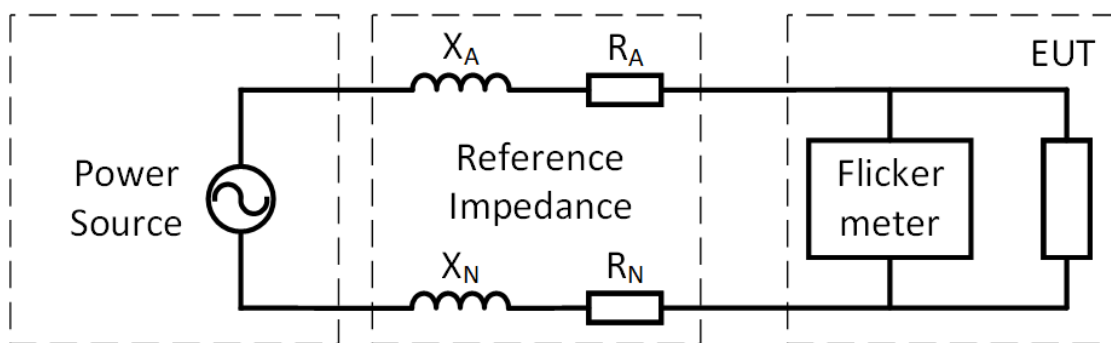


FIGURE 7.1: Flicker test diagram

The parameters with their corresponding limits, which were used to evaluate the flicker test performance of the EUT in this dissertation, are summarised as follows:

- Max  $D_c = 3.3\%$
- Max  $D_{max} = 6\%$
- Max  $T_{max} = 500ms$
- Max  $P_{st} = 1$  for an observation period of ten minutes
- $P_{lt} = 0.65$

For the flicker test performance evaluation, the  $D$ -values are considered. These  $D$ -values represent the voltage change characteristics at the terminals of the EUT [22]. For each half period,  $D(t)$  is calculated as the time function of the relative (with respect to the previous measurement) half period RMS voltage change [22]. The half period RMS measurement for this variable is illustrated in Figure 7.2 [22] for a 50Hz supply voltage. The half period is measured between two consecutive zero-crossings of the supply voltage. The sample points in blue do not represent the actual sampling interval of the test equipment.

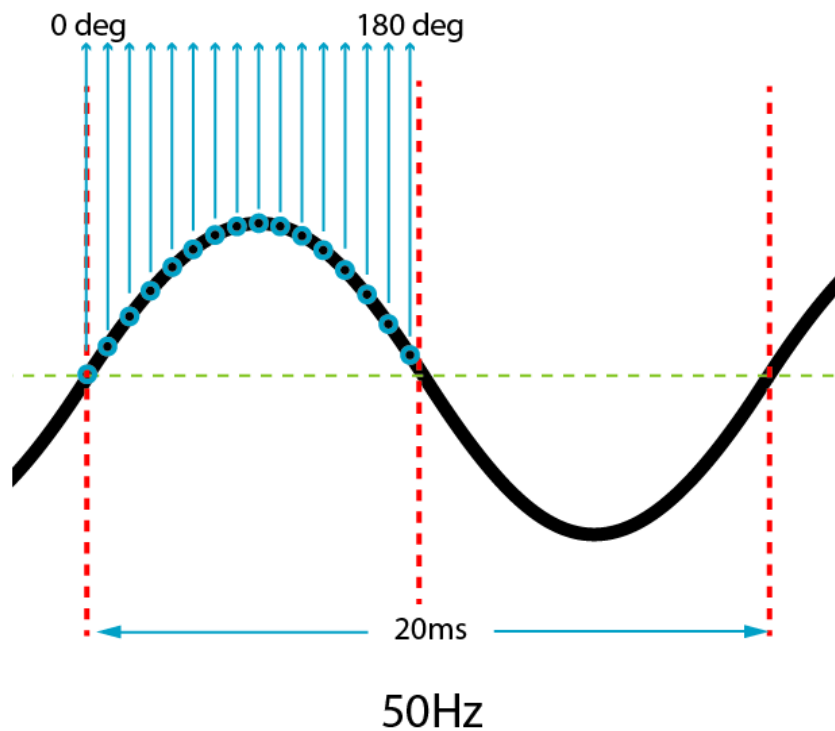


FIGURE 7.2: Illustration of the half period RMS measurement

$D_c$  represents the maximum steady state voltage change during an observation period [22]. An example of a steady state voltage change may be considered between motor standstill and the motor starting period.  $D_{max}$  represents the maximum relative voltage change during an observation period [22]. This relative voltage change is considered between two consecutive half period measurements.  $T_{max}$  represents the maximum time period during which the half period RMS voltage change exceeds its limit. This limit represents a voltage change of  $D(t) = 3.3\%$  and is accumulated until a new steady state condition is established [22]. This may occur during the motor start, where the new steady state condition may be represented by the motor having reached its rated speed.

$P_{st}$  is defined as the short term flicker severity and is calculated as per IEC61000-4-15, the standard observation time is ten minutes [22].  $P_{lt}$  represents the long term flicker sensitivity [22].

## 7.2 Direct On Line Start

In order to provide a performance comparison to the proposed current controller designs, a direct on line test was carried out. The motor was connected directly to the supply and the resulting total current, consisting of the motor winding and auxiliary winding currents, was recorded. Figures 7.3 and 7.4 show the total current during a locked rotor test and a motor start without a locked rotor and no load applied.

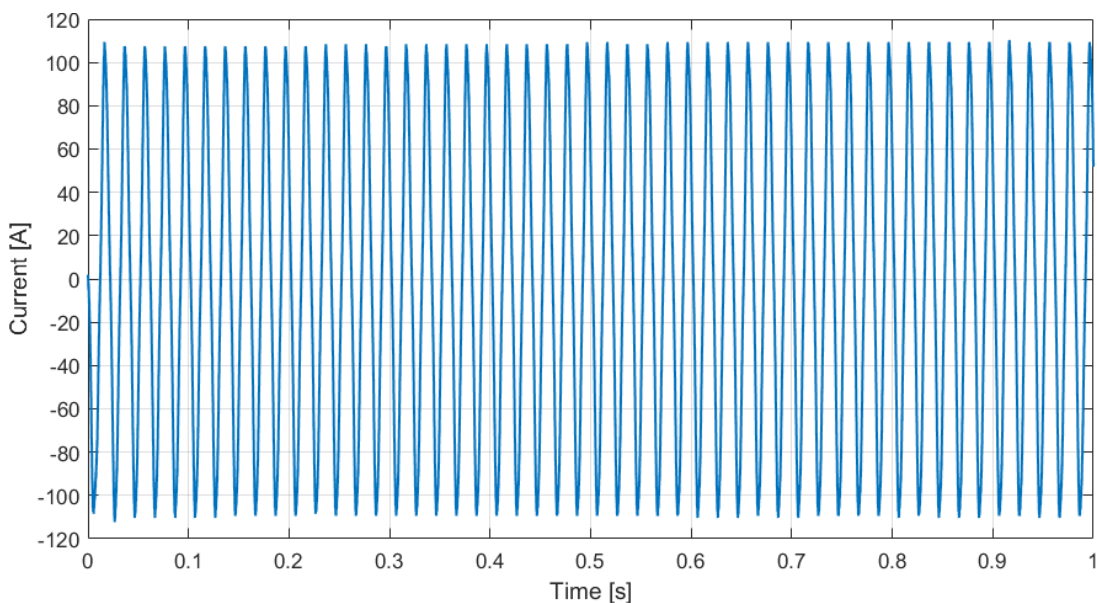


FIGURE 7.3: Direct on line locked rotor test

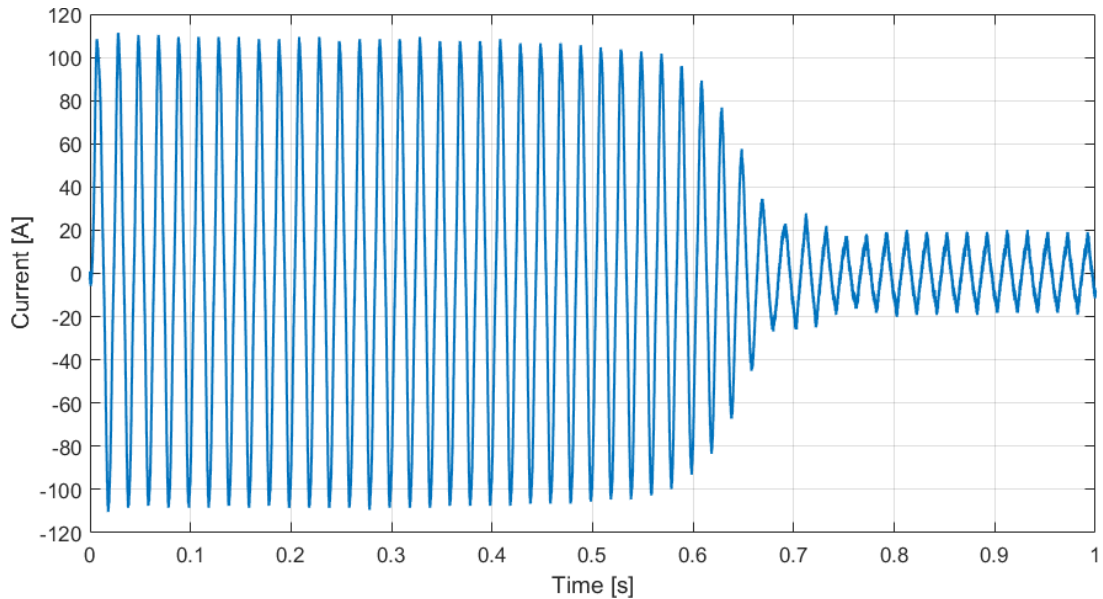


FIGURE 7.4: Direct on line start

During the locked rotor test, the motor continuously draws the inrush current. This inrush current was measured to peak at a value of  $109.44A$  with an RMS value of  $71.93A$ . During the non-locked rotor test, the motor start is completed after approximately  $0.67s$ , after which the motor draws a current close to its rated current. This may occur due to friction introduced from the disc-brake. From this test it becomes clear that starting the motor in the DOL configuration results in an inrush current, which is greater than the rated current by a factor of at least 5.

While this provides a short motor starting time, such a large inrush current causes the voltage to dip. This affects other appliances connected in parallel to the motor and hence necessitates using a dedicated motor starter. The starting torque produced by the motor in the DOL configuration was measured to be  $2.25Nm$ . Both the locked rotor test and the motor start failed the flicker test, exceeding the maximum test parameters significantly. The corresponding flicker test reports are attached in Appendix A.

## 7.3 30% Duty Cycle Controller Design

The current controller operating point of this section is based on a 30% duty cycle and a supply voltage of  $v_S = 325V$  in the linearisation process of the state feedback regulator design. The resulting equilibrium point parameters of the state feedback regulator are shown in (7.2). The best possible supply current response was obtained for both controllers. As low supply currents will be achieved using a duty cycle of 30%, the design of the controllers is more restricted as the regions of operations must not be violated. This can lead to some deviations in the expected waveforms. The resulting parameters are tabulated in Table 7.1.

$$i_S^* = 13.43A \quad (7.2a)$$

$$i_L^* = 44.77A \quad (7.2b)$$

$$v_C^* = 322.31V \quad (7.2c)$$

TABLE 7.1: 30% controller parameters

Parameter	State feedback regulator
$\zeta$ [ ]	0.02
$\omega_n$ [rad/s]	$2\pi \times 4800$
Real Pole [1/s]	-800
$K_1$ [ ]	-0.0041
$K_2$ [ ]	0.0194
$K_3$ [ ]	$-2.441 \times 10^{-5}$
$g$ [ ]	0.0391
Parameter	HDMS prototype controller
$i_{ref}$ [A]	24
$K_1$ [A]	15
$K_I$ [A <sup>-1</sup> ]	100

### 7.3.1 State Feedback Regulator

#### 7.3.1.1 Locked Rotor Simulation Results

The state feedback regulator based on the 30% duty cycle linearisation condition is tested in the simulation model. The resulting duty cycle and the supply and motor winding currents are shown in Figures 7.5 and 7.6 respectively. The duty cycle reduces to a value of  $d = 0.366$  after the first half cycle. The supply current initially peaks at a value of  $i_S = 20.25A$  and drops to a value of  $i_S = 15.54A$  when

the duty cycle reaches its lowest value. The motor winding current can be seen to peak at a value of  $i_L = 43.18A$ . The fact that the state feedback regulator achieves these values shows that it manages to operate with the deviation in the supply voltage well enough. The supply current response was kept as flat as possible using this equilibrium operation point. While the supply current is far from sinusoidal, the main winding current retains a mostly sinusoidal shape. Due to the low value of the duty cycle, very good current amplification is achieved.

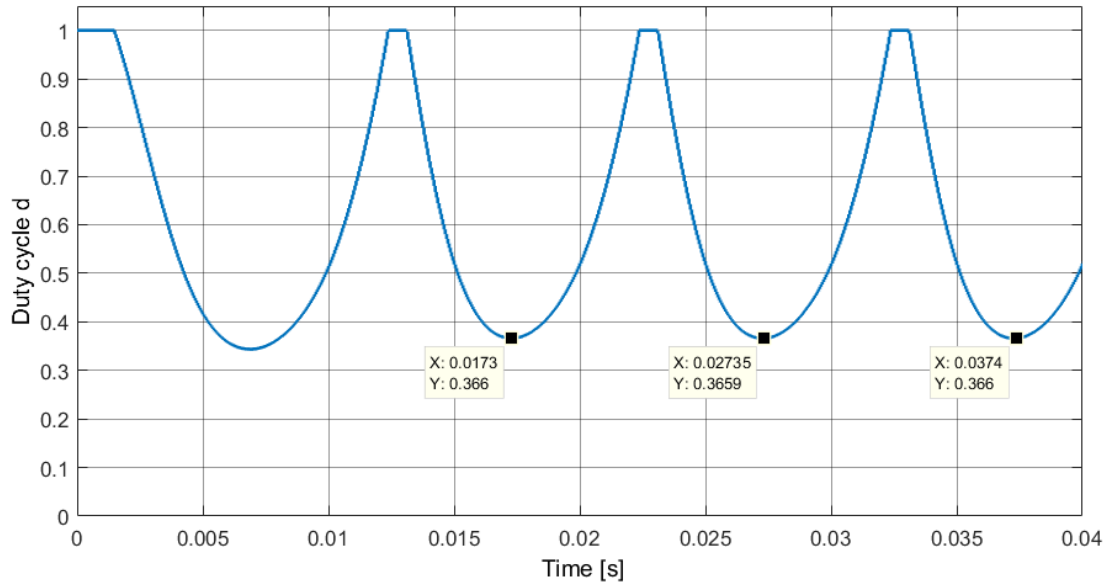


FIGURE 7.5: 30% state feedback regulator simulation model duty cycle response

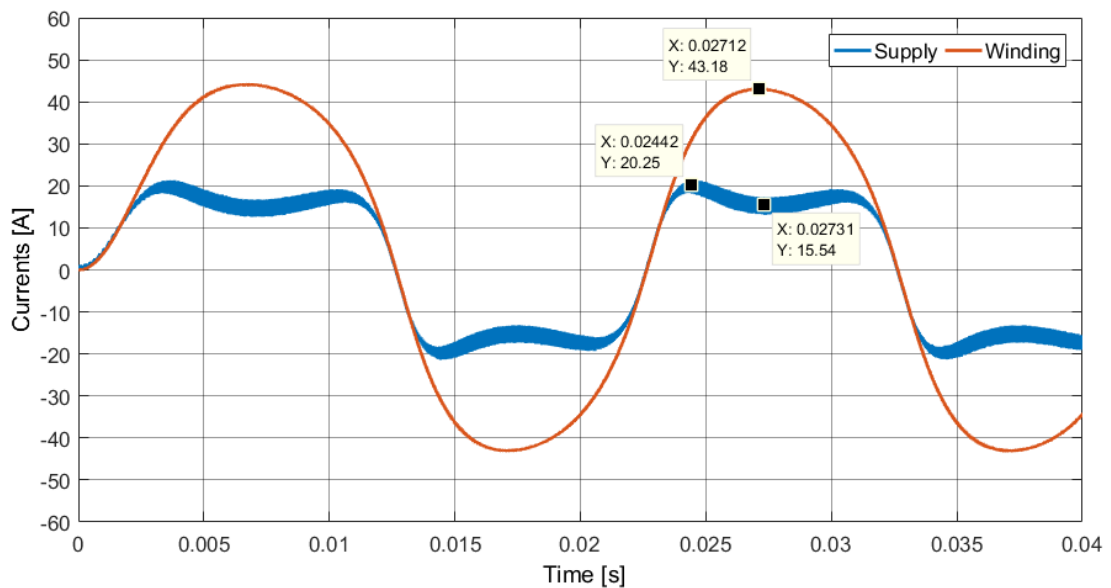


FIGURE 7.6: 30% state feedback regulator simulation model supply and motor winding current response

### 7.3.1.2 Locked Rotor Hardware Results

The locked rotor test is carried out on the hardware prototype by engaging the disc brake and locking the rotor. The resulting duty cycle and currents for the state feedback regulator are shown in Figures 7.7 and 7.8 respectively. The duty cycle reduces to a value of  $d = 0.3$  after the first half cycle. This is slightly lower to the  $d = 0.366$  in the simulation model.

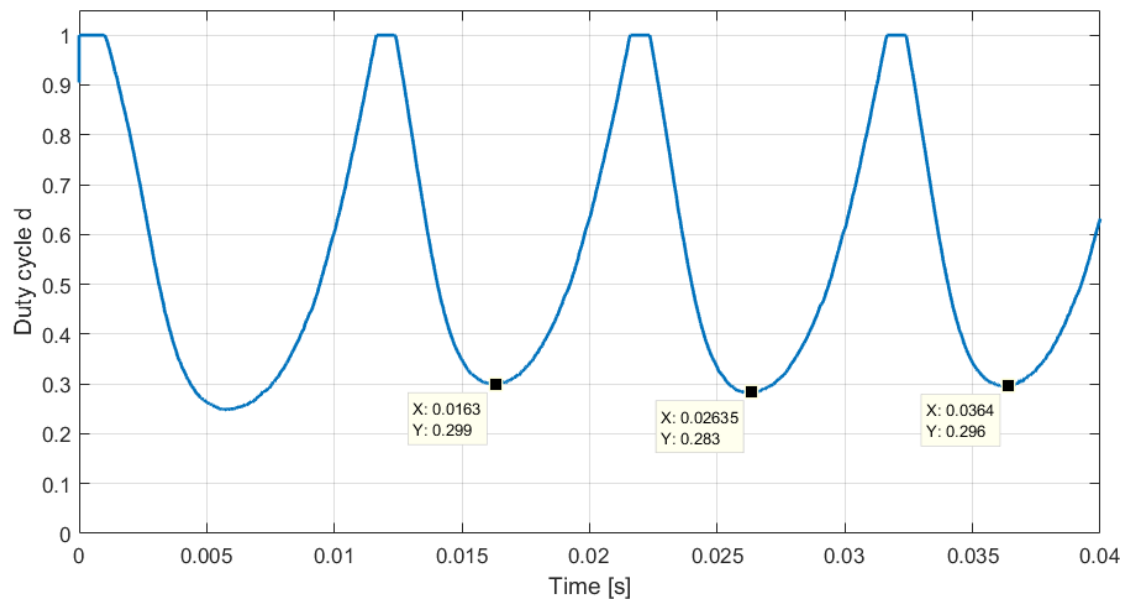


FIGURE 7.7: 30% state feedback regulator hardware duty cycle response

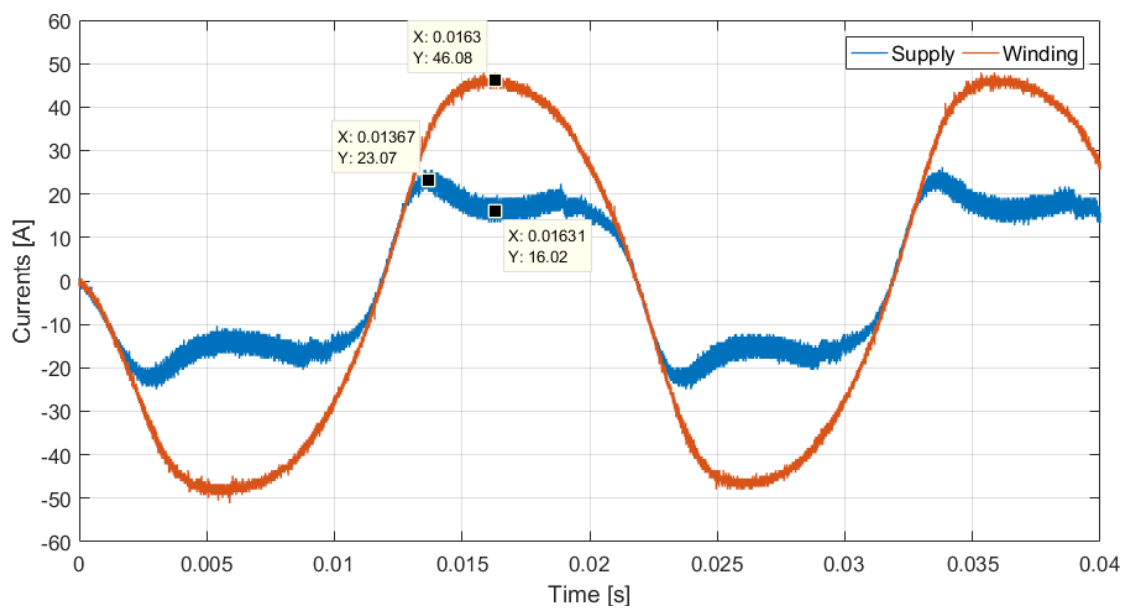


FIGURE 7.8: 30% state feedback regulator hardware supply and motor winding current response

The supply current more closely matches the expected values. It can be seen to peak at  $i_S = 23.1A$  and drop to  $i_S = 16.0A$  as the duty cycle reaches its lowest value. With a similar supply current but a slightly lower duty cycle, the main winding current is also slightly increased. This peaks at a value of  $i_L = 46.1A$ . This test was repeated with the auxiliary winding connected and the starting torque was recorded. A flicker test was also carried out in order to investigate the effect of the total supply current  $i_T$ , consisting of the supply current  $i_S$  and the auxiliary winding current  $i_{aux}$ , on the power supply. Connecting the auxiliary winding does not affect the control algorithm's performance and the amplitude or shape of the motor winding current. It only draws an additional current from the power supply, which is rather small and out of phase with the supply current considered for the control algorithm. This is shown in Figure 7.9 for the 30% state feedback regulator.

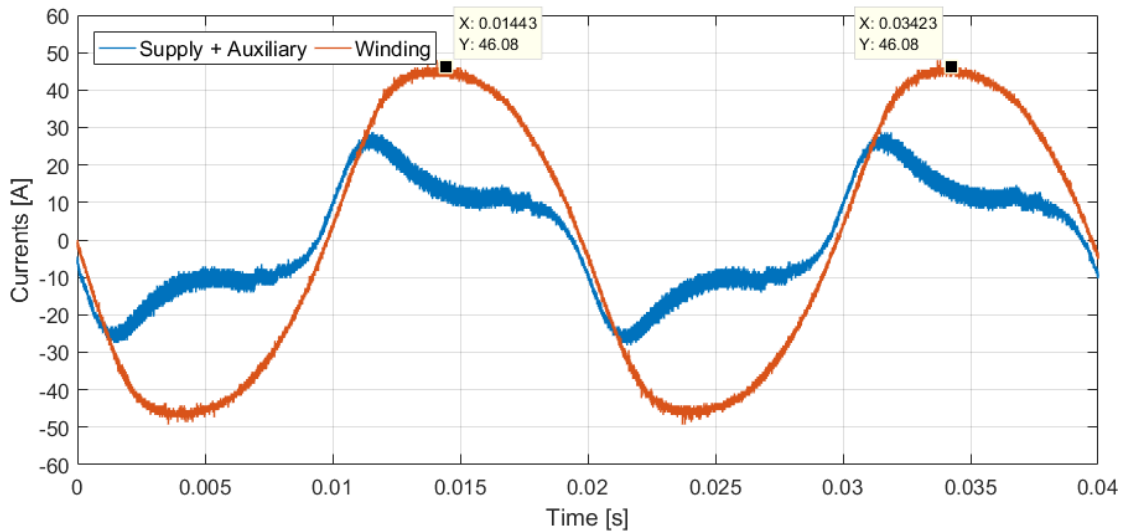


FIGURE 7.9: 30% state feedback regulator hardware supply and motor winding current response with auxiliary winding connected

Hence, no relevant information is gained by plotting the currents again for the locked rotor test with the auxiliary winding connected. Instead, the measured peak and RMS values of the total and main winding currents are provided together with the flicker test result. The total and main winding currents peaked at values of  $28.8A$  and  $48.0A$  respectively. The RMS values of the currents were found to be  $15.05A$  and  $34.13A$  respectively. The resulting starting torque was averaged over five tests and found to be  $0.7284Nm$ . The flicker test was passed and the resulting flicker test report is attached in Appendix A. The current peak and RMS values, starting torque and flicker test parameters of all controllers will be compared in more detail in the conclusion of the chapter.

### 7.3.1.3 Motor Soft-Start Hardware Results

Figure 7.10 shows a full soft-start sequence using the 30% state feedback regulator. The plot contains the total current  $i_T$  and the motor winding current  $i_L$ . Before the soft-start commences at  $t = 0s$ , the total current can be seen to consist only of the auxiliary current, as the auxiliary winding is energised before the motor soft-start. During the soft-start the supply current is reduced successfully and consistently. Towards the end of the soft-start, the main winding current reduces due to the increasing speed of the motor and the bypass relay is switched on. This completes the soft-starting sequence and connects the motor winding directly to the supply. The starting time is approximately equal to  $1.65s$  for this algorithm. Once the starting sequence is completed the total and main winding currents are not equal since the auxiliary and supply currents are out of phase. If the auxiliary current was not measured, the two plotted currents would be equal after the bypass relay is switched on. The flicker test report for this soft-start is attached in Appendix A.

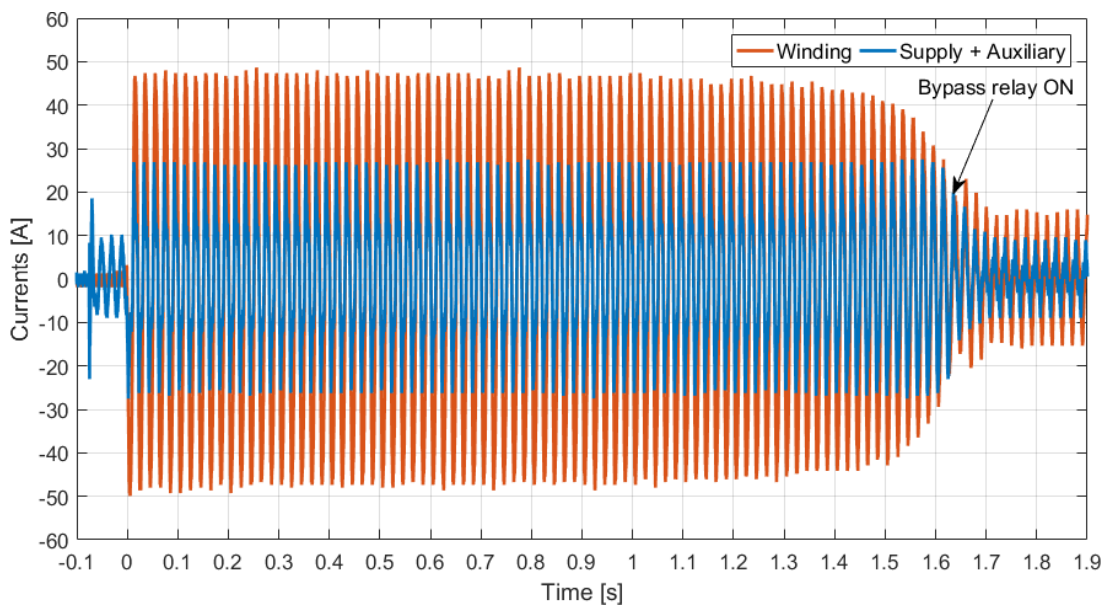


FIGURE 7.10: Motor soft-start with 30% state feedback regulator

## 7.3.2 HDMS Prototype Controller

### 7.3.2.1 Locked Rotor Simulation Results

The corresponding 30% HDMS prototype controller designed to match the state feedback regulator's motor winding current is presented in this section. It is first tested in the simulation model and the resulting duty cycle, supply and motor winding currents are shown in Figures 7.11 and 7.12 respectively.

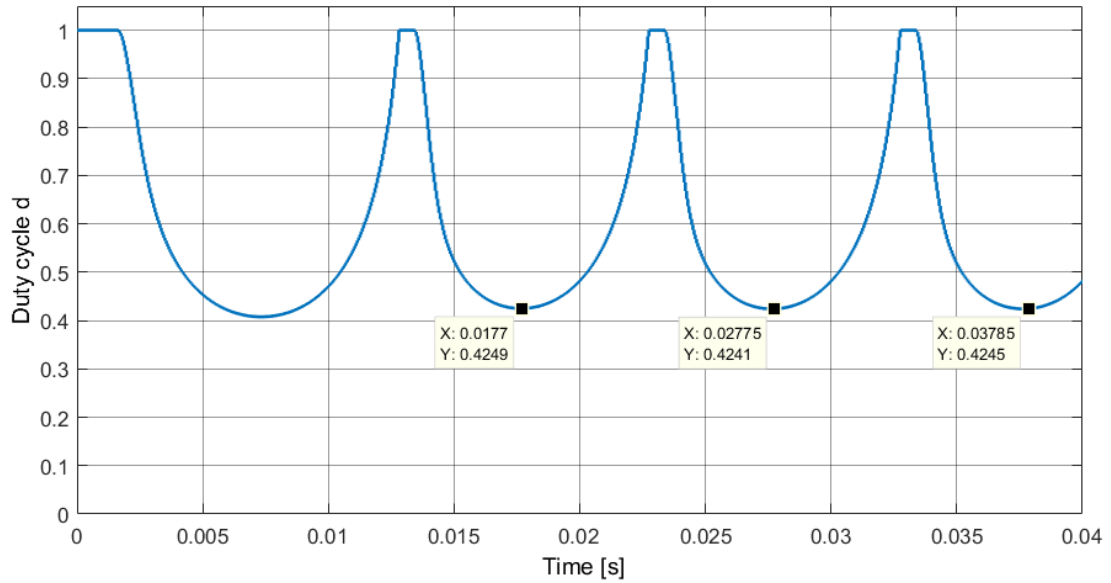


FIGURE 7.11: 30% HDMS prototype current controller simulation model duty cycle response

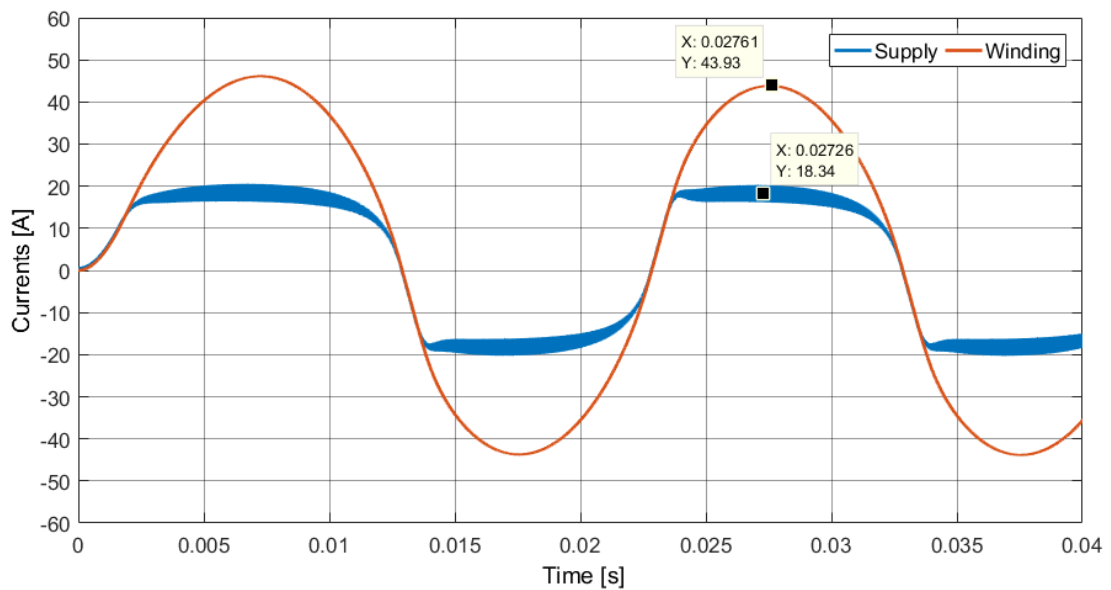


FIGURE 7.12: 30% HDMS prototype current controller simulation model supply and motor winding current response

From these figures, the duty cycle can be seen to reduce to a value of  $d = 0.42$ , which is higher than the state feedback regulator's duty cycle. The supply current reaches a value of  $i_S = 18.34A$  when the duty cycle is at its lowest. The main winding current peaks at a value of  $i_L = 43.93A$ , which is very close to the state feedback regulator's main winding current of  $i_L = 43.2A$ .

The shape of the supply current is rather flat. This supply current response was the best response obtainable considering a peak main winding current of approximately  $43.2A$  was desired in order to match the state feedback regulator. This is done in order to achieve a rather fair performance comparison of the controllers. Additionally, the constraint to remain within the regions of operation, namely to achieve a duty cycle of 1.0 before the current's zero crossover, further restricted the design of this controller.

### 7.3.2.2 Locked Rotor Hardware Results

The locked rotor test for the 30% HDMS controller was implemented on the hardware prototype to compare its performance to the simulation model and the state feedback regulator. The resulting duty cycle, supply and motor winding currents are shown in Figures 7.13 and 7.14 respectively. The duty cycle can be seen to reach a value of approximately  $d = 0.36$ . This is lower than the duty cycle obtained in the simulation model but is again higher than the state feedback regulator, which yielded a duty cycle of  $d = 0.3$ . The shape of the supply current matches the simulation model and it reaches a value of  $i_S = 19.21A$  when the duty cycle is at its lowest, compared to the simulation model's  $i_S = 18.34A$ . The main winding current peaks at a value of  $i_L = 46.72A$ , which is as expected higher than the simulation model's  $i_L = 43.93A$ . However, it only slightly deviates from the state feedback regulator's  $i_L = 46.08A$ .

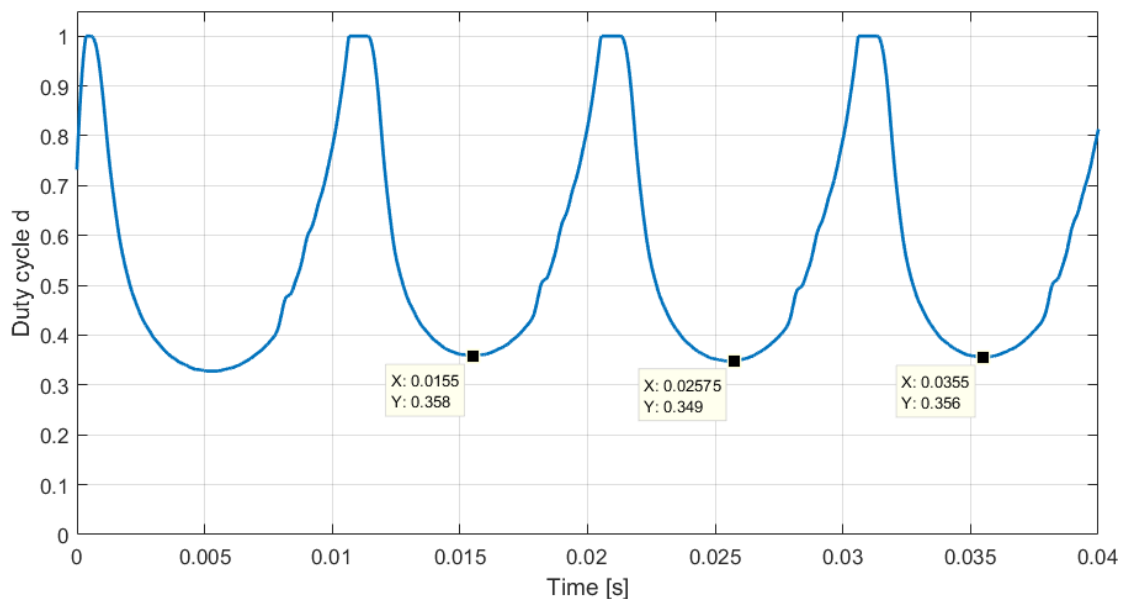


FIGURE 7.13: 30% HDMS prototype current controller hardware duty cycle response

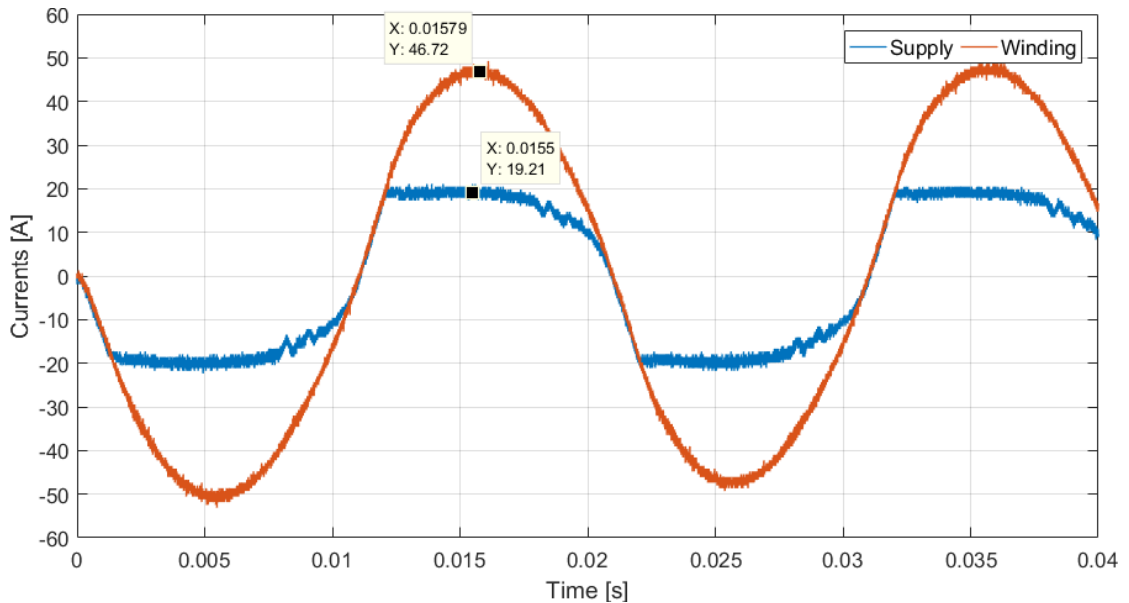


FIGURE 7.14: 30% HDMS prototype current controller hardware supply and motor winding current response

The auxiliary winding was again connected in order to measure the algorithm's starting torque and flicker test performance. The resulting total and motor winding current peak values were measured to be  $24.29A$  and  $49.92A$  respectively, while the RMS values were measured to be  $14.56A$  and  $34.64A$  respectively. The starting torque was averaged over five tests and was found to be equal to  $0.7538Nm$ . The algorithm passed the flicker test and the flicker test report is attached in Appendix A.

### 7.3.2.3 Motor Soft-Start Hardware Results

The disc brake is released in order to allow for a motor soft-start together with the auxiliary winding connected. Figure 7.15 shows both total and the motor winding currents during the motor soft-start. As can be seen during the motor starting sequence, the desired current reduction is achieved. This ensures that the supply current remains reduced throughout the motor start, while producing an amplified motor winding current. The bypass relay is switched on, connecting the motor winding directly to the supply, at approximately  $t = 1.65s$ . The algorithm passed the flicker test and the corresponding report is attached in Appendix A.

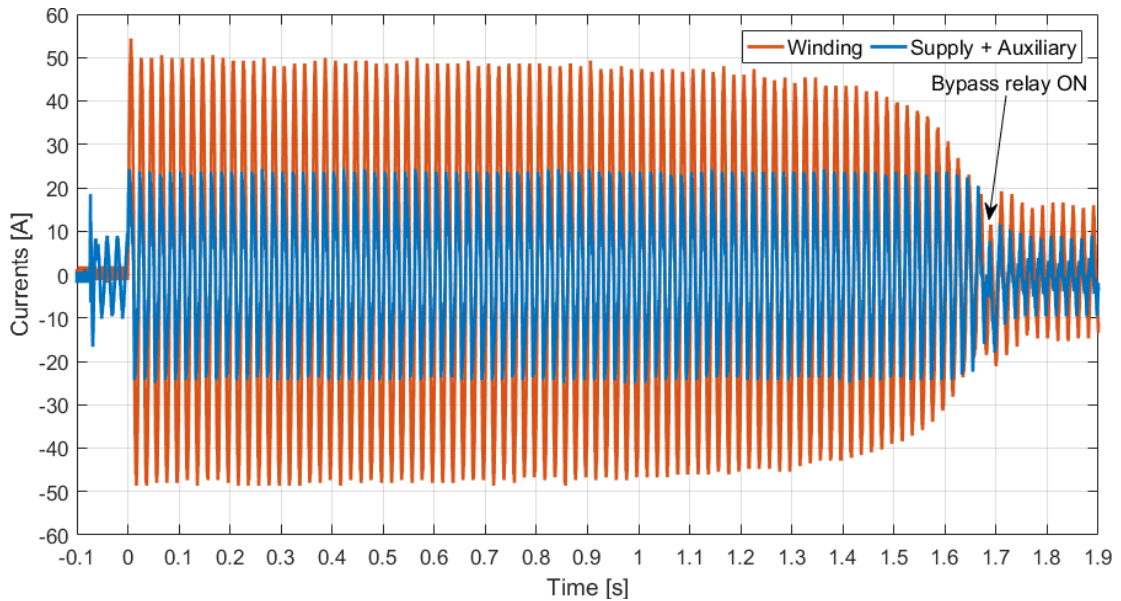


FIGURE 7.15: Motor soft-start with 30% HDMS prototype current controller

### 7.3.3 Conclusion

Table 7.2 summarises the results obtained in this section for the 30% controller designs. The state feedback regulator resulted in a higher peak total current due to the initial overshoot observed. However, the peak winding and RMS currents are comparable for both controllers with only slight deviations. This is confirmed in the algorithms' starting torques. Consequently, both algorithms resulted in similar starting times for the motor soft-start tests. Both algorithms performed similarly well in the flicker tests, remaining within  $\pm 10\%$  of each other. As both algorithms are still well within the maximum test parameters, the linearisation parameters of the controller design may be increased in order to produce a higher starting torque and a shorter motor starting time.

TABLE 7.2: 30% controller results

Parameter	SFR	HDMS
Peak total current [A]	28.80	24.29
RMS total current [A]	15.05	14.56
Peak winding current [A]	48.00	49.92
RMS winding current [A]	34.13	34.64
Starting torque [Nm]	0.7284	0.7538
Starting time [s]	1.65	1.65

## 7.4 40% Duty Cycle Controller Design

### 7.4.1 Introduction

The current controllers in this section are based on a 40% duty cycle and a supply voltage of  $v_S = 325V$  in the linearisation process of the state feedback regulator design. The resulting equilibrium point parameters of the state feedback regulator are shown in (7.3). The controller parameters for both the state feedback regulator and the HDMS prototype current controller are tabulated in Table 7.3.

$$i_S^* = 23.72A \quad (7.3a)$$

$$i_L^* = 59.31A \quad (7.3b)$$

$$v_C^* = 320.26V \quad (7.3c)$$

TABLE 7.3: 40% controller parameters

Parameter	State feedback regulator
$\zeta$ [ ]	0.02
$\omega_n$ [rad/s]	$2\pi \times 4800$
Real Pole [1/s]	-600
$K_1$ [ ]	-0.0031
$K_2$ [ ]	0.0136
$K_3$ [ ]	$-1.545 \times 10^{-5}$
$g$ [ ]	0.0222
Parameter	HDMS prototype controller
$i_{ref}$ [A]	45
$K_1$ [A]	35
$K_I$ [A <sup>-1</sup> ]	50

### 7.4.2 State Feedback Regulator

#### 7.4.2.1 Locked Rotor Simulation Results

The 40% state feedback regulator was tested in the simulation model and the resulting duty cycle and supply current together with the motor winding current are shown in Figures 7.16 and 7.17 respectively. The duty cycle can be seen to reduce up to a value of  $d = 0.51$ . The supply current peaks at 28.94A and settles

at a value of 27.09A. Due to the current amplification introduced from the reduced duty cycle, the main winding current peaks at a value of 53.39A. This motor winding current can be seen to be more sinusoidal than the supply current, which was designed to produce a flat response.

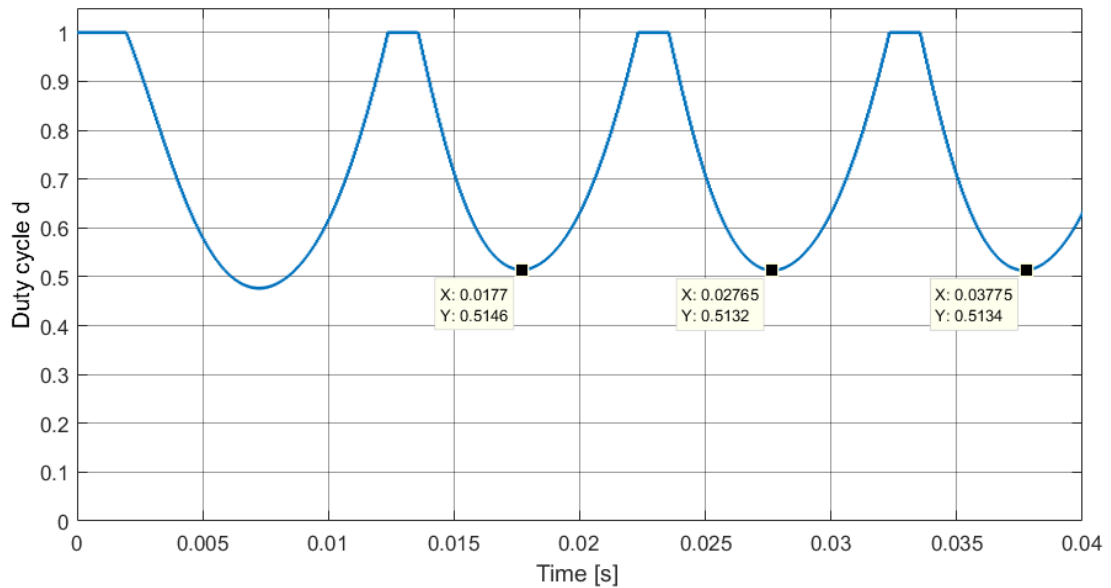


FIGURE 7.16: 40% state feedback regulator simulation model duty cycle response

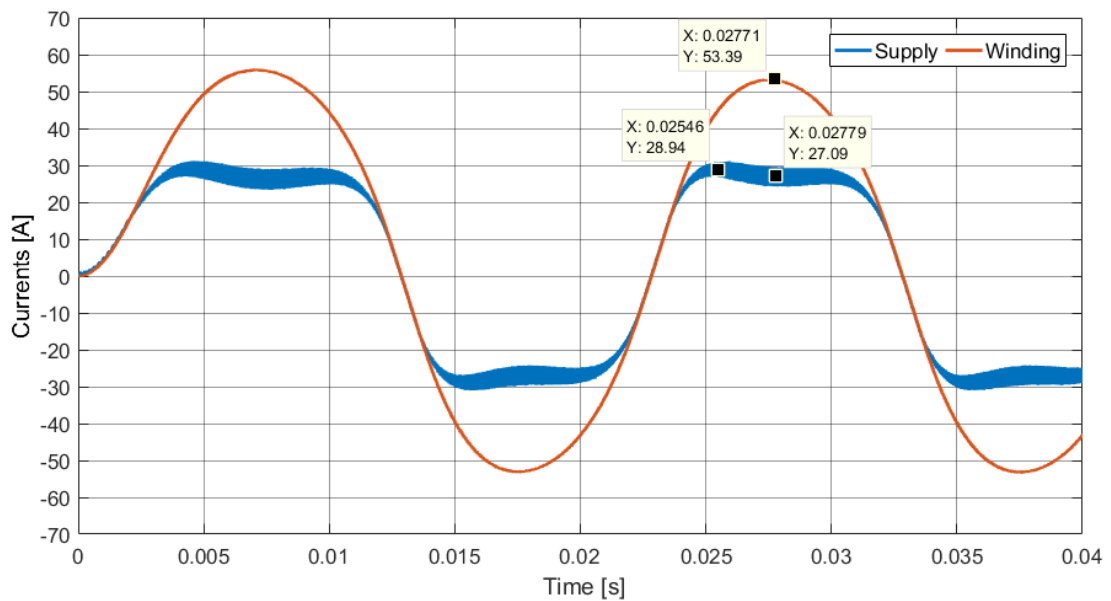


FIGURE 7.17: 40% state feedback regulator simulation model supply and motor winding current response

### 7.4.2.2 Locked Rotor Hardware Results

The locked rotor test is carried out with the hardware prototype. The resulting duty cycle and the supply and motor winding currents were captured on the microcontroller and can be seen in Figures 7.18 and 7.19 respectively. The duty cycle can be seen to reduce to a value of  $d = 0.41$ , as opposed to the  $d = 0.51$  previously seen in the simulation model.

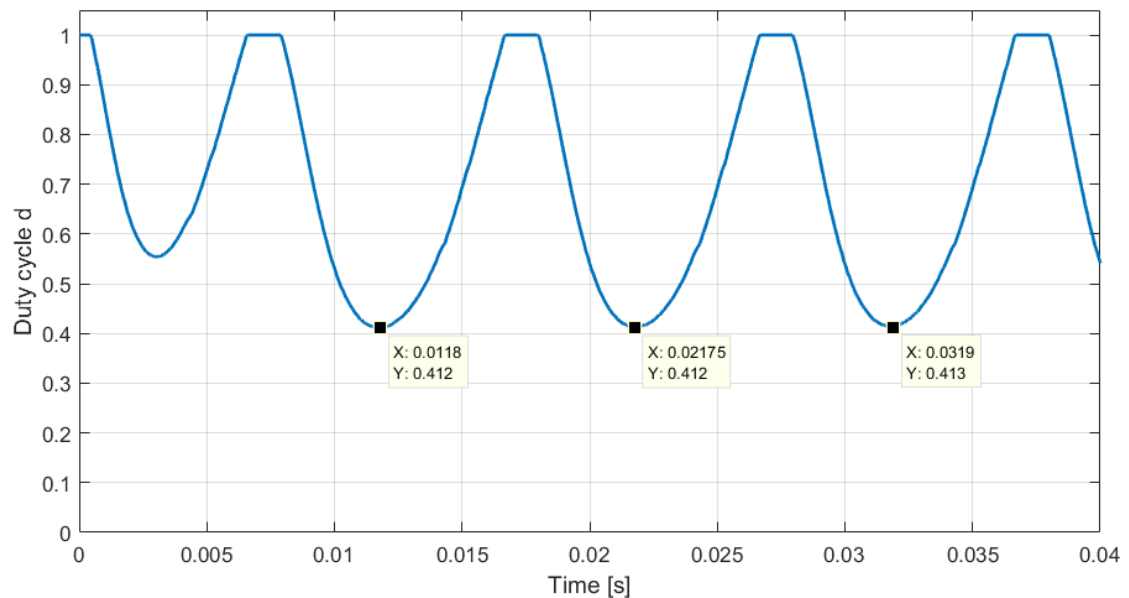


FIGURE 7.18: 40% state feedback regulator hardware duty cycle response

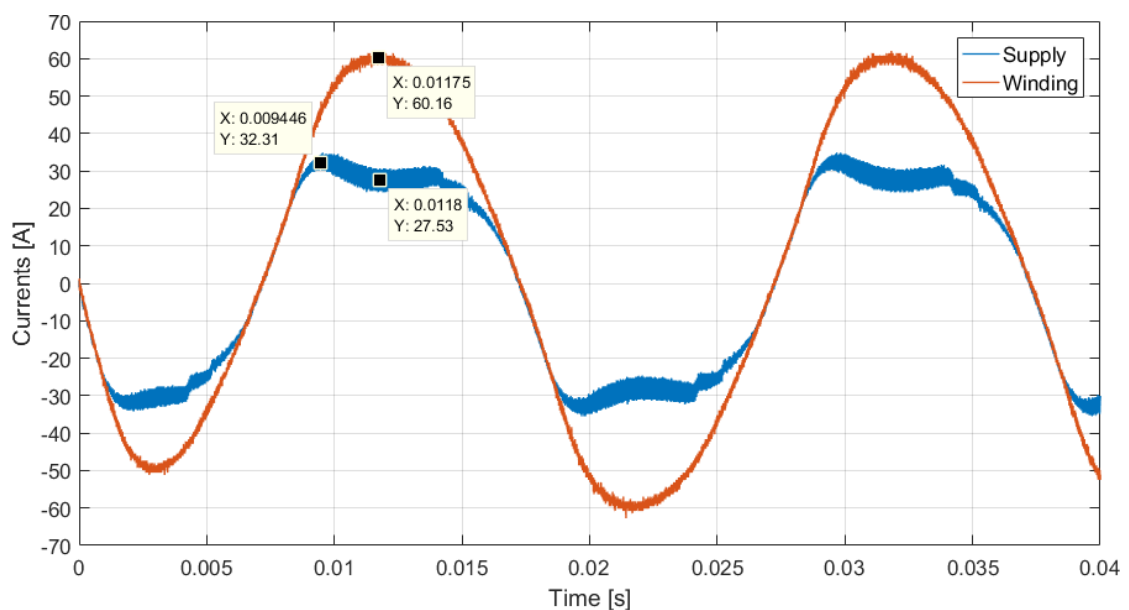


FIGURE 7.19: 40% state feedback regulator hardware supply and motor winding current response

The supply current peaks at a value of  $32.31A$  and settles at  $27.53A$ . This matches the expected result from the simulation model more closely than the duty cycle. The shape of the supply current is also similar to the simulation model. The desired supply current reduction is achieved. However, due to the discrepancy in the duty cycle a larger motor winding current is produced. The motor winding current peaks at a value of  $60.16A$  compared to the  $53.39A$  obtained from the simulation model. The auxiliary winding is connected in order to measure the starting torque and the flicker test results. The total and motor winding currents peak at  $37.74A$  and  $62.72A$  respectively. Their RMS values were found to be  $23.06A$  and  $43.29A$  respectively. The resulting starting torque was averaged over five tests and was found to be  $0.9075Nm$ . The algorithm passed the flicker test and the flicker test report is attached in Appendix A.

### 7.4.2.3 Motor Soft-Start Hardware Results

With the auxiliary winding connected, the disc brake is released and the state feedback regulator is allowed to perform a full motor soft-start. Figure 7.20 shows the total and motor winding currents during this soft-start. Throughout the soft-start, the total and motor winding currents can be seen to remain reduced as desired. At approximately  $t = 1.15s$ , the bypass relay is switched on completing the soft-start and connecting the motor winding directly to the supply. The algorithm passed the flicker test and the corresponding flicker test report is attached in Appendix A.

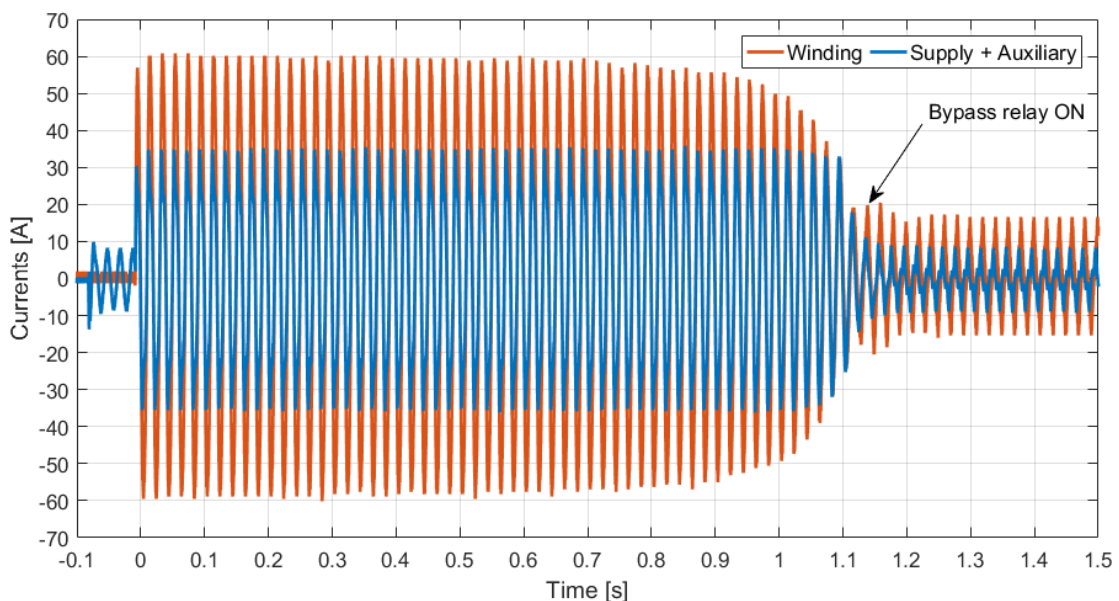


FIGURE 7.20: Motor soft-start with 40% state feedback regulator

### 7.4.3 HDMS Prototype Controller

#### 7.4.3.1 Locked Rotor Simulation Results

The corresponding 40% HDMS prototype controller is first tested in the simulation model and the resulting duty cycle and supply current together with the motor winding current are shown in Figures 7.21 and 7.22 respectively.

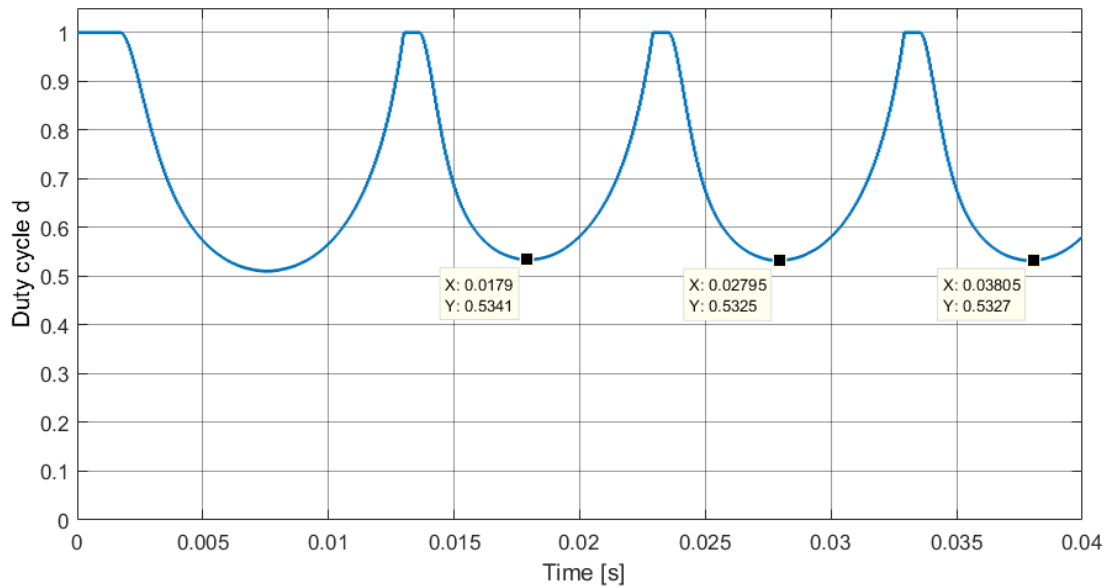


FIGURE 7.21: 40% HDMS prototype current controller simulation model duty cycle response

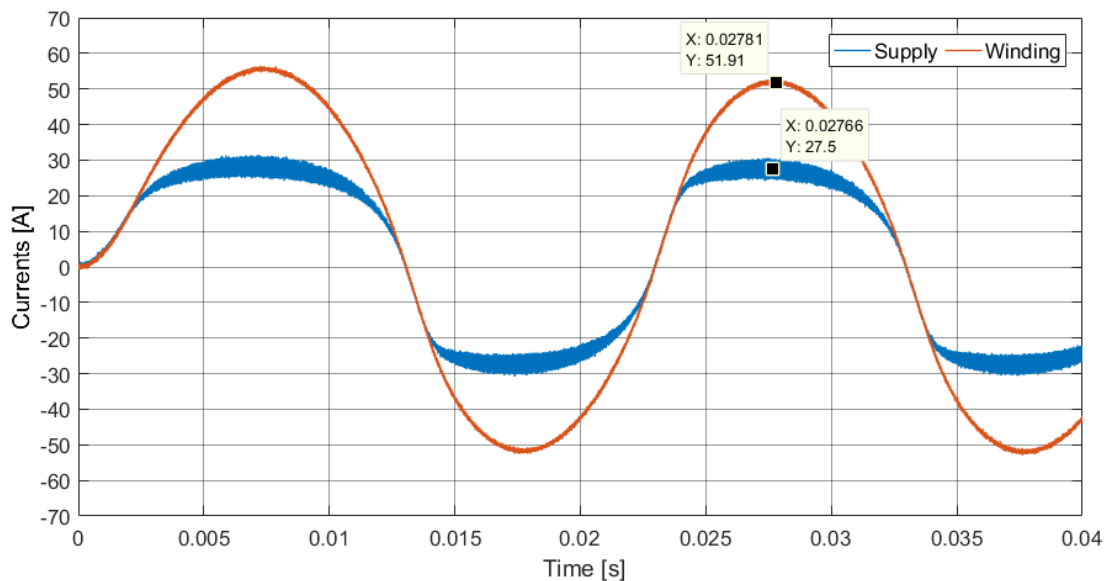


FIGURE 7.22: 40% HDMS prototype current controller simulation model supply and motor winding current response

The duty cycle can be seen to reach a value of  $d = 0.53$ . The supply current obtained from this controller is more sinusoidal than the one obtained with the state feedback regulator, which produced a flatter current. The supply current can be seen to reach a value of  $27.5A$ , with no overshoot as previously seen with the state feedback regulator. The motor winding current peaks at a value of  $51.91A$  due to the current amplification.

### 7.4.3.2 Locked Rotor Hardware Results

The locked rotor test for the 40% HDMS controller is implemented on the hardware prototype. The resulting duty cycle and supply and motor winding current responses captured by the HDMS' microcontroller are shown in Figures 7.23 and 7.24 respectively. The duty cycle can be seen to reach a value of  $d = 0.45$ , which is again lower than the 0.53 previously observed in the simulation model. The supply current also slightly deviates from the previously observed  $27.5A$  to a value of  $30.07A$ . Consequently, a larger motor winding current is produced. This peaks at a value of  $59.52A$ , compared to the  $51.91A$  from the simulation model. However, the motor winding current matches the one produced by the state feedback regulator in its amplitude.

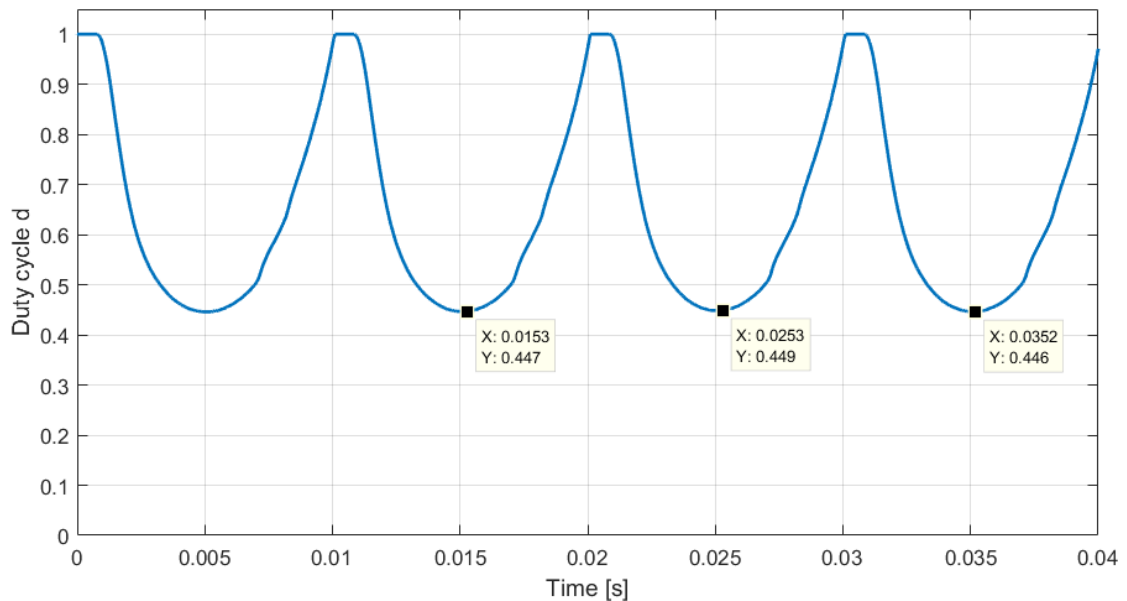


FIGURE 7.23: 40% HDMS prototype current controller hardware duty cycle response

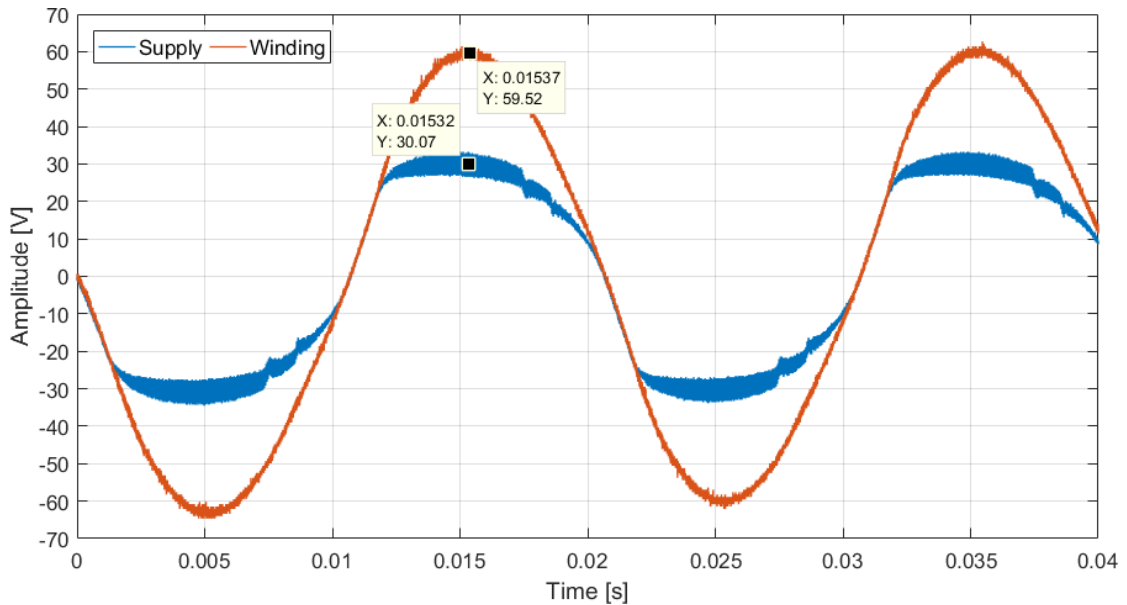


FIGURE 7.24: 40% HDMS prototype current controller hardware supply and motor winding current response

The auxiliary winding is again connected in order to measure the algorithm's starting torque and record its flicker test results. The total and motor winding currents peaked at values of  $33.60A$  and  $62.72A$  respectively. The corresponding RMS values were found to be  $22.0A$  and  $42.35A$  respectively. The algorithm's starting torque was averaged over five tests and resulted in  $0.8948Nm$ . The algorithm passed the flicker test and its flicker test report is attached in Appendix A.

#### 7.4.3.3 Motor Soft-Start Hardware Results

The disc brake is again released in order to allow for a motor soft-start together with auxiliary winding connected. Figure 7.25 shows both total and the motor winding currents during the motor soft-start. During the starting sequence, the desired current reduction is achieved, while producing an amplified motor winding current. The bypass relay is switched on, connecting the motor winding directly to the supply at approximately  $t = 1.3s$ . The algorithm passed the flicker test and the corresponding flicker test report is attached in Appendix A.

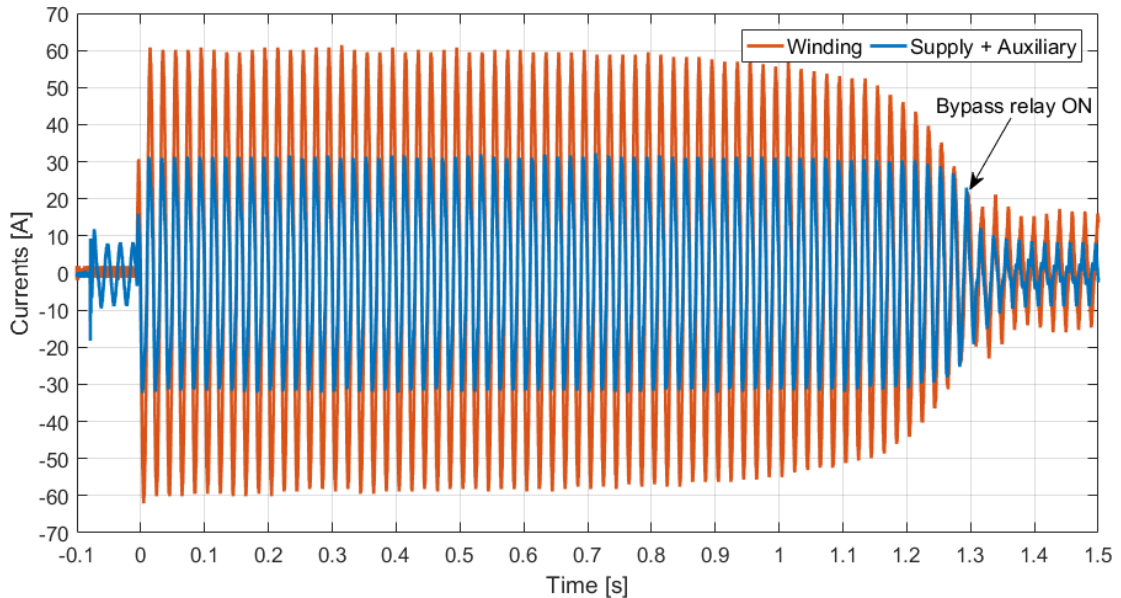


FIGURE 7.25: Motor soft-start with 40% HDMS prototype current controller

#### 7.4.4 Conclusion

Table 7.4 provides a performance summary of the 40% controller designs. The state feedback regulator again results in a larger peak total current due to its initial overshoot. The remaining parameters deviate by no more than 3% from each other. There is a discrepancy in the approximated soft-starting time. However, this may be attributed to the fact that the algorithms did not start in the same supply voltage position as they overall performed similarly. The HDMS current controller outperforms the state feedback regulator in both locked rotor and soft-starting flicker tests, which are attached in Appendix A. Both algorithms more closely approached the maximum flicker test parameters with this controller design. A further controller design is considered, however it is likely to fail the flicker tests.

TABLE 7.4: 40% controller results

Parameter	SFR	HDMS
Peak total current [A]	37.74	33.60
RMS total current [A]	23.06	22.00
Peak winding current [A]	62.72	62.72
RMS winding current [A]	43.29	42.35
Starting torque [Nm]	0.9075	0.8948
Starting time [s]	1.15	1.30

## 7.5 50% Duty Cycle Controller Design

The current controller operating point of this section is based on a 50% duty cycle and a supply voltage of  $v_S = 325V$  in the linearisation process of the state feedback regulator design. The equilibrium point values of the state variables resulting from these linearisation conditions are shown in (7.4). The controller parameters resulting from this design point are listed in Table 7.5.

$$i_S^* = 36.76A \quad (7.4a)$$

$$i_L^* = 73.53A \quad (7.4b)$$

$$v_C^* = 317.65V \quad (7.4c)$$

TABLE 7.5: 50% controller parameters

Parameter	State feedback regulator
$\zeta$ [ ]	0.02
$\omega_n$ [rad/s]	$2\pi \times 4400$
Real Pole [1/s]	-500
$K_1$ [ ]	-0.0043
$K_2$ [ ]	0.0101
$K_3$ [ ]	$-5.938 \times 10^{-6}$
$g$ [ ]	0.0125
Parameter	HDMS prototype controller
$i_{ref}$ [A]	70
$K_1$ [A]	50
$K_I$ [A <sup>-1</sup> ]	50

### 7.5.1 State Feedback Regulator

#### 7.5.1.1 Locked Rotor Simulation Results

The state feedback regulator based on the 50% duty cycle in the linearisation stage was tested in the simulation model. The duty cycle, supply and motor winding currents resulting from this test are shown in Figures 7.26 and 7.27 respectively. The duty cycle can be seen to reduce to a value of  $d = 0.65$  after the initial half cycle. The supply current is flattened as desired for the the state feedback regulator. This current peaks at a value of  $i_S = 40.0A$  without any considerable overshoot. The motor winding current peaks at  $i_L = 60.92A$  when the duty cycle is at its

lowest. It is already noticeable that the current amplification is reduced compared to the previous controller designs due to the large duty cycle. Additionally, while the regulator performs as desired in terms of the produced current shapes, their amplitudes deviate from the designed equilibrium point.

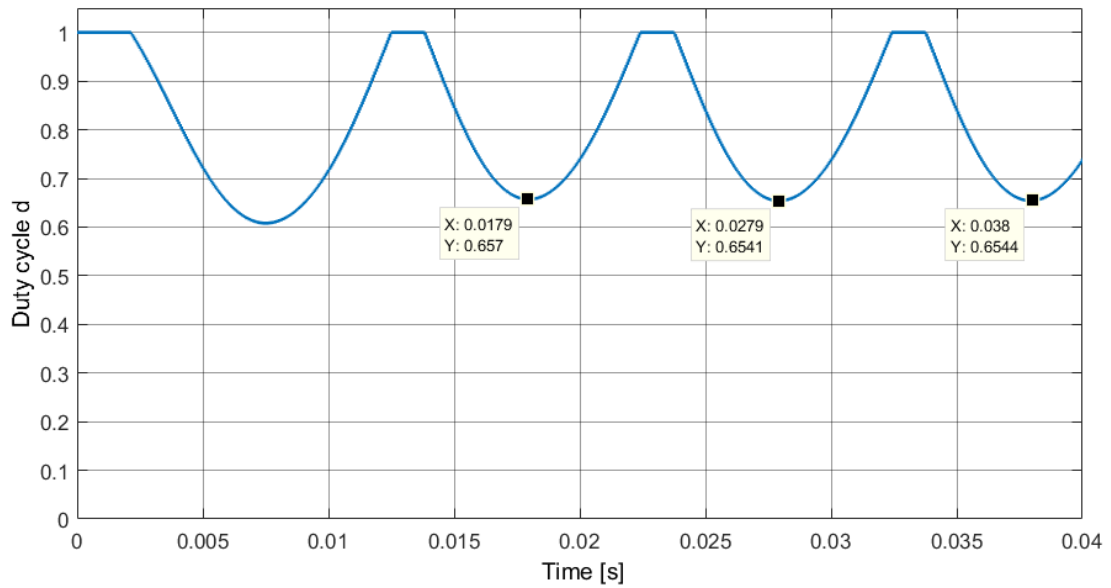


FIGURE 7.26: 50% state feedback regulator simulation model duty cycle response

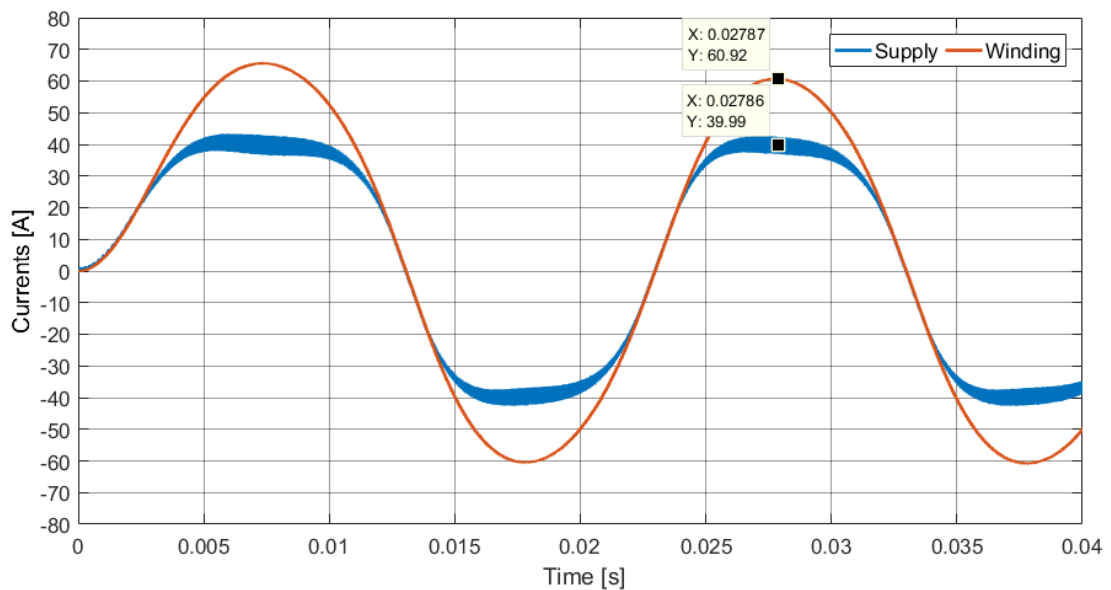


FIGURE 7.27: 50% state feedback regulator simulation model supply and motor winding current response

### 7.5.1.2 Locked Rotor Hardware Results

The locked rotor test was carried out on the hardware prototype. The duty cycle and currents for the state feedback regulator resulting from this test are shown in Figures 7.28 and 7.29 respectively. The duty cycle reduces to a value of approximately  $d = 0.53$  in the third and fourth half cycles. In the second half cycle it slightly varies to  $d = 0.51$ .

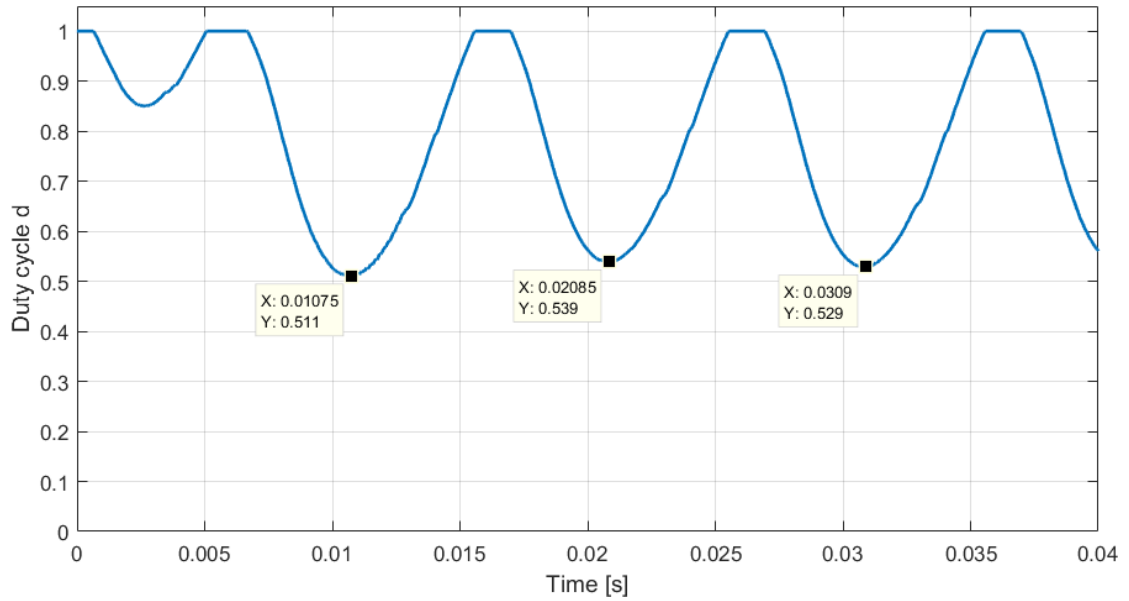


FIGURE 7.28: 50% state feedback regulator hardware duty cycle response

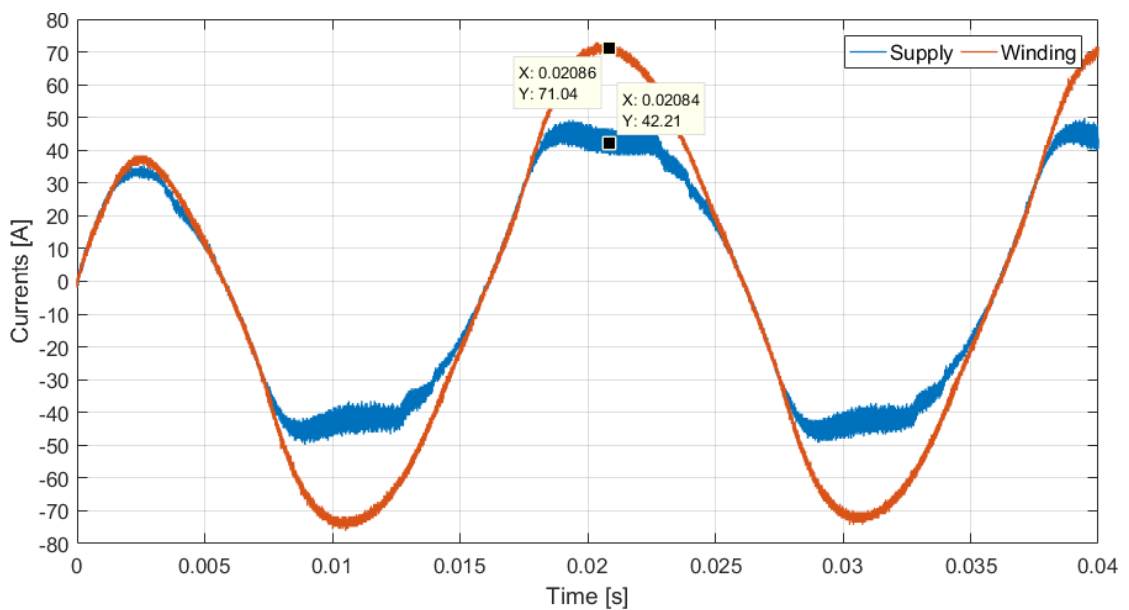


FIGURE 7.29: 50% state feedback regulator hardware supply and motor winding current response

The supply current can be seen to reach  $i_S = 42.21A$  as the duty cycle reaches its lowest value, with a minor overshoot. The motor winding current peaks at a value of  $i_L = 71.04A$ . These results deviate slightly from the simulation model but more closely match the expected values from the equilibrium point.

This test was repeated with the auxiliary winding connected and the starting torque was recorded. The total and main winding currents peaked at values of  $48.64A$  and  $73.60A$  respectively. The RMS values of the currents were found to be  $32.30A$  and  $49.10A$  respectively. The resulting starting torque was averaged over five tests and found to be  $1.1530Nm$ . The flicker test was failed and the resulting flicker test report is attached in Appendix A.

### 7.5.1.3 Motor Soft-Start Hardware Results

Figure 7.30 shows a full soft-start sequence using the 50% state feedback regulator. The algorithm successfully starts the motor with current reduction being achieved successfully and consistently during the soft-start. The starting time is approximately equal to  $1.05s$  for this algorithm. The flicker test report for this soft-start is attached in Appendix A.

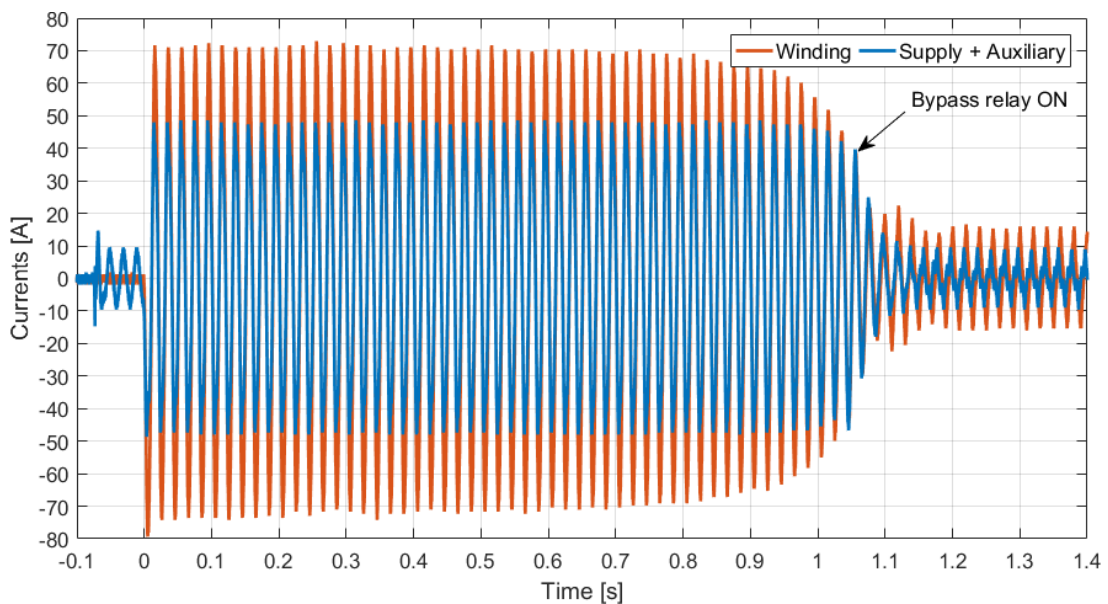


FIGURE 7.30: Motor soft-start with 50% state feedback regulator

## 7.5.2 HDMS Prototype Controller

### 7.5.2.1 Locked Rotor Simulation Results

The corresponding 50% HDMS prototype controller designed to match the state feedback regulator's motor winding current is presented in this section. It is first tested in the simulation model and the duty cycle, supply and motor winding currents resulting from this test are shown in Figures 7.31 and 7.32 respectively.

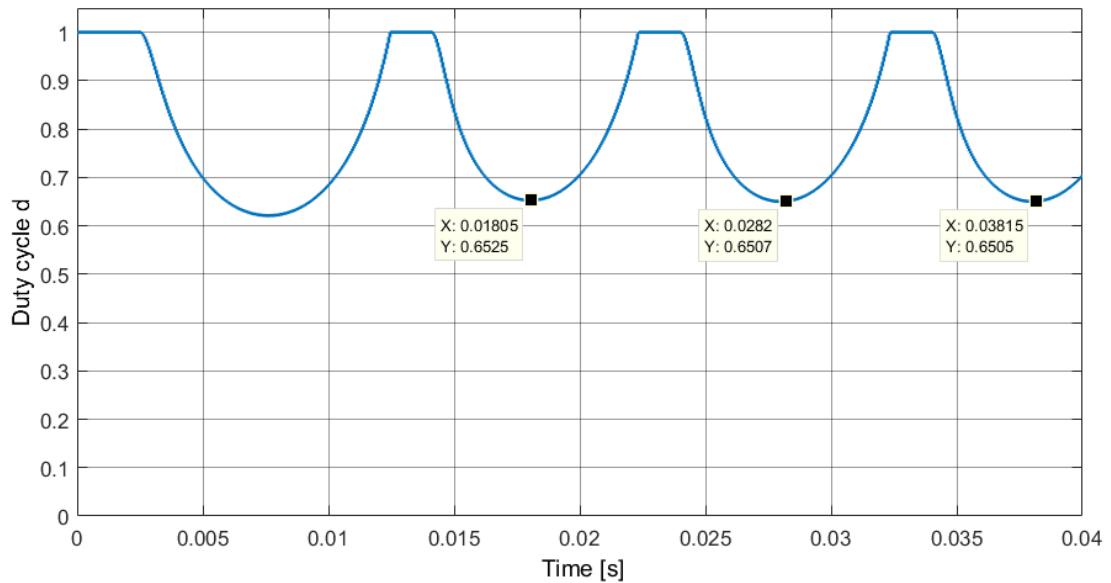


FIGURE 7.31: 50% HDMS prototype current controller simulation model duty cycle response

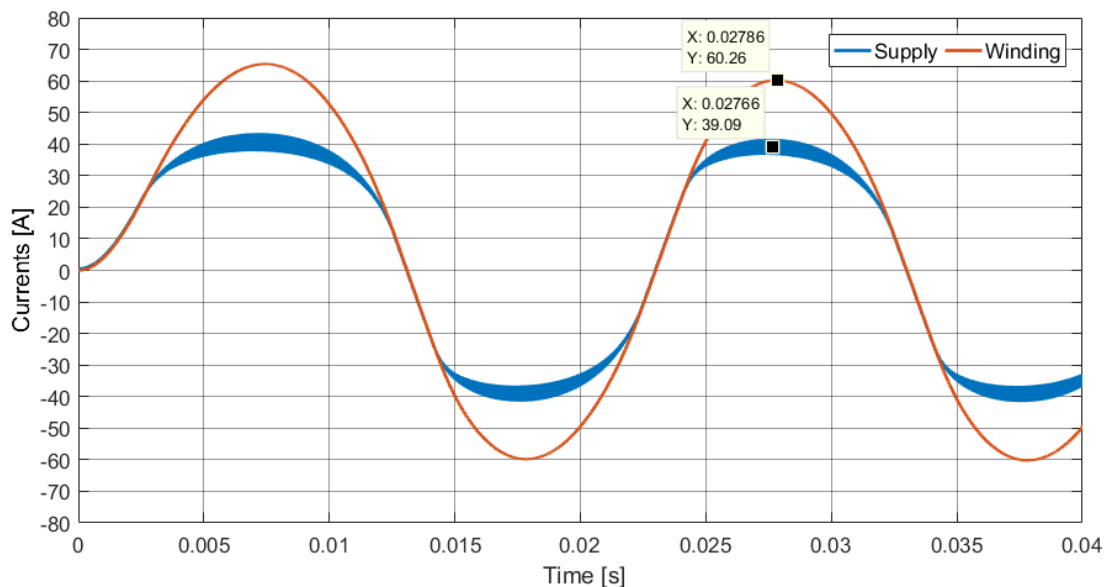


FIGURE 7.32: 50% HDMS prototype current controller simulation model supply and motor winding current response

From these figures, the duty cycle can be seen to reduce to a value of  $d = 0.65$ , which is equal to the state feedback regulator's simulation model duty cycle. The supply current reaches a value of  $i_S = 39.09A$  when the duty cycle is at its lowest. The main winding current peaks at a value of  $i_L = 60.26A$ . The currents are also identical to the state feedback regulator's currents of  $i_S = 40.0A$  and  $i_L = 60.92A$ . The shape of the supply current peak is more rounded off compared to the state feedback regulator's flat peak. Due to the high duty cycle the current amplification is again lower than in the previous controller designs, as expected.

### 7.5.2.2 Locked Rotor Hardware Results

The locked rotor test for the 50% HDMS controller was implemented on the hardware prototype to compare its performance to the simulation model and to the state feedback regulator. The duty cycle, supply and motor winding currents resulting from this test are shown in Figures 7.33 and 7.34 respectively. The duty cycle can be seen to reach a value of approximately  $d = 0.56$ . This is lower than the simulation model duty cycle  $d = 0.65$ , which results in larger current amplification. The supply current shape matches the simulation model and it reaches a value of  $i_S = 43.55A$  with the duty cycle at its lowest, compared to the simulation model's  $i_S = 39.09A$ . The main winding current peak occurs at a value of  $i_L = 69.12A$ , which is as expected higher than the simulation model's  $i_L = 60.25A$  due to the increased current amplification.

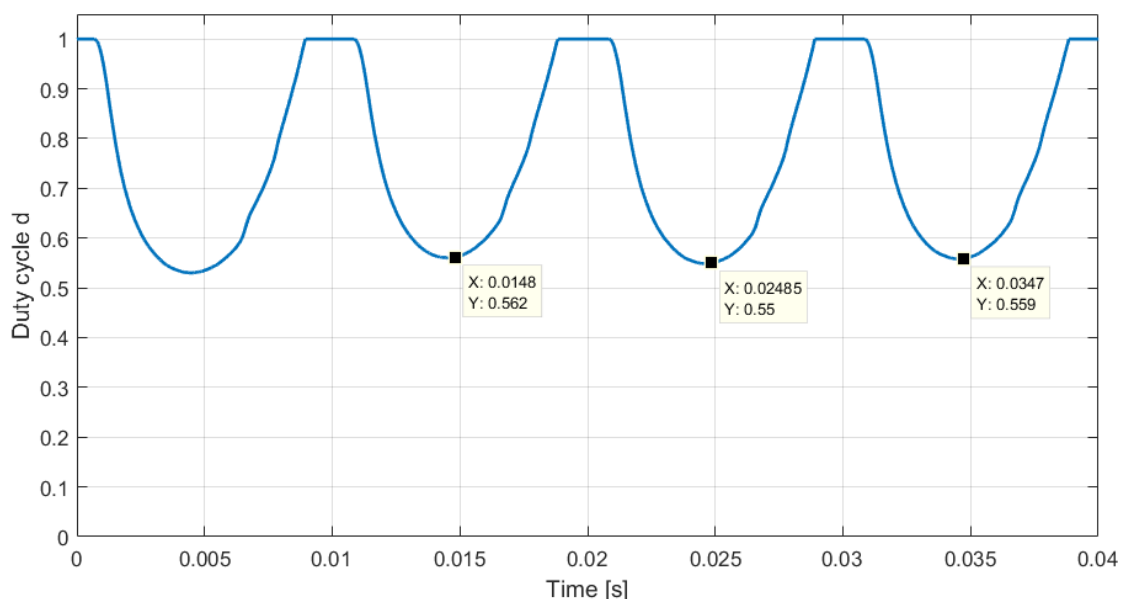


FIGURE 7.33: 50% HDMS prototype current controller hardware duty cycle response

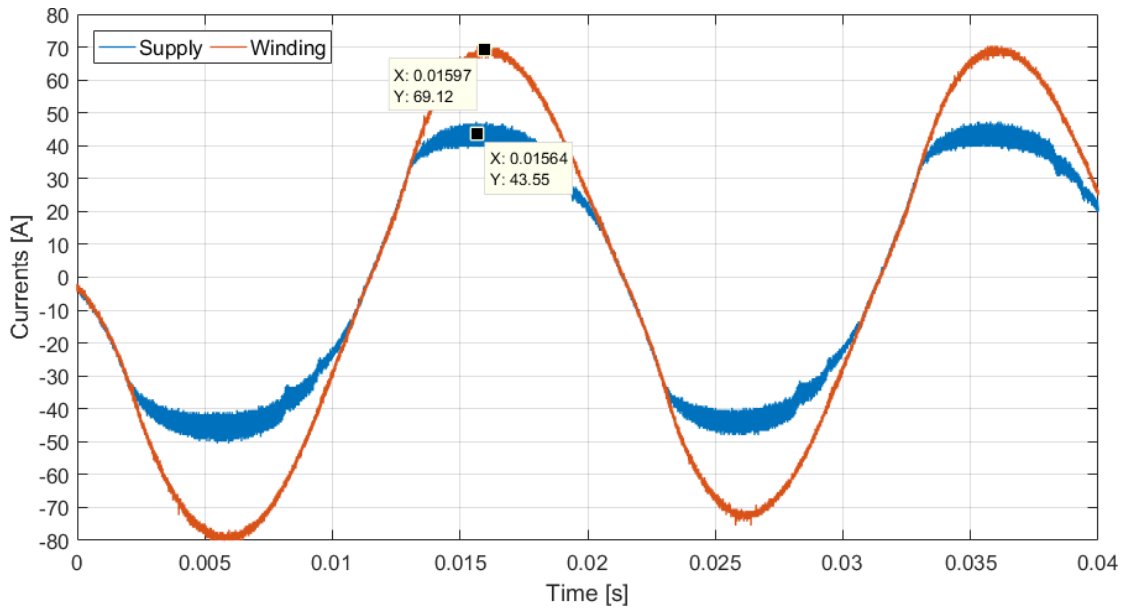


FIGURE 7.34: 50% HDMS prototype current controller hardware supply and motor winding current response

The locked rotor test was repeated with the auxiliary winding connected in order to measure the algorithm's starting torque. The total and main winding currents peaked at values of  $44.16A$  and  $69.76A$  respectively. Their RMS values were found to be  $30.52A$  and  $47.32A$  respectively. The starting torque, which was averaged over five locked rotor tests was found to be  $1.0974Nm$ . The algorithm failed the flicker test for the locked rotor scenario and the corresponding flicker test report is attached in Appendix A.

### 7.5.2.3 Motor Soft-Start Hardware Results

The disc brake is released in order to allow for a motor soft-start together with auxiliary winding connected. Figure 7.35 shows both total and the motor winding currents during the motor soft-start. The bypass relay is switched on, connecting the motor winding directly to the supply, at approximately  $t = 1.1s$ . The algorithm failed the flicker test and the corresponding report is attached in Appendix A.

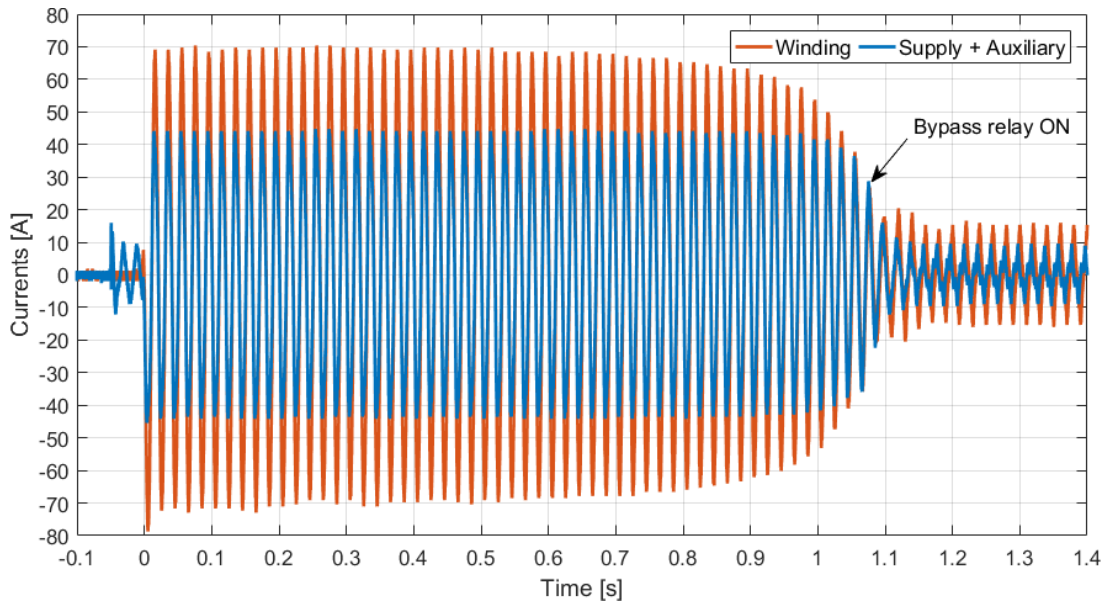


FIGURE 7.35: Motor soft-start with 50% HDMS prototype current controller

### 7.5.3 Conclusion

Table 7.6 shows the controller performances for this controller design. Once more the state feedback regulator results in a larger peak total current. Additionally, the state feedback regulator also resulted in larger RMS currents and starting torque. However, the deviation does not exceed 6%. Consequently the state feedback regulator also resulted in a slightly shorter soft-starting time. Both algorithms failed the locked rotor and soft-starting flicker tests, making further controller designs unnecessary.

TABLE 7.6: 50% controller results

Parameter	SFR	HDMS
Peak total current [A]	48.64	44.16
RMS total current [A]	32.30	30.52
Peak winding current [A]	73.60	69.76
RMS winding current [A]	49.10	47.32
Starting torque [Nm]	1.1530	1.0974
Starting time [s]	1.05	1.10

## 7.6 Robustness Testing

### 7.6.1 Introduction

In this section, the 40% HDMS prototype current controller is investigated for its robustness to changes in the motor winding parameters and changes in the grid impedance. The 40% HDMS controller was considered as it outperformed the state feedback regulator, which was concluded in Section 7.4.4. The controller robustness testing was carried out in the simulation model established in Chapter 3.

Carrying out the robustness testing on the locked rotor motor winding without the auxiliary winding is sufficient, as the auxiliary winding has no effect on the control algorithm. Hence, if the algorithm remains stable during this test scenario, it will also remain stable in the actual application with the auxiliary winding connected. However, the deviations in the motor winding and grid impedance parameters considered for the robustness testing may affect the controller's starting and flicker test performances.

### 7.6.2 50% increase in motor winding parameters

The 40% HDMS current controller was tested for a 50% increase in the RL parameters of the motor winding. This results in a motor winding of resistance and inductance:

$$R_2 = 3.24\Omega \quad (7.5a)$$

$$L_2 = 17.48mH \quad (7.5b)$$

Figures 7.36 and 7.37 provide the response of the duty cycle and the supply and motor winding currents due to the 50% increase in the motor winding parameters. The duty cycle, due to the increased motor winding impedance, now reduces less and reaches a value of  $d = 0.65$ , compared to the duty cycle of  $d = 0.53$  observed with the original motor winding parameters. The supply current in Figure 7.37 reaches a slightly lower value of  $i_S = 26.52A$ , compared to the  $i_S = 27.5A$  of the original motor winding parameters. The changes in the supply current and more importantly the duty cycle are reflected in the motor winding current. The current can be seen to now peak at  $i_L = 41.02A$ , compared to the previous  $i_L = 51.91A$ . This occurs due to the reduced amplification resulting from a higher duty cycle.

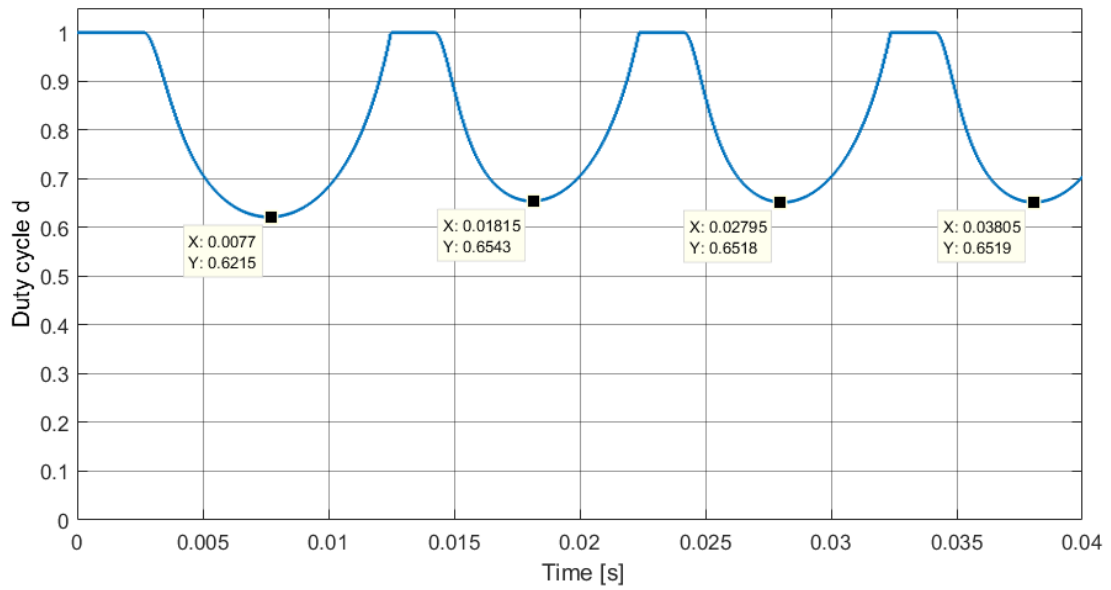


FIGURE 7.36: Duty cycle response for 50% increase in motor winding parameters

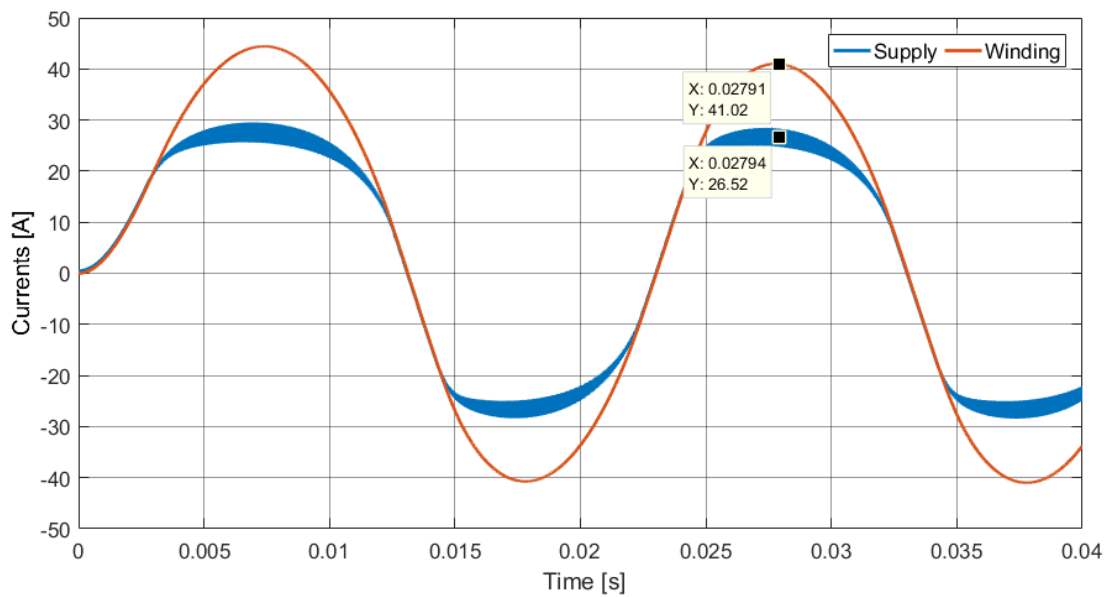


FIGURE 7.37: Supply and motor winding currents response for 50% increase in motor winding parameters

### 7.6.3 50% reduction in motor winding parameters

The 40% HDMS current controller was tested for a 50% reduction in the motor winding RL parameters, resulting in a motor winding resistance and inductance:

$$R_2 = 1.08\Omega \quad (7.6a)$$

$$L_2 = 5.83mH \quad (7.6b)$$

Figures 7.38 and 7.39 show the response of the duty cycle and the supply and motor winding currents due to a 50% reduction in the motor winding parameters. The duty cycle now reduces to a value of  $d = 0.41$  due to the lower motor winding impedance, compared to the original  $d = 0.53$ . The supply current also reaches a higher value of  $i_S = 34.98A$ , compared to  $i_S = 27.5A$ . Subsequently, the motor winding current is more amplified and peaks at a value of  $i_L = 83.86A$ .

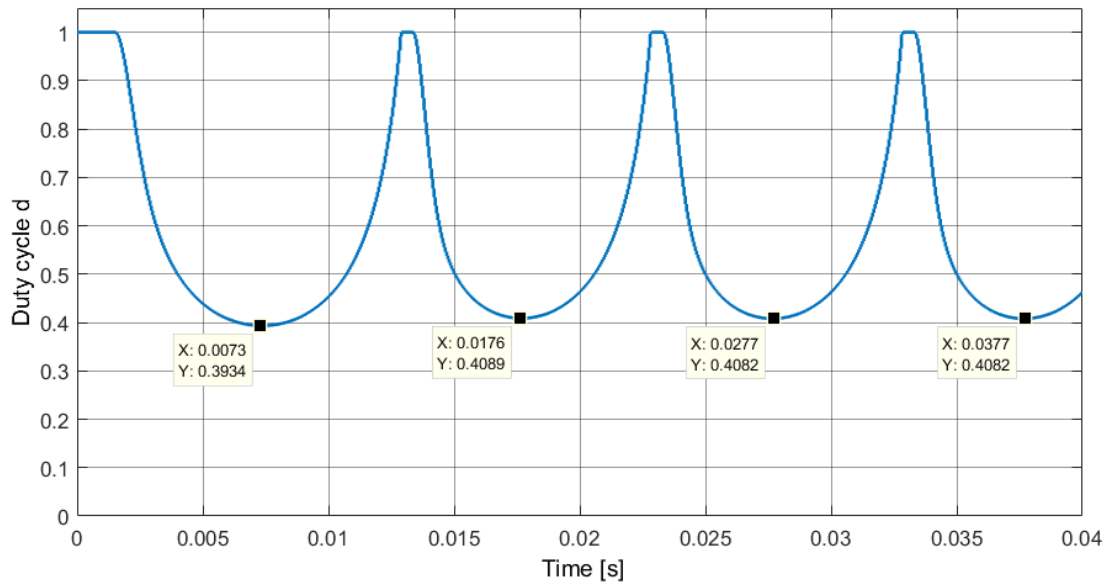


FIGURE 7.38: Duty cycle response for 50% reduction in motor winding parameters

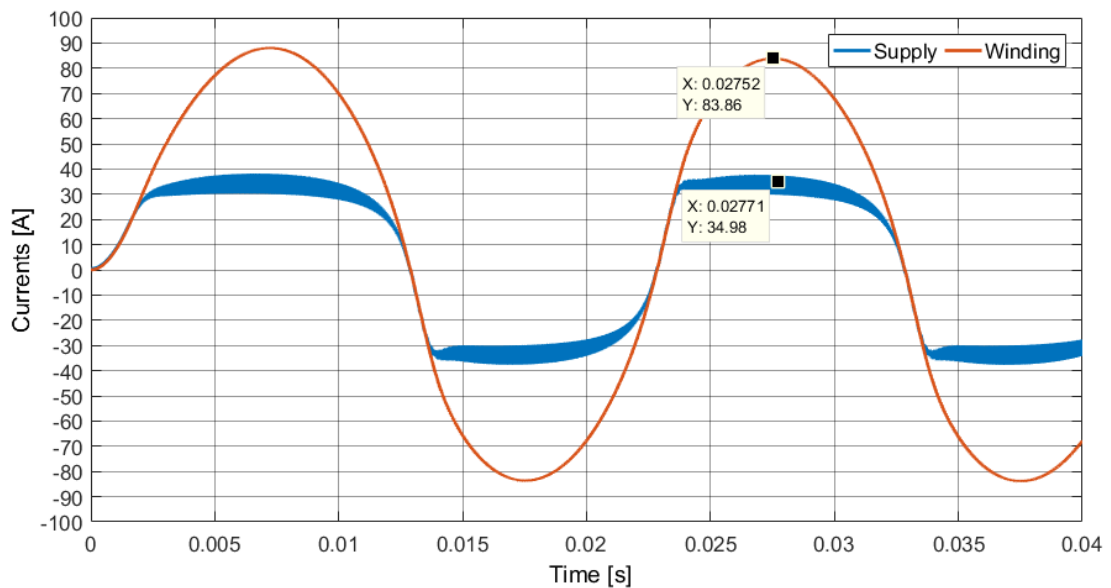


FIGURE 7.39: Supply and motor winding currents response for 50% reduction in motor winding parameters

The 40% HDMS current controller still operates in a stable manner, however the duty cycle is saturated at  $d = 1.0$  for only a short amount of time. This could result in the current controller not entering region 2 early enough, causing the HDMS switching devices to switch during the motor winding current zero-crossing. Hence, if the motor winding parameters are to reduce even further, the controller parameters  $i_{ref}$ ,  $K_1$  and  $K_I$  should be re-adjusted in order to avoid this.

#### 7.6.4 Addition of grid impedance

A worst case grid impedance equal to  $2 \times Z_{test}$  was connected between the power source and the HDMS prototype controller. This was added in addition to the already present LC filter resistance and inductance and results in (7.7). The grid impedance introduced by  $Z_{test}$  is  $Z_{test} = 0.25\Omega + j0.25\Omega$ , which at 50Hz results in an inductance of  $L_{test} = 800\mu H$ .

$$R'_1 = R_1 + 2 \times R_{test} = 0.2\Omega + 2 \times 0.25\Omega = 0.7\Omega \quad (7.7a)$$

$$L'_1 = L_1 + 2 \times L_{test} = 190\mu H + 2 \times 800\mu H = 1.79mH \quad (7.7b)$$

Figure 7.40 shows the supply and motor winding currents with the introduction of  $2 \times Z_{test}$ . This shows that the 40% HDMS current controller goes unstable, resulting in both currents exhibiting oscillations of increasing amplitude. This occurs as the introduction of  $2 \times L_{test}$  reduces the LC filter resonance to 1.735kHz.

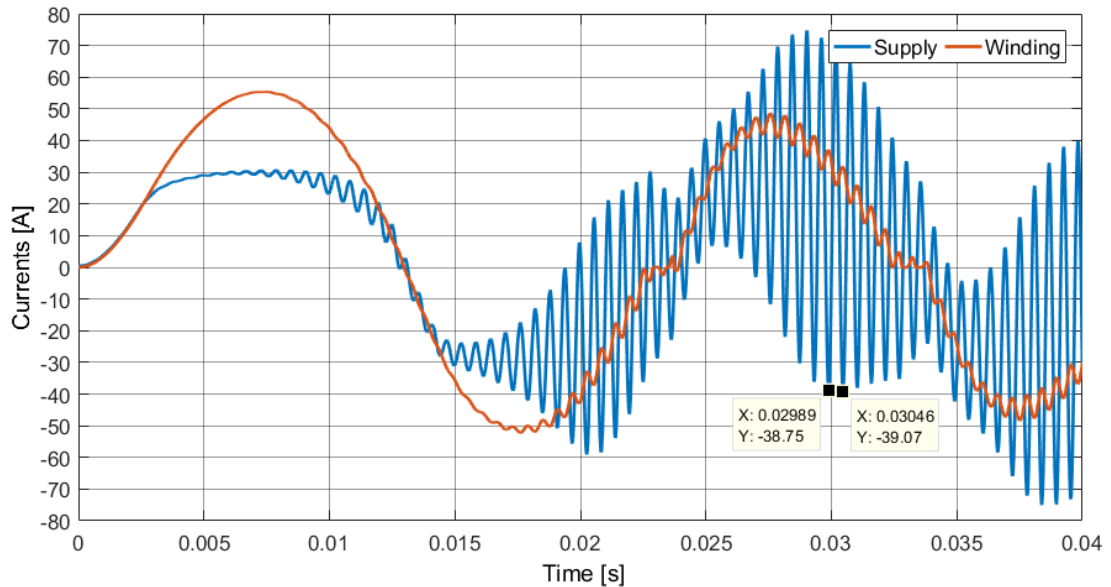


FIGURE 7.40: Supply and motor winding currents response for  $2 \times Z_{test}$

In order to avoid excitation of the new LC filter frequency, the HDMS current controller parameters  $K_I = 35A$  and  $K_I = 50A^{-1}$  were reduced to  $K_I = 25A$  and  $K_I = 20A^{-1}$ . The resulting response of the duty cycle and the supply and motor winding currents are shown in Figures 7.41 and 7.42 respectively.

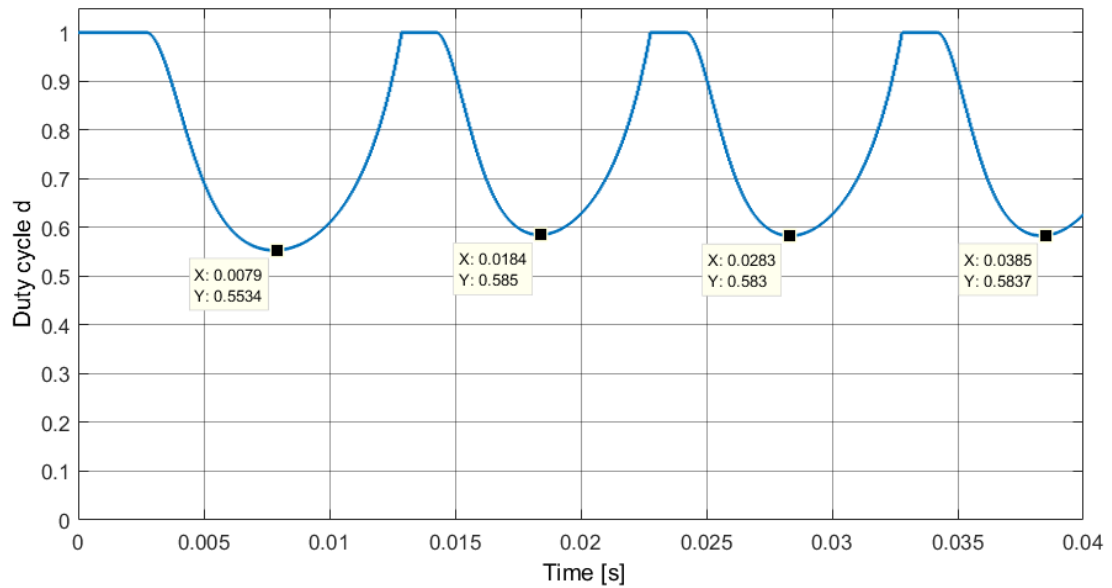


FIGURE 7.41: Duty cycle response for  $2 \times Z_{test}$  with new  $K_I$  and  $K_I$

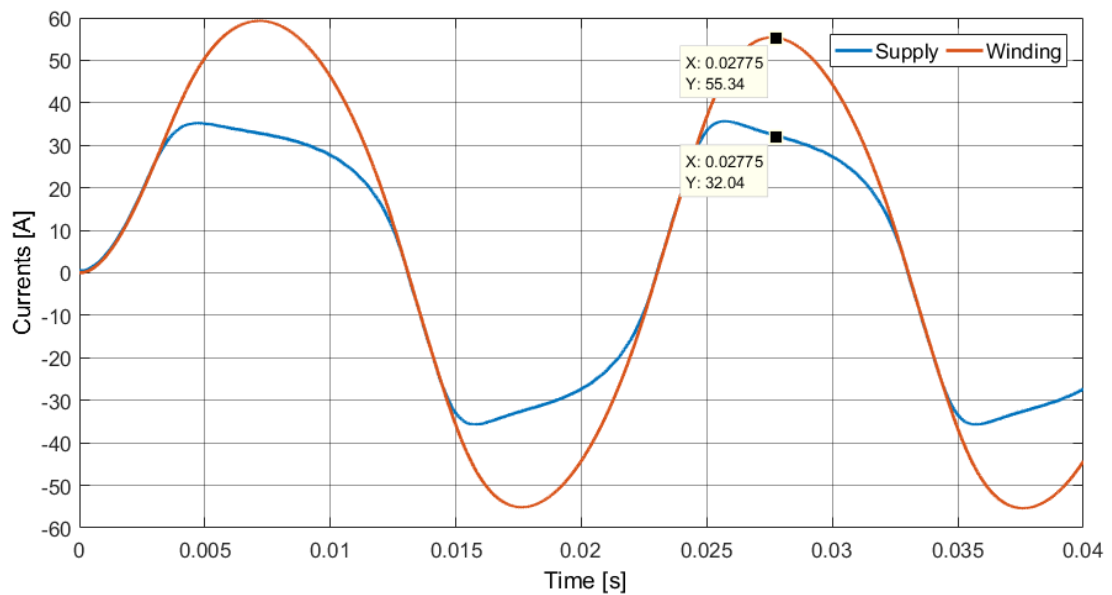


FIGURE 7.42: Supply and motor winding currents response for  $2 \times Z_{test}$  with new  $K_I$  and  $K_I$

The current controller can be seen to remain stable with the reduced parameters. The duty cycle reaches a value of approximately  $d = 0.58$ , as opposed to the original  $d = 0.53$ . The new controller parameters also affect the supply current shape, resulting in a larger supply current  $i_S = 32.04A$ , compared to  $i_S = 27.5A$ . The motor winding current peaks at  $55.34A$ , which is larger than the  $i_L = 51.91A$  observed with the original parameters. The now reduced LC filter resonance frequency also appears to filter out the 20kHz switching in the supply current.

## 7.7 Conclusion

This chapter has covered the controller performance tests carried out for this dissertation. Three controller settings were proposed and tested for the state feedback regulator and HDMS prototype current controller. These controller settings were based on the linearisation process of the state feedback regulator, for which a duty cycle of 30%, 40% and 50% was considered. The HDMS current controller was then adjusted in its parameters in order to produce an equivalent motor winding current. Both control algorithms were designed and then tested in the simulation model of Chapter 3. The simulation model's response was confirmed in the hardware test setup using the locked rotor test. In all three controller settings, some deviations were observed in the supply current and the duty cycle responses. The deviations remained within 20% with the hardware setup always resulting in a lower duty cycle. This consequently resulted in larger motor winding currents.

All three settings were tested for their resulting starting torque and for their soft-starting performance. While doing so, flicker tests were also carried out in order to investigate the control algorithms' effect on the supply network. Additionally, a direct on line start was also carried out to provide a contrast to the control algorithms' performances.

The tests carried out in this chapter showed that both control algorithms performed similarly well for the 30% controller setting. From the flicker test results, which both control algorithms passed, it was also concluded that their supply current may be further increased. Both control algorithms also performed similarly well for the 40% controller setting, with the HDMS current controller slightly outperforming the state feedback regulator in the flicker tests. However, both algorithms passed the flicker tests. From the 50% controller design tests it was concluded that this

controller setting did not pass the flicker tests. The controller setting tests have shown that while a higher duty cycle results in a larger motor winding current, the current amplification is reduced. Hence, a larger supply current is required, which affects the controllers' flicker test performance. The best trade-off between a sufficiently large motor winding current amplification, without violating the flicker test parameters, was obtained with the 40% controller setting. The HDMS 40% current controller resulted in a soft-starting time of approximately 1.3s with a starting torque of 0.8948Nm. A direct on line start results in a starting time of approximately 0.67s with a starting torque of 2.25Nm. However, the direct on line start results in a peak and RMS supply current of 109.44A and 71.93A respectively, in contrast to the HDMS' 33.60A and 22.00A. This is also reflected in the direct on line start's flicker test results, which fails by a significant margin.

The 40% HDMS algorithm was tested for robustness, with changes in the motor winding and line impedance parameters being considered. For the changes in the motor winding parameters of  $\pm 50\%$ , the current controller remained operational. However, attention must be paid to region 2 with reduced motor winding parameters. An adjustment in the controller parameters  $K_1$  and  $K_I$  may be required to ensure that the controller enters region 2 at a sufficiently high value of the motor winding current  $i_L$ . Increasing the grid impedance for robustness testing has shown that this lowers the resonance frequency of the LC filter. This may cause the current controller to excite the LC filter resonance frequency, potentially causing instability of the current controller. Reducing the controller parameters  $K_1$  and  $K_I$  has been shown to be effective to ensure stability of the controller, however this may alter its performance.

# Chapter 8

## Conclusion

The aim of this dissertation was to carry out a stability analysis of the HDMS prototype's current control system. The HDMS is based on the Buck converter principle, which is usually applied to DC converters. The hardware circuit is extended to allow the application of the Buck converter principle for positive and negative currents. The HDMS contains an LC input filter for supply current ripple reduction and dedicated regions of operation, which allows to apply the Buck converter principle to an application sourced by an alternating supply voltage. Using this operating principle, it introduced a novel approach to soft-starting a single-phase induction motor without the use of a starting capacitor. The stability of the existing HDMS current control system was thoroughly analysed. Furthermore, an alternative current controller was developed and the performance of both current controllers was compared through several tests.

Chapter 3 introduced a Matlab Simulink simulation model based on the HDMS power electronics components, which was used throughout the dissertation. In order to accurately model the HDMS prototype, the motor winding parameters of the single-phase induction motor used in this dissertation were obtained through a low-voltage test. The control algorithm in this simulation model was implemented in the digital time domain, emulating the behaviour of the HDMS prototype's microcontroller. The established simulation model was explained in detail, including the procedure of obtaining the 2.3kHz low-pass filter characteristic of the voltage and current data acquisition channels.

The stability of the HDMS prototype current control system was analysed in Chapter 4. The Buck converter circuit was first expressed in state space and was found to be non-linear due to the multiplication of state variables in the system's

state equations. The non-linear system state equations were implemented in a Simulink simulation model.

The closed-loop system, consisting of the Buck converter circuit and the HDMS prototype current controller, was analysed for its stability next. This was again expressed in state space and implemented in a simulation model. The system was found to enter non-decaying oscillations of a fixed frequency of 5.325kHz, which represents the input LC filter resonance frequency of the Buck converter circuit. The supply voltage, at which the linearised system entered instability was identified to be  $v_S = 55.1V$ . The non-linear system was found not to go unstable, but rather enter a stable limit cycle. The occurrence of this limit cycle was also confirmed in the component-level simulation model. A supply voltage  $v_S = 124V$  caused the system to enter the limit cycle. The discrepancy in the supply voltage at which the system enters the limit cycle, was attributed to the fact that the component-level simulation model implemented a discrete time control algorithm and was not based on the average Buck converter model, hence using non-ideal switching devices. However, it was concluded that the actual application does not enter a limit cycle due to the 2.3kHz low-pass filters in the microcontroller data acquisition.

Chapter 5 presented the configuration of the hardware components used for this dissertation. The test setup used to carry out locked rotor tests on the single-phase induction motor was also presented. Furthermore, the calibration process of the load cell used to measure the motor's starting torque during the locked rotor tests was explained.

The state feedback regulator, which represents the dissertation's alternative current controller for the HDMS was proposed and tested in Chapter 6. The controller's methodology and design procedure were explained in this chapter. The controller was initially designed and then tested for a step in the reference supply current to verify the controller's functionality. For the design procedure, a direct pole placement approach was used. When the controller was tested for a changing supply voltage, rather than for a step in the reference current, it produced an undesirable response. While the controller was active around the peak of the supply voltage, as desired, it resulted in a large overshoot in the supply current. The controller was tuned by heuristically changing the position of the closed-loop poles until a more desirable response was obtained. The tuned controller was able to regulate the supply current around a fixed value near the peak of the supply voltage and produced a duty cycle  $d = 1.0 = 100\%$  when the supply voltage deviated from its

peak. This allowed the HDMS to enter region 2, which is critical to its operation. The controller design was verified in the component-level simulation model and in the hardware prototype.

In Chapter 7, the proposed state feedback regulator and the HDMS prototype current controller were compared for their performance. Three controller settings were proposed, with different supply current values. The controller settings were designed and then tested in the component-level simulation model for both controllers. Their operation was then confirmed in the HDMS hardware prototype. The tests consisted of locked rotor tests and motor soft-starts. The locked rotor tests evaluated the controllers' supply and motor winding current amplitudes in terms of their peak and RMS values. The resulting starting torque was also recorded. The motor soft-starts confirmed the controllers' ability to soft-start the motor and the resulting starting time was approximated. Flicker tests were also carried out for both locked rotor and motor soft-starting tests. The flicker tests were carried out in compliance with IEC 61000-3-11 and the custom parameters provided by this dissertation's industrial partner. The 40% HDMS prototype current controller design was found to provide the best trade-off between the supply current reduction, starting torque and flicker test results. It was hence chosen for robustness testing, where the controller's response was evaluated for changes in the motor winding and grid impedance parameters. It was concluded that it remains operational for a  $\pm 50\%$  variation in the motor winding parameters. However, it might need some adjustment in the controller parameters  $K_1$  and  $K_I$  in order to remain operational for large increases in the grid impedance, as this will lower the resonance frequency of the Buck converter's LC input filter.

# Chapter 9

## Future Work

Further work for this dissertation may be dedicated to an investigation into the data acquisition RC low-pass filters in order to find the most optimal cut-off frequency. This may further raise the system stability, as in this dissertation the low-pass filters have been analytically proven to significantly improve system stability.

In addition, the state feedback regulator design procedure may be improved through the application of gain scheduling. Gain scheduling may enhance the state feedback regulator's design procedure as the controller is based on a linearised system model. The large changes in supply voltage cause the system to deviate greatly from the equilibrium point used for the controller design.

Lastly, more extensive testing may be carried out for different combinations of the HDMS prototype current controller parameters  $i_{ref}$ ,  $K_I$  and  $K_1$  in order to obtain the most optimal starting torque and flicker test results. For this, a more detailed flicker test analysis may be carried out. Such an analysis would comprise a comprehensive investigation into the exact effect of the controller parameters on the supply current shape and subsequently their effect on the flicker test results.

# References

- [1] K. Ogata, *Modern Control Engineering Fifth Edition*. London, England: Pearson, 2010.
- [2] J.-J. E. Slotine and W. Li, *Applied Nonlinear Control*. Upper Saddle River, New Jersey 07458: Prentice Hall, 1991.
- [3] H. K. Khalil, *Nonlinear Systems Third Edition*. Upper Saddle River, New Jersey 07458: Prentice Hall, 2002.
- [4] N. Daw, “Comparison of lab work and simulation results for speed control of single phase induction motor capacitor starting,” 12 2016, pp. 397–402.
- [5] A. Alnaib, *Single-Phase Induction Motors*, 05 2019.
- [6] Electrical4U, “Single phase induction motor,” <https://www.electrical4u.com/single-phase-induction-motor/>.
- [7] J. Rees, M. Kjellberg, and S. Kling, *Softstarter Handbook*, ABB, November 2010.
- [8] MachineDesign, “Soft starters,” <https://www.machinedesign.com/learning-resources/engineering-essentials/article/21833971/soft-starters>.
- [9] L. Zhang, D. Luo, L. Su, D. Cao, and Z. Luo, “Design of a dc motor soft start based on avr microcontroller,” in *Applied Mechanics and Materials*, vol. 55-57, 2011, pp. 382–387.
- [10] L. Guangqiang, L. Guangfu, Y. Hongxiang, and J. Yanchao, “Energy conservation of a novel soft starter controlled by igbt for induction motors with minimum current,” in *2004 IEEE International Symposium on Industrial Electronics*, vol. 2, 2004, pp. 1351–1356.

- 
- [11] L. Tie and J. Le-jia, "Adaptive neuro fuzzy based soft starting of dc motor," in *2010 International Conference on Electrical and Control Engineering*, 2010, pp. 3261–3264.
- [12] M. G. Giesselmann, "Averaged and cycle by cycle switching models for buck, boost, buck-boost and cuk converters with common average switch model," in *IECEC-97 Proceedings of the Thirty-Second Intersociety Energy Conversion Engineering Conference (Cat. No.97CH6203)*, vol. 1, 1997, pp. 337–341 vol.1.
- [13] "Arm cortex-m4 32b mcu+fpu, 210dmips, up to 1mb flash/192+4kb ram, usb otg hs/fs, ethernet, 17 tims, 3 adcs, 15 comm. interfaces and camera," STMicroelectronics, Tech. Rep. STM32F407xx.
- [14] A. V. Oppenheim, *Discrete Time Signal Processing Third Edition*, 3rd ed. Upper Saddle River, NJ: Pearson Higher Education, 8 2009.
- [15] A. Boglietti, A. Cavagnino, and M. Lazzari, "Computational algorithms for induction-motor equivalent circuit parameter determination—part i: Resistances and leakage reactances," *Industrial Electronics, IEEE Transactions on*, vol. 58, pp. 3723 – 3733, 10 2011.
- [16] A. K. Shogenov, "On equivalent circuits of low-power high-frequency induction motors powered by transistor frequency converters," *Russian electrical engineering*, vol. 91, pp. 385–389, 6 2020.
- [17] "Electromagnetic compatibility (emc) - part 3-11: Limits - limitation of voltage changes, voltage fluctuations and flicker in public low-voltage supply systems - equipment with rated current less than or equal to 75a and subject to conditional connection," <https://webstore.iec.ch/publication/27902>, International Electrotechnical Commission (IEC).
- [18] "Fc22 compression load cell," TE Connectivity, Tech. Rep. FC2231-0000-0050-L.
- [19] G. F. Franklin, J. D. Powell, and A. Emami-Naeini, *Feedback Control of Dynamic Systems Third Edition*. Addison-Wesley, 1993.
- [20] W. L. Brogan, *Modern Control Theory Second Edition*. Englewood Cliffs, New Jersey 07632: Prentice Hall, 1985.
- [21] "Three-phase flicker impedances up to 75a," AMETEK, Tech. Rep. AIF 503N SERIES.

- [22] N. Ltd, “Electromagnetic compatibility – iec61000-3-3:2013 a technical guide to flicker measurement,” <https://www.newtons4th.com/electromagnetic-compatibility-iec61000-3-32013-flicker-analysis/>.

# Appendix A

## Flicker Test Reports

Flicker Results					
Standard Specific Results for IEC 61000-3-11 (Edition 1)					
Standard Group:	Industry				
Standard Name:	IEC 61000-3-11 (Edition 1) Limitation of voltage changes, voltage fluctuations and flicker in public low-voltage supply systems - Equipment with rated current $\leq 75$ A and subject to conditional connection				
Test Condition:	Customized				
Analysis Status:	FAIL				
Flicker Measurements Settings					
Main line:	230V, 50Hz				
Flicker Meter:	230V / 50Hz				
Flicker Impedance:	Ztest				
Observation Time:	1 x 10 min				
Measurements performed:	1				
Flicker Measurements					
	P <sub>It</sub>	Max P <sub>st</sub>	Max D <sub>c</sub>	Max D <sub>max</sub>	Max T <sub>max</sub>
Line 1:	0.889	2.036	9.456	9.912	0.55
Limits:	0.65	1	3.3	6	0.5
Results:	FAIL	FAIL	FAIL	FAIL	FAIL

FIGURE A.1: DOL flicker test result for locked rotor test

Flicker Results					
Standard Specific Results for IEC 61000-3-11 (Edition 1)					
Standard Group:	Industry				
Standard Name:	IEC 61000-3-11 (Edition 1) Limitation of voltage changes, voltage fluctuations and flicker in public low-voltage supply systems - Equipment with rated current $\leq 75$ A and subject to conditional connection				
Test Condition:	Customized				
Analysis Status:	FAIL				
Flicker Measurements Settings					
Main line:	230V, 50Hz				
Flicker Meter:	230V / 50Hz				
Flicker Impedance:	Ztest				
Observation Time:	1 × 10 min				
Measurements performed:	1				
Flicker Measurements					
	P <sub>It</sub>	Max P <sub>st</sub>	Max D <sub>c</sub>	Max D <sub>max</sub>	Max T <sub>max</sub>
Line 1:	0.694	1.589	0.616	10.111	0.85
Limits:	0.65	1	3.3	6	0.5
Results:	FAIL	FAIL	PASS	FAIL	FAIL

FIGURE A.2: DOL flicker test result for soft-start

Flicker Results					
Standard Specific Results for IEC 61000-3-11 (Edition 1)					
Standard Group:	Industry				
Standard Name:	IEC 61000-3-11 (Edition 1) Limitation of voltage changes, voltage fluctuations and flicker in public low-voltage supply systems - Equipment with rated current $\leq 75$ A and subject to conditional connection				
Test Condition:	Customized				
Analysis Status:	PASS				
Flicker Measurements Settings					
Main line:	230V, 50Hz				
Flicker Meter:	230V / 50Hz				
Flicker Impedance:	Ztest				
Observation Time:	1 $\times$ 10 min				
Measurements performed:	1				
Flicker Measurements					
	$P_{It}$	Max $P_{st}$	Max $D_c$	Max $D_{max}$	Max $T_{max}$
Line 1:	0.217	0.497	0.026	1.967	0
Limits:	0.65	1	3.3	6	0.5
Results:	PASS	PASS	PASS	PASS	PASS

FIGURE A.3: 30% state feedback regulator flicker test result for locked rotor test

Flicker Results					
Standard Specific Results for IEC 61000-3-11 (Edition 1)					
Standard Group:	Industry				
Standard Name:	IEC 61000-3-11 (Edition 1) Limitation of voltage changes, voltage fluctuations and flicker in public low-voltage supply systems - Equipment with rated current $\leq 75$ A and subject to conditional connection				
Test Condition:	Customized				
Analysis Status:	PASS				
Flicker Measurements Settings					
Main line:	230V, 50Hz				
Flicker Meter:	230V / 50Hz				
Flicker Impedance:	Ztest				
Observation Time:	1 $\times$ 10 min				
Measurements performed:	1				
Flicker Measurements					
	$P_{It}$	Max $P_{st}$	Max $D_c$	Max $D_{max}$	Max $T_{max}$
Line 1:	0.177	0.405	1.856	2.004	0
Limits:	0.65	1	3.3	6	0.5
Results:	PASS	PASS	PASS	PASS	PASS

FIGURE A.4: 30% state feedback regulator flicker test result for soft-start

Flicker Results					
Standard Specific Results for IEC 61000-3-11 (Edition 1)					
Standard Group:	Industry				
Standard Name:	IEC 61000-3-11 (Edition 1) Limitation of voltage changes, voltage fluctuations and flicker in public low-voltage supply systems - Equipment with rated current $\leq 75$ A and subject to conditional connection				
Test Condition:	Customized				
Analysis Status:	PASS				
Flicker Measurements Settings					
Main line:	230V, 50Hz				
Flicker Meter:	230V / 50Hz				
Flicker Impedance:	Ztest				
Observation Time:	1 $\times$ 10 min				
Measurements performed:	1				
Flicker Measurements					
	$P_{fk}$	Max $P_{st}$	Max $D_c$	Max $D_{max}$	Max $T_{max}$
Line 1:	0.231	0.53	0.025	2.043	0
Limits:	0.65	1	3.3	6	0.5
Results:	PASS	PASS	PASS	PASS	PASS

FIGURE A.5: 30% HDMS prototype current controller flicker test result for locked rotor test

Flicker Results					
Standard Specific Results for IEC 61000-3-11 (Edition 1)					
Standard Group:	Industry				
Standard Name:	IEC 61000-3-11 (Edition 1) Limitation of voltage changes, voltage fluctuations and flicker in public low-voltage supply systems - Equipment with rated current $\leq 75$ A and subject to conditional connection				
Test Condition:	Customized				
Analysis Status:	PASS				
Flicker Measurements Settings					
Main line:	230V, 50Hz				
Flicker Meter:	230V / 50Hz				
Flicker Impedance:	Ztest				
Observation Time:	1 $\times$ 10 min				
Measurements performed:	1				
Flicker Measurements					
	$P_{It}$	Max $P_{st}$	Max $D_c$	Max $D_{max}$	Max $T_{max}$
Line 1:	0.156	0.357	1.94	2.144	0
Limits:	0.65	1	3.3	6	0.5
Results:	PASS	PASS	PASS	PASS	PASS

FIGURE A.6: 30% HDMS prototype current controller flicker test result for soft-start

Flicker Results					
Standard Specific Results for IEC 61000-3-11 (Edition 1)					
Standard Group:	Industry				
Standard Name:	IEC 61000-3-11 (Edition 1) Limitation of voltage changes, voltage fluctuations and flicker in public low-voltage supply systems - Equipment with rated current $\leq 75$ A and subject to conditional connection				
Test Condition:	Customized				
Analysis Status:	PASS				
Flicker Measurements Settings					
Main line:	230V, 50Hz				
Flicker Meter:	230V / 50Hz				
Flicker Impedance:	Ztest				
Observation Time:	1 $\times$ 10 min				
Measurements performed:	1				
Flicker Measurements					
	$P_{It}$	Max $P_{st}$	Max $D_c$	Max $D_{max}$	Max $T_{max}$
Line 1:	0.354	0.812	0.057	3.48	0.21
Limits:	0.65	1	3.3	6	0.5
Results:	PASS	PASS	PASS	PASS	PASS

FIGURE A.7: 40% state feedback regulator flicker test result for locked rotor test

Flicker Results					
Standard Specific Results for IEC 61000-3-11 (Edition 1)					
Standard Group:	Industry				
Standard Name:	IEC 61000-3-11 (Edition 1) Limitation of voltage changes, voltage fluctuations and flicker in public low-voltage supply systems - Equipment with rated current $\leq 75$ A and subject to conditional connection				
Test Condition:	Customized				
Analysis Status:	PASS				
Flicker Measurements Settings					
Main line:	230V, 50Hz				
Flicker Meter:	230V / 50Hz				
Flicker Impedance:	Ztest				
Observation Time:	1 $\times$ 10 min				
Measurements performed:	1				
Flicker Measurements					
	$P_{It}$	Max $P_{St}$	Max $D_c$	Max $D_{max}$	Max $T_{max}$
Line 1:	0.277	0.634	3.269	3.452	0.41
Limits:	0.65	1	3.3	6	0.5
Results:	PASS	PASS	PASS	PASS	PASS

FIGURE A.8: 40% state feedback regulator flicker test result for soft-start

Flicker Results					
Standard Specific Results for IEC 61000-3-11 (Edition 1)					
Standard Group:	Industry				
Standard Name:	IEC 61000-3-11 (Edition 1) Limitation of voltage changes, voltage fluctuations and flicker in public low-voltage supply systems - Equipment with rated current $\leq 75$ A and subject to conditional connection				
Test Condition:	Customized				
Analysis Status:	PASS				
Flicker Measurements Settings					
Main line:	230V, 50Hz				
Flicker Meter:	230V / 50Hz				
Flicker Impedance:	Ztest				
Observation Time:	1 $\times$ 10 min				
Measurements performed:	1				
Flicker Measurements					
	$P_{\text{t}}$	Max $P_{\text{st}}$	Max $D_{\text{c}}$	Max $D_{\text{max}}$	Max $T_{\text{max}}$
Line 1:	0.352	0.807	0.046	3.28	0
Limits:	0.65	1	3.3	6	0.5
Results:	PASS	PASS	PASS	PASS	PASS

FIGURE A.9: 40% HDMS prototype current controller flicker test result for locked rotor test

Flicker Results					
Standard Specific Results for IEC 61000-3-11 (Edition 1)					
Standard Group:	Industry				
Standard Name:	IEC 61000-3-11 (Edition 1) Limitation of voltage changes, voltage fluctuations and flicker in public low-voltage supply systems - Equipment with rated current $\leq 75$ A and subject to conditional connection				
Test Condition:	Customized				
Analysis Status:	PASS				
Flicker Measurements Settings					
Main line:	230V, 50Hz				
Flicker Meter:	230V / 50Hz				
Flicker Impedance:	Ztest				
Observation Time:	1 $\times$ 10 min				
Measurements performed:	1				
Flicker Measurements					
	$P_{It}$	Max $P_{St}$	Max $D_c$	Max $D_{max}$	Max $T_{max}$
Line 1:	0.24	0.549	3.138	3.282	0
Limits:	0.65	1	3.3	6	0.5
Results:	PASS	PASS	PASS	PASS	PASS

FIGURE A.10: 40% HDMS prototype current controller flicker test result for soft-start

Flicker Results					
Standard Specific Results for IEC 61000-3-11 (Edition 1)					
Standard Group:	Industry				
Standard Name:	IEC 61000-3-11 (Edition 1) Limitation of voltage changes, voltage fluctuations and flicker in public low-voltage supply systems - Equipment with rated current $\leq 75$ A and subject to conditional connection				
Test Condition:	Customized				
Analysis Status:	FAIL				
Flicker Measurements Settings					
Main line:	230V, 50Hz				
Flicker Meter:	230V / 50Hz				
Flicker Impedance:	Ztest				
Observation Time:	1 $\times$ 10 min				
Measurements performed:	1				
Flicker Measurements					
	$P_{\text{f}}$	Max $P_{\text{st}}$	Max $D_{\text{c}}$	Max $D_{\text{max}}$	Max $T_{\text{max}}$
Line 1:	0.518	1.187	0.08	5.11	0.51
Limits:	0.65	1	3.3	6	0.5
Results:	PASS	FAIL	PASS	PASS	FAIL

FIGURE A.11: 50% state feedback regulator flicker test result for locked rotor test

Flicker Results					
Standard Specific Results for IEC 61000-3-11 (Edition 1)					
Standard Group:	Industry				
Standard Name:	IEC 61000-3-11 (Edition 1) Limitation of voltage changes, voltage fluctuations and flicker in public low-voltage supply systems - Equipment with rated current $\leq 75$ A and subject to conditional connection				
Test Condition:	Customized				
Analysis Status:	FAIL				
Flicker Measurements Settings					
Main line:	230V, 50Hz				
Flicker Meter:	230V / 50Hz				
Flicker Impedance:	Z <sub>test</sub>				
Observation Time:	1 × 10 min				
Measurements performed:	1				
Flicker Measurements					
	P <sub>it</sub>	Max P <sub>st</sub>	Max D <sub>c</sub>	Max D <sub>max</sub>	Max T <sub>max</sub>
Line 1:	0.408	0.935	0.518	5.114	1.06
Limits:	0.65	1	3.3	6	0.5
Results:	PASS	PASS	PASS	PASS	FAIL

FIGURE A.12: 50% state feedback regulator flicker test result for soft-start

Flicker Results					
Standard Specific Results for IEC 61000-3-11 (Edition 1)					
Standard Group:	Industry				
Standard Name:	IEC 61000-3-11 (Edition 1) Limitation of voltage changes, voltage fluctuations and flicker in public low-voltage supply systems - Equipment with rated current $\leq 75$ A and subject to conditional connection				
Test Condition:	Customized				
Analysis Status:	FAIL				
Flicker Measurements Settings					
Main line:	230V, 50Hz				
Flicker Meter:	230V / 50Hz				
Flicker Impedance:	Ztest				
Observation Time:	1 $\times$ 10 min				
Measurements performed:	1				
Flicker Measurements					
	$P_{it}$	Max $P_{st}$	Max $D_c$	Max $D_{max}$	Max $T_{max}$
Line 1:	0.492	1.127	0.074	4.837	0.51
Limits:	0.65	1	3.3	6	0.5
Results:	PASS	FAIL	PASS	PASS	FAIL

FIGURE A.13: 50% HDMS prototype current controller flicker test result for locked rotor test

Flicker Results					
Standard Specific Results for IEC 61000-3-11 (Edition 1)					
Standard Group:	Industry				
Standard Name:	IEC 61000-3-11 (Edition 1) Limitation of voltage changes, voltage fluctuations and flicker in public low-voltage supply systems - Equipment with rated current $\leq 75$ A and subject to conditional connection				
Test Condition:	Customized				
Analysis Status:	FAIL				
Flicker Measurements Settings					
Main line:	230V, 50Hz				
Flicker Meter:	230V / 50Hz				
Flicker Impedance:	Ztest				
Observation Time:	1 $\times$ 10 min				
Measurements performed:	1				
Flicker Measurements					
	$P_{It}$	Max $P_{st}$	Max $D_c$	Max $D_{max}$	Max $T_{max}$
Line 1:	0.371	0.849	0.534	4.842	1.07
Limits:	0.65	1	3.3	6	0.5
Results:	PASS	PASS	PASS	PASS	FAIL

FIGURE A.14: 50% HDMS prototype current controller flicker test result for soft-start